Singlet exciton fission-enhanced silicon photovoltaics: Interfacial engineering, device design and spectroscopic technique development

by

Narumi Nagaya

M.Eng., Imperial College London (2019)

Submitted to the Department of Chemical Engineering
in partial fulfillment of the requirements for the degree of
DOCTOR OF PHILOSOPHY IN CHEMICAL ENGINEERING
at the
MASSACHUSETTS INSTITUTE OF TECHNOLOGY
February 2025

Authored by: ________________________________
Narumi Nagaya
Department of Chemical Engineering
September 22nd, 2024

Certified by: ________________________________
William A. Tisdale
Warren K. Lewis Professor in Chemical Engineering
Thesis Supervisor

Certified by: ________________________________
Marc A. Baldo
Dugald C. Jackson Professor in Electrical Engineering and Computer Science
Director, Research Laboratory of Electronics
Thesis Supervisor

Accepted by: ________________________________
Hadley D. Sikes
Willard Henry Dow Professor in Chemical Engineering
Graduate Officer

Singlet exciton fission-enhanced silicon photovoltaics: Interfacial engineering, device design and spectroscopic technique development

By

Narumi Nagaya

Submitted to the Department of Chemical Engineering on September 22nd, 2024 in partial fulfillment of the requirements for the degree of Doctor of Philosophy in Chemical Engineering

Abstract

The growing global energy demand combined with resource and space limitations necessitate enhancements in crystalline silicon solar cells, which are the current dominant solar technology. However, their efficiencies have only increased incrementally over the recent 20 years, as they are starting to approach the theoretical efficiency limit. The main source of loss is thermalization, where energy in excess of the bandgap absorbed by silicon is lost as heat. Singlet exciton fission in organic molecules has been proposed to reduce these losses. By having the organic layer absorb the high energy light and transferring the triplet excitons generated from the singlet fission process to silicon, the photocurrent in this spectral region can be doubled, with the potential of raising the efficiency from the traditional limit of 29.4 % to up to 42 %.

The greatest challenge with these devices has been to demonstrate an increase in the silicon photocurrent, a necessary condition to show that the technology is viable. Scientifically, there are three main components to this problem. The first is to successfully couple the triplet excitons to silicon. The second is that not much is understood regarding the exciton and charge carrier dynamics at this interface. Finally, the silicon solar cell architecture should also be considered to extract transferred carriers effectively.

This thesis tackles these three parts from an interfacial materials, device architecture and spectroscopy approach. Using tetracene as the singlet fission layer and n-doped silicon, we show that defect-induced states in a thin interlayer of hafnium oxynitride that lie near the band edge of silicon are beneficial for triplet exciton transfer. We also identify that triplet-induced electric field-effect passivation is beneficial for the triplet sensitization process of silicon, and design a new bilayer interface consisting of a zinc phthalocyanine donor layer that introduces preferential near-silicon band edge states, and an ultrathin oxide chemical passivation layer. We then study various device architectures, confirming the importance of using a device designed to extract surface charge carriers efficiently, demonstrating the first enhancements in single-junction silicon solar cell external quantum efficiencies and photocurrent from singlet fission. Finally, we build and use advanced spectroscopy techniques and numerical frameworks to study exciton and charge carrier dynamics in singlet fission-sensitized solar cell materials, confirming that the triplet excitons are contributing to all the positive effects observed in the devices.

These results have shown that singlet fission-sensitized silicon solar cells are a viable technology for enhancing silicon solar cell efficiencies beyond the conventional single-junction limit. This interface remains a rich area for fundamental scientific studies, involving coupling between molecular dark states to bulk silicon. We hope that the key findings can help direct research efforts towards scalable implementation of this technology, and stress that the fundamental understanding of the interface also has broad implications to other silicon technologies that can benefit from enhanced quantum yields, including photodetectors.

Thesis supervisor: William A. Tisdale
Title: Warren K. Lewis Professor of Chemical Engineering

Thesis supervisor: Marc A. Baldo
Title: Dugald C. Jackson Professor of Electrical Engineering and Computer Science
Director, Research Lab of Electronics

Acknowledgements

Throughout my time at MIT, I was very fortunate to receive the help and support of many wonderful people as part of my PhD journey. First and foremost, I would like to thank my research advisors, Professors Marc Baldo and Will Tisdale. Their combined mentorship, guidance, enthusiasm and approach to research have shaped my growth throughout graduate school. I am lucky to have had the opportunity to be a part of two different labs, gaining skills in both device fabrication and spectroscopy. Marc, I am particularly grateful for your generosity with time. Your willingness to make time for all of my questions, ideas and discussions ultimately led to many of our breakthroughs in this thesis. Will, I am particularly grateful for your flexibility. Thanks to you, I was able to explore the overarching research question from multiple avenues, which allowed me to gain a well-rounded perspective as a scientist and as an engineer. Outside of science, I also highly appreciate how both of you truly cared about my wellbeing, providing support and helping me get through when things were tough. You are both great role models for me, not just in research, but also in life.

I would also like to thank my thesis committee members, Professors Bill Green and Vladimir Bulovic, for asking many insightful questions and providing advice, proposing interesting new ideas and perspectives to my results, and offering support as I needed during my thesis committee meetings.

A huge part of my PhD experience has been the opportunity to work alongside some of the most brilliant researchers in both labs. From the Baldo lab, I would like to thank Cole Perkinson in particular, for being the best mentor and lab partner I could have asked for when I first joined the project, teaching me everything from cleanroom skills, handling the Old Angstrom (over phone zoom with the tripod!), magnetic field-dependent silicon spectroscopy (much love to the comically large focusing lens), and most importantly how to be a good scientist and a good person. I look back fondly over our many conversations in the office debating about the interpretation of our latest results, and our fun times together both in and outside of the lab. I would also like to thank the other past and current members of the singlet fission solar cell team: Alice Wu, Kangmin Lee, Aaron Li, Janet Wang, Willem Verheijen, Jaekang Song, Tomi Baikie. In particular, many thanks to Kangmin, to whom I owe most of my knowledge about silicon solar cells. Without his support and his immense understanding of the fundamentals of silicon solar cells, our singlet fission cells would not be anywhere near where they are now. Huge shoutout to Aaron as well, who brought many interesting perspectives that I hadn't considered when discussing different observations, and for always being willing to help me with additional experiments. Janet: Although our overlap was short, I had a lot of fun times both in the lab and outside with you. Beyond the fission team, I would also like to give a shoutout to Oliver Nix for our many discussions on the fundamentals and origins of magnetic field effects, and for all his work on restoring the Old Angstrom back to operation. Ting-An Lin, thank you for being a great office-mate. Our numerous coffee breaks helped me get through long fab days. Jan Tiepelt, thank you for always being willing to help improve lab infrastructure – your 3D-printed holders saved us a lot of time in our measurements. I would also like to thank all other former and current members of the Baldo lab that I overlapped with: Joseph Finley, Dong-Gwang Ha, Brooke McGoldrick, Dooyong Koh, and our wonderful group administrator Cathy Bourgeois.

From the Tisdale lab, I would like to thank the members of team Spirit bay: Nannan Mao, Eric Powers, Chana Honick, Maya Chattoraj and Tejas Deshpande. In particular, Nannan taught

me the art of SHG microscopy, and helped tremendously with the z-polarized SHG microscopy setup and setting up the PMT for the transient SHG setup. Eric taught me all I know about the NOPA, and has also been an exemplary labmate who I turned to for advice as I progressed through my PhD. Chana contributed significantly to my growth as an ultrafast spectroscopist, helping me brainstorm ideas for finding time zero and suggesting different ways to make my setup better. I would also like to give a huge shoutout to Maya for working with me on the transient SHG and TA setups, and more importantly, for being an encouraging and supportive close friend, gym buddy and fellow ARMY. In my early PhD days, I learnt a lot from Kris Williams and Wenbi Shcherbakov-Wu who mentored me on the Montana diffusion imaging setup and taught me basic spectroscopy skills. I would also like to thank Seung Kyun Ha for preparing high quality perovskite single crystal samples for diffusion imaging. Thank you to Woo Seok Lee, fellow Tisdale lab cohort member, who has been with me since day one. Eliza Price: thank you for our conversations on the minute details of the MCMC fitting algorithm and for a fantastic time together at AIChE. Thomas Sheehan: thank you for your support with various one-off experiments in the Mira bay, including showing me how to use the transient PL setup and the IR APD, and for fun times outside of the lab. Thank you as well to Nick Samulewicz and Justin Griffith for goofy times both in the office and outside. The Tisdale lab has been a fantastic place for learning and support, and I would like to thank all other former and current Tisdale lab members that I overlapped with who contributed to this lovely environment: Sam Winslow, Abby Taussig, Oat Paritmongkol, Tomoaki Sakurada, Fabio Marangi, Ruomeng Wan, Niamh Brown, Seryio Saris, Jimin Kwag, Giulia Lo Gerfo Morganti, and our delightful group administrator Barb Balkwill.

Many of the results in this thesis would not have been possible without the support of my fantastic collaborators. I would like to thank Alexa Alexiu, Leah Weisburn and Professor Troy Van Voorhis for providing much of the theory support to our singlet fission experimental results. I would also like to acknowledge the support of Professor Moungi Bawendi for access to their laser lab for excitation wavelength-dependent measurements and the InGaAs detector for silicon spectroscopy. I am deeply appreciative for our collaboration with Youri Lee and Professor Kwanyong Seo at UNIST for sending us high quality silicon solar cells to work with. I am very thankful to Xinjue Zhong, Sujin Lee and Professor Antoine Kahn at Princeton University for the ultraviolet photoelectron spectroscopy measurements, and for being wonderful hosts during my brief visit. I would like to thank Professor Jim Swan, for his vast knowledge of numerical methods. I fondly remember our meetings where I would present code which he would take a look at and come back to me with code that ran 1000x faster, and patiently explain all the different numerical tricks that he used to do so. I am also extremely grateful to Zachary VanOrman and Professor Sascha Feldmann for access to their transient absorption and reflection setup during the time that the Spirit laser was sent away for repair. I also acknowledge the support of the facilities and staff at MIT.nano and MRL.

Outside of research, my friends were an important part of my PhD journey. I would like to thank the friends I made in MIT ChemE, particularly Wanny Wu, Devashish Gokhale, Sungyun Yang, Era Chen, Pavan Inguva, Kelsey Reed, Abdul AlMashaan, Jing Ying Yeo, K'yal Bannister, Pushkal Sharma, Dousabel Tay, and Jianqiao Cui, many of whom were key to getting me through the first semester of classes. I would also like to thank the officer crew at Ashdown for our marathon karaoke sessions, particularly Shek Nga Chan, Akhilan Boopathy, Lisa Lin, Wentao Cui, Bunyamin Kartal, Ufuk Keskin, Christina Ji, Ian Sabula, Tzu-An Sheng, Haochen Wang, Raymond Wang, and Zheng Dai. My fellow intern friends from Apple, Kevin Kam and Ye Zhang,

thank you for our AP dinners and biking sessions. I would also like to thank my friends around the world, Michelle Lai, Michelle Wong, Phoebe Tso and Jess Quigley for their ongoing support throughout my journey at graduate school.

Finally, I would like to give many thanks to T. for their unwavering support, patience, and our countless hours of going down rabbit holes from interesting papers, Wikipedia articles, to random shenanigans. And last but not least, to my brother, my dad and my mom: thank you for always being there for me throughout this journey. Thank you for believing in me. I could not have made it this far without your constant encouragement, advice and support.

Table of Contents

List of Figures

List of Tables

Chapter 1.
Introduction

Global energy consumption has been steadily on the rise since the Industrial Revolution[1]. A plot of the consumption from the year 1800 onwards is presented in Figure 1-1. Despite the progress in recent years in shifting towards renewable resources for producing energy, fossil fuel sources continue to dominate the energy production.

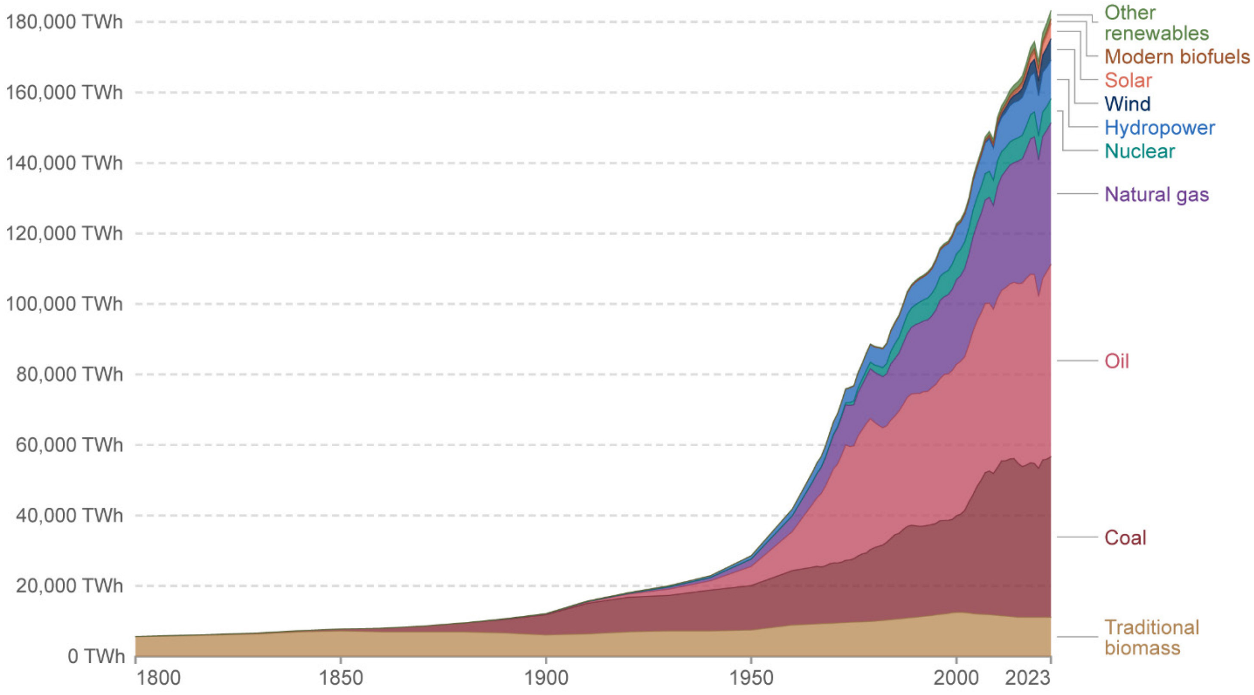

Figure 1-1. Global primary energy consumption over the years by source. Reproduced with permission from Ritchie *et al.*[2], using data from Energy Institute[1] and Smil[3].

The Sun is a key source of renewable energy – the amount of energy that reaches the Earth, if it can be harnessed, is more than enough to meet the rising global energy demand[4]. One of the most valuable conversion processes for utilizing the energy from the Sun is through the photovoltaic effect, where energy from light is converted to electricity.

The market for photovoltaics has been growing rapidly over the past 10 years, due in part to dramatic reductions in pricing, increased production particularly in China, and subsidy policies around the world[5,6]. Crystalline-silicon (*c*-Si) solar cells continue to dominate solar cell technology, accounting for 97 % of the total global production in 2023[5].

However, Figure 1-1 shows that in 2023, solar energy only constituted about 2.3 % of the total energy consumption[2]. Although costs of solar energy are no longer as big of a barrier to implementation of solar than they were several years ago, some cited oppositions to installation include visual concerns and loss of agricultural land[7]. Additionally, there are concerns regarding the overall sustainability of silicon module production, given the large energy costs required to process crystalline-silicon at high purities needed for silicon solar cells[8–10]. As a result, there is a need to improve efficiencies of silicon solar cells for better space and resource utilization, and reduce the net energy cost for the life cycle of silicon modules.

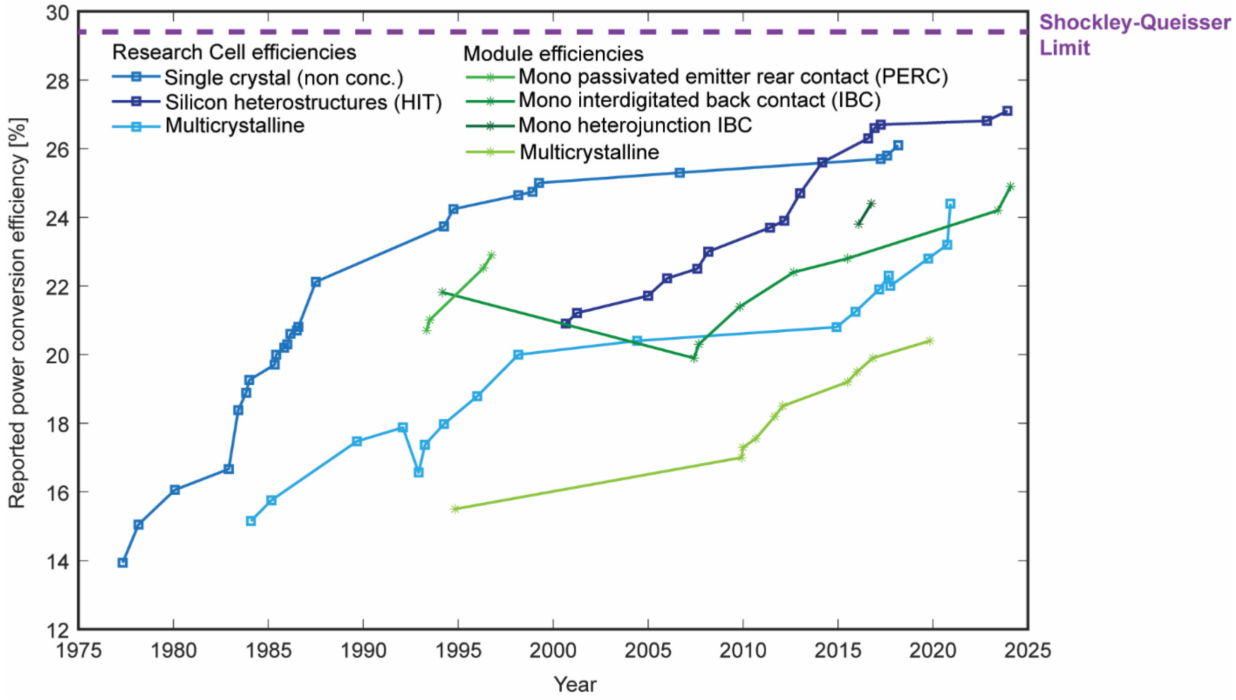

Figure 1-2. Record efficiencies of crystalline-silicon research cells (squares) and modules (stars) plotted over the years. Data for the research cells[11] and modules[12] were obtained from NREL. The Shockley-Queisser limit for single-junction crystalline-silicon solar cells[13,14] is plotted as a dashed purple line for reference.

The efficiencies of crystalline-silicon research cells and modules over the years have been plotted in Figure 1-2. Notably, improvements in efficiencies for *c*-Si cells relative to other technologies have been slow, especially from the mid-1990s onwards, as these cells are starting to approach the theoretical single-junction efficiency limit, also known as the Shockley-Queisser limit[13], of 29.4 %[14]. For reference, the current record silicon lab cell is at 27.3 %[15,16]. Thus, new technologies to overcome the theoretical limit are of utmost interest, and form the main motivation for the research presented in this dissertation.

1.1. Conventional theoretical efficiency limit for crystalline-silicon solar cells

In the most general case, the Carnot efficiency limit for a terrestrial solar cell, as governed by the Second Law of Thermodynamics, is given by $\eta = 1 - T_{sc}/T_{sun} = 95\ \%$[17]. Here, we assume that the Sun can be described as a black-body with a temperature of 6000 K and that the solar cell is at 300 K. We note that this derivation is not specific to the nature of energy conversion, and could apply not just to the conversion of the Sun's heat to electricity generated by a solar cell, but also to any other form of solar energy conversion. However, this calculation assumes that there is no entropy generated in the process of transmission, absorption and conversion of sunlight, which Planck has shown to be untrue[18].

Instead, a more realistic efficiency limit accounting for entropy can be obtained by treating the solar cell as a black-body absorber with reciprocal absorption and emission of light with the Sun[17]. This yields a 'direct' efficiency limit of $\eta_{dir} = 86.6\ \%$, where the term direct refers to the condition when all the light emitted by the cell is directed to the Sun, achievable in theory by solar tracking and concentrator optics. This efficiency limit can also be obtained by using a tandem-cell structure with an infinite number of cells and a solar concentrator[19]. In reality, the Earth's atmosphere scatters the sunlight to generate 'diffuse' light; accounting for this results in an efficiency limit of $\eta_{diff} = 68.2\ \%$[17].

The above efficiency calculations assumed an ideal absorber at each spectral energy. The crystalline-silicon solar cells currently on the market are single-junction solar cells, with a lower theoretical efficiency limit first proposed by Shockley and Queisser as the detailed-balance limit[13]. These cells are limited by a variety of loss processes, detailed in Figure 1-3. The energy that arrives from the Sun is wavelength-dependent, as shown in Figure 1-4. However, silicon has an indirect bandgap (E_g) of 1.1 eV. As a result, when silicon absorbs light from regions of the solar spectrum with energies greater than the bandgap, the hot carriers relax to the band edge through thermalization, producing heat, as depicted Figure 1-3a. These thermalization losses result in up to 33 % of the energy not being utilized by the cell (Figure 1-4)[20]. Additionally, silicon cannot absorb any of the light below its bandgap (Figure 1-3b), resulting in another 19 % loss[20]. Other losses include balancing between collection of electrons and holes before recombination (Figure 1-3c) and extracting these carriers at as high of an electrical potential (qV) as possible (Figure 1-3d), contributing to electronic losses. The maximum efficiency of a single-solar cell with a band gap of 1.1 eV (as is the case of silicon) is 29.4%[13,14] and the portion of the spectrum utilized is shown in Figure 1-4.

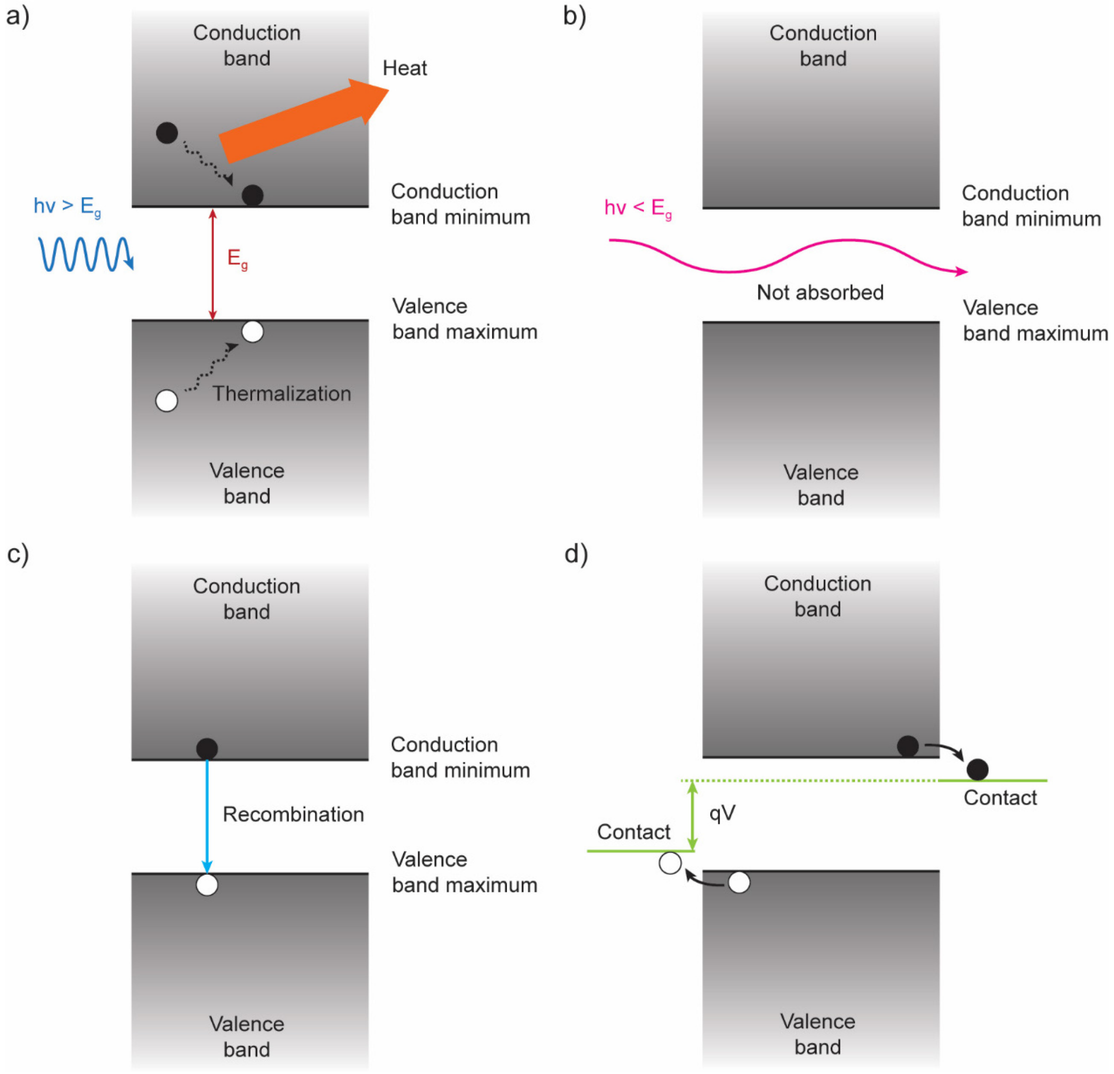

Figure 1-3. Diagram showing some of the loss processes for solar cells. a) Thermalization losses. When a photon of energy hν greater than the bandgap (E_g) is absorbed by the semiconductor, an electron is excited from the valence band to the conduction band, and the electrons and holes rapidly thermalize to the band edge. This process produces heat. b) Absorption losses. When a photon of energy hν less than the bandgap (E_g) is incident on the semiconductor, the energy is not absorbed by the cell. c) Electrons can relax to the valence band, resulting in recombination losses. This process can be radiative or non-radiative. d) Charge carriers need to be collected by contacts for useful electricity. Contact energies set the useable electronic energy qV, usually below the bandgap energy, contributing to electronic losses.

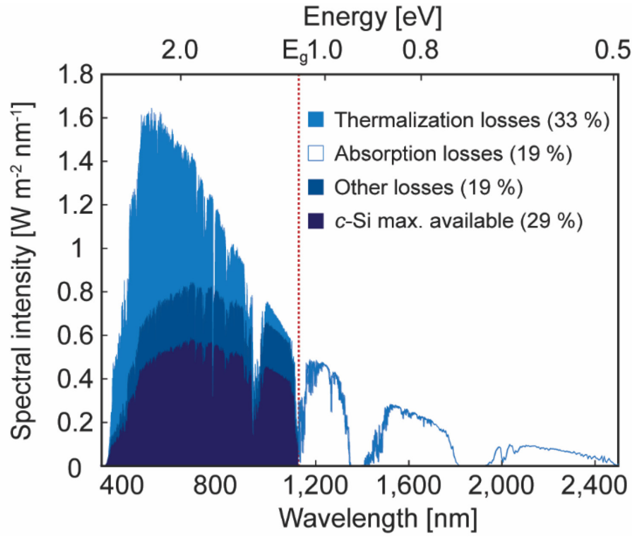

Figure 1-4. AM 1.5 terrestrial solar spectrum, with losses contributing to the *c*-Si single-junction theoretical efficiency limit shown. The silicon bandgap ($E_g = 1.1$ eV) is plotted in red for reference. Thermalization losses occur when photons above the bandgap are absorbed and the carriers thermalize to the band edge, producing heat. Absorption losses occur because photons below the bandgap are not absorbed. The maximum available solar energy is 29.4 %[13,14]. Loss fractions were calculated from Semonin *et al.*[20] and accounting for additional losses[14].

1.2. Singlet fission-sensitized silicon solar cells

The Shockley-Queisser limit assumes several conditions[13]:

1. One electron-hole pair per incoming excited photon
2. Thermalization of hot carriers
3. Illumination with non-concentrated light
4. Single-junction

Naturally, by overcoming these assumptions, it is possible to surpass the limit. Many configurations have been proposed to overcome these limitations, including tandem cells[19], use of concentrating optics[21,22], spectral shifting[23], photon upconversion[24,25], and carrier multiplication processes[26–29].

The most mature technology out of these options is the tandem configuration[19,30–32]. A tandem cell involves coupling two or more solar cells together, with each solar cell optimized for absorbing light at a certain frequency range of the spectrum. A typical two-cell tandem design would involve using a high bandgap solar cell on top to absorb the lower wavelength part of the solar spectrum, while transmitting the higher wavelength part of the spectrum through to the bottom cell which absorbs the remainder of the light. Popular material configurations include using a crystalline-silicon cell as the bottom cell, and perovskite solar cells as the top cell[33]. However, these structures involve many layers, optimization is complicated, and devices can be costly[31,32].

An alternative method for overcoming the single-junction limit is to use a phenomenon known as singlet exciton fission, a process found to occur in some organic semiconducting materials[34]. This process can be used to reduce thermalization losses by converting the energy from absorbing a high energy photon to two lower energy excited states. In 1979, D. L. Dexter first proposed the idea of coupling a singlet fission layer to a solar cell in order to enhance their efficiencies[27]. By using this singlet fission material as an extra coating layer on top of silicon solar cells, and transferring the energy from these lower energy excited states to the silicon cell[27], thermalization losses can be greatly reduced in addition to generating up to two electron-hole pairs per photon absorbed in the solar cell[26,28,29,35]. In theory, singlet fission has the potential to enhance silicon solar cell power conversion efficiencies from 29.4 % up to 35-42 %[26,36,28,37,38].

In contrast to their tandem counterparts, singlet fission-enhanced silicon solar cells have simpler structures that can be more easily integrated with existing silicon wafer fabrication processes, without additional changes needed to be made to the base silicon cell[38]. Materials for singlet fission may be deposited *via* solution-processing roll to roll techniques[39], or through vacuum thermal evaporation techniques (currently utilized at scale by the OLED industry)[40]. Without the need to current-match or optimize tunnel junctions as needed for series tandem cells[29], simulations suggest that singlet fission-enhanced silicon cells are also more robust to spectral changes, irradiation changes and temperature variations[41], expected during normal operation of a solar cell. Additionally, reduction of thermalization losses can also improve the lifespan of the silicon solar cell by ~15 % due to operating temperature reduction by the singlet fission layer[42].

1.3. Organization of thesis

Despite the huge potential for singlet fission-enhanced silicon solar cells, the longstanding challenge since the first proposal by Dexter in 1979 has been to couple the singlet fission layer to silicon solar cells and show improvements in the device performance. While quantum efficiencies over 100 % have been realized for organic solar cells using singlet fission[43], progress in sensitization of silicon has been challenging as transferring the low energy excited states, also known as triplet excitons, formed from singlet fission through the interface between organic semiconducting molecules and inorganic bulk semiconductors has not been well understood[44,45,35]. One of the primary difficulties has been understanding the mechanism for the transfer process and the role that the interface between the organic molecular semiconductor and the silicon surface plays in the transfer of the excited state, as seemingly depositing a singlet fission layer directly on silicon does not show an enhancement from the fission process[44–47].

Additionally, probing for the sensitization process of the silicon by the triplet excitons requires fabricating full devices[29], which may not yield improvements for reasons other than the lack of excited state transfer. Simpler spectroscopic probes are desired to better understand the materials in these solar cells and study how carriers behave in the bulk and at the interfaces to put together a mechanistic picture of the sensitization process.

The primary motivation of this thesis is to understand how to sensitize silicon solar cells using singlet exciton fission. The thesis is split into two parts, with the first part focusing on interfacial materials and device development, and the second part focusing on spectroscopic technique and data analysis development for studying the bulk materials and interfaces in singlet fission-sensitized silicon solar cells. In Part I, Chapter 2 provides the theory and background on excitons, singlet exciton fission, and operating principles of crystalline-silicon solar cells. Chapter 3 details a historical overview of the progress in singlet fission-sensitized silicon photovoltaics prior to this thesis work. Chapter 4 and Chapter 5 present a series of experimental material studies of the interface between the singlet fission material and the silicon layer. In particular, Chapter 4 combines computational calculations and composition-dependent experimental studies to explore the role of defect states in the triplet transfer process through hafnium oxynitride interlayers. Chapter 5 probes the role of triplet-driven passivation in the sensitization process of silicon by singlet fission through introduction of a new two-part interlayer designed specifically for a charge separation mechanism at the organic-silicon interface involving a donor layer (zinc phthalocyanine) and a passivating layer (ultra-thin oxide). Following the material studies, the role of device architecture is studied by incorporation of the new interlayer design in silicon-heterojunction and interdigitated back-contacted solar cells (Chapter 6) and shallow junction microwire and pyramidally-textured planar solar cells (Chapter 7). By careful interfacial material engineering and device architecture development, we demonstrate the *first increase in both* *crystalline-silicon photocurrent and power conversion efficiency* from direct transfer of triplet excitons.

In the second part of this thesis, we move from device-oriented studies to spectroscopy techniques for studying the carrier transport in these devices. For obtaining carrier dynamics and timescales of the transfer processes involved in solar cells, advanced spectroscopy techniques with ultrafast time resolution and spatial mapping capabilities are needed. We start with Chapter 8 which describes the experimental techniques of transient photoluminescence microscopy, time-resolved second harmonic generation, and transient absorption/reflection in detail. Chapter 9 presents a detailed framework for numerical modeling of charge carrier transport within bulk semiconducting materials from transient photoluminescence microscopy measurements, with applications to experimental data collected on single crystal 3D perovskite and bulk CdS. From bulk transport, we then move to developing a setup for studying interfacial transport: time-resolved second harmonic generation, and detail the key considerations and challenges encountered when building the setup in Chapter 10. As the final experimental chapter, we probe exciton dynamics in singlet fission-sensitized silicon devices using magnetic field-dependent transient absorption and transient reflection measurements, as well as longer time-scale transient photoluminescence measurements in Chapter 11. The thesis concludes with Chapter 12, which provides a summary of the key findings and outlines some potential future directions for the reader.

Part I: Interfacial materials and device development

Chapter 2.
Theoretical framework of materials for singlet fission-sensitized silicon solar cells

In this chapter, we introduce some of the theoretical background to support the remainder of Part I of this thesis. We start with an introduction to organic molecular semiconductors, focusing on their electronic structures, including electronic spin and exciton theory. We then follow with a discussion of excitonic processes in organic semiconductors, covering exciton transport, singlet fission, triplet-charge annihilation, and using magnetic field-dependent measurements to probe these excitonic processes. We then move onto crystalline-silicon as a bulk inorganic semiconductor, introducing the operating principles of silicon solar cells, including the p-n junction, characterization of solar cells, and highlighting common loss pathways.

2.1. Organic molecular semiconductors

Organic molecular semiconductors have vast applications, including in organic light emitting diodes (OLEDs)[48–50], organic photovoltaics (OPVs)[51–53], and organic field effect transistors (OFETs)[54,55]. They consist of materials that are largely made of carbon atoms, hydrogen atoms with some heteroatoms such as sulfur, oxygen and nitrogen. Unlike their inorganic semiconductor counterparts, which will be described in more detail in Section 2.2, the dielectric constants of these organic materials are low, at around $\varepsilon_r = 3.5$[56]. Thus, when the organic molecules absorb light, the photogenerated electron-hole pair is bound by a coulomb energy of 0.5–1.0 eV.

A class of well-studied molecular semiconductors are flat aromatic compounds known as polyacenes, which include naphthalene, anthracene, tetracene and pentacene. Tetracene (Figure 2-1a) is of particular interest in this thesis, and a large part of the following discussions will be centered around it. These molecules have filled outer orbitals and are electrically neutral. The molecules are attracted via weak van-der-Waals interactions, which often results in herringbone packing arrangements when crystals are grown[56,57]. These polyacenes are π-conjugated molecules, where the carbon atom spacing is such that the neighboring p_z orbitals overlap, resulting in electronic density delocalized over the entire molecule, above and below the plane of the carbon atoms[58]. Other π-conjugated molecules of relevance to this thesis include phthalocyanines, which are frequently used in pigments and dyes[59]. Zinc phthalocyanine is pictured in Figure 2-1b.

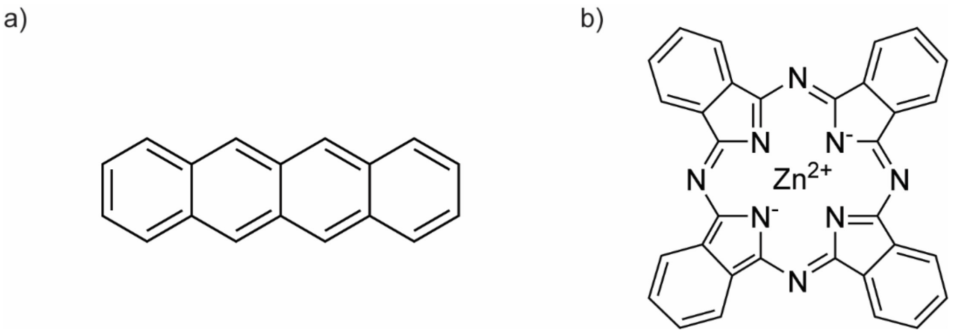

Figure 2-1. Organic molecules used extensively in this thesis. a) Tetracene. b) Zinc phthalocyanine.

2.1.1. Electronic structure

Optical and electronic processes in molecules are determined by the energy of their molecular orbitals. Molecular orbitals, Ψ, can be described as a linear combination of atomic orbitals ϕ_i:

$$\Psi = \sum_i c_i \phi_i, \tag{2-1}$$

where c_i are weighting coefficients. These coefficients are determined by solving the Schrödinger equation:

$$\hat{H}\Psi = E\Psi. \tag{2-2}$$

The Hamiltonian includes the kinetic energy of each electron and the potential energies from nuclei repulsion, electron-electron interactions and electron-nuclei interactions.

Molecular orbitals are populated by electrons according to the following rules:

1. Aufbau principle: Electrons occupy orbitals in order from lowest energy to highest.
2. Pauli exclusion principle: No two electrons can have an identical set of quantum numbers. Therefore, each orbital can only have two electrons maximum, with opposite spins.
3. Hund's rule: All orbitals of identical energies (degenerate) will be singly occupied before they may be doubly occupied, and the electrons must have the same spin in the singly occupied orbitals.

Electrons are fermions with spin $\frac{1}{2}$, and can exist in either a spin state of up $+\frac{1}{2}$ or down $-\frac{1}{2}$. The ground state configuration (Figure 2-2) of a molecule is achieved when the electron occupancy of the molecular orbitals is obtained following the above rules. For most molecules, the highest occupied molecular orbital (HOMO) level has two electrons with opposite spins. The next molecular orbital with no electrons in the ground state is referred to as the lowest unoccupied molecular orbital (LUMO). The HOMO and LUMO levels are also known as frontier orbitals, and play an important role in the optical and electronic processes of the molecule.

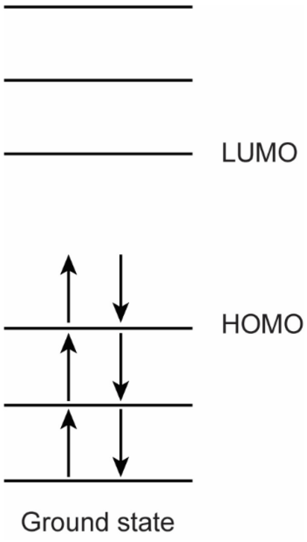

Figure 2-2. Electronic ground state configuration of a molecule.

2.1.1.1. Excited states

The wavefunction of electrons can be broken down into a product of the electronic wavefunction that depends only on the electron's spatial coordinates and the spin wavefunction that depends only on the electron's spin.

Electrons can be promoted from the HOMO level to the LUMO level to create an excited state, for example, upon absorption of light. Quantum mechanics tells us that excited states must have simultaneous eigenstates to $\hat{S}^2$ and $\hat{S}_z$, where $\hat{S}$ is the spin angular momentum operator, and $\hat{S}_z$ is the projection of this operator in the z-direction. These excited states have the total spin S and total secondary spin quantum number M_s as eigenvalues[56].

In the excited state, the electrons in the HOMO and LUMO levels are at different energy levels, and so there are four possible spin configurations to pair these two electrons. These configurations, or basis states, can be expressed using the secondary spin quantum number of each electron m_s:

$$
\begin{aligned}
|\uparrow\uparrow\rangle &= \left|m_{s1} = +\frac{1}{2}, m_{s2} = +\frac{1}{2}\right\rangle \\
|\uparrow\downarrow\rangle &= \left|m_{s1} = +\frac{1}{2}, m_{s2} = -\frac{1}{2}\right\rangle \\
|\downarrow\uparrow\rangle &= \left|m_{s1} = -\frac{1}{2}, m_{s2} = +\frac{1}{2}\right\rangle \\
|\downarrow\downarrow\rangle &= \left|m_{s1} = -\frac{1}{2}, m_{s2} = -\frac{1}{2}\right\rangle
\end{aligned}
\tag{2-3}
$$

Then, we can write the eigenstates to $\hat{S}^2$ and $\hat{S}_z$ as linear combinations of these basis sets:

$$
\begin{gathered}
\text{Singlet state: } |S = 0, M_s = 0\rangle = \frac{1}{\sqrt{2}}(|\uparrow\downarrow\rangle - |\downarrow\uparrow\rangle) \\
\text{Triplet state: } \begin{cases} |S = 1, M_s = 1\rangle = |\uparrow\uparrow\rangle \\ |S = 1, M_s = 0\rangle = \dfrac{1}{\sqrt{2}}(|\uparrow\downarrow\rangle + |\downarrow\uparrow\rangle). \\ |S = 1, M_s = -1\rangle = |\downarrow\downarrow\rangle \end{cases}
\end{gathered}
\tag{2-4}
$$

Of these states, three have a total spin number of $S = 1$, and these are referred to as *triplet* states, while the remaining state has a total spin number of $S = 0$, referred to as a *singlet* state. The vector diagram illustrations of the orientations of the two electron spins for the singlet and triplet states are presented in Figure 2-3.

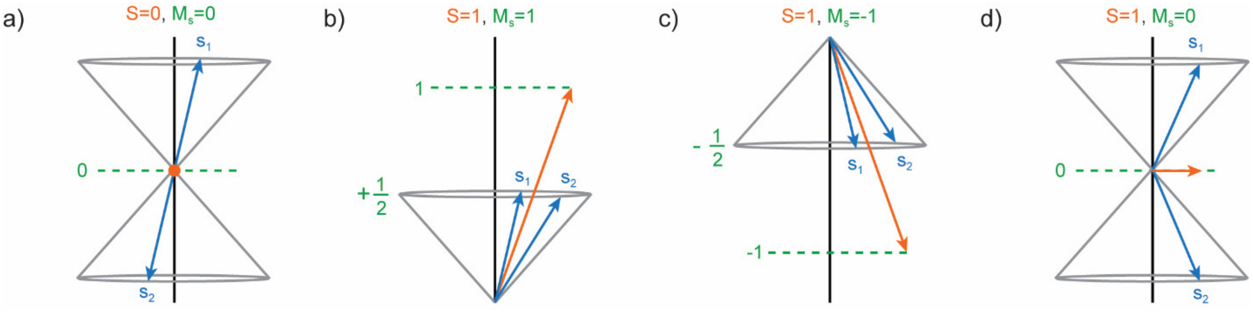

Figure 2-3. Vector diagram illustrations showing the orientations of the two electron spins and the corresponding eigenvalues: total spin number S and total secondary spin quantum number M_s. a) Singlet state. The electrons are antiparallel and 180° out of phase with each other. b-d) Triplet states. In d), the electrons are in phase with each other.

The first singlet excited state energy is greater than the triplet excited state energy by the exchange energy, which is two times the exchange integral[60]. A very simplistic view of this energy difference can be thought of by considering that the parallel spin in the triplet excited states leads to reduced electron repulsion, and a more detailed derivation can be found elsewhere should the reader desire[60].

2.1.1.2. Interactions with light

To describe how molecules interact with light, we use Fermi's golden rule:

$$k = \frac{2\pi}{\hbar} \left| \langle \Psi_f | \hat{H}' | \Psi_i \rangle \right|^2 \rho, \tag{2-5}$$

where k is the rate of transition between an initial state Ψ_i and a final state Ψ_f, $\hat{H}'$ is the perturbing Hamiltonian for the transition of states, and ρ is the density of final states.

We can describe the molecular wavefunction as a combination of electronic, spin and vibrational wavefunctions, and use a dipole operator $e\hat{\boldsymbol{r}}$ for the perturbation for optical transitions which only acts on the electronic wavefunction; we assume that only the positions of the electrons are affected by incident light. The expression that results is:

$$k = \frac{2\pi}{\hbar} \rho \left| \langle \Psi_{el,f} | e\hat{\boldsymbol{r}} | \Psi_{el,i} \rangle \right|^2 \left| \langle \Psi_{spin,f} | \Psi_{spin,i} \rangle \right|^2 \left| \langle \Psi_{vib,f} | \Psi_{vib,i} \rangle \right|^2, \tag{2-6}$$

where we can see that the rate of an optical transition (absorption and emission properties) is dependent on three factors.

The first factor is the electronic factor: $\left| \langle \Psi_{el,f} | e\hat{\boldsymbol{r}} | \Psi_{el,i} \rangle \right|^2$. When this term is non-zero, we have a dipole-allowed transition. This integral scales with overlap between the initial and final wavefunctions, consequently, rates between orbitals that are around the same parts of the molecule are larger than across different parts of the molecule. Larger transition dipole moments will also result in larger rates. Strength of absorption and emission signals from a molecule can be correlated to this factor, by measurements of oscillator strength.

The second factor is the spin factor: $\left| \langle \Psi_{spin,f} | \Psi_{spin,i} \rangle \right|^2$. When the spins of the initial and final states are identical, $\langle \Psi_{spin,f} | \Psi_{spin,i} \rangle = 1$. Otherwise, when the spins are different, $\langle \Psi_{spin,f} | \Psi_{spin,i} \rangle = 0$. As a result, transitions between singlet states or between triplet states are *spin-allowed*. In most molecules, the ground state is a singlet state with paired spin as per the Pauli exclusion principle. The transition from the singlet excited state to the singlet ground state leads to fluorescence, and this spin-allowed process is fast (~ ns)[61]. Transitions going from triplet states to singlet states and vice versa are classically *spin-forbidden*. However, in some cases, we can experimentally observe luminescence going from the triplet excited state to the singlet ground state, referred to as phosphorescence, with timescales typically much slower than fluorescence (ms or greater)[61]. This transition between the triplet and singlet state (and vice versa) is possible through an effect known as spin-orbit coupling, and the degree of coupling is proportional to the atomic number, resulting in a greater effect with molecules that have heavy atoms, such as platinum. These transitions are also referred to as intersystem crossing.

The final factor in Equation (2-6) is the vibrational factor: $\left|\left\langle \Psi_{vib,f} \middle| \Psi_{vib,i} \right\rangle\right|^2$. This term can be thought to affect the spectral shape of the molecule's absorption and emission. When a photon is absorbed by the molecule, the electronic distributions change much faster than the heavier nuclei (Born-Oppenheimer approximation). As a result, the vibrational level of the excited state should be identical with the ground state with respect to the nuclear position and momentum. This is represented by a vertical transition (see Figure 2-4), and is referred to as the Franck-Condon principle. In molecules like tetracene with rigid bonds and therefore smaller displacement between ground and excited state potential energy curves, the 0-0 transition is dominant. After absorption, relaxation to the ground state occurs through vibrational relaxation followed by a vertical transition. As a result, the emission spectrum is at a lower energy, and this phenomenon is referred to as Stokes shift. In tetracene, the Stokes shift is typically less than 10 nm.

A summary of all the excited state transitions discussed in this section is presented in Figure 2-5.

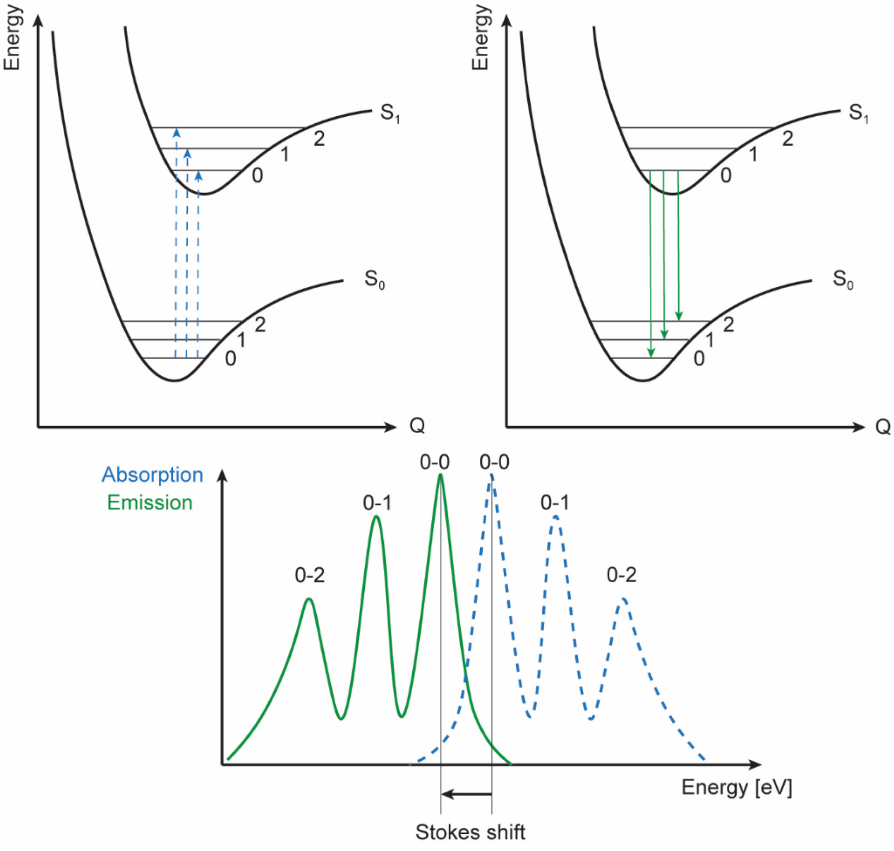

Figure 2-4. Illustration of the Franck-Condon principle and Stokes shift. Potential energy surfaces for the two states are shown, with Q as the nuclear configuration coordinate, and vertical transitions corresponding to the vibrational peaks in the absorption (dotted blue) and emission (solid green) spectra are shown. The Stokes shift is illustrated as the energy difference between the first absorption and emission peaks.

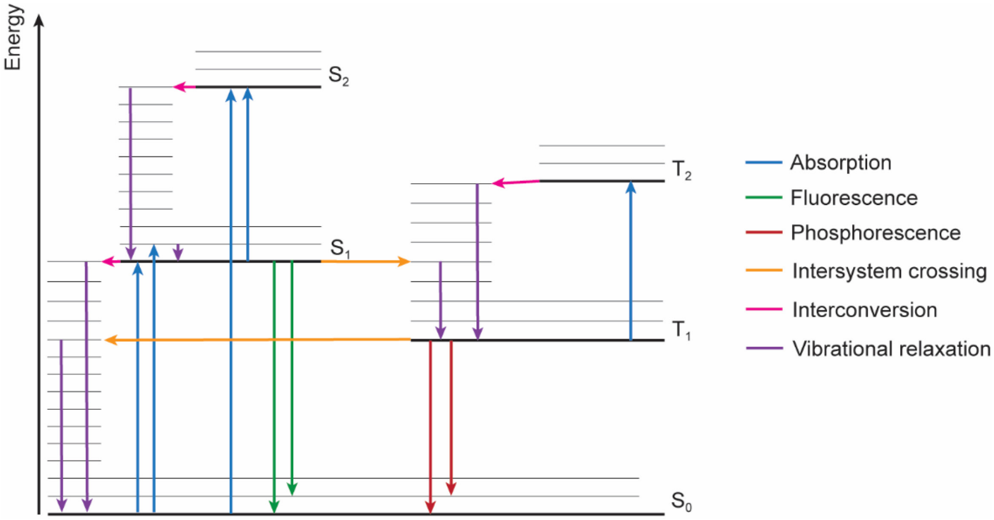

Figure 2-5. Jablonski diagram showing a summary of the covered transitions in this section. Bold lines are electronic states, while thinner lines are vibronic states.

2.1.2. Excitonic processes

2.1.2.1. Excitons

As the energy of the excited states can be transferred from molecule to molecule, it is useful to picture them as quasiparticles of bound electron-hole pairs known as *excitons*. As the electrons and holes are coulombically bound, their energies are not exactly equivalent to the energy difference between the HOMO and LUMO levels.

The Hartree-Fock energy of the neutral system (ground-state) can be described as:

$$E_{gs} = \sum_{i} \langle \Psi_i | \hat{h} | \Psi_i \rangle + \frac{1}{2} \sum_{i,j} [\Psi_i \Psi_i | \Psi_j \Psi_j] - [\Psi_i \Psi_j | \Psi_j \Psi_i]. \tag{2-7}$$

To get the energy of the excited state, we can remove an electron from the HOMO and add it to the LUMO and calculate the energy of the excited state.

The exciton energy can be obtained by calculating the difference in energy between the excited state and ground state. Invoking Koopman's theorem results in the following expression[62]:

$$\begin{aligned} E_{es} - E_{gs} = \{\epsilon_{LUMO} - \epsilon_{HOMO}\} - [\Psi_{HOMO}\Psi_{HOMO}|\Psi_{LUMO}\Psi_{LUMO}] \\ + [\Psi_{HOMO}\Psi_{LUMO}|\Psi_{LUMO}\Psi_{HOMO}]. \end{aligned} \tag{2-8}$$

The first term on the right hand side is the energy difference between the LUMO and HOMO levels. The second term is the Coulomb interaction term, which accounts for the attractive Coulombic interaction between the electron and the hole. The third term is the exchange term, which is present when the ground and excited states are of the same multiplicity (provides destabilizing contribution for singlet states, but vanishes to zero for triplet states). The sum of the last two terms is often referred to as the exciton binding energy.

Compared to their inorganic semiconductor counterparts, excitons in organic molecular semiconductors are highly-localized to each molecule (Frenkel excitons)[63]. In inorganic semiconductors, the excitons are more delocalized over multiple lattice sites (Wannier-Mott excitons) with low binding energies[64].

2.1.2.2. Exciton transport

Excitons can be generated optically or electrically (*via* charge injection directly). As optical excitations involve the transition from the ground state to the excited state, singlet excitons are usually generated through this process. For electrical excitations, both singlet and triplet excitons can be formed at a 1:3 ratio based on spin statistics. Excitons typically diffuse according to Fick's law[65]:

$$\frac{\partial n_{ex}(\boldsymbol{r},t)}{\partial t} = D_{ex}\nabla^2 n_{ex} - A n_{ex} + G, \tag{2-9}$$

where $n_{ex}(\boldsymbol{r},t)$ is the exciton density as a function of space and time, D_{ex} is the exciton diffusivity, A is the first-order decay constant (inversely proportional to the exciton lifetime τ), and G is the exciton generation rate. The exciton diffusion length L is defined as the average distance that an exciton diffuses before decay, and can be obtained by $L = \sqrt{D_{ex}\tau}$. In tetracene, this length has been reported to be around 30 nm–4 μm, depending on whether polycrystalline thin films or ultra-pure single crystals are used[66–68].

Excitons can transfer radiatively or non-radiatively (Figure 2-6). For a radiative transfer process, an exciton radiatively recombines to emit a photon, which can then be reabsorbed by another molecule.

$$\begin{gathered} D^* \rightarrow D + h\nu \\ h\nu + A \rightarrow A^*, \end{gathered} \tag{2-10}$$

where D indicates the energy donor, and A indicates the energy acceptor. For radiative transfer to occur, the emission spectra of the donor should overlap with the absorption spectra of the acceptor, and the emission and absorption processes should be efficient. Otherwise, no other interactions are required between the donor and acceptor, and the transfer is long range. Previously discussed selection rules for radiative processes still apply (*i.e.* less likely to see this form of transfer from triplet to singlet excited states).

Excitons can also transfer their energy non-radiatively, either through Förster resonance energy transfer (FRET) or Dexter transfer. FRET occurs through the coupling of the transition dipole moments between the donor and acceptor chromophores. Förster expressed the rate of energy transfer by[69,70]:

$$k_{FRET} = \frac{9 \ln 10}{N_A} \frac{1}{2^7 \pi^5 n^4} \frac{\Phi_D}{\tau_D^0} \frac{\kappa^2}{R^6} \int I_D(\lambda) \varepsilon_A(\lambda) \lambda^4 d\lambda = \frac{1}{\tau_D^0} \left(\frac{R_0}{R}\right)^6, \tag{2-11}$$

where N_A is Avogadro's number, n is the refractive index of the medium surrounding the donor and acceptor, Φ_D is the quantum yield of the donor fluorescence in the absence of the acceptor, τ_D^0 is the lifetime of the donor in the absence of the acceptor, κ^2 is the orientation factor of the donor and acceptor transition dipole moment, $\int I_D(\lambda)\varepsilon_A(\lambda)\lambda^4 d\lambda = J$ is the spectral overlap between the donor emission $I_D(\lambda)$ and acceptor absorption $\varepsilon_A(\lambda)$, and R is the distance between the donor and acceptor chromophore. Typically, FRET occurs over distances of 1–10 nm as a result of the $\frac{1}{R^6}$ dependence of the rate[65]. Because the donor undergoes a transition from the excited to the ground state, typically FRET is only observed for singlet exciton transfer. Although, when strong spin-orbit coupling is present, the nominal triplet exciton can also be transferred through FRET[71,72].

Dexter transfer occurs through exchange interactions, with the electrons exchanged between the donor and acceptor chromophores. The rate constant of the Dexter transfer process is described by[73]:

$$k_{Dexter} = KJe^{-\frac{2R}{L}}, \tag{2-12}$$

where K is an experimental constant, J is the spectral overlap integral defined earlier, R is also the earlier defined distance between the donor and acceptor chromophore, and L is a constant that relates to the effective average orbital radius of the donor and acceptor states. Because of the negative exponential dependence on distance, Dexter transfer is very short-range, on the order of about 1 nm. As exchange interactions do not rely on allowed transitions, triplet excitons transfer primarily *via* this mechanism. Singlet excitons may also undergo Dexter transfer, although the short-range limitation results in higher likelihood of observing FRET.

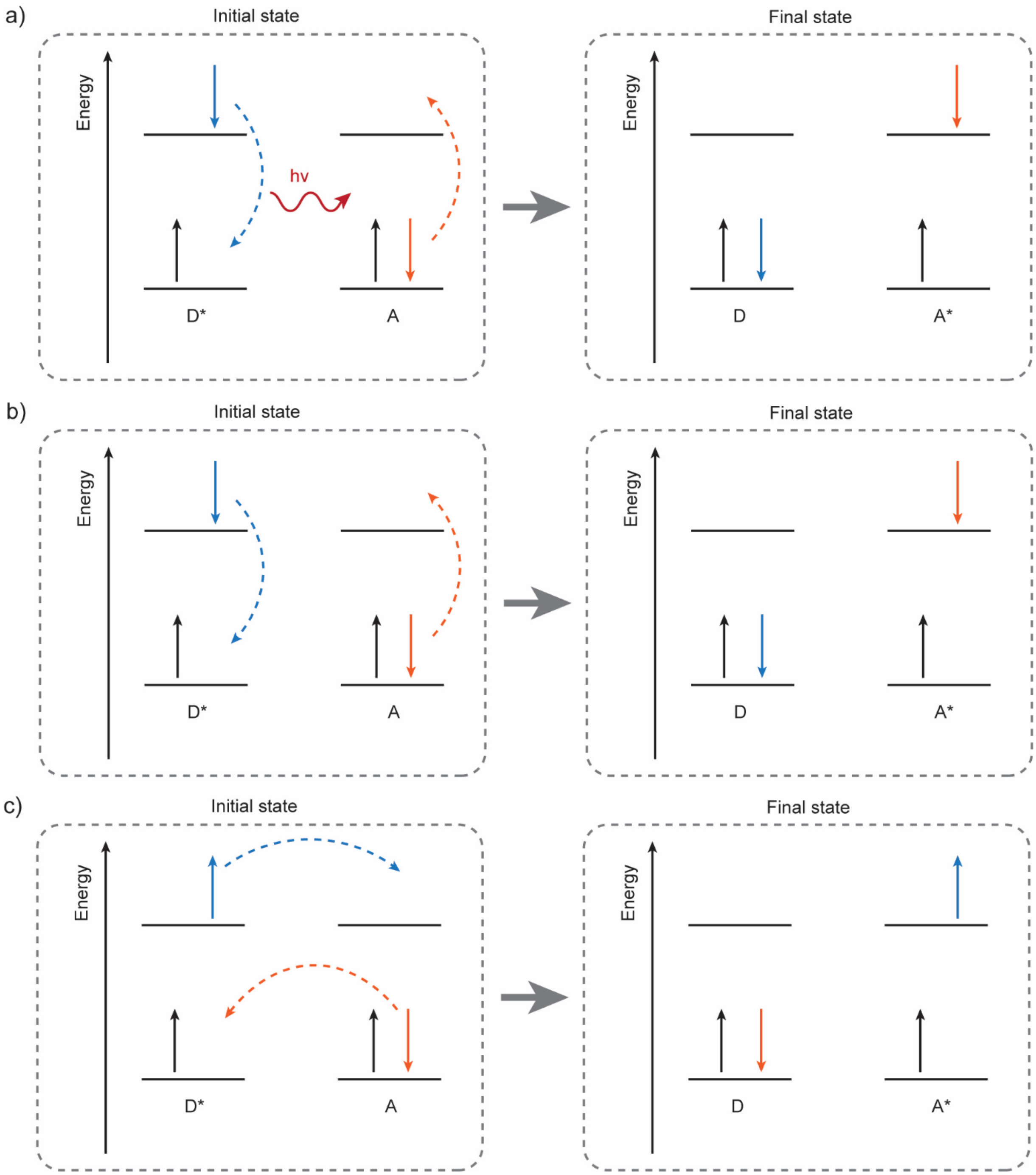

Figure 2-6. Schematic of exciton transfer mechanisms. a) Radiative energy transfer. The donor molecule radiatively emits a photon, which gets reabsorbed by the acceptor molecule. b) Förster resonance energy transfer (FRET). The donor couples non-radiatively with the acceptor through dipole-dipole interactions to transfer energy. c) Dexter transfer. The donor transfers energy to the acceptor through electronic exchange interactions.

Excitons can also dissociate at interfaces such that charge transfer occurs. Depending on the alignment of orbital energies at the interface, electrons can be transferred to a lower energy state (or holes can be transferred to a higher energy state). Whether energy transfer or charge transfer occurs at an interface often depends on the energy level alignment between the two materials at the interface. Depending on the relative alignment of the HOMO and LUMO levels, a type I, type II or type III heterojunction can be formed (see Figure 2-7). For type I heterojunctions, energy transfer is more commonly observed as it is energetically downhill to transfer both the electron and the hole from material A to material B, and the transitions are favorable for both carriers. Charge transfer may still occur at this energy alignment, as we shall see discussed later in this thesis. For type II heterojunctions, charge transfer is more commonly observed as it is favorable for the electron to transfer from material A to B but the hole would prefer to transfer from material B to A. This type of heterojunction is commonly utilized in organic photovoltaics to dissociate the exciton and extract carriers from light. Finally, in type III heterojunctions, charge dissociation is also possible.

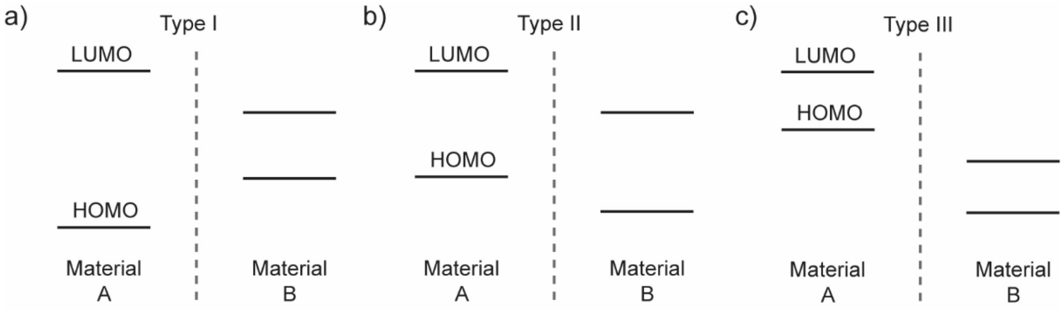

Figure 2-7. Heterojunctions that can be formed at interfaces between two molecular materials. a) Type I heterojunction. b) Type II heterojunction. c) Type III heterojunction.

2.1.3. Singlet exciton fission

Singlet exciton fission is the process by which one singlet excited state on a chromophore shares its energy with a neighboring ground state chromophore and both chromophores are converted into two triplet excited states (Figure 2-8). The chromophores can be the same (homofission) or different (heterofission) and the fission process can occur between molecules (intermolecular) or within the same molecule on two chromophoric sites (intramolecular). This process is spin-allowed since the two triplet excited states are formed from an intermediate triplet-triplet pair state with overall spin-singlet character referred to as a *correlated triplet pair*, $^1(TT)$[34]. This process may be written using the following simplified kinetic scheme:

$$S_0 + S_1 \underset{k_{-1}}{\overset{k_1}{\rightleftharpoons}} {}^1(TT) \underset{k_{-2}}{\overset{k_2}{\rightleftharpoons}} T_1 + T_1. \tag{2-13}$$

Whilst the exact detailed mechanism for singlet fission has been debated for some time, it is convenient to express the singlet fission process as proceeding through this two-step mechanism. The wavefunction of $^l(TT)$ (where l = 1, 3, or 5) can be thought of as a superposition of the nine possible sublevel wavefunctions that arise from the two-triplet combination, which are a mix of singlet, triplet and quintet characters. The reverse process to singlet fission can also occur, where the fusion of triplets back to a singlet, known as *triplet-triplet annihilation*, can be used in upconversion processes.

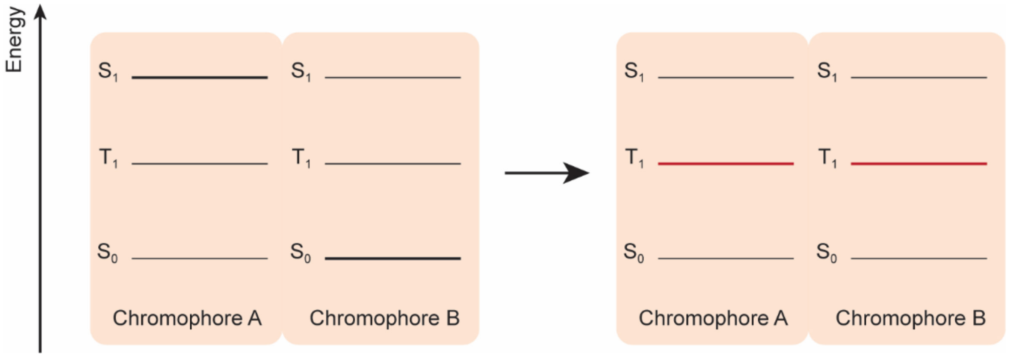

Figure 2-8. The process of singlet fission. A singlet excited state on chromophore A shares its energy with neighboring chromophore B in the ground state. As a result, two triplet excited states are formed.

Singlet fission can occur in certain molecules, such as in highly symmetric, planar polyacenes, where the exchange energy is large enough that the singlet-triplet energy split is such that the singlet exciton is close to or greater than twice the energy of the triplet exciton. In molecules where the energy of the singlet excited state is greater than twice the energy of the triplet excited states, $E(S_1) \geq 2E(T_1)$ (*i.e.* pentacene), the fission process occurs on ps or faster timescales[34]. Fission can still occur in the endothermic case when $2E(T_1)$ is slightly above $E(S_1)$, however the fission rate is notably not as fast.

The fission process was first invoked in 1965 to explain time-dependent fluorescence measurements on single crystal anthracene[74]. Since then, a variety of studies have been performed on singlet fission materials, with particular interest in these materials for the application of enhancing performance of solar cells[26]. For tetracene, $E(S_1) = 2.40$ eV and $E(T_1) = 1.25$ eV such that $E(S_1) \approx 2E(T_1)$[35]. The triplet energy is just above that of the band gap of silicon (1.1 eV), and ideally, the formation of two excitons from the high-energy photon in tetracene can generate two photoelectrons, such that when combined with the silicon, thermalization losses are reduced and the power conversion efficiency (PCE) is increased[27,28,35]. While the fission process is slightly endothermic, a high triplet yield $\eta \approx 200$ % has been reported for crystalline tetracene, often attributed to the entropic gain from two triplet excitons as the product of fission[75]. All the studies in this thesis are focused on tetracene as the archetypal singlet fission layer candidate for coupling to silicon; however, its poor photostability[76,77] makes it unsuitable for industrial roll out. Alternative candidates for singlet fission materials for coupling to silicon are discussed in Section 3.1.

2.1.4. Triplet-charge annihilation

The interaction between triplet excitons and charge carriers is a commonly observed detrimental process in OLEDs with triplet-based emitters[78], and can also constitute a loss pathway for singlet fission photovoltaics[79]. In triplet-charge annihilation, a triplet exciton encounters a charge (*e.g.* a molecular anion, a polaron, *etc.*) and decays non-radiatively. A schematic of the process is depicted in Figure 2-9.

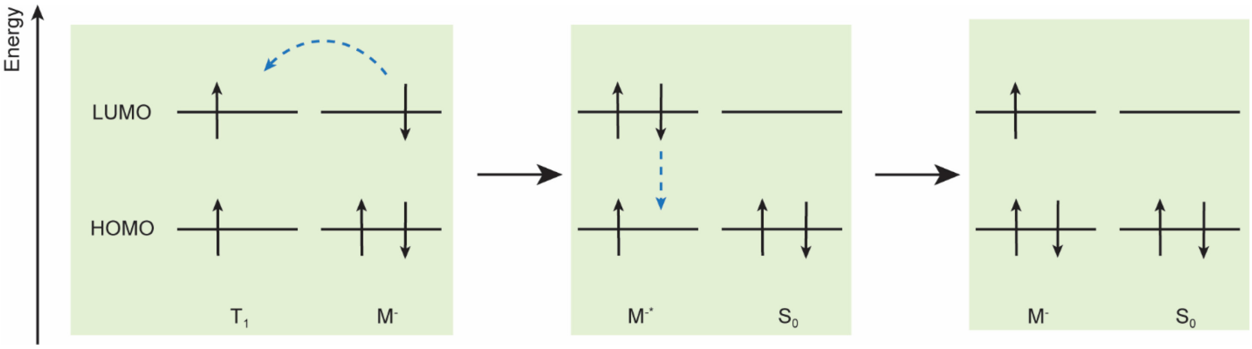

Figure 2-9. Schematic of triplet-charge annihilation in the molecular orbital picture. T_1 is the excited triplet state on a molecule, C^- is a negatively-charged molecule, C^{-*} is a negatively-charged molecule in the excited state, and S_0 is the ground state of the molecule.

The process may be described through the following kinetic scheme:

$$T_1 + C^{\pm} \underset{k_{-3}}{\overset{k_3}{\rightleftharpoons}} (TC) \overset{k_4}{\rightarrow} C^{\pm} + S_0. \tag{2-14}$$

In the above kinetic scheme, the process is mediated by a triplet-charge pair-state (TC), where the number of pair-state intermediates with overall spin character of charge determines the overall rate of the TCA process[79].

2.1.5. Spectroscopic probes for excitonic processes

As organic semiconducting materials interact with light, a variety of spectroscopy techniques can be used to probe the excitonic processes described earlier. In this section, we go into detail for techniques relevant to Part I of this thesis. More details on advanced spectroscopic techniques relevant to Part II, such as transient photoluminescence, transient absorption/reflection and time-resolved second harmonic generation are detailed in Chapter 8.

Typically, singlet excitons can be probed using absorption and emission experiments as these are sensitive to the transitions between molecular singlet excited and ground states. Triplet excitons are harder to probe optically, but phosphorescence of molecules with high spin-orbit coupling can be used to probe triplet exciton energies and lifetimes.

2.1.5.1. Magnetic field-dependent studies on singlet fission systems

Singlet fission (and the reverse process of triplet-triplet annihilation) can be studied by applying an external magnetic field and measuring the resulting photoluminescence[80,81]. Johnson and Merrifield postulated that the probability of the triplet annihilation process, as well as the overall singlet fission process, depends on the number of the nine sublevels of (TT) that show singlet character[81]. Applying an external magnetic field affects the number of these intermediate states with singlet character[81]. We start with an updated rate equation of the fission and fusion processes:

$$S_1 \underset{k_{-1}}{\overset{k_1}{\rightleftharpoons}} (TT)^i \underset{k_{-2}}{\overset{k_2}{\rightleftharpoons}} T_1 + T_1. \tag{2-15}$$

k_1 and k_{-1} are the forward and reverse rate constants for the conversion of the singlet exciton to the intermediate (TT) pair state. k_2 and k_{-2} are the forward and reverse rate constants for the conversion of the intermediate (TT) pair state to the uncorrelated triplet excitons. The superscript i denotes one of the 9 possible (TT) pair states.

The $(TT)^i$ wavefunction can be obtained by considering the spin Hamiltonian of the triplet-pair[82]:

$$\hat{H} = g\beta\mathbf{B}\cdot\left(\hat{S}_A + \hat{S}_B\right) + D\left(S_{z_A}^2 + S_{z_B}^2\right) + E\left(S_{x_A}^2 + S_{x_B}^2 - S_{y_A}^2 - S_{y_B}^2\right), \tag{2-16}$$

where g is the g-factor (parameter sensitive to the environment), β is the Bohr magneton, $\mathbf{B}$ is the magnetic field vector, D and E are the triplet exciton zero-field splitting parameters, and $\hat{S}$ is the spin operator denoted for each exciton (on molecules A and B). The first term in the sum is the Zeeman interaction, which describes the effect of the external magnetic field, while the second and third terms are related to the zero-field splitting. We note that this expression of the Hamiltonian does not account for interaction terms between the two triplets, which was found to have a negligible influence on the spin part of the wavefunction[82].

From Equation (2-15), we can derive time-dependent equations describing the singlet, (TT) and triplet exciton populations[83]:

$$\begin{aligned} \frac{dN_{S_1}}{dt} &= -k_1\sum_{i=1}^{9}\left|C_S^i\right|^2 N_{S_1} + \sum_{i=1}^{9} k_{-1}\left|C_S^i\right|^2 N_{(TT)^i} \\ \frac{dN_{(TT)^i}}{dt} &= -k_1\left|C_S^i\right|^2 N_{S_1} - \left(k_{-1}\left|C_S^i\right|^2 - k_2\right) N_{(TT)^i} + k_{-2}N_{T_1}^2 \\ \frac{dN_{T_1}}{dt} &= 2k_2\sum_{i=1}^{9} N_{(TT)^i} - k_{-2}N_{T_1}^2. \end{aligned} \tag{2-17}$$

$C_S^i = \langle S_1|(TT)^i\rangle$ is the inner product of the singlet and (TT) pair state, and gives the singlet character of the i-th $(TT)^i$ state. Assuming steady-state conditions for the intermediate (TT) state, we set $\frac{dN_{(TT)^i}}{dt} = 0$ and obtain the following expressions:

$$\begin{aligned} \frac{dN_{S_1}}{dt} &= -\gamma_{sf}N_{S_1} + \gamma_{ta}N_{T_1}^2 \\ \frac{dN_{T_1}}{dt} &= 2\gamma_{sf}N_{S_1} - \gamma_{ta}N_{T_1}^2. \end{aligned} \tag{2-18}$$

The pseudo-rate constants are defined as:

$$\gamma_{sf} = \sum_{i=1}^{9} \frac{k_1 \left|C_S^i\right|^2}{1 + \frac{k_{-1}}{k_2}\left|C_S^i\right|^2}$$

$$\gamma_{ta} = \frac{1}{9} k_{-2} \sum_{i=1}^{9} \frac{\frac{k_{-1}}{k_2}\left|C_S^i\right|^2}{1 + \frac{k_{-1}}{k_2}\left|C_S^i\right|^2}. \tag{2-19}$$

We see from these constants that the overall rate of singlet fission depends on the magnetic field, as the $\left|C_S^i\right|^2$ term changes with the externally applied field. Thus, the number of (TT) states with singlet character will consequently increase the singlet fission and triplet-triplet annihilation rates.

When no magnetic field is applied, the pair eigenstates to the spin Hamiltonian are defined by the molecular fine structure axes ($|x\rangle, |y\rangle, |z\rangle$). The eigenstates of total spin can be expressed as combinations of the zero-field pair wavefunctions[82]:

$$\begin{aligned}
\text{Singlet: } |S\rangle &= \frac{1}{\sqrt{3}}(|xx\rangle + |yy\rangle + |zz\rangle) \\
|T_x\rangle &= \frac{1}{\sqrt{2}}(|yz\rangle - |zy\rangle) \\
\text{Triplets: } |T_y\rangle &= \frac{1}{\sqrt{2}}(|zx\rangle - |xz\rangle) \\
|T_z\rangle &= \frac{1}{\sqrt{2}}(|xy\rangle - |yx\rangle) \\
|Q_x\rangle &= \frac{1}{\sqrt{2}}(|yz\rangle + |zy\rangle) \\
|Q_y\rangle &= \frac{1}{\sqrt{2}}(|zx\rangle + |xz\rangle) \\
\text{Quintets: } \quad |Q_z\rangle &= \frac{1}{\sqrt{2}}(|xy\rangle + |yx\rangle) \\
|Q_a\rangle &= \frac{1}{\sqrt{2}}(|xx\rangle - |yy\rangle) \\
|Q_b\rangle &= \frac{1}{\sqrt{6}}(|xx\rangle + |yy\rangle - 2|zz\rangle).
\end{aligned} \tag{2-20}$$

We see that there are three pair states that have singlet character: $|xx\rangle$, $|yy\rangle$ and $|zz\rangle$.

With an intermediate magnetic field strength, the Zeeman term in the spin Hamiltonian is no longer 0. This results in distribution of the singlet character over all pair states that are even under interchange of the two triplets (singlet and quintet states listed above). Hence, compared to the zero-field case, we observe an increase in the singlet fission and triplet fusion rates.

At high magnetic fields, the Zeeman term dominates in the spin Hamiltonian and the pair eigenstates can instead be defined by the direction of the magnetic field ($|0\rangle$, $|+\rangle$ and $|-\rangle$). In the same manner as earlier, the pure spin state eigenstates are[82]:

$$\begin{aligned}
&\text{Singlet: } |S\rangle = \frac{1}{\sqrt{3}}\left(|00\rangle - |+-\rangle - |-+\rangle\right) \\
&\text{Triplets: } \begin{cases} |T_0\rangle = \frac{1}{\sqrt{2}}\left(|+-\rangle - |-+\rangle\right) \\ |T_{\pm1}\rangle = \frac{1}{\sqrt{2}}\left(|\pm 0\rangle - |0 \pm\rangle\right) \end{cases} \\
&\text{Quintets: } \begin{cases} |Q_0\rangle = \frac{1}{\sqrt{6}}\left(2|00\rangle + |+-\rangle + |-+\rangle\right) \\ |Q_{\pm1}\rangle = \frac{1}{\sqrt{2}}\left(|\pm 0\rangle + |0 \pm\rangle\right) \\ |Q_{\pm2}\rangle = |\pm\pm\rangle. \end{cases}
\end{aligned} \tag{2-21}$$

We see that there are only two pair states that have singlet character: $|00\rangle$ and $\frac{1}{\sqrt{2}}\left(|+-\rangle + |-+\rangle\right)$. Thus, compared to the zero-field case, the singlet fission and triplet fusion rates decrease.

This effect of the magnetic field on the overall rates of singlet fission and triplet-triplet annihilation result in characteristic responses for molecular fluorescence and phosphorescence as the net population of the singlet and triplet excitons are changed (see Figure 2-10 for an example). Magnetic field-dependent measurements on anthracene and tetracene luminescence have been well-characterized[80–82,84,85].

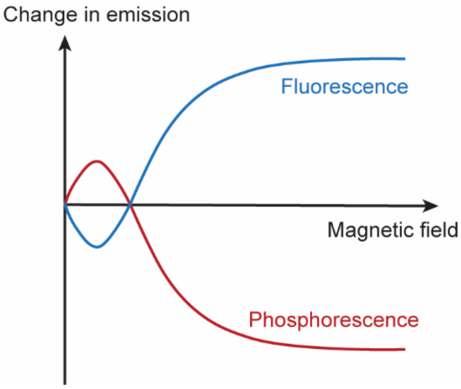

Figure 2-10. A schematic of the effect of an external magnetic field on the fluorescence and phosphorescence of molecules. The magnetic field modulates the rate of the overall singlet fission process, which results in a change in the population of singlet and triplet excitons respectively.

2.1.5.2. Magnetic field-dependent studies on triplet-charge annihilation systems

In a similar manner, the rate of triplet-charge annihilation is also magnetic field-dependent. We rewrite the expression as follows:

$$T_1 + C^{\pm} \underset{k_{-3}}{\overset{k_3}{\rightleftharpoons}} (TC)^i \overset{k_4}{\rightarrow} C^{\pm}. \tag{2-22}$$

Here, the superscript i denotes one of the 6 triplet-charge intermediate states (TC).

Analogous to the analysis performed in the previous section, we can obtain a pseudo-rate constant for the TCA process[79]:

$$\gamma_{TCA} = \frac{k_4}{N_{T_1} N_{C^{\pm}}} \sum_{m=1}^{6} \sum_{n=1}^{6} \rho_{mn} \left(\mathcal{D}_n^{+*} D_m^{+} + \mathcal{D}_n^{-*} D_m^{-} \right), \tag{2-23}$$

where ρ is the spin density-matrix of the intermediate (TC) states, and $\mathcal{D}_m^{\pm} = \langle D^{\pm} | m \rangle$ is the overlap of the m^th eigenstate of the triplet-doublet Hamiltonian with the up/down-doublet-spin eigenstate of the total spin. The overlap factor changes with the magnetic field strength such that γ_{TCA} decreases with increasing magnetic field strength. If TCA is present as a loss/competing pathway in device operation, the photocurrent dependence with a changing external magnetic field will look like Figure 2-11.

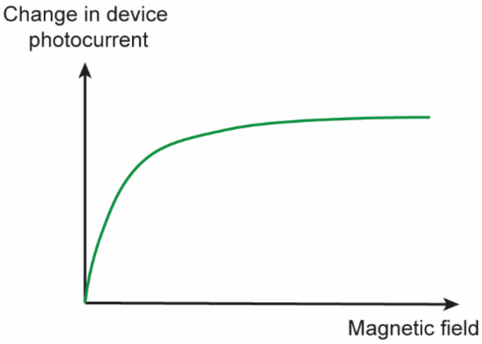

Figure 2-11. A schematic showing the magnetic field-dependence of device photocurrent where triplet-charge annihilation acts as a loss pathway for triplets which contribute to device performance. As the magnetic field increases, the rate of TCA decreases and a greater population of triplet states are present to contribute positively to the device photocurrent.

Often, in the devices discussed in this thesis, singlet fission and TCA are competing pathways. As a result, the magnetic field-dependence of device performance may include contributions from both features to varying degrees. The varying contributions may be modeled by creating a kinetic model that accounts for both features.

2.2. Crystalline-silicon as a bulk inorganic semiconductor

We shift gears now to briefly introduce crystalline-silicon. Unlike tetracene and the other organic molecular semiconductors introduced earlier, crystalline-silicon is a bulk inorganic semiconductor. In these materials, the dielectric constant (ease at which charges are displaced in the material in response to an electric field) is much higher, $\varepsilon_r \approx 12$, such that dielectric screening is significant and interactions between electrons can be considered negligible compared to in molecules[56].

2.2.1. Electronic structure

In silicon crystals, the atoms are bonded together by strong covalent bonds. The highest filled and lowest empty atomic orbitals form broad valence and conduction bands, where electrons can move coherently as a Bloch wave until they are scattered by phonons. These bands constitute a continuous density of electronic states. The energy difference between the conduction band minimum and the valence band maximum is referred to as the band gap of the semiconductor, and determines its optical and electrical properties. A schematic of the conduction and valence bands is presented in Figure 2-12.

When an inorganic bulk semiconductor is optically excited at energies above or equal to the band gap, an electron can be promoted from the valence band to the conduction band, resulting in a positive charge (hole) in the valence band. Unlike the excitons that are formed in organic molecules, the coulombic interaction between the electron and the hole is screened by the high dielectric constant. As a result, the transport is governed by free charge carriers at room temperature. This also implies similar values for the optical gap and the electrical gap. Excitons can still exist in inorganic bulk semiconductors at low temperatures, although unlike the Frenkel exciton that is highly-localized, we observe Wannier-Mott excitons that extend over multiple lattice sites (with binding energy of 14.7 meV for silicon)[86]. Usually, there is an equilibrium distribution between free charge carriers and excitons depending on the sample temperature and carrier density, and this can be obtained from the Saha equation[87].

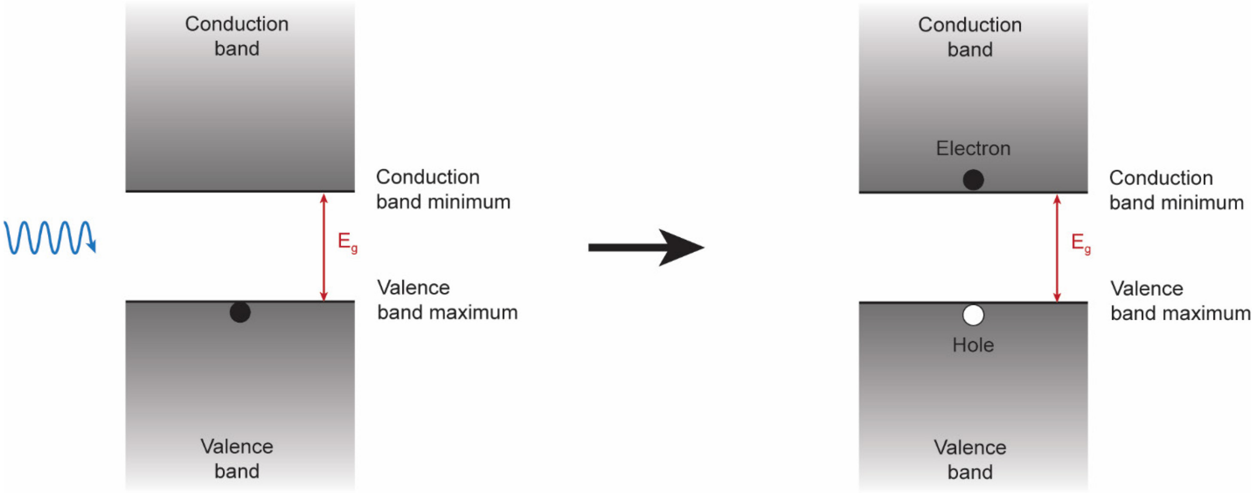

Figure 2-12. Optical excitation of an inorganic bulk semiconductor by a photon. An electron is promoted from the valence band to the conduction band, leaving behind a hole in the valence band.

The Fermi-Dirac distribution describes the probability that an energy level with energy E is occupied by an electron:

$$f(E) = \frac{1}{1 + \exp\left(\frac{E - E_F}{kT}\right)}, \tag{2-24}$$

where E_F is the Fermi level of the material, k is the Boltzmann constant, and T is the temperature. The Fermi level is defined as the energy at which there is a 50 % chance of being occupied by an electron. The energy of the Fermi level for a material can be calculated as follows:

$$E_F = \frac{E_C + E_V}{2} + \frac{kT}{2}\ln(N_V/N_C), \tag{2-25}$$

with E_C as the energy of the conduction band minimum, E_V as the energy of the valence band maximum, N_V as the effective density of states of holes in the valence band, and N_C as the effective density of states of electrons in the conduction band.

The conductivity of crystalline-silicon can be increased by intentionally introducing impurities, also known as *doping*. Replacing a silicon atom in the lattice with an element in the column to the right of it in the periodic table with 5 valence electrons (*e.g.* phosphorus) results in an extra electron that requires much less energy to be ionized. As a result, the Fermi level shifts closer to the conduction band, as depicted in Figure 2-13. This process is referred to as n-doping. Likewise, replacing a silicon atom in the lattice with an element in the column to the left with 3 valence electrons (*e.g.* boron) results in a hole and increased positive conductivity of the semiconductor.

The Fermi level shifts closer to the valence band as depicted in Figure 2-13, and we obtain a p-doped semiconductor.

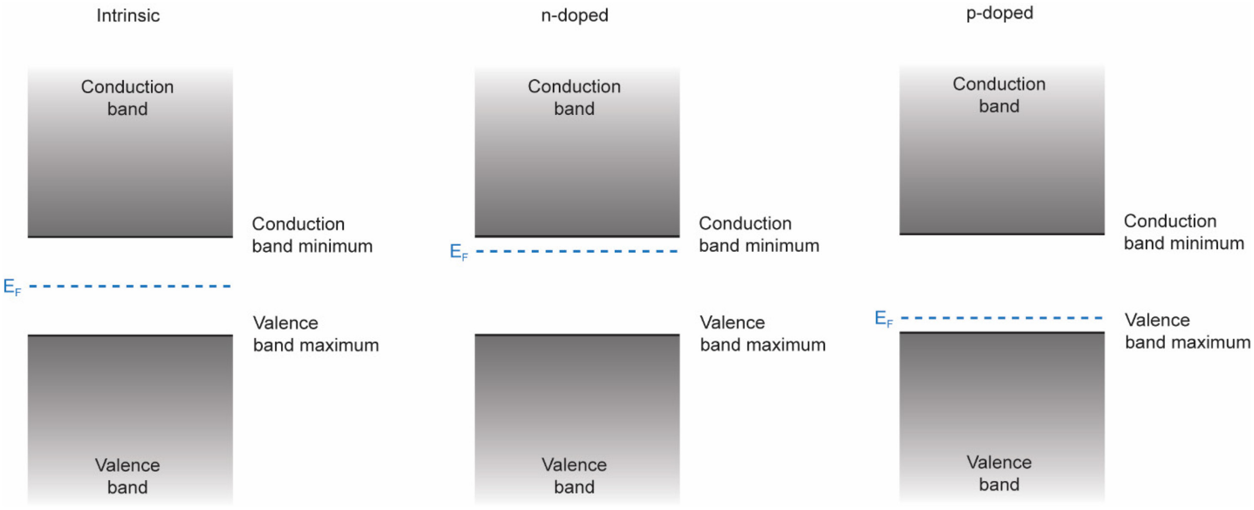

Figure 2-13 Fermi level position for intrinsic semiconductors, n-doped semiconductors and p-doped semiconductors.

Absorption of light by inorganic semiconductors depends on the nature of its band gap. For direct band gap semiconductors such as GaAs, the minimum energy of the conduction band lies directly above the maximum energy of the valence band in momentum-space. Thus, absorption of a photon with sufficient energy can directly excite the electron from the valence band to the conduction band. However, for indirect band gap semiconductors such as silicon, the conduction band minimum lies at a different crystal momentum from the valence band maximum. For these materials, absorption of a photon corresponding to its band gap energy requires a change in momentum of the electron which can be induced by thermal vibrations of the lattice (*i.e.* phonon-assisted). As a result, the absorption probability is lower in silicon compared to GaAs, and the corresponding wafer thicknesses used in silicon solar cells is thicker to compensate for the reduced absorption. This is captured in the absorption coefficient of silicon α_{Si}, plotted in Figure 2-14 as a function of wavelength for silicon[88].

The absorption coefficient can be used to calculate the number of photons absorbed at a certain depth in the sample:

$$I_{abs}(z) = I_{abs,0} \exp\left(-\alpha_{Si,\lambda} z\right), \tag{2-26}$$

where $I_{abs}(z)$ is the number of photons at depth z from the surface, $I_{abs,0}$ is the number of photons incident at the surface and $\alpha_{Si,\lambda}$ is the wavelength-dependent absorption coefficient. The absorption depth is usually defined as the inverse of the absorption coefficient. From Figure 2-14, we see that lower wavelength light is absorbed closer to the surface of silicon, while higher wavelength light is absorbed deeper.

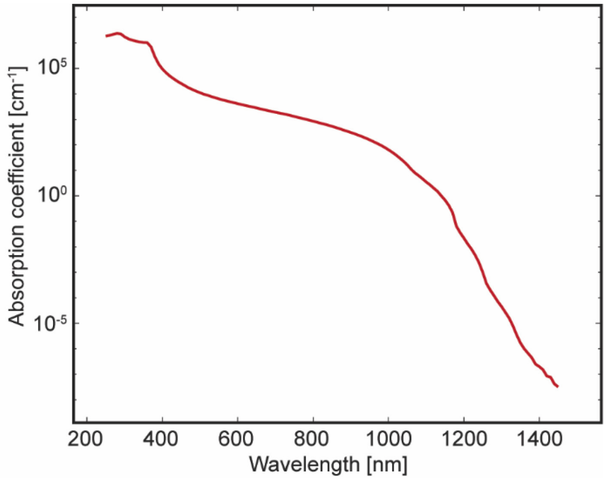

Figure 2-14. Absorption coefficient of silicon as a function of wavelength. Data was obtained from Green *et al.*[88]

2.2.2. The p-n junction

When you place a p-doped material and an n-doped material together, the extra electrons diffuse from the n-type material to the p-type material and vice versa for the holes until an equilibrium is reached. This results in positively-charged fixed donor ions in the n-type material and negatively-charged fixed acceptor ions in the p-type material. This creates an electric field at the junction that creates a potential barrier, referred to as the depletion zone. The width of this zone depends on the doping concentration of the p- and n-doped materials. This is illustrated in Figure 2-15. When we place the p- and n-type materials together, the Fermi level aligns and determines the energy level alignment, as demonstrated in Figure 2-15c. This results in band bending at the interface between the two materials.

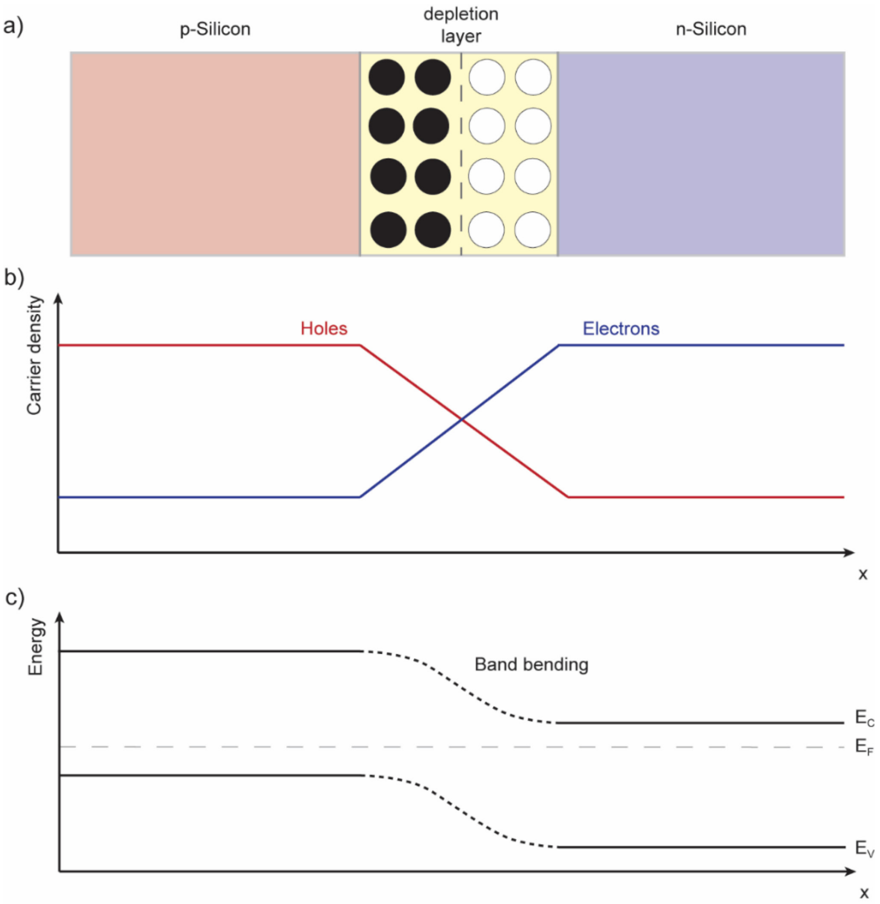

Figure 2-15. a) p-n junction formed when connecting p-doped silicon and n-doped silicon together. b) Concentration profile of holes and electrons as a function of position along the p-n junction. c) Energy level diagram of the p-n junction, showing the Fermi energy is aligned across the two materials. This results in band bending at the junction. It is favorable for electrons to flow from p-Si to n-Si, and for holes to flow from n-Si to p-Si.

At equilibrium, the potential barrier prevents carriers from diffusing across the depletion zone any further. However, if we apply an electric bias by connecting electrodes and a power source to the p- and n-doped ends, we can provide the carriers with additional energy to overcome this barrier. This is the operating principle of a diode, whose current-voltage characteristics are shown in Figure 2-16. In the forward bias regime, the p-type material is connected to the positive terminal and the n-type material is connected to the negative terminal of a voltage source. This decreases the width of the potential barrier and carriers gain enough energy to overcome the barrier, resulting in high current flow. In the reverse bias regime, the connections are reversed. This results in the carriers being extracted away from the depletion region, increasing the width of this layer and increasing the resistance further. Eventually, if a negative voltage beyond the breakdown voltage of the diode is applied, current begins to flow through a Zener or avalanche breakdown process.

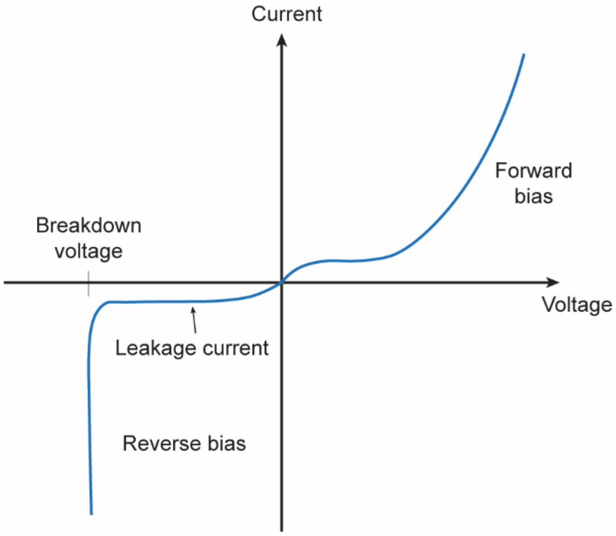

Figure 2-16. Current-voltage characteristic curve for diodes.

2.2.3. Silicon solar cell operation

The basic operation of silicon solar cells can be described by a p-n junction. When the p-n junction is illuminated by light, the carriers generated in the depletion region, or one diffusion length from the junction, will move under the influence of the built-in electric field such that electrons are attracted to n-Si and holes are attracted to p-Si. These charges can be collected by electrodes attached to both sides of the junction, generating photocurrent. Because the collection of carriers relies on the position of the p-n junction, junction depth (how far the p-n junction is relative to the surface of the device) becomes an important parameter in device operation.

The governing equations for semiconductor device physics (in the one-dimensional limit for simplicity) are as follows:

$$\text{Current equations:} \begin{cases} J_n = q\left(\mu_n nE + D_n \dfrac{dn}{dx}\right) \\ J_p = q\left(\mu_p pE - D_p \dfrac{dp}{dx}\right) \end{cases} \tag{2-27}$$

$$\text{Poisson's equation:} \frac{dE}{dx} = \frac{q}{\varepsilon\varepsilon_0}(p - n + N_D^+ - N_A^-)$$

$$\text{Continuity equations: } \begin{cases} \frac{1}{q}\frac{dJ_n(x)}{dx} = R - G \\ \frac{1}{q}\frac{dJ_p(x)}{dx} = G - R, \end{cases}$$

where J is the current density for n (electron density) or p (hole density), q is the elementary charge, μ is the mobility of the charge carrier, E is the electric field, D is the carrier diffusivity, ε and ε_0 are the relative permittivities in the material and in vacuum, N_D^+ is the dopant concentration for donors and N_A^- is the dopant concentration for acceptors, G is the generation term and R is the recombination term.

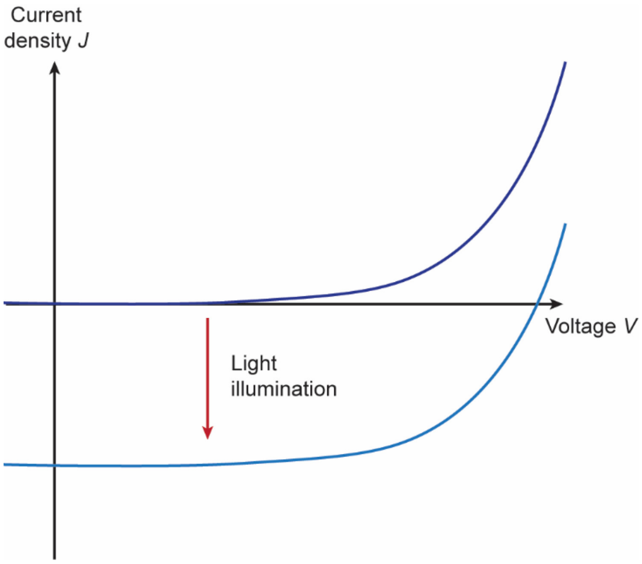

Figure 2-17. J-V characteristic curve for a solar cell under dark (dark blue) and light (light blue) operation. The curve is shifted down into the fourth-quadrant upon illumination of the cell.

From these equations, we can derive the current density of a solar cell upon illumination by light:

$$J = J_0\left(\exp\left(\frac{qV}{nkT}\right) - 1\right) - J_L, \tag{2-28}$$

where J_0 is the reverse saturation current density and J_L is the light-generated current density. As a result, light illumination shifts the J-V curve into the fourth quadrant, as depicted in Figure 2-17.

2.2.4. Characterizing solar cells

2.2.4.1. Short-circuit current

For simplicity, we usually flip the sign on the characteristic equation so the curve can be plotted in the first quadrant:

$$J = J_L - J_0 \left(\exp\left(\frac{qV}{nkT} \right) - 1 \right). \tag{2-29}$$

The short-circuit current density J_{SC} is defined as the current density obtained when there is no voltage ($V = 0$) in the cell:

$$J_{SC} = J_L. \tag{2-30}$$

For silicon solar cells, under AM 1.5 radiation, the peak J_{SC} is 44 mA/cm^2 [89]. The short-circuit current depends on the generation rate of solar cells and diffusion lengths of the carriers. Incorporating a singlet fission layer to increase the charge carriers in the silicon cell will therefore increase the short-circuit current and overall achievable current in the device, as we will see later on in this thesis.

2.2.4.2. Open-circuit voltage

The open-circuit voltage can be obtained when there is no current in the cell, *i.e.* $J = 0$. This results in:

$$V_{OC} = \frac{nkT}{q} \ln\left(\frac{J_L}{J_0} + 1 \right). \tag{2-31}$$

Very high-quality silicon solar cells have been reported with V_{OC} over 760 mV[90]. It should be noted that using a singlet fission material on its own for a solar cell compared to using a material with the same band gap as the singlet energy would result in doubled photocurrent for the solar cell, but half the voltage. Thus, the benefit of the singlet fission layer is maximized when combined with a solar cell whose bandgap is equivalent or less than the energy of the triplet exciton.

2.2.4.3. Fill factor

The fill factor is defined as the following ratio:

$$FF = \frac{V_m J_m}{V_{OC} J_{SC}}, \tag{2-32}$$

where V_m and J_m are the voltage and current densities at the optimal operating point of the cell, depicted in Figure 2-18. The closer the characteristic curve is to a rectangular shape, the higher the fill factor will be. It depends on the quality of the junction and the degree of recombination losses in the solar cell. Normally, fill factors lie in the range of 0.75 to 0.85[89].

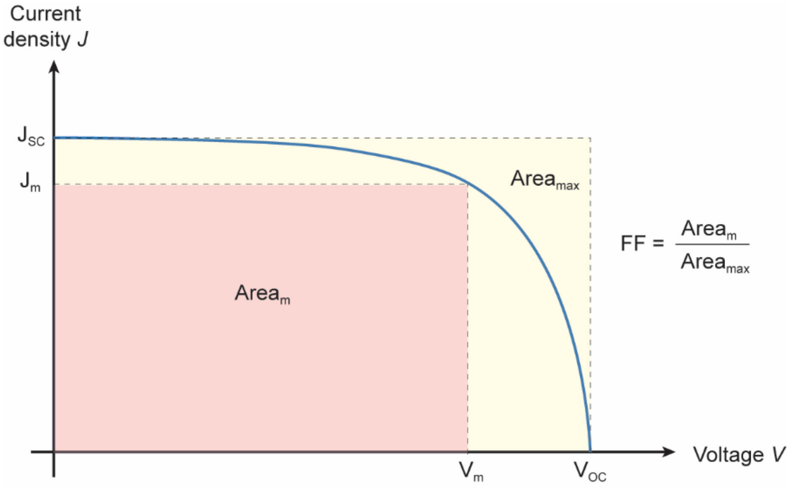

Figure 2-18. Current density-voltage characteristic curve of a solar cell represented in the first quadrant. The important solar cell parameters of short-circuit current density J_{sc}, open-circuit voltage V_{OC}, and fill factor FF are represented, along with the current density and voltage at maximum power J_m and V_m.

2.2.4.4. Power conversion efficiency

The power conversion efficiency of a solar cell is defined as:

$$PCE = \frac{FF \cdot V_{OC} \cdot J_{SC}}{P_{light}}, \tag{2-33}$$

where P_{light} is the power of incident light on the cell. The limit of power conversion efficiencies has been described in detail in Section 1.1.

2.2.4.5. Quantum efficiency

In addition to the power conversion efficiency, we can also measure the quantum efficiency of a solar cell. The external quantum efficiency (EQE) is defined as the ratio of the number of charge carriers collected by the solar cell to the number of photons incident on the solar cell:

$$EQE = \frac{\text{\# of photogenerated charge carriers}}{\text{\# of incident photons}}. \tag{2-34}$$

A representative EQE spectra collected from a reference silicon cell is presented in Figure 2-19. We see that in the blue wavelength region, the EQE drops as the carriers are absorbed closer to the surface and are more susceptible to surface recombination losses. Additionally, silicon reflects more light at this wavelength. At intermediate wavelengths, the EQE is not at 100 % due to reflection and extraction losses with respect to collection of the charge carriers. At wavelengths in the infrared, the EQE drops strongly due to reduced absorption of light approaching the band gap energy. The EQE can be significantly boosted by incorporating passivating layers to reduce surface recombination and antireflection coatings/structuring techniques to reduce reflection losses.

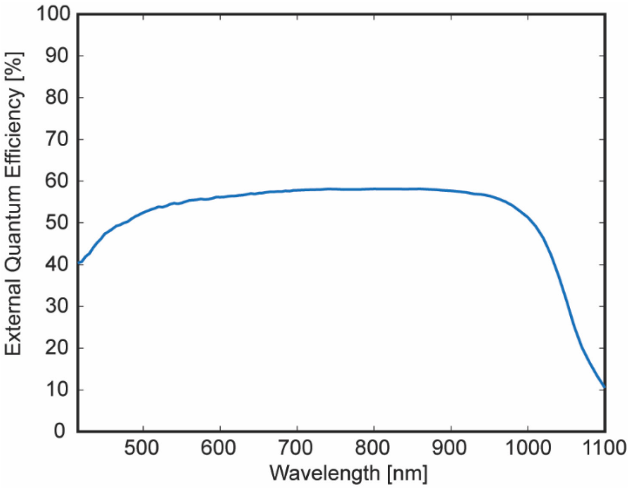

Figure 2-19. Planar cell external quantum efficiency spectra measured with a 1 nm-thick AlO_x passivating layer.

The internal quantum efficiency is defined as the ratio of the number of charge carriers collected by the cell to the number of photons absorbed by the cell:

$$IQE = \frac{\#\text{ of photogenerated charge carriers}}{\#\text{ of absorbed photons}} = \frac{EQE}{(1-R)}. \tag{2-35}$$

The IQE can be obtained from the EQE by measuring the reflectance of the cell R, and correcting for the reflection losses (assuming the solar cell is sufficiently thick that there are no transmission losses).

2.2.5. Loss pathways

Bulk recombination contributes to losses in the solar cell as the carriers recombine before they can be extracted through the electrodes. We introduce three different kinds of recombination mechanisms.

Radiative recombination (also referred to as band-to-band recombination) can be thought of as analogous to the inverse of absorption. The electron returns from the conduction band to the valence band, annihilating with the hole. The energy radiated during this process corresponds to the band gap of the semiconductor. In silicon, because of the indirect band gap, this recombination also occurs at low probability due to the requirement of change in momentum space. As a result, the carrier lifetimes in silicon are reported to be on the order of ms as opposed to ns–μs in GaAs[91].

Auger recombination is a three-particle process where an electron gives its energy to a third carrier which gets excited into a higher energy level within the same band. The third carrier then loses its energy *via* thermalization back to the band edge. The process of Auger recombination is depicted in Figure 2-20. Because the process involves three carriers, Auger recombination is usually most significant at high carrier densities (can be noticeable at dopant concentrations higher than 10^{18} cm^{-3})[92].

In silicon solar cells, Shockley-Read-Hall recombination dominates[93,94]. Also referred to as trap-assisted recombination, this recombination process occurs when impurities or crystal defects introduce *trap states* that lie between the band gap of the material. These trap states can be shallow (near the band edges) or deep (closer to the middle of the gap), as shown in Figure 2-21a. According to the Shockley-Read-Hall model, four different processes can occur to carriers with respect to the trap states. These are depicted in Figure 2-21b.

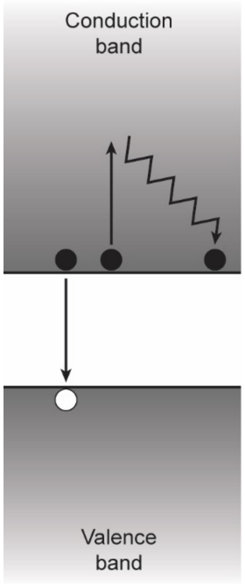

Figure 2-20. Auger recombination process involving a third carrier (electron) in the conduction band. The recombination of the electron-hole pair excites the third carrier further up into the conduction band, which then thermalizes back to the band edge.

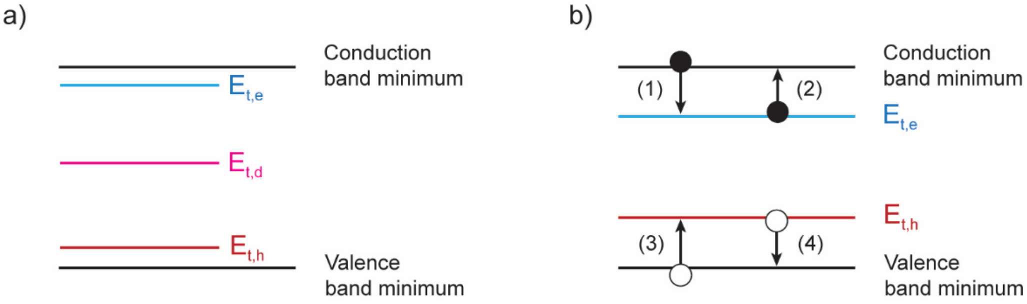

Figure 2-21. a) Trap states introduced in the middle of the band gap by impurities or crystal defects. Illustrated are examples of shallow electron traps $E_{t,e}$ (blue), shallow hole traps $E_{t,h}$ (red) and deep traps $E_{t,d}$ (pink). b) Possible events for carriers in the SRH model. (1) Electron is trapped in an electron trap state, (2) electron can be excited to the conduction band from the electron trap level, (3) hole is trapped in a hole trap state, (4) hole can be released to the valence band from the hole trap level.

Trap-assisted recombination is particularly prevalent at the surface and at interfaces in the solar cell. At the surface, dangling bonds from discontinuation of the crystal lattice can create defect states that lie in the gap of silicon. In particular, since some solar cell configurations involve contacts located on the front and back side of the silicon wafer, managing recombination losses at the contact-silicon interface is crucial. Additionally, the singlet fission-sensitized silicon solar cells that are the subject of this thesis, are particularly sensitive to silicon surface recombination, as these can act to quench the triplet excitons during the transfer process from the organic singlet fission layer to the silicon. As such, surface passivation is necessary to mitigate these losses.

A typical measure of the surface passivation quality is the surface recombination velocity, which is defined by:

$$J_{rec} = qU_s = qS\Delta n_d, \tag{2-36}$$

where J_{rec} is the current density that flows into the surface to recombine, U_S is the recombination rate at the surface per unit area, S is the surface recombination velocity, and Δn_d is the excess carrier concentration near the surface.

Surface recombination losses can be reduced by two means, as shown in Figure 2-22. Firstly, reducing the density of defect states at the surface can be achieved through chemical passivation by depositing layers that react with the dangling bonds on the silicon surface. This typically involves oxides or nitride layers grown using atomic layer deposition or chemical vapor deposition techniques.

Additionally, dielectric layers can be used to generate an electric field at the surface to repel minority carriers from the surface trap states through introduction of fixed charges in the layer. Typical examples include SiO_2 for n-doped silicon and Al_2O_3 for p-type silicon[95–98].

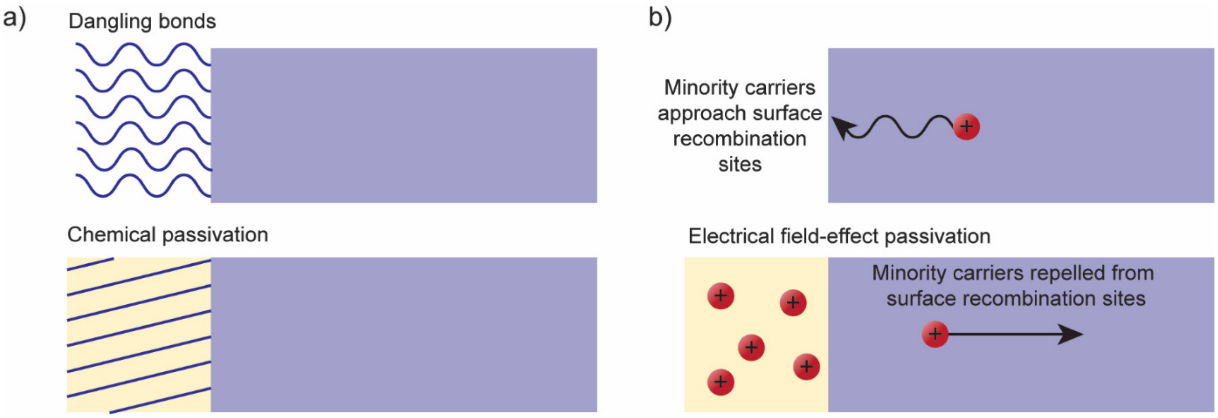

Figure 2-22. Surface passivation schemes for silicon solar cell surfaces. a) Chemical passivation involves growing a layer that forms bonds with the dangling bonds on the surface, eliminating surface trap states. b) Electric field-effect passivating layers introduce an electric field on the surface to repel minority carriers from surface trap states.

Chapter 3.

Historical perspective of singlet fission-sensitization of silicon solar cells

In this chapter, we provide a review of the historical progress and highlight key challenges for singlet fission-sensitized silicon solar cells. First proposed by Dexter back in 1979[27], coupling singlet fission to silicon solar cells has the potential to enhance efficiencies from 29.4 % up to 35–42 %[26,36,28,37,38], depending on whether endothermic fission is accounted for. We note that not only does successful coupling have huge implications for solar cell technologies, the additional boosts in quantum efficiencies can also benefit silicon-based photodetectors and other optoelectronic devices that would benefit from triplet excitons through an organic/inorganic interface. In this section, we break down the triplet exciton sensitization process into three parts and cover the progress made in each area prior to this thesis: we start with material considerations for the singlet fission layer, followed by different triplet sensitization processes at the interface, and then finally cover the silicon solar cell architectures that have been studied. Schematically, these three areas are represented in Figure 3-1.

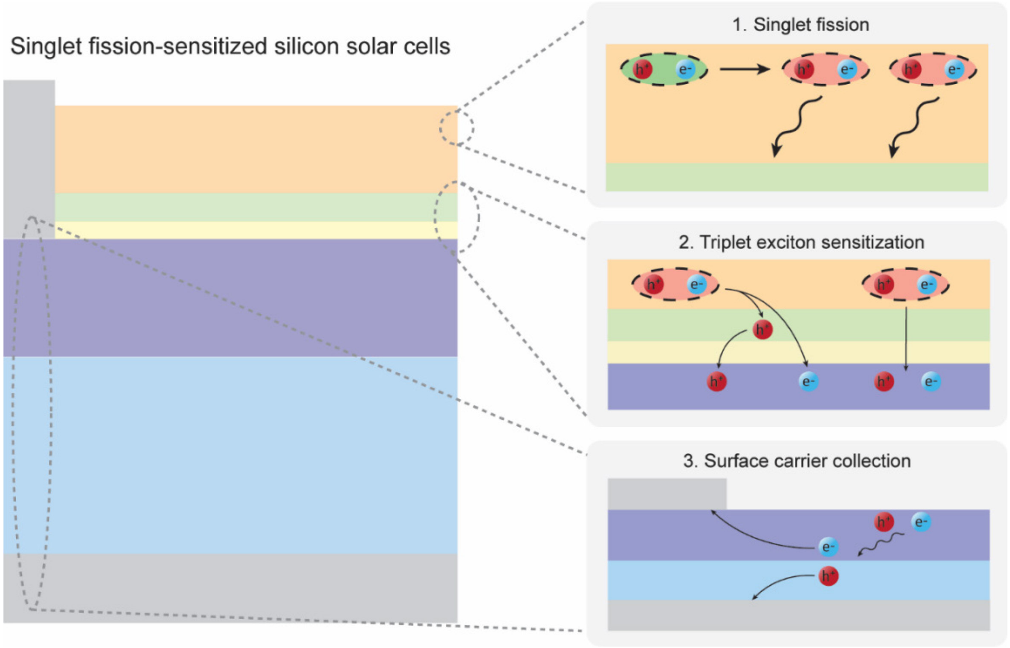

Figure 3-1. The processes involved in successful singlet fission sensitization of silicon solar cells. 1. The top layer must perform singlet fission at high yields and fast kinetics, and the triplets should diffuse to the silicon interface. 2. Triplet excitons need to sensitize the silicon, either by direct transfer or energy transfer. 3. Generated carriers at the silicon cell surface need to be effectively extracted by the solar cell.

3.1. Singlet fission material considerations for enhancing silicon solar cells

The ideal candidate for the singlet fission material for silicon would meet the following requirements:

1. **Triplet energy $\boldsymbol{E_{T1} \gtrsim E_g = 1.1}$ eV.** The triplet energy needs to be greater than the band gap of silicon such that there is sufficient enthalpic driving force for the triplet exciton sensitization process. The triplet energy cannot also be significantly greater than the silicon band gap, otherwise there will still be thermalization losses from the excess energy. There may be a possibility that sensitizing silicon with a triplet energy slightly less than the band gap is possible through an entropic benefit argument, although this has yet to be demonstrated. Additionally, if a radiative sensitization method is employed, for example through quantum dots[99], additional Stokes shifts are expected which may require even higher energy triplet excitons. We point the reader towards Perkinson *et al.* for details on searching for blue fission candidates[100].
2. **Fast singlet fission rate $\boldsymbol{k_{SF}}$.** When the singlet fission material is placed next to silicon, the most likely competing pathway is singlet transfer from the layer to silicon. To avoid this loss, having a singlet fission rate that occurs faster than the corresponding singlet transfer process is ideal. Usually, a fast singlet fission rate is synonymous with $E_{S_1} > 2E_{T_1}$, *i.e.* that the singlet fission process is exothermic. However, studies have shown that endothermic fission has the potential to raise the efficiency limit of singlet fission-sensitized solar cells from 41.9 % to 45.9 %[37]. In relation, having a slow competing triplet-triplet annihilation rate is also desired.
3. **High triplet exciton yield $\boldsymbol{100\,\% < \eta \leq 200\,\%}$.** For there to be a positive contribution from fission to the silicon photocurrent, the yield of triplet excitons from the fission process needs to be sufficiently high such that the benefit from fission outweighs the absorption loss incurred by silicon as a result of the fission layer placed on top of the cell. As the sensitization is a multi-step process, as close to 200 % triplet yields are ideal.
4. **High absorption at singlet energies and above.** To maximize the effect from fission and reduce thermalization losses, it would be great for the singlet fission layer to absorb the energies greater than double the band gap very efficiently while transmitting the rest of the solar spectrum through to silicon. Device architectures can also be used to help achieve

increased absorption, for example by introducing an additional absorber layer to funnel to tetracene, or by using nanostructured surface texturing.

5. **High triplet diffusion length and lifetime.** Once the triplet excitons are formed from fission, they need to be transported to the interface. Materials with long triplet diffusion lengths and lifetimes can be beneficial for this reason.
6. **Material stability.** The underlying silicon solar cell has lifetimes that last from 20-30 years[101]. To get the maximum benefit from fission, the singlet fission layer would also have similarly long-term stability. However, we note that unlike the case with tandem solar cells connected in series, if the singlet fission material degrades faster than the silicon, the bottom silicon solar cell can still operate on its own as a regular silicon solar cell. The singlet fission material should ideally be resistant to thermal, light and chemical degradation. This can be quite challenging as oxygen has a triplet ground state, and quenching of the triplet excitons by triplet oxygen can result in formation of singlet oxygen which usually causes a photooxidation reaction that can degrade the organic material[102].

Figure 3-2 shows the energy alignments described above for the singlet fission layer relative to the band gap of silicon, as well as the competing pathways to triplet exciton transfer.

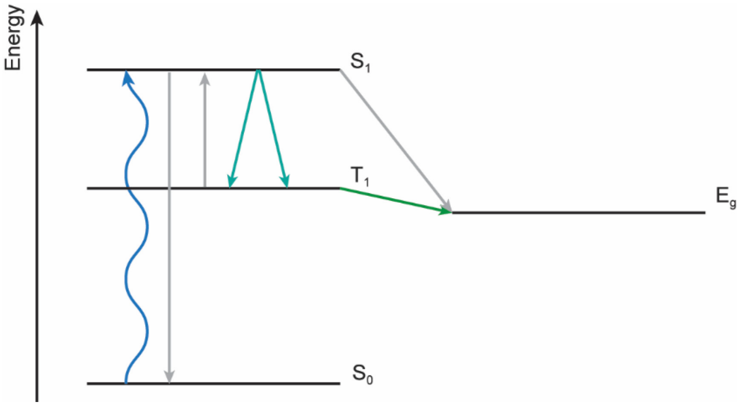

Figure 3-2. Energy level alignments for the singlet exciton and triplet exciton in the singlet fission layer relative to the silicon band gap for efficient triplet exciton sensitization of silicon. The relevant transitions are shown in color: (blue) absorption of light by the singlet fission layer, (teal) singlet fission of the singlet exciton to two triplet excitons, (green) triplet exciton transfer to silicon. In grey, we show the competing pathways of singlet decay, triplet-triplet annihilation and singlet transfer to silicon.

Most studies for coupling to silicon have been performed with acenes, specifically, tetracene, pentacene and their derivatives. Tetracene is a good candidate for probing triplet sensitization for crystalline-silicon because its triplet energy at 1.25 eV is just above the band gap of silicon, it shows near 200 % yield of triplet excitons, and the fission process has been extensively characterized[34,35,75]. Additionally, fission occurs endothermically, as a result this may provide some extra entropic boost in efficiencies from the sensitization process[37]. Pentacene undergoes exothermic singlet fission and has a triplet energy of 0.85 eV and is not suitable on its own for sensitizing silicon[103]. However, 1.1 eV PbSe quantum dots have been reported to successfully harvest the triplet excitons from pentacene and have been used to sensitize a thin layer of amorphous silicon[103,104]. Unfortunately, acenes face a significant barrier to industrial implementation due to their poor photostability in the presence of oxygen[105,106]. As most of the studies presented in this thesis are proof-of-concept demonstrations, we use tetracene as our singlet fission layer. However, we expect that many of the scientific findings can be extended to other singlet fission layers beyond tetracene.

Other singlet fission materials that may be of interest for silicon sensitization include perylenediimides (PDI) and their derivatives. PDIs are used as industrial pigments, benefiting from improved photochemical and thermal stability compared to the acenes[107,108]. They exhibit endothermic fission and have high molar extinction coefficients (good absorbers), and have even been reported to yield triplet excitons of around 1.1 eV with 140 % yield[109–112].

Additionally, there have been a large range of studies performed on intramolecular fission materials. While these molecules have reported high rates of singlet fission, the generated triplets are spatially localized near each other and have a consequently higher chance of fusion back to the singlet state[113]. As a result, further improvements for extracting triplet excitons efficiently are desired for device application.

We point the reader towards the review by Casillas *et al*. which has a very comprehensive list of singlet fission materials and their properties for further reading[114].

3.2. Singlet fission enhancement methods of silicon solar cells

There are several methods for enhancing silicon solar cell performance through singlet fission. In this section, we cover tandem structures, QD-mediated transfer, exciton dissociation through single-charge transfer, and direct triplet exciton transfer. These methods are highlighted in Figure 3-3.

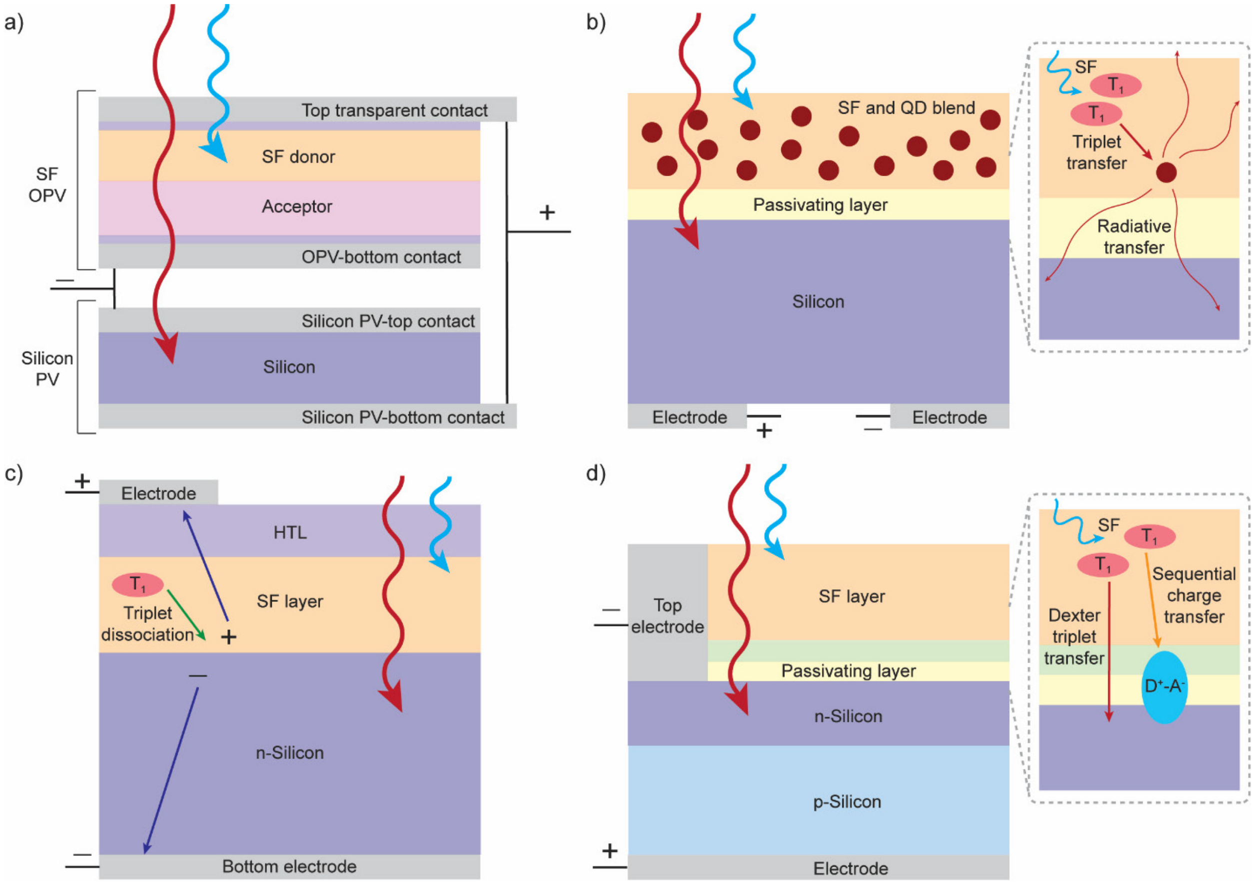

Figure 3-3. Singlet fission enhancement methods for silicon solar cells. a) Incorporating a singlet fission organic photovoltaic (OPV) top cell in tandem with a silicon bottom solar cell. The top cell absorbs the high energy light and generates photocurrent. The bottom cell absorbs the transmitted low energy light and generates photocurrent. b) Quantum dot-mediated triplet exciton sensitized silicon solar cells. The top singlet fission and quantum dot (SF and QD blend) layer absorbs the high energy light and the QDs are sensitized by the triplet excitons. The QDs then radiatively emit light to the silicon at lower energy to generate photocurrent. c) The SF layer absorbs the high energy light and triplet excitons are dissociated at the SF layer/silicon interface. Holes are transported through the SF layer and the hole transport layer (HTL) to get to the top electrode, while electrons are transported through n-Si to get to the bottom electrode. d) Triplet exciton-sensitized silicon solar cells through direct triplet exciton transfer. The SF layer absorbs the high energy light and triplet excitons are transferred either through Dexter transfer or sequential charge transfer. The carriers then diffuse to the p-n junction of the silicon cell and are separated and extracted through their respective electrodes.

3.2.1. Tandem configuration

Similar to the multi-junction tandem solar cells introduced previously, a singlet fission-silicon tandem solar cell structure can be built. As depicted in Figure 3-3a, this would involve a singlet fission top cell that absorbs the high energy light and allows low energy light to be transmitted to the bottom silicon solar cell. Pazos-Outón *et al.* demonstrated a singlet fission-silicon tandem structure that was voltage-matched and showed quantum efficiencies exceeding 100 % at the absorption peak of the SF layer when a special reflection configuration was utilized[115]. A pentacene-C_{60} organic photovoltaic cell (OPV) was used as the singlet fission cell, and connected in parallel with a back-contacted silicon solar cell[115]. While this structure showed clear contributions from carrier multiplication in enhancing the silicon solar cell performance, as evidenced by peaks corresponding to the absorption spectrum of pentacene in the overall device EQE, parasitic absorption losses were significant[115]. Further optimization of the device to enhance absorption by the singlet fission top cell is necessary. Additional engineering will also be needed to incorporate the two cells together through a common shared middle contact to simplify fabrication complexity. We note that as mentioned earlier on tandem cells, unlike single-junction solutions, this architecture does have increased complexity due to the need for current/voltage-matching between the two solar cells, which puts tighter requirements on optimization of the various layers involved in the two cells, and introduces some barriers to industrial implementation with existing solar cell manufacturing lines.

3.2.2. Quantum dot-mediated triplet exciton transfer

We now turn to singlet fission sensitization for single-junction architectures. One approach for sensitizing silicon photovoltaics is through using quantum dots to mediate the triplet exciton energy transfer process, as shown in Figure 3-3b. While triplet exciton transfer to bulk inorganic semiconductors such as *c*-Si has proven challenging, there have been several demonstrations of successful triplet exciton sensitization of quantum dots, such as in PbS[116] and PbSe[117]. The triplet excitons formed from the singlet fission process are dark states and are limited to short-range transfer processes to the silicon. However, by using quantum dot intermediates, the absorbed triplet exciton energy can be radiatively emitted to silicon by the quantum dot, enabling much longer-range energy transfer processes such as FRET.

Most of the work with this sensitization method has been largely focused on the triplet exciton transfer from singlet fission materials to the quantum dots, and less so with respect to the coupling with bulk silicon. The early work was focused on using bilayers, where a thin film of either tetracene or pentacene was deposited onto a layer of quantum dots. A triplet transfer efficiency of 90 % was demonstrated from tetracene to PbS nanocrystals[116], and 95 % from pentacene to PbSe nanocrystals[117]. More recently, the field has progressed towards using singlet fission-based ligands directly on the nanocrystals to maximize absorption from singlet fission and reduce triplet diffusion losses to the quantum dot. While there are challenges with ensuring the triplet excitons formed from fission are injected sequentially to the quantum dot to prevent biexciton formation, 5,12-bis((triisopropylsilyl)ethynyl)tetracene) (TIPS-tetracene) carboxylic acid ligands on PbS quantum dots have been shown to work, demonstrating singlet fission and sequential triplet transfer yields of near unity[118]. Follow up studies on the same TIPS-tetracene ligand on PbS quantum dot system in solution have been performed to minimize QD parasitic absorption losses[99]. Additionally, triplet exciton transfer from perylene ligands to Si quantum dots has also been shown, although the reverse process is also possible in this system, which may limit device applications[119].

The main challenge with using quantum dot-intermediates is that this introduces multiple routes for efficiency loss during the sensitization process. The overall sensitization efficiency can be described using the following equation:

$$\eta = \eta_{SF} \cdot \eta_{TD} \cdot \eta_{TT} \cdot \eta_{PL} \cdot \beta \cdot \eta_{Si}, \tag{3-1}$$

where η_{SF} is the singlet fission efficiency, η_{TD} is the triplet diffusion efficiency from the SF material to the QD, η_{TT} is the triplet transfer efficiency from the SF material to the QD, η_{PL} is the efficiency of radiative emission from the QD, β is a geometric factor that accounts for the actual amount of radiative emission from the QD absorbed by the silicon, and η_{Si} is the quantum efficiency of silicon at the QD emission wavelength. In particular, $\eta_{PL} \cdot \beta \cdot \eta_{Si}$ is the most challenging aspect as all of the quantum dots studied emit too far in the infrared below the silicon bandgap, and additional light-trapping structures will be needed to avoid radiative losses in the direction away from the silicon. QD concentrations will need to be optimized to avoid aggregation and re-absorption losses. Finding suitable quantum dots and bluer fission materials is crucial for this sensitization method to progress.

3.2.3. Charge-transfer approach

Instead of using quantum dots to mediate the triplet exciton transfer process which can introduce additional losses in sensitization efficiency, there is interest in directly harnessing the energy from the triplet exciton. One approach is the charge-transfer strategy, where the triplet exciton is dissociated at the interface between the singlet fission material and silicon. MacQueen *et al.* implemented this in a silicon solar cell architecture with tetracene deposited directly on hydrogen-terminated silicon[46]. The exciton is dissociated at this interface and the tetracene also acts as a layer that supports hole transfer from the interface to a PEDOT:PSS hole transport layer (depicted in Figure 3-3c). Since whether charge transfer or exciton transfer occurs at the interface can depend on the energy level alignment of the materials, the solar cell structure was designed to support both sensitization mechanisms, although it would be less efficient if only full triplet exciton transfer was occurring. Unfortunately, device EQE measurements did not yield any enhancements from tetracene, instead, dips correlating to the absorption spectrum of tetracene were observed[46]. Optical modeling of the EQE spectra suggest an exciton-to-photocurrent conversion yield of 8 % out of a maximum of 200 %, indicating that a very small amount of sensitization is occurring, although not enough to improve the photocurrent[46].

Follow-up studies to this work include finer tuning to the energy level alignment at the interface performed by Niederhausen *et al*[120]. Different approaches to offset the energy level alignment between tetracene and silicon were performed by modifying a hydrogen-terminated silicon surface with 2,2′-(perfluoronaphthalene-2,6-diylidene)dimalononitrile (F6TCNNQ), C_{60}, and NF_3[120]. While modification to the energy level alignments were confirmed, none of the functionalized interfaces used in the charge transfer solar cell architecture with the PEDOT:PSS hole transport layer showed enhancements in the device EQEs. It is suspected that the functionalized interfaces also affected the morphology of tetracene, which in turn could affect the singlet fission rates and triplet diffusion through the layer[121–124]. The *c*-Si surface electronic structure may also have been affected by the surface treatment, resulting in unfavorable electronic conditions for charge transfer.

While single charge transfer from tetracene to silicon is entirely possible, a high efficiency of carrier extraction and sensitization efficiency is necessary to observe enhancements in photocurrent. We denote the sensitization efficiency in these devices as:

$$\eta = \eta_{SF} \cdot \eta_{TD} \cdot \eta_{CT} \cdot \eta_{Si}, \tag{3-2}$$

where η_{CT} is the efficiency of charge transfer from the triplet exciton to silicon at the interface, and the other parameters are as defined previously. The charge dissociation-type device structure studied may not be the ideal platform for such observations due to the additional transport requirements for the hole through the tetracene layer, affecting η_{Si}. The photogenerated carriers in the silicon layer itself also have to travel through the tetracene layer to be extracted by the top electrodes. Additionally, presence of holes and triplets may result in triplet-charge annihilation, which is a competing pathway to triplet sensitization and can be difficult to mitigate, affecting η_{SF}.

Another sensitization attempt involved a tri-layer solar cell where the triplet exciton is dissociated at a pentacene-PbSe nanocrystal interface[104]. The electron is transported through the PbSe nanocrystal layer to a thin layer of amorphous silicon, before collection at the electrode. The hole is transported through the pentacene layer to the other electrode. The amorphous silicon layer also acts as a solar cell for absorbing higher wavelength light. Although demonstration of slight peaks from pentacene was observed in the device EQE, the core photovoltaic device made up of amorphous silicon meant that the power conversion efficiencies that were measured for the tri-layer device was 2 %[65].

3.2.4. Direct triplet exciton sensitization

Finally, we introduce the sensitization method that has had the most progress for the single-junction configurations. Instead of dissociating the exciton at the interface, the exciton can be directly transferred to the silicon, either through a Dexter transfer mechanism where both of the carriers transfer simultaneously, or through a sequential charge transfer-type mechanism where the carriers transfer one after the other, *via* an intermediate donor-acceptor state (D^+-A^-), as depicted in Figure 3-3d.

Initial studies for the direct transfer process were performed by depositing tetracene directly onto silicon with varying thicknesses of LiF spacer layers in between[44,45]. In both studies, increasing the thickness of the LiF layer resulted in increased fluorescence intensity from the tetracene. The transient photoluminescence measurements of the tetracene fluorescence showed a quenching of the prompt fluorescence intensity with and without the LiF layer, indicating quenching of singlet excitons but with no evidence of triplet exciton transfer[88].

The first successful demonstration of triplet exciton sensitization of bulk crystalline-silicon was demonstrated using a thin layer of hafnium oxynitride (HfO_xN_y) deposited between n-Si and tetracene[35]. The sensitization was observed *via* magnetic field-dependent photocurrent and silicon photoluminescence measurements, showing a characteristic field-dependence that tracked the population of triplet excitons from singlet fission[35]. As the triplet population from fission decreased, the photocurrent and silicon photoluminescence also decreased correspondingly. The HfO_xN_y interlayer was hypothesized to play a bifunctional role, acting to passivate silicon surface defects while mechanistically supporting the triplet exciton transfer process. The sensitization process was found to strongly depend on the interlayer thickness, attributed to competing effects between improved passivation of silicon surface defects, and increased tunneling distance for exciton carrier transport across the interlayer, resulting in an optimum interlayer thickness of 8 Å. Additional excitation wavelength-dependent silicon photoluminescence measurements showed that the triplet excitons were not just transferring across the interface, but also contributing to electric field-effect passivation of the silicon surface as a result of charge generation at the interface following illumination of tetracene[35]. The contributions of triplet transfer and field-effect passivation to the magnetic field effect were quantified using both a monochromatic and a bichromatic experiment. By applying a model which accounts for these two contributions in both experiments, a value for the triplet transfer yield of 76% ± 7% was obtained[35]. However, interdigitated back contacted (IBC) devices fabricated using the 8 Å-thick layer did not show any enhancements in the EQE from singlet fission[35]. The thin passivation layers necessitated by the transfer process results in poor carrier collection from the silicon surface due to surface recombination. Additional mechanistic understanding of the role HfO_xN_y plays in the coupling of the triplet excitons for direct transfer to silicon is desirable for further advancements in observing device performance enhancements.

Following the study with HfO_xN_y, there have been a sampling of other studies on tetracene deposited directly on hydrogen-terminated silicon[47], as well as on pyrene linkers covalently-bonded to the silicon surface[125]. The latter study did not show conclusive evidence of triplet exciton sensitization. The former study however, found that aging the tetracene/silicon IBC in air resulted in magnetic field effects in photocurrent and silicon photoluminescence that also tracked with the triplet population from singlet fission[47]. The effect was attributed to a change in tetracene polymorphism, that could result in triplet exciton transfer through orientation of the tetracene molecules on the silicon surface[47]. However, as seen in the case with HfO_xN_y[35], electric field-effect passivation from tetracene can also give rise to a similar effect, and this effect was not studied in this system. Additionally, aged IBC cells fabricated with tetracene did not show enhancements from fission[47].

To probe the effect of morphology, tetracene seed layers were covalently bound at different linker positions to the silicon surface to directly modify the orientation of tetracene relative to the silicon surface[126]. Magnetic field-dependent silicon photoluminescence measurements showed a characteristic dependence that tracks with the singlet population in singlet fission, suggesting dominance of singlet exciton sensitization over triplet exciton sensitization[126]. These results suggest that morphology of the closest tetracene layers to the silicon surface are not the only decisive factor for triplet exciton transfer.

We can define the sensitization efficiency for the direct triplet exciton sensitization process as follows:

$$\eta = \eta_{SF} \cdot \eta_{TD} \cdot \eta_{TT} \cdot \eta_{Si}, \tag{3-3}$$

where η_{TT} is the triplet transfer efficiency from the singlet fission layer across the interfacial layer to silicon. It is clear that one of the main challenges for the direct triplet exciton transfer (and charge-transfer) approach is the importance of the silicon surface passivation, which affects both η_{TT} and η_{Si}.

A summary of the sensitization methods and their respective advantages and disadvantages discussed in this section are presented in Table 3-1.

Table 3-1. Summary of singlet fission enhancement methods and respective advantages and challenges detailed in this chapter.

Singlet fission enhancement method	Advantages	Challenges
Tandem configuration	• Quantum efficiencies > 100 % demonstrated	• Multi-junction fabrication complexity • Needs current/voltage-matching
Quantum dot-mediated triplet exciton transfer	• Compatible with thicker silicon passivation layers • Simpler device structure than tandem (single junction)	• Requires management of radiative losses • Coupling the right energy quantum dots to silicon is challenging
Charge transfer approach	• Does not require whole triplet exciton transfer • Simpler device structure than tandem (single junction)	• Restricted to thin silicon passivation layers • Base silicon solar cell efficiency impacted by required hole transfer through singlet fission layer
Direct triplet exciton transfer	• Simpler device structure than tandem (single junction) • Most progress in triplet exciton transfer to silicon (prior to thesis)	• Restricted to thin silicon passivation layers

3.3. Methods for probing singlet fission enhancement of silicon

3.3.1. Quantum efficiency measurements of devices

Perhaps a significant part of the challenges in progress for this field has been the lack of an indirect probe of triplet exciton transfer. The most definitive direct probe of triplet exciton transfer involves fabricating a device and measuring its external quantum efficiency (EQE). In regular single-junction crystalline-silicon devices, the maximum achievable EQE is 100 %, that is, one electron (and corresponding hole) generated per photon incident on the device. If singlet fission is incorporated, because of the generation of two photoelectrons from the triplet excitons, the maximum achievable EQE is 200 %. Therefore, any singlet fission-sensitized single-junction devices that demonstrate > 100 % EQE must have definitive triplet exciton transfer to the silicon. In reality, because of reflection losses and the ratio of absorption between the singlet fission layer and silicon, showing a device IQE with > 100 % is also definitive proof of triplet exciton transfer. However, obtaining accurate reflectance measurements is challenging for certain nanostructured devices, which can make the IQE difficult to measure. Generally, if peaks from the singlet fission material can be observed in the EQE/IQE spectra, and if the peaks are performing better than the baseline silicon cell, it can be inferred that efficient triplet exciton transfer is occurring. Examples of simulated EQE and IQE at different tetracene IQEs are provided in Figure 3-4.

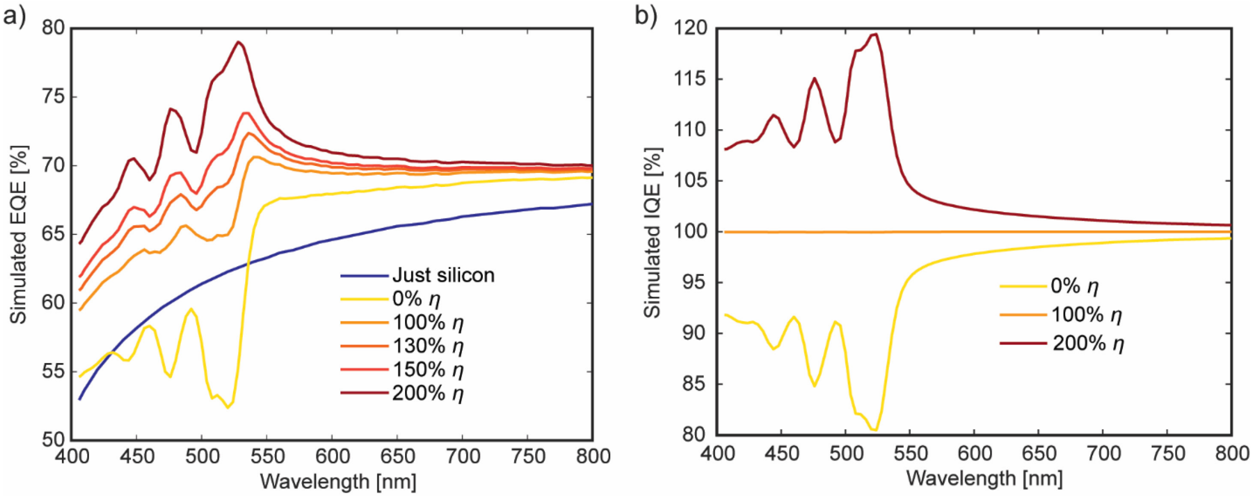

Figure 3-4. Transfer matrix modeling-based simulations of a) device EQE and b) device IQE with 30 nm of tetracene on silicon. Note that due to refractive index effects, peaks are only distinguishable in the EQE spectra if there is more than 130 % singlet fission sensitization efficiency η, whereas in the simulated IQE, the peaks are present at any η over 100%.

However, measuring device EQE and IQE requires fabrication of a full device and only provides quantitative measures of the overall singlet fission sensitization efficiency η, which as we introduced earlier, is actually comprised of multiple efficiencies. Hence, even with high triplet exciton transfer efficiencies, if the carrier collection by the silicon device η_{Si} is poor, peaks will not be observed in the quantum efficiency spectra.

3.3.2. Transient photoluminescence measurements of tetracene

As an alternative, transient photoluminescence measurements of the tetracene layer have been used as an intermediate probe for triplet transfer[45,125]. Transient photoluminescence (PL) measurements of tetracene have been extensively characterized – an example of measured transient PL of a thermally-evaporated 30 nm film of tetracene is presented in Figure 3-5. Tetracene shows a prompt fluorescence decay on the order of 80–250 ps, and a much longer delayed fluorescence with a lifetime that can range from 200 ns to μs depending on the quality of the film (polycrystalline *vs.* single crystal)[45]. The prompt fluorescence decay is usually attributed to the decay of initially excited singlet excitons that have not had the time to undergo singlet fission yet, while the delayed fluorescence is often attributed to the decay of singlet excitons that have been formed from uncorrelated triplet excitons that have encountered each other to undergo triplet-triplet annihilation[127]. As a result, if there is triplet exciton transfer from tetracene to silicon, we would expect the delayed fluorescence lifetime in tetracene to be quenched as a result. Likewise, any singlet exciton transfer could also result in quenching of the prompt fluorescence lifetime. However, we note that quenching of the delayed fluorescence lifetime cannot distinguish between other loss pathways that affect the triplet exciton population. For example, a similar quenching can be observed if triplet excitons are quenched by charges through triplet-charge annihilation, or even through silicon surface defect states. As a result, it is a *necessary but insufficient* condition for triplet exciton transfer and cannot be used on its own as a probe for triplet transfer.

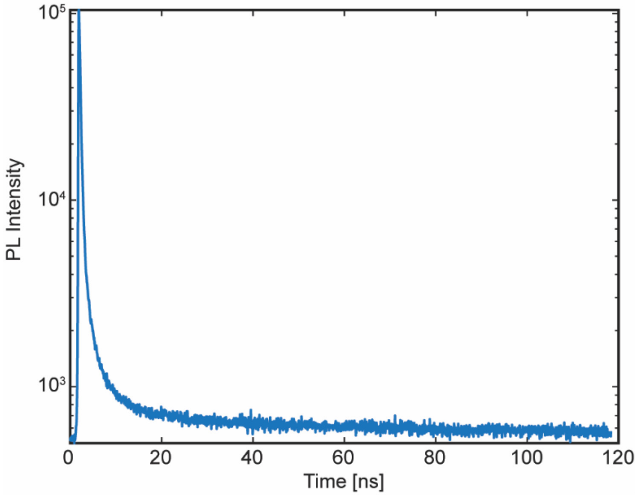

Figure 3-5. Transient photoluminescence measurement of a 30 nm-thick thermally evaporated film of tetracene on glass. The film was excited by a 405 nm laser.

3.3.3. Magnetic field-dependent measurements

Another intermediate probe that has been used are magnetic field-dependent measurements of the silicon photoluminescence and device photocurrent[29,35,47]. From a simplistic view, the triplet population in tetracene has a characteristic fission dependence on the magnetic field. If the silicon photoluminescence and device photocurrent tracks with this, it can be inferred that the triplet population is contributing positively to the device performance. However, as shown by Einzinger *et al.*, this cannot be used as definitive evidence of triplet exciton transfer, as triplet excitons were found to also contribute positively to silicon performance by providing electric field-effect passivation[35]. The contributions from triplet exciton transfer and electric field-effect passivation can be differentiated by performing bichromatic experiments, with light sources chosen carefully depending on the system studied. In the case of HfO_xN_y, a monochromatic and bichromatic experiment were used[35]. The monochromatic experiment involved photoexciting the sample at 532 nm and measuring the PL of silicon. The resulting PL was found to be brighter than when silicon was illuminated on its own[35]. Because both silicon and tetracene absorb the light at this energy, this increase in the measured PL could be a result of both the electric field-effect passivation as well as triplet transfer from tetracene to silicon. In the bichromatic experiment, a second beam of 785 nm light with 18 times greater photon flux was added to the 532 nm light[35]. This 785 nm light only excites silicon, so the PL measured in this scenario is sensitive only to electric-field-effect passivation. By using a combination of these two excitation measurements with the magnetic field-dependence, they were able to extract the contribution from triplet exciton transfer, see Figure 3-6.

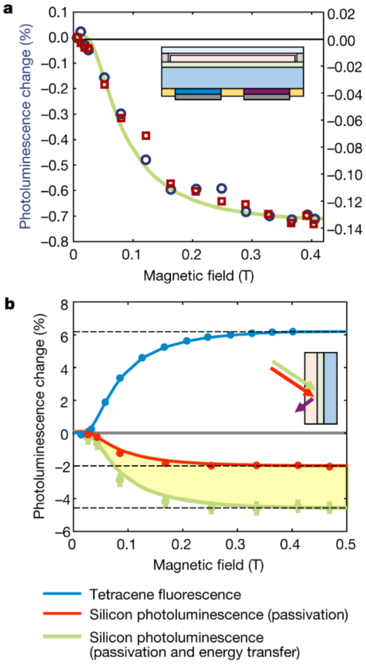

Figure 3-6. Magnetic field-dependent photocurrent and silicon photoluminescence of devices fabricated with a HfO_xN_y interlayer. a) The measurements were taken using 532 nm excitation. b) Silicon photoluminescence measured using the monochromatic and bichromatic experimental conditions. The monochromatic measurements probe triplet exciton effects on passivation and exciton transfer, while the bichromatic measurements probe only passivation. Figure obtained from Einzinger et al. *with permission*[35].

However, there are caveats with magnetic field-dependent measurements. First, we note that, for magnetic field effects to be observable, there needs to be a competing pathway such that the rate dependence can be observed, as derived in Section 2.1.5.1. Thus, for a perfect system where the singlet fission yield is at 100 % and there are no competing singlet decay/extraction channels, this device would, in theory, show no magnetic field dependence at all. Additionally, there can be other triplet exciton interactions which occur in devices such as triplet-charge annihilation which also have magnetic field-dependent rates[79]. If singlet fission and triplet transfer is dominant, the magnetic field would only modulate a small percentage change in the singlet fission rate. In this case, triplet-charge annihilation will have a larger percentage modulation in the rate from the magnetic field as it does not outcompete triplet transfer. As a result, the silicon PL change with magnetic field will track the triplet-charge annihilation process as opposed to the singlet fission characteristic, even though singlet fission and triplet transfer is dominant in the device.

3.3.4. Transient pump-probe spectroscopy

Time-resolved pump-probe spectroscopic measurements are popular for studying singlet fission systems. Measurements like transient absorption have been used to study singlet fission and triplet transfer to nanocrystals and ZnO[128,129,117,118,130], but have yet to be performed for studying triplet exciton transfer to bulk crystalline-silicon prior to this thesis. We note that these measurements are likely to be very complicated to conduct on bulk silicon solar cell samples. Firstly, the measurements will need to be conducted in reflection mode, and due to the presence of many layers in device architectures, extracting and attributing features to specific phenomena can quickly become complex. Additionally, typical pump-probe measurements require high fluences for improved signal-to-noise ratio, which may not be representative of typical device operation. Finally, silicon spectroscopy is notably difficult, as its indirect gap makes its absorption and emission efficiencies low, leading to signal-to-noise challenges.

3.3.5. Computational studies

Finally, we note that computational studies for the interface between tetracene and silicon is exceptionally complex. Simulating two very different material systems (organic molecular semiconductors and bulk inorganic semiconductors) is non-trivial, and can easily become challenging as more thin interlayers are added to the interface between the two materials. As a result, there have only been a handful of studies performed to try to simulate the triplet exciton transfer across the interface[131,132].

3.4. Considerations for the silicon solar cell architectures

Much of the work in this field has been focused on the triplet sensitization process, with barely any studies on collection of the carriers by the silicon solar cell, which affects the parameter η_{Si}. In this section, we evaluate some of the important considerations for the silicon solar cell design, and cover silicon solar cell architectures that have been utilized prior to this thesis. For the single-junction cells, the carriers from triplet exciton sensitization are expected to be located very close to the near-surface region of silicon which interfaces with the singlet fission layer. As a result, choosing silicon solar cell architectures that are effective at extracting near-surface silicon charge carriers is ideal. There are two main losses that should be considered for these cells, as depicted in Figure 3-7a.

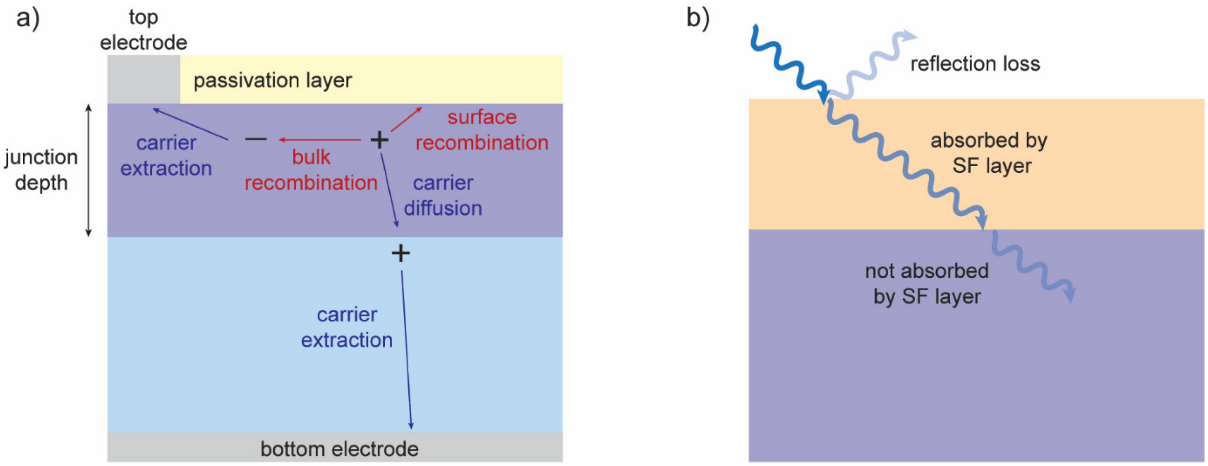

Figure 3-7. Considerations for silicon solar cell architecture designs. a) Carriers from triplet excitons will be located in the near-surface region of the silicon device. These carriers are prone to surface recombination and bulk recombination losses. The carriers need to diffuse to the p-n junction for efficient carrier extraction by their respective electrodes. b) For maximum effect of the SF layer, increasing absorption by this layer by reducing reflection losses and transmission losses is necessary.

The first are surface recombination losses. The presence of silicon surface defects can greatly hinder the extraction of generated near-surface carriers as they are more likely to recombine with the surface defects before they can diffuse to the p-n junction for carrier extraction. Surface passivation layers can be applied to mitigate these recombination effects, however depending on the triplet exciton sensitization mechanism, there may be a very tight passivation layer thickness requirement for carrier tunneling, which can put limitations on the passivation quality[35].

Additionally, bulk recombination losses can also contribute significantly as the carriers near the surface of the cell need to diffuse to the p-n junction for collection by their respective electrodes. Thus, if the junction depth is very deep into the cell, this can cause larger bulk recombination losses[133].

Most of the previous device work in the field was performed on either planar heterojunction solar cells where a heterojunction was formed between tetracene and silicon, or on planar interdigitated-back-contacted (IBC) silicon solar cells. While the heterojunction cell enables probing both charge transfer and triplet exciton transfer, the reliance of hole transport through the tetracene layer, and depositing a water-based PEDOT:PSS hole transport layer[46] raises some concerns on the carrier extraction efficiency of triplet excitons by the device, and the stability effect on the tetracene layer.

As for the IBC cells, incorporation of the singlet fission layer is simplest since in theory, only the top surface of the cell needs to be modified. However, the electrodes are located on the back side, resulting in large junction depths[35]. For probing triplet sensitization effects, thinner IBC silicon cells will need to be used.

Another consideration is the absorption of the singlet fission layer, as seen in Figure 3-7b. Ideally, for maximal benefit from singlet fission, this layer should absorb as much of the high energy light as possible. Light-trapping modifications can be utilized to enhance absorption by the singlet fission layer and has been utilized to achieve EQEs greater than 100 % in SF-OPVs[43]. In industry, texturing of silicon solar cell surfaces has also been employed for reduced reflection losses[134,135]. Intentionally fabricating nanostructures has also been proposed[133]. Coupling these methods with singlet fission layers can be interesting, but may also bring about some challenges, especially since the morphology of tetracene is reported to affect the singlet fission rate and triplet transport in the layer[121–124]. Conformal deposition techniques for 3D architectures will become desirable in these cases.

3.5. Outstanding questions

The studies mentioned previously raise many questions about the exact role of the HfO_xN_y layer. Morphology does not appear to be the main reason why HfO_xN_y worked. So why did this interlayer work while all other interlayers did not work? What is the mechanism of the triplet exciton transfer process through this interlayer? What is the role of the electric field-effect passivation and is this beneficial for the triplet exciton transfer process? Why did the device not show any enhancement from fission even though efficient triplet exciton transfer was demonstrated? How can we better understand carrier transport in the solar cell materials? What are the transient dynamics of the triplet sensitization process at the interface? This thesis seeks to address many of these questions, and provides a direct follow up to the HfO_xN_y studies through a combination of interfacial material studies, device work and advanced spectroscopic studies of the interface.

Chapter 4.
Triplet exciton sensitization of silicon mediated by defect states in hafnium oxynitride

The basis of this chapter has been adapted from:

Narumi Nagaya, Alexandra Alexiu, Collin F. Perkinson, Oliver M. Nix, Moungi G. Bawendi, William A. Tisdale, Troy Van Voorhis, Marc A. Baldo. "Triplet Exciton Sensitization of Silicon Mediated by Defect States in Hafnium Oxynitride." *In preparation* (2024)

4.1. Introduction

The adoption of crystalline-silicon (*c*-Si) photovoltaics is limited by the price of solar cells and the cost of their installation. Improving cell efficiency is an important goal because maximizing energy generation reduces the effective cost of both cells and installation. Singlet exciton fission (SF) has been proposed as a method for enhancing silicon solar cell efficiencies beyond the conventional theoretical limit[27]. It generates two triplet excitons from one singlet exciton[34]. If a SF material such as tetracene (Tc) is used to absorb the high energy photons of the solar spectrum, then transfer of the resulting triplet excitons to *c*-Si could increase the silicon cell efficiencies from 29% to 35%–42%[26,37,28].

Unfortunately, transfer of triplet excitons directly from Tc to *c*-Si has proven to be exceptionally challenging[44,45,120,125,126]. The fundamental obstacle is that Tc triplets are non-emissive states and incapable of near-field or radiative coupling to Si. Instead, triplet diffusion in molecular films typically relies on Dexter transport and involves simultaneous tunneling of the electron and hole from donor to acceptor molecules. Tunneling is inherently short range, limiting the thickness of silicon passivation layers, and increasing the impact of silicon surface defect states that quench triplet excitons[35].

Previous bichromatic magnetic field-dependent measurements show that using a thin layer of hafnium oxynitride (HfO_xN_y) between Tc and *c*-Si enables triplet exciton sensitization of silicon[35]. The sensitization effect is strongly dependent on the thickness of the HfO_xN_y interlayer, with an optimum thickness of 8 Å. The Si-HfO_xN_y-Tc samples also exhibit signatures of electric-field effect passivation when optically exciting both tetracene or silicon. But the exact role of the HfO_xN_y interlayer and the mechanism of the triplet exciton transfer are not well understood.

Post-deposition annealing of hafnium oxide (HfO_2) films in different nitrogen based gases has been suggested to introduce deep and shallow mid-gap, as well as near-band-edge defect states for silicon surfaces[136]. We hypothesize that defect states in the HfO_xN_y interlayer could therefore be participating in the triplet exciton sensitization process. In this work, we perform periodic density functional theory (DFT) calculations to probe the positions of defect states in various O and N compositions for the HfO_xN_y interlayer. We then grow HfO_xN_y interlayers with different compositions and fabricate optical Si-HfO_xN_y-Tc samples to measure the interlayer-thickness-dependent silicon photoluminescence change of these samples under a magnetic field. Our results suggest that defect states in HfO_xN_y may be mediating sequential charge transfer of the triplet exciton.

4.2. Methods and materials

4.2.1. Materials

n-doped prime-grade single-side-polished silicon wafers with 0.25-0.75 Ωcm resistivity were purchased from UniversityWafer. Tetracene was purchased from Sigma Aldrich (99.99% purity) and purified *via* sublimation in a tube furnace once.

4.2.2. Sample preparation

The silicon wafers were diced into 1-inch squares and cleaned by sonicating in detergent solution (Micro-90), deionized water, and acetone, followed by immersion in boiling isopropanol. The wafers were then dried with pressurized nitrogen and transferred to a clean room. We performed a standard Radio Corporation of America (RCA) cleaning process on the wafers, which left a thin oxide layer on the silicon surface. Following the clean, the wafers were quickly transferred for atomic layer deposition of the HfO_xN_y layers (Cambridge Nanotech Savannah). The base pressure of the chamber was 0.4 torr at a nitrogen flow of 40 cm^3 min^{-1}.

For the $HfO_{0.25}N_{1.17}$ layer, tetrakis(dimethylamino)hafnium (TDMAH) was used as the Hf precursor and ammonia was used as the nitrogen precursor, with oxygen likely from residual oxygen in the chamber and from film exposure to air post-deposition. The TDMAH precursor was heated to 75 °C and the ALD reaction chamber was set to 150 °C. The TDMAH precursor was pulsed for 30 ms, and the NH_3 precursor was pulsed for 15 ms for every cycle.

For the $HfO_{0.58}N_{0.72}$ layer, tetrakis(ethylmethylamino)hafnium (TEMAH) was used as the Hf precursor and NH_3 was used as the nitrogen precursor, with oxygen likely from residual oxygen in the chamber and from film exposure to air post-deposition. The TEMAH precursor was heated to 110 °C and the ALD reaction chamber was set to 150 °C. The TEMAH precursor was pulsed for 30 ms, and the NH_3 precursor was pulsed for 15 ms for every cycle.

For the $HfO_{1.63}$ layer, TEMAH was used as the Hf precursor and water was used as the oxygen precursor. The TEMAH precursor was heated to 110 °C and the ALD reaction chamber was set to 200 °C. The TEMAH precursor was pulsed for 250 ms, and the H_2O precursor was pulsed for 15 ms for every cycle.

After deposition of the HfO_xN_y interlayer, the samples were quickly transferred to a vacuum chamber at a pressure of $< 1\times10^{-6}$ torr for tetracene deposition *via* thermal evaporation. 30 nm of tetracene was evaporated at a rate of 1 Å/s. The samples were then encapsulated with a glass slide and ultraviolet curable epoxy in a dry nitrogen atmosphere (< 1 ppm O_2). A square foil piece was used to cover the active area during UV exposure.

4.2.3. X-ray photoelectron spectroscopy (XPS)

XPS measurements were performed using a PHI VersaProbe II X-ray photoelectron spectrometer with monochromated Al K-α X-rays. Compositional depth-profiles were obtained by sputtering the surface with C_{60} ions (operated at 2 kV, 1 μA, over a 2 x 2-mm area) and measuring the photoelectron peak areas for C1s, N1s, O1s, Si2p, Hf4f in 1-minute intervals. The reported compositions were obtained after 5 minutes of sputtering on 25 nm-thick films to remove surface impurities and obtain compositions close to the sample surface.

4.2.4. Magnetic field-dependent photoluminescence measurements

Optical samples were placed between the poles of an electromagnet and excited by an optically-chopped (281 Hz) 200 mW 532-nm laser (Coherent Verdi G18). The tetracene fluorescence was collected by a silicon photodetector (Newport 818-SL) connected to a lock-in amplifier (Stanford Research Systems SR 830), with a 532 nm notch filter and a 550 nm longpass filter in front of the detector. The silicon photoluminescence was collected by an IR photodetector (Newport 818-IR), with 900 nm and 1000 nm longpass filters in front of the detector to ensure collection of only the silicon photoluminescence. The electromagnet was periodically switched on and off at different field strengths for 4-cycle loops at each field strength to obtain the measurements. For the thickness-dependent magnetic field-dependent measurements, the above experiments were conducted for a magnetic field strength of 0.4 T, as measured by a gaussmeter (Lakeshore HMMT-6J04-VF).

4.2.5. Density functional theory calculations

Calculations shown in this chapter were performed by Alexa Alexiu in the Van Voorhis group.

4.3. Results and discussion

Two potential mechanisms have been proposed to explain triplet exciton transfer from Tc to *c*-Si through a HfO_xN_y layer[35]. Depicted in Figure 4-1a, the triplet exciton could transfer through a sequential charge transfer mechanism, where the triplet exciton dissociates and the electron and hole transfer successively one after the other[28], or through a Dexter transfer mechanism[73], where the electron and hole transfer simultaneously to the silicon.

Previous studies of LiF interlayers[44,45], pyrene passivation layers[125] and covalently bound tetracene-derivative seed layers[126], have not provided strong support for the effectiveness of Dexter transport at interfaces between molecules and *c*-Si. Indeed, for maximum efficiency gain, SF should generate triplets with energies close to the bandgap of silicon, where the probability of simultaneous electron and hole tunneling may be lower than individual tunneling of each respective charge carrier.

We propose that triplet excitons are transferred through a sequential charge transfer mechanism, mediated by defect states in the HfO_xN_y layer. One possible pathway is presented in Figure 4-1b, where the electron is initially transferred to the silicon conduction band (E_C) and the hole is supported at a HfO_xN_y defect state (E_D) near the valence band edge of silicon. The hole is then subsequently transferred to the silicon valence band (E_V).

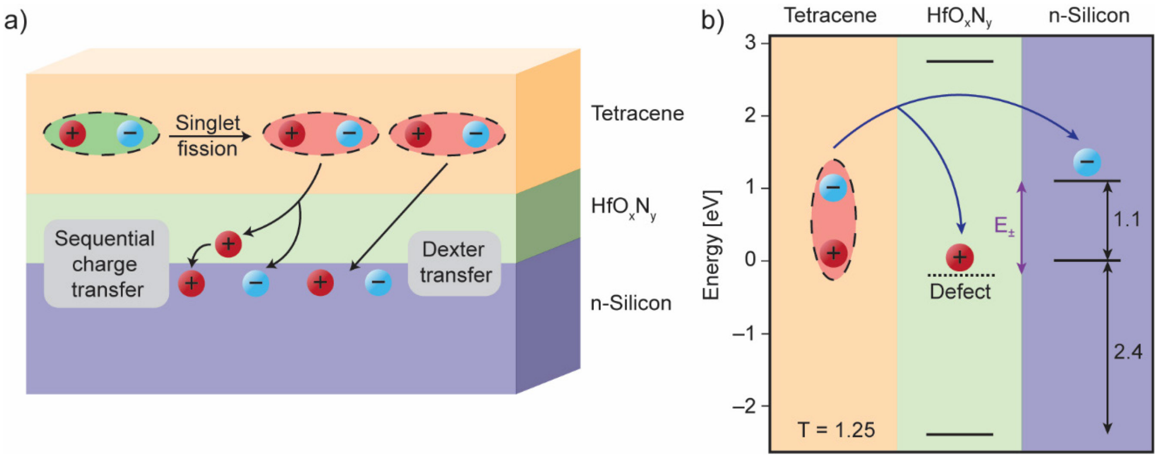

Figure 4-1. a) Schematic of the silicon-HfO_xN_y-tetracene structure studied in this work. Triplet excitons are formed from the singlet exciton in the tetracene layer through singlet fission. The triplet excitons can then either undergo a sequential charge transfer process or a Dexter transfer process to transfer to the *c*-silicon layer. b) Schematic showing the energy level alignment of the silicon-HfO_xN_y-tetracene structure, as previously reported.[35] Overlaid, one possible example of a defect state in HfO_xN_y helping mediate the triplet exciton dissociation and sequential charge transfer process of the triplet exciton from tetracene. This forms an intermediate charge-separated state with energy $E_\pm$ (assuming negligible binding energy[137,138]), where the electron is on the silicon conduction band and the hole is on the defect state level in HfO_xN_y.

Hafnium oxide has been shown to be a good passivating interlayer in Si solar cells, due to both chemical passivation of Si dangling bonds and field-effect passivation[139,140]. HfO_x thin films can either be positively or negatively charged, depending on the stoichiometry[140]. In materials with a large concentration of oxygen vacancies, hafnia films develop a build-up of positive charge[139]. This partially-charged interlayer interface would be beneficial for the passivation of n-type Si, as it would repel holes, the bulk minority carriers that control the electron-hole recombination rate at the Si surface.

Analogously, Einzinger *et al*. demonstrate that Tc with HfO_xN_y passivates n-doped Si[35]. Trapping of minority (hole) carriers in the HfO_xN_y interlayer is thought to be largely responsible for the electric field passivation effect, because electron traps only slightly affect the concentration of the majority carriers and have little effect on the rate of surface recombination. In our hypothesis, we propose that hole traps mediate a charge-separated state ($D_{HfOxNy}{}^{+}–A_{Si}{}^{-}$).

Such a defect state additionally needs to have significant density of states close to the Si valence band edge, and ideally, the energy of the charge-separated state ($E_{\pm}$) is lower than the triplet energy in Tc (~1.25 eV, within thermal energy)[35]: $E_{\pm} \leq E_{T,Tc}$. We assume binding energy can be neglected for the charge-separated state energy due to expected charge screening in silicon[137,138]. Furthermore, the energy barrier for the subsequent hole transfer from HfO_xN_y to Si must be sufficiently low, to avoid permanent trapping of the minority carriers in defect states.

These requirements are summarized in Figure 4-1b. The Si band gap and offset between the HfO_xN_y and Si valence band edges are assumed to be 1.1 eV and 2.4 eV, respectively, as calculated from ultraviolet photoelectron spectroscopy experiments by Einzinger *et al.*[35] Other experimental works obtained a range of values between 2.4-3 eV[141–145] for the valence band offset, depending on the exact deposition setup and any post-deposition annealing treatments. We highlight that our computational conclusions will be dependent on this exact value, however we choose 2.4 eV as the valence band offset for consistency with the experiments of Einzinger *et al.*[35]

4.3.1. Computational investigation of HfO_xN_y

To evaluate the hypothesis that defect states near the valence band edge of silicon may support a charge-separated state, we perform density functional theory (DFT) calculations to assess the density of states (DOS) for a range of materials of interest.

We start with hafnium oxide (HfO_2), a well-studied wide band-gap metal oxide. Most hafnia thin films reported in literature exhibit amorphous structures, with polycrystalline phases only appearing after annealing at high temperatures (>500 ^oC)[146,147]. A lack of crystallinity precludes us from making direct comparisons with experiments, therefore we chose to focus on the thermally accessible phases of HfO_2, which are the monoclinic ground state (*$P2_1/c$*) and the orthorhombic state (*Pbca*), which is only 11.1 meV/atom higher in energy. Analysis of point defects in monoclinic HfO_2 shows agreement with previous computational and experimental results[136,148,149]. Overwhelmingly, these studies show that O vacancies in HfO_2 can act as electron traps, and defects associated with N atoms may cause additional trap states. The aforementioned computational works use DFT in the generalized gradient approximation (GGA), which severely underestimates the band gap and could affect the accuracy of the calculated energy levels. To better reproduce the experimental band gap and density of states, we use the global hybrid functional PBE0[150,151].

Based on the work of Einzinger *et al.*[35], we are interested in HfO_xN_y, rather than pure hafnia, as an interlayer material in singlet fission solar cells. We carry out a systematic interpolation between HfO_2 and Hf_3N_4, to establish the likelihood that different O:N ratios will be conducive to efficient triplet exciton transfer from Tc to Si. For a smooth interpolation, the two endmembers should have similar crystal structures, which is why we focus on orthorhombic HfO_2 (*Pbca*) and Hf_3N_4 (*Pnma*), as there is no thermally accessible monoclinic Hf_3N_4.

Oxygen atoms were gradually substituted by nitrogen atoms, maintaining the overall stoichiometry, to yield a range of compositions of the form HfO_xN_y, with N substitution percentages varying from 13-91% (see Figure 4-2a for a representative unit cell).

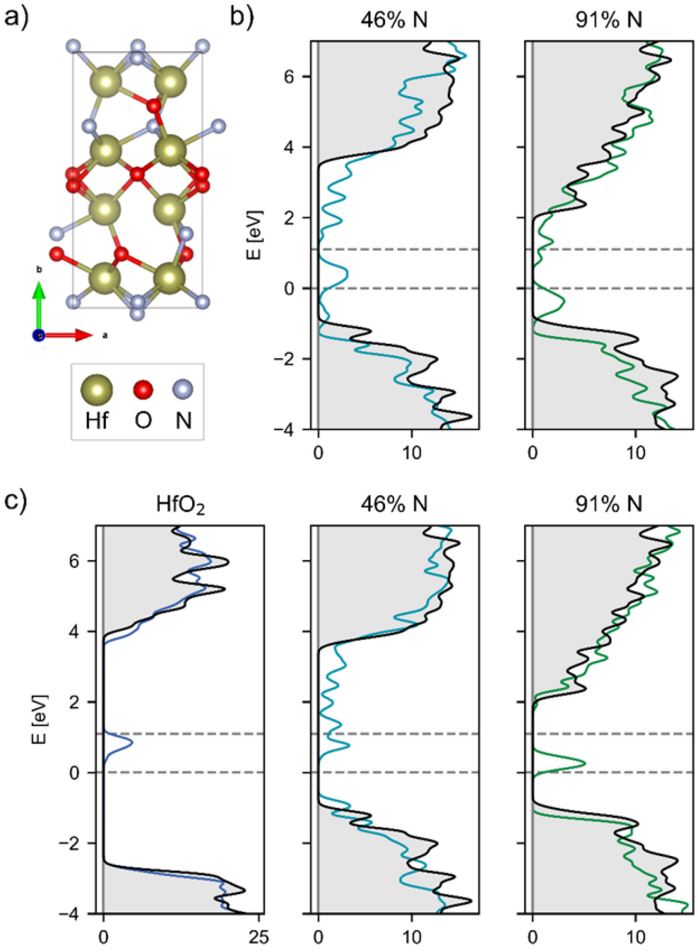

Figure 4-2. a) Representative unit cell of HfO_xN_y (with 46% N). b) Density of states plots for N vacancy defects in two representative HfO_xN_y compositions. The DOS of the pristine unit cell (grey shaded region) is compared with the defective DOS (colored). The Si valence band maximum (VBM) and conduction band minimum (CBM) are marked by dotted grey lines. The energy axis is shifted such that the Si VBM is at 0 energy. c) DOS plots for O vacancy defects in HfO_2 and HfO_xN_y.

In agreement with previous experimental and computational results[152–154], the band gap of hafnium oxynitride decreases monotonically with increasing N content. The band gaps of all pristine samples are free of any defect states that could realistically support a charge-separated state with the Si band edges.

4.3.1.1. Defective structures

We introduced a variety of point defects, at a density of 1 per unit cell: O, N, and Hf vacancies. All defects considered are charge neutral to remove the dependence of their formation energy on the Fermi level. An analysis of charged defects could make the object of a further study. Hf vacancies are found to form no mid-gap states of interest.

Representative DOS plots are shown in Figure 4-2b for N vacancies in two HfO_xN_y compositions, a more N-poor case that exhibits a trap state in the middle of the Si band gap and a N-rich case where the defect state could conceivably trap holes. Similarly for O vacancies, a comparison is shown between the same two HfO_xN_y compositions and HfO_2 in Figure 4-2c.

A summary of all vacancy energy levels is shown in Figure 4-3, for HfO_2, HfO_xN_y, and Hf_3N_4. Only the maximum of each defect peak in the DOS plots is shown, although each peak is in reality broadened by up to 0.5 eV each (see Figure 4-2b and c for examples of realistic DOS plots).

O vacancies cause electron traps for low N compositions, shifting to potential hole traps as the N content increases. N vacancies generally lead to the formation of hole traps; for higher N content, the defect states can even lie slightly below the Si VBM, which could promote a barrierless hole transfer from the defect energy level to the silicon VBM (see Figure 4-1). The overall trend is for vacancy defect levels to decrease in energy as the N content increases.

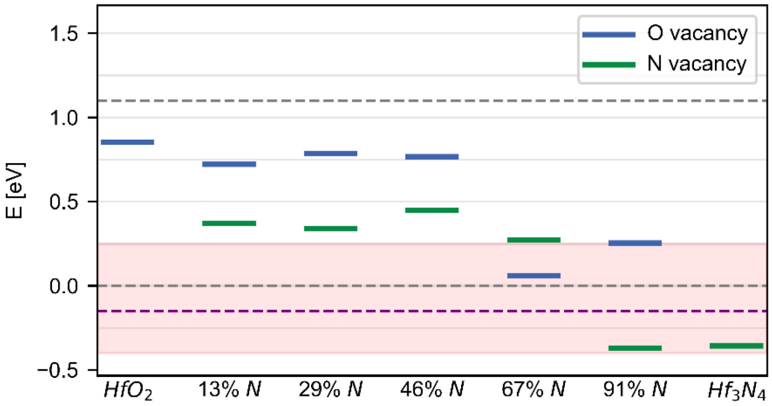

Figure 4-3. Summary of defect energy levels caused by O vacancies (blue) and N vacancies (green). The Si valence band maximum (VBM) and conduction band minimum (CBM) are marked with dotted grey lines, and the dotted purple line represents the minimum energy a defect state could have such that $\boldsymbol{E_{\pm}} \leq \boldsymbol{E_{T,Tc}}$. The red shaded box marks the energy region for potential hole traps. The energy axis is shifted such that the Si VBM is at 0 energy.

4.3.1.2. Defect formation energies

The relative alignment of potential trap states offers an explanation for which types of defects could be responsible for the success of using the HfO_xN_y interlayer in singlet-fission solar cells, but gives no information about the prevalence of such defects. Computing their formation energies provides some insight into their thermodynamic stabilities and the likelihood of defect formation in a real material.

Defect formation energies and concentrations are highly dependent on the conditions under which these materials are synthesized, most notably the experimental temperature and the chemical potentials of N and O. The chemical potentials can vary ranging from low (O- or N-poor) to high (O- or N-rich) limits, depending on the deposition environment.

Given the ALD procedure outlined by Einzinger *et al.*[35], we argue that experimental conditions are O-poor, because the only source is residual oxygen initially present in the ALD chamber. Similar synthetic procedures for HfO_2 led to high concentrations of vacancies[155] and sub-stoichiometric Hf:O ratios of 1.91 or less[156]. As for nitrogen, we choose an average chemical potential between the N-rich and poor limits. The results shown in Figure 4-4 therefore follow O-poor and N-intermediate conditions.

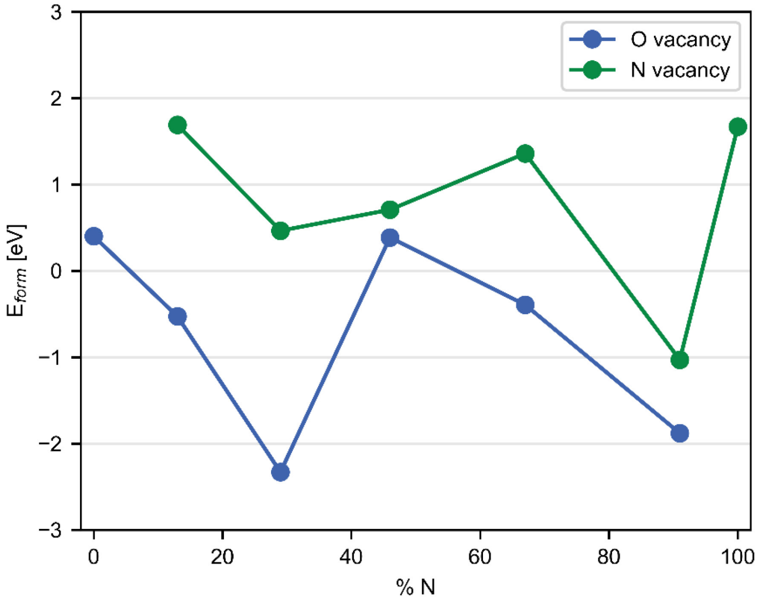

Figure 4-4. Formation energies for O vacancies (blue) and N vacancies (green), in a range of N compositions. O vacancies form more readily than N vacancies, with both forming spontaneously at the 91% N composition.

As implied by the low or even negative formation energies, oxygen vacancies form readily, at any nitrogen composition, according to our assumption of O-poor conditions. A negative formation energy suggests spontaneous defect formation, explaining the tendency of HfO_2 and HfO_xN_y being synthesized in sub-stoichiometric ratios. Nitrogen vacancies form to a lower extent, although it is of particular interest to note that the lowest N vacancy formation energy is obtained for the 91% N HfO_xN_y composition.

Using a temperature of 423 K, in line with the reaction chamber temperature used by Einzinger *et al.*[35], we can also estimate defect concentrations using an Arrhenius-like expression. Oxygen vacancy concentrations are large irrespective of the HfO_xN_y composition, estimated to be on the order of 10^{16} cm^{-3} in HfO_2. This estimate is in accordance with previous computational[157] and experimental[155,158] studies, perhaps even underestimating the concentration of oxygen vacancies in a real material. High nitrogen vacancy concentrations are obtained for the material with 91% N (10^{31} cm^{-1}). Interstitial defects only occur at very low concentrations in these growth conditions, so we do not include them in the current study.

4.3.2. Experimental variation of HfO_xN_y composition

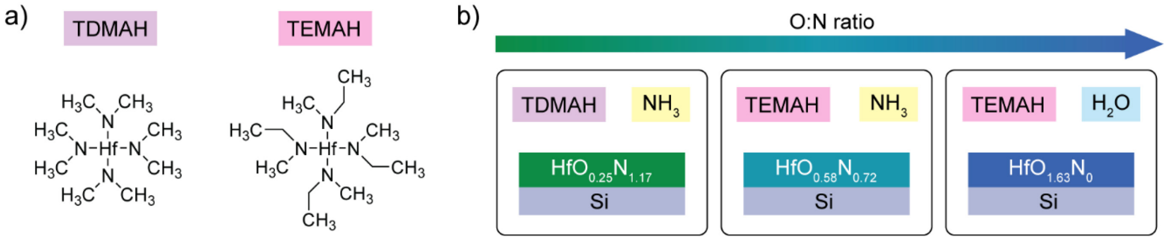

Figure 4-5. a) Hafnium precursors used to grow the HfO_xN_y interlayers in this work: tetrakis(dimethylamino)hafnium (TDMAH) and tetrakis(ethylmethylamino)hafnium (TEMAH). b) Combinations of precursors used in the atomic layer deposition process for each layer and the corresponding compositions of the HfO_xN_y films that were grown. The compositions were obtained using X-ray photoelectron spectroscopy on thicker films that were sputtered for 5 minutes to remove surface contaminants.

To probe the results from the periodic DFT calculations, we grow HfO_xN_y films on cleaned silicon surfaces using atomic layer deposition (ALD) with different precursors to achieve varying ratios of O:N. Figure 4-5a shows the chemical structures of the two hafnium precursors used in this work: tetrakis(dimethylamino)hafnium (TDMAH) and tetrakis(ethylmethylamino)hafnium (TEMAH). The HfO_xN_y interlayers are grown following recipes for growth of Hf_3N_4[35,159]; the oxygen present in the films could come from residual oxygen in the reaction chamber, as well as from oxygen diffusion through post-deposition exposure of the films to air. TEMAH is reported to show unfavorable reactivity with the nitrogen precursor ammonia (NH_3)[159]. Thus, we expect the HfO_xN_y films grown using TEMAH to have a lower nitrogen content. We also prepare a HfO_x film for comparison with no nitrogen content, since hafnium oxide is reported as a passivation layer for silicon solar cells[160]. The precursor combinations and corresponding compositions of the grown HfO_xN_y films are presented in Figure 4-5b.

4.3.2.1. X-ray photoelectron spectroscopy of hafnium oxynitride and hafnium oxide films

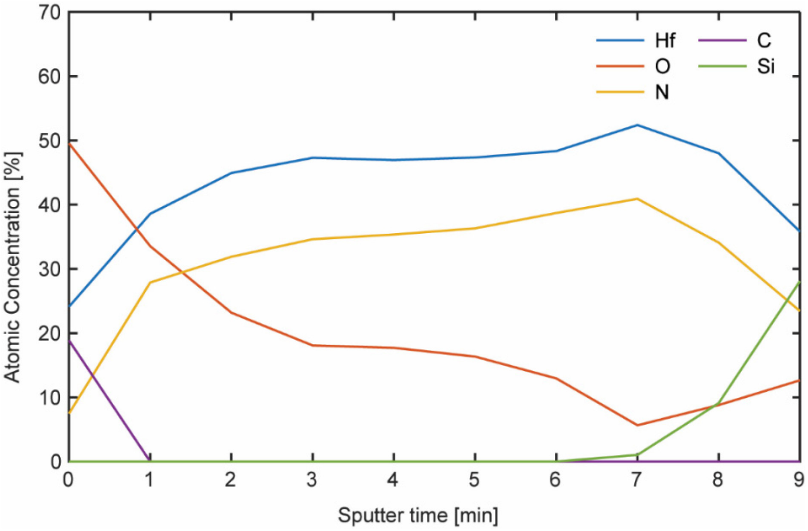

Figure 4-6. Compositional depth-profiles obtained from X-ray photoelectron spectroscopy measurements on the HfO_xN_y film deposited using tetrakis(dimethylamino)hafnium (TDMAH) and NH_3 precursors. C_{60} ions were used to sputter the surface, and the photoelectron peak areas for C1s, N1s, O1s, Si2p, Hf4f were measured in 1-minute sputtering intervals.

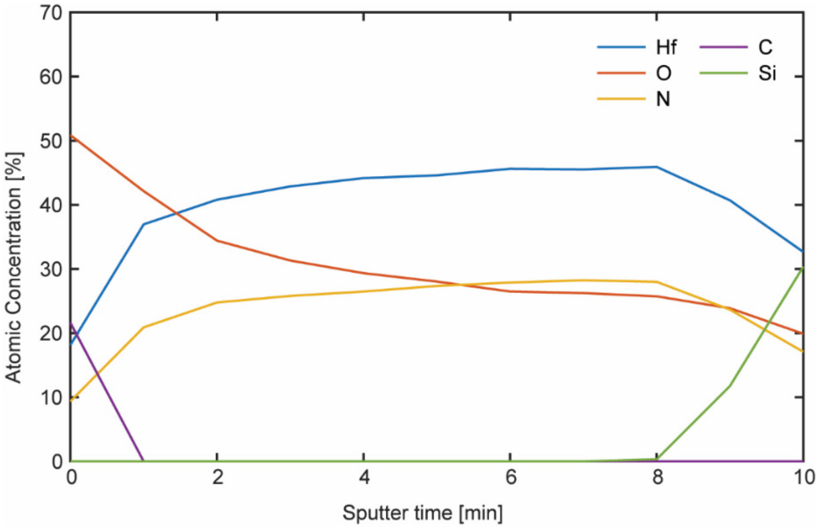

Figure 4-7. Compositional depth-profiles obtained from X-ray photoelectron spectroscopy measurements on the HfO_xN_y film deposited using tetrakis(ethylmethylamino)hafnium (TEMAH) and NH_3 precursors. C_{60} ions were used to sputter the surface, and the photoelectron peak areas for C1s, N1s, O1s, Si2p, Hf4f were measured in 1-minute sputtering intervals.

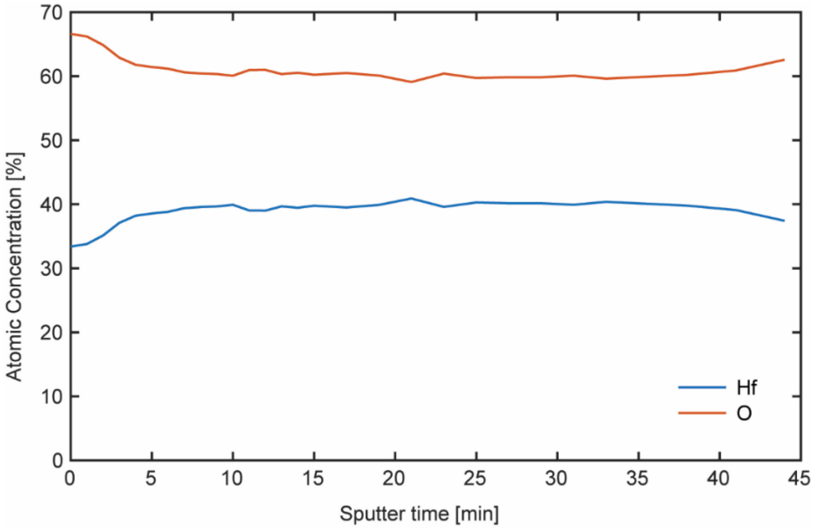

Figure 4-8. Compositional depth-profiles obtained from X-ray photoelectron spectroscopy measurements on the HfO_x film deposited using tetrakis(ethylmethylamino)hafnium (TEMAH) and H_2O precursors. C_{60} ions were used to sputter the surface, and the photoelectron peak areas for O1s, Hf4f were measured in 2-minute sputtering intervals.

4.3.3. Optical sample characterization

To investigate the triplet sensitization efficiencies, we prepare optical samples of silicon with the deposited HfO_xN_y interlayers of different thicknesses, and then deposit 30 nm of Tc on top. We characterize the optical samples by measuring the silicon photoluminescence (PL) change under an applied magnetic field.

When the Tc layer is excited, it absorbs photons to generate singlet excitons. The singlet exciton can undergo singlet fission to generate a correlated triplet pair state with spin-singlet character, which either diffuses into separated triplet excitons or recombines through triplet-triplet annihilation to form a singlet exciton. Triplet excitons in Tc can also transfer their energy to silicon. Figure 4-9a shows a summary of the processes that can occur in the silicon-HfO_xN_y-tetracene optical samples. The coupling of the singlet exciton and the correlated triplet pair state can be modulated by a magnetic field, affecting the equilibrium population of singlet and triplet excitons, as described by the Merrifield model[81]. At low fields, the overall singlet fission rate is increased, followed by a decrease at high fields. This results in a characteristic response of the steady-state Tc fluorescence signal to an external magnetic field, as shown in Figure 4-9b[161]. Measuring the silicon PL shows the same characteristic response but inverted, which aligns with the expectation that triplet excitons from Tc are sensitizing the Si. It should be noted that the sensitization effects potentially include both energy transfer and electric-field-effect passivation induced by defect charging at the interface[35].

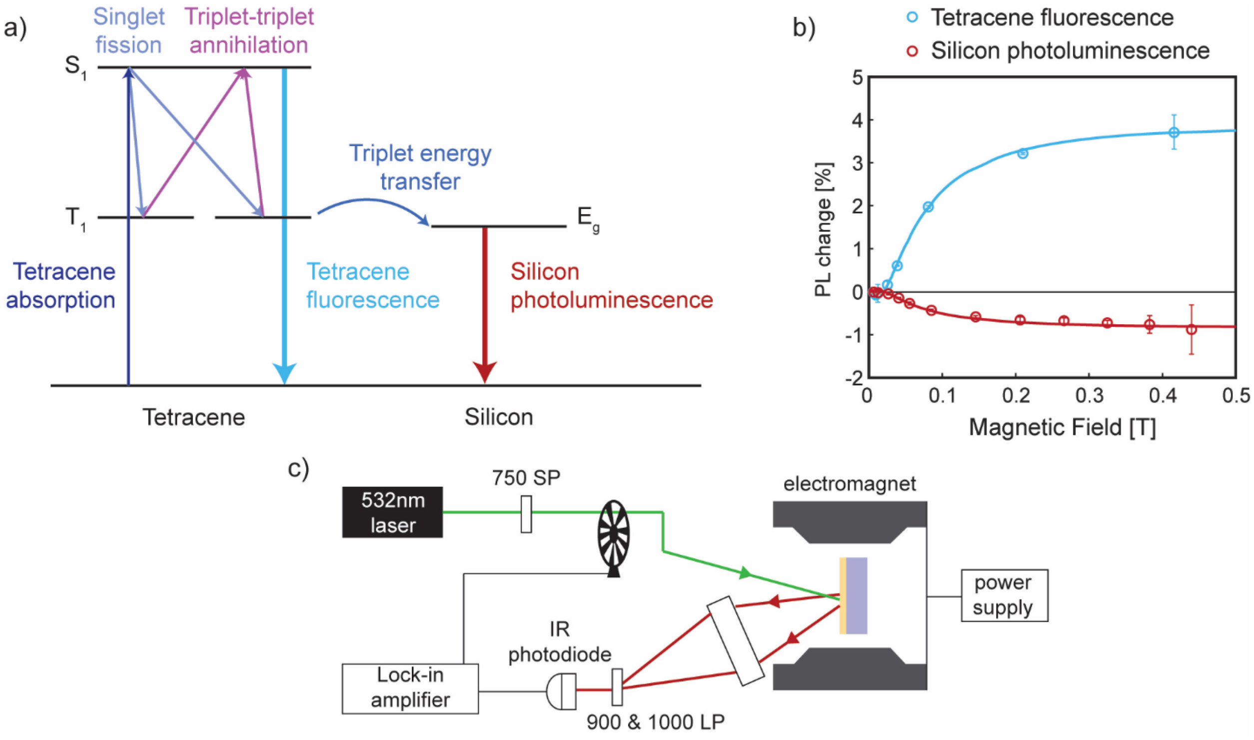

Figure 4-9. a) Schematic showing the processes that can occur in the silicon-HfO_xN_y-tetracene optical sample. Tetracene can absorb photons to generate singlet excitons that can undergo singlet fission to form two triplet excitons each. The triplet excitons could either combine via triplet-triplet annihilation to form a singlet exciton, or transfer to the silicon. Tetracene singlet excitons can decay to the ground state to emit fluorescence. The excited silicon can decay to the ground state to emit photoluminescence. b) Photoluminescence change measured as a function of magnetic field for tetracene fluorescence and for silicon photoluminescence. c) The experimental setup used to measure the silicon photoluminescence change as a function of magnetic field.

To infer the triplet exciton transfer efficiency, we measure the percentage change in silicon PL from the Si-HfO_xN_y-Tc samples upon application of a 0.4 T magnetic field. The samples are excited by a 532 nm laser source and the silicon PL is captured and focused onto an IR photodetector. The experimental setup is depicted in Figure 4-9c.

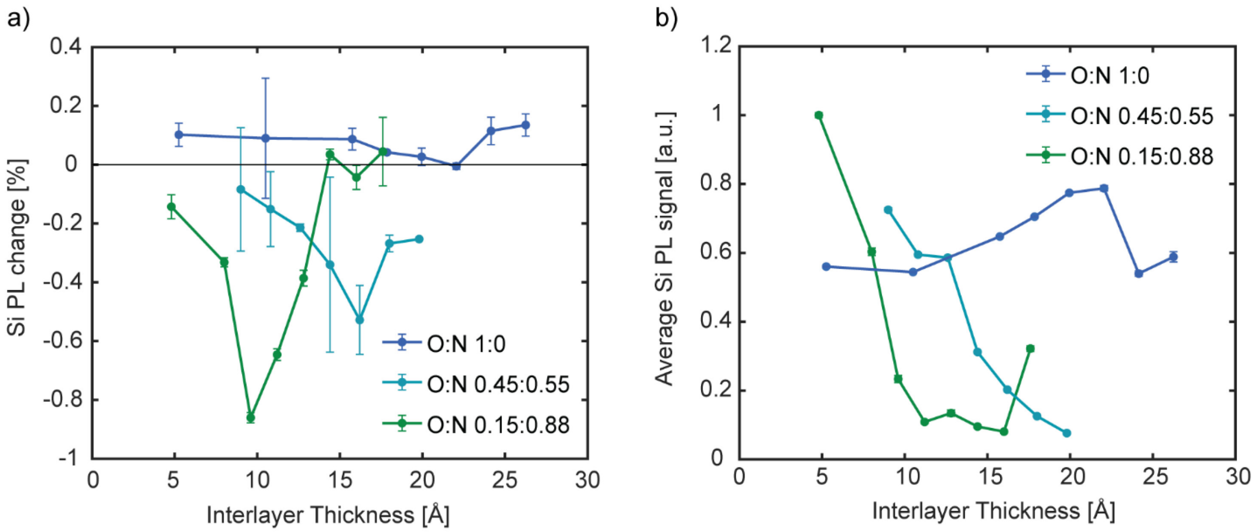

Figure 4-10. a) Percentage silicon photoluminescence change of Si-HfO$_x$N$_y$-Tc samples upon application of a 0.4 T magnetic field at different HfO$_x$N$_y$ interlayer thicknesses and compositions. The magnitude of the silicon PL change increases with higher nitrogen content in the HfO$_x$N$_y$ layer. b) Average silicon photoluminescence signal of Si-HfO$_x$N$_y$-Tc samples at different HfO$_x$N$_y$ interlayer thicknesses and compositions. The average silicon PL is roughly constant with thickness for HfO$_x$, but trends downwards with increasing thickness of the HfO$_x$N$_y$ interlayers.

Previous work on HfO$_x$N$_y$ layers found a strong thickness-dependence of the sensitization effect[35]. As a result, we measure the interlayer thickness-dependent silicon PL change for the samples with different interlayer compositions. The results are presented in Figure 4-10a. Notably, we observe that the magnitude of the silicon PL change and the thickness-dependence differ between the films of different composition. The HfO$_x$ films with no nitrogen showed no negative Si PL change with applied field at all thicknesses. With increasing nitrogen content in the HfO$_x$N$_y$ interlayer, the samples exhibit a higher magnitude of silicon PL change with an applied magnetic field, implying a greater sensitization effect. The optimum thickness also appears to decrease with greater nitrogen content.

The experimentally observed lower optimum transfer thickness and higher silicon PL change magnitude for the HfO$_x$N$_y$ films with higher N concentrations are consistent with our hypothesis from our computational studies which suggests that near-band-edge states are helping to mediate the triplet exciton transfer process. Additionally, the defect formation energy calculations suggest that HfO$_x$N$_y$ films with higher N concentrations could favor the formation of N vacancies compared to the films with moderate N concentrations.

For the HfO_2 layer, calculations suggest that oxygen vacancies could result in defect states near the conduction band of silicon, which could support triplet exciton transfer through an initial hole transfer. However, we note that the magnetic field-dependent measurements detect both energy transfer and passivation. The wafers used in the study are n-doped with holes as the minority carriers. Thus, the electrons in the HfO_x layer create an electric-field that attracts the minority carriers to the surface, resulting in recombination of any transferred triplet excitons.

We also measure the average silicon PL signal as a function of interlayer thickness and composition, as in Figure 4-10b. The silicon PL signal can be used as an indicator for mid- and near-band-edge defect states for the silicon. Unlike the thickness-dependence of the samples with the HfO_x interlayers, the samples with both HfO_xN_y interlayers show a nearly monotonically decreasing silicon PL signal with increasing interlayer thickness, supporting the calculation results that indicate the presence of mid-gap and near-band-edge defect states from the nitrogen. On the other hand, the HfO_x layer shows a relatively constant silicon PL signal with thickness, suggesting the presence of fewer mid-gap defect states, consistent with the calculation results.

4.4. Conclusion

In conclusion, we show that sequential charge transfer of triplet excitons from tetracene to crystalline-silicon can be mediated through defect states in the HfO_xN_y interlayer. Our results suggest that HfO_xN_y films with higher nitrogen content are more likely to form N vacancy defects, introducing a density of near-band-edge states that lie below the silicon valence band maximum. These states correlate with increased magnitudes of magnetic field-induced silicon photoluminescence change and reduced optimum interlayer thickness for triplet sensitization of silicon. However, we also find that defects in HfO_xN_y interlayers introduce many deep mid-gap states which can quench the overall silicon photoluminescence. Future efforts for achieving high efficiency singlet fission-sensitized silicon photovoltaics will require alternate interlayers that deliberately introduce only near-band-edge states while still providing good passivation of the silicon surface.

Chapter 5.
Dynamic triplet-driven passivation of silicon surfaces

The basis of this chapter has been adapted from, with some additional details not intended to be published:

Narumi Nagaya, Collin F. Perkinson, Aaron Li, Tomi K. Baikie, Willem P. A. Verheijen, Kangmin Lee, Youri Lee, Jaekang Song, Zachary VanOrman, Oliver M. Nix, Moungi G. Bawendi, Sascha Feldman, Kwanyong Seo, William A. Tisdale, Marc A. Baldo. “Dynamic triplet-driven passivation of silicon surfaces.” *In preparation* (2024)

5.1. Introduction

Surface passivation is important for achieving high-efficiency silicon solar cells. Traditional passivation layers reduce photo-generated carrier recombination at the surface through a two-fold mechanism: firstly, by chemical passivation of dangling bonds on the silicon surface, and secondly by forming an electric field on the surface to repel minority carriers away from the surface states[162], as depicted in Figure 5-1a. Use of dielectric layers with fixed charges such as aluminum oxide (Al_2O_3) for p-type silicon and silicon dioxide (SiO_2) for n-type silicon has been reported, with thicknesses ranging from 10s of nm to 100s of nm[95–98]. Recently, ultra-thin tunnel oxide passivation layers are of key interest for many high-efficiency silicon solar cell architectures, including tunnel oxide passivated contact (TOPCon) cells[163,164], heterojunction with intrinsic thin layer (HIT) solar cells[165], and singlet fission-sensitized silicon solar cells[35]. For example, growing a 14 Å-thick wet chemical SiO_x layer between the metal contact and the silicon surface for TOPCon cells is found to passivate the surface while allowing carrier extraction by tunneling through the layer, resulting in improvements to the open-circuit voltage (V_{oc}) and reduction in interfacial recombination[163].

In particular, the singlet fission-sensitized silicon solar cells (Figure 5-1b) present an interesting scientific and engineering challenge. In these cells, a singlet fission layer absorbs the high energy portion of the solar spectrum, generating two triplet excitons from the photogenerated singlet exciton through the singlet exciton fission process[34]. If these triplet excitons can be transferred from the singlet fission layer to silicon, the silicon photocurrent can be doubled, with the added bonus of reduced thermalization losses, potentially boosting the silicon efficiency from the classical limit of 29.4 % to 35–42 %[26,36,28,37,38]. However, as these triplet excitons are optically dark states, their transfer distance is limited to ~ 1 nm. Surface passivation of the silicon is also vital, as surface defect states can quench the triplet excitons throughout, and even after the transfer process, as the transferred carriers are expected in the near-surface region of silicon. Indeed, the first demonstration of successful triplet exciton transfer from a singlet fission material, tetracene (Tc), to n-doped silicon used an 8 Å-thick hafnium oxynitride (HfO_xN_y) layer to passivate silicon surface defects while allowing carriers from triplet excitons generated in the molecular singlet fission layer to tunnel through[35]. Such thin passivating layers do not have enough fixed charges to provide electric field-effect passivation; however, electric field-effect passivation is still observed in the Tc/HfO_xN_y/n-Si structures, resulting in an 8 to 9-fold enhancement of silicon photoluminescence where tetracene absorbs[35]. This passivation effect is likely driven by triplet excitons given the singlet fission yield in tetracene[34], and can play an important role in the triplet exciton sensitization process.

In this work, we design a controlled bilayer interface to support a triplet-driven passivation scheme of n-doped silicon surfaces for enhanced triplet exciton sensitization. A schematic of the passivation scheme is presented in Figure 5-1c. First, triplets are generated by the singlet fission layer, and dissociate across the donor-silicon interface, leaving a hole behind in the donor layer. The electron donation to n-silicon introduces an electric field at the interface, which provides electric field-effect passivation by repelling the holes (minority carriers) in n-doped silicon. Energetically, the charge-separated state (D^+-A^-_{Si}) is shown in Figure 5-1d, where the electron is located on the conduction band of silicon, and the hole is located on the HOMO level of the donor. This state can only be accessed from the singlet fission layer if its energy lies below the triplet exciton energy (Figure 5-1e) such that $E_{T1} \gtrsim E_{\pm}$. However, for triplet exciton sensitization of silicon to still occur, D^+-A^-_{Si} cannot be the lowest energy state, and we also need to ensure that there are no mid-gap states in silicon (see Chapter 4). Thus, we aim for $E_{T1} \gtrsim E_{\pm} \gtrsim E_g$.

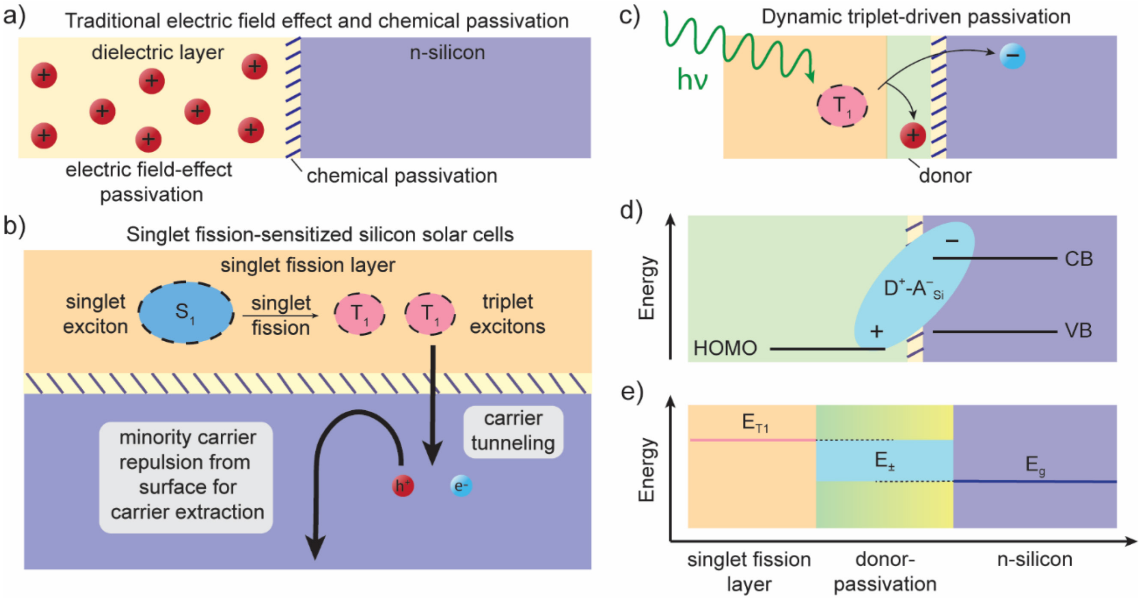

Figure 5-1. a) Schematic of traditional passivation layers, which provide chemical passivation by reacting with silicon surface dangling bonds, and electric field-effect passivation through introduction of a concentration of fixed charges. b) Schematic of singlet fission-sensitized silicon solar cells through the direct triplet exciton sensitization process. Triplet excitons are generated in the singlet fission layer from the singlet exciton. A passivation layer is necessary to prevent triplet exciton quenching, however, as the triplet excitons are transferred through a tunneling process, the passivation layer must be thin, permitting only chemical passivation. c) Schematic of triplet-driven passivation. Triplet excitons in the singlet fission layer dissociate across the donor layer-silicon interface, leaving behind a hole in the donor layer that can generate an electric-field at the interface. d) Energy level schematic of the charge-separated state (D^+-A^-_{Si}) formed across the donor-passivation-silicon interface, with the hole in the donor layer highest occupied molecular orbital (HOMO) level and the electron in the silicon conduction band (CB). e) State energy schematic, showing that the range of ideal energies for the D^+-A^-_{Si} state ($E_{\pm}$) should lie between the triplet exciton energy (E_{T1}) in the singlet fission layer and the band gap (E_g) of silicon.

We use tetracene (Tc) as our singlet fission layer, producing triplet excitons with high yield through singlet fission[34]. For our donor layer, we use zinc phthalocyanine (ZnPc) for its electron-donating capabilities[166], and its expected energy level alignment with n-doped silicon (n-Si) valence and conduction band edges[167] which would support formation of the charge-separated state with the electron in silicon and the hole in ZnPc from the triplet excited state in Tc. An extremely thin layer of aluminum oxide (AlO_x) or hafnium oxide (HfO_x) is deposited on the silicon surface for chemical passivation of the silicon dangling bonds. In practice, we see no major differences in the comparative triplet-driven passivation property of the devices, with only some slight differences in the overall passivation quality at all wavelengths, suggesting the role of this oxide layer is more for chemical passivation. By using magnetic field-dependent photoluminescence measurements, we probe the formation of the electric field from triplet excitons at the ZnPc/n-Si interface. We then assess the passivation efficiency from triplet excitons by performing excitation wavelength-dependent silicon photoluminescence (PL) measurements. Our results show that triplet excitons can be used for light-induced electric-field-effect passivation of silicon surfaces, with exciting opportunities for high-efficiency silicon solar cells.

5.2. Experimental methods

5.2.1. Fabrication of optical samples

n-doped silicon wafers (PureWafer, n-type Si:P, prime, [100], 280 µm, 1-5 Ωcm) were diced into 1” x 1” pieces and sonicated in detergent solution (2 vol% Micro-90), de-ionized (DI) water and acetone, before immersion in boiling isopropyl alcohol. The wafers were dried using nitrogen gas and transferred to a cleanroom.

The substrates were then cleaned through a standard RCA clean process: SC-1 (5:1:1 DI water, hydrogen peroxide (30%) and ammonium hydroxide (29%)) for 15 mins at 80 °C, HF-etch (4 vol% HF in DI water) for 1 minute at 25 °C, and SC-2 (6:1:1 DI water, hydrogen peroxide (30%) and hydrochloric acid (37%)) for 15 mins at 80 °C. This process leaves an oxide layer on the silicon surface that is approximately 0.8–1 nm-thick (below the ellipsometer resolution limit).

The substrates were dried using nitrogen gas, and then transferred immediately to an atomic layer deposition (ALD) chamber (Cambridge Nanotech Savannah). 2 cycles of AlO_x or HfO_x were deposited at reaction temperatures of 200 °C, resulting in an overall oxide thickness (including the oxide from the RCA clean) of around 1.2 nm. Trimethylaluminum (TMA) was used as the aluminum precursor, tetrakis(ethylmethylamino)hafnium (TEMAH) was used as the hafnium precursor, and water was used as the oxygen precursor. The samples were then immediately transferred to a nitrogen glovebox for organic layer deposition.

Zinc phthalocyanine (Luminescence Technology Corp, sublimed grade > 99% purity) was used as received. Tetracene (Sigma Aldrich, sublimed grade, 99.99% trace metal basis) was purified using a tube furnace. The organic layers were deposited by thermal evaporation in a vacuum chamber at a pressure of $< 1 \times 10^{-6}$ torr. 1.5 nm of ZnPc was deposited at a 0.2 Å/s rate, followed by 30 nm of Tc deposited at a 1 Å/s rate.

Following deposition of the organic layers, samples were encapsulated using quartz substrates and UV-curable epoxy under low oxygen and water conditions (< 5 ppm). The active area of the samples was protected during the UV light exposure.

5.2.2. Magnetic field-dependent silicon photoluminescence measurements

Samples were mounted between two poles of an electromagnet. The samples were excited by either a mechanically-chopped (273 Hz) 200 mW 532 nm laser (Coherent, Verdi G18) or a similarly-chopped 50 mW 660 nm laser (Newport, LQA660-110C). The silicon photoluminescence was collected using an IR photodetector (Newport, 818-IR) connected to a lock-in amplifier (Stanford Research Systems SR 830), with 900 nm and 1000 nm longpass filters in front of the detector to ensure collection of only the silicon photoluminescence. For each magnetic field strength point, the magnet was periodically switched on and off 4 times and the average silicon photoluminescence change was calculated. The field strength was measured using a gaussmeter (Lakeshore HMMT-6J04-VF).

5.2.3. Excitation wavelength-dependent silicon photoluminescence measurements

A tunable broadband supercontinuum laser (NKT Photonics, SuperK EXW-12 with an acousto-optic tunable filter SuperK SELECT) was used to excite the optical samples across the visible spectrum. An additional 110 mW 660 nm laser (Newport, LQA660-110C) and white LED light source (Thorlabs, MCWHLP2) were used as optical biases to increase the overall measurement signal-to-noise ratio and ensure linear power-scaling with the visible laser excitation. The silicon photoluminescence was collected using a liquid-nitrogen-cooled InGaAs detector (Princeton Instruments, OMA V:512). For the results presented in this work, we subtract the silicon photoluminescence measured with the bias only from the photoluminescence measured with the bias and the tunable visible laser, and correct for the measured power of the laser.

5.3. Generation of charges at the silicon surface

The additional charged layer at the surface can reduce surface recombination losses and provide a boost in the performance of singlet fission-sensitized silicon solar cells. To probe the generation of charges from triplet excitons at the silicon surface, we prepare optical samples with 30 nm of tetracene, 1.5 nm of zinc phthalocyanine, and 1 nm of AlO_x on n-doped silicon.

5.3.1. Magnetic field-dependent measurements

If the charging at the interface is generated from triplet excitons, magnetic field-dependent measurements can be used to probe this process as electronic spin plays an important role. In our system, if there is a buildup of charge carriers, as well as triplet excitons present, we expect triplet-charge annihilation (TCA) to occur[168]. A schematic of the TCA process is shown in Figure 5-2a: the triplet exciton is destroyed after interaction with a charge[79]. The rate of this process can be modulated by applying an external magnetic field[85,168,79], such that increasing the magnetic field strength results in a monotonically decreasing rate of TCA (k_{TCA}). More detail on the magnetic field-dependence is provided in Section 2.1.5.1.

As the k_{TCA} has a characteristic magnetic field-dependence, we can probe for its signature by measuring how the silicon photoluminescence of the Tc/ZnPc/AlO_x/n-Si structure changes as we apply differing external magnetic field strengths. Changes to k_{TCA} result in changes to the overall population of triplet excitons. Using the measured changes in silicon photoluminescence as an indicator of changes in silicon surface passivation quality, we can probe the effect of changing the triplet population on the passivation quality, and simultaneously probe the origin of this effect by exciting using 532 nm light which selectively excites Tc and 660 nm light, which selectively excites ZnPc, whose absorption spectra are plotted in Figure 5-2b.

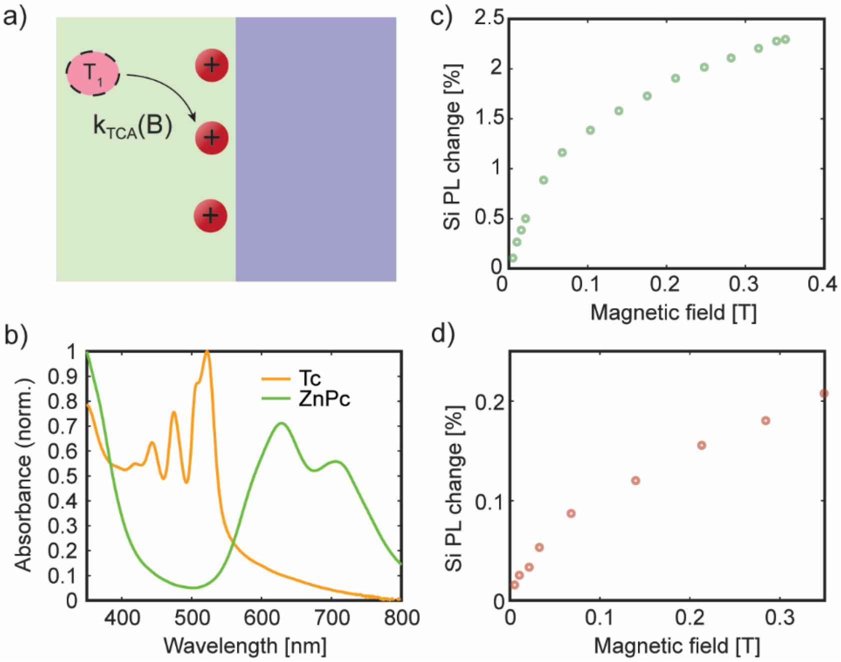

Figure 5-2. a) Schematic showing the process of triplet-charge annihilation (TCA). The rate of the TCA process (k_{TCA}) can be modulated by an applied external magnetic field. b) Absorption spectra of the singlet fission layer tetracene (Tc) and the donor layer zinc phthalocyanine (ZnPc). c) Magnetic field-induced silicon photoluminescence change of a Tc/ZnPc/AlO_x/n-Si sample excited with a 532 nm laser as a function of magnetic field strength. d) Magnetic field-induced silicon photoluminescence change of a Tc/ZnPc/AlO_x/n-Si sample excited with a 660 nm laser as a function of magnetic field strength.

We measure the change in the silicon photoluminescence as a function of magnetic field in Figure 5-2c with 532 nm excitation. We observe that the silicon photoluminescence change is increasingly positive with increasing applied magnetic field, with the shape of the curves tracking with expected TCA features. With the triplet excitons contributing positively to the silicon photoluminescence through the triplet exciton sensitization, TCA constitutes as a competitive loss process that reduces the overall photoluminescence from the silicon due to the decreased passivation effect. As a result, reducing k_{TCA} through an increased magnetic field should result in increased silicon photoluminescence, consistent with what is observed experimentally. We note that the singlet fission process in tetracene is also magnetic field-dependent, thus we perform fits to the measurements using a model that incorporates both singlet fission and TCA. Our modeling suggests that the magnetic field-dependence is dominated by TCA-rate modulation over the fission-rate modulation, which implies that the singlet fission and subsequent triplet transfer is occurring very efficiently in these systems.

Signatures of TCA can also be observed by exciting only ZnPc with 660 nm (Figure 5-2d). This is most likely from expected intersystem crossing in ZnPc which generates some triplet excitons[169]. However, as our ZnPc layer is significantly thinner than the tetracene, and the triplet sensitization of tetracene is much higher, the magnitude of the silicon photoluminescence change is lower than when exciting with 532 nm. We also note no observation of magnetic field-dependence when exciting with 1064 nm, which only pumps the silicon with no triplet excitons generated, see Figure 5-3a. Additionally, replacing the ZnPc layer with platinum octaethylporphyrin (PtOEP), which has a reported triplet exciton energy of 2.0 eV[170] that tetracene cannot sensitize, turns off the TCA feature as well (Figure 5-3b), although the energy level alignment of this layer with respect to silicon may not be the same as with ZnPc. These results are strongly indicative of triplet-induced charging at the interface, with the triplet excitons contributing positively to the silicon photoluminescence.

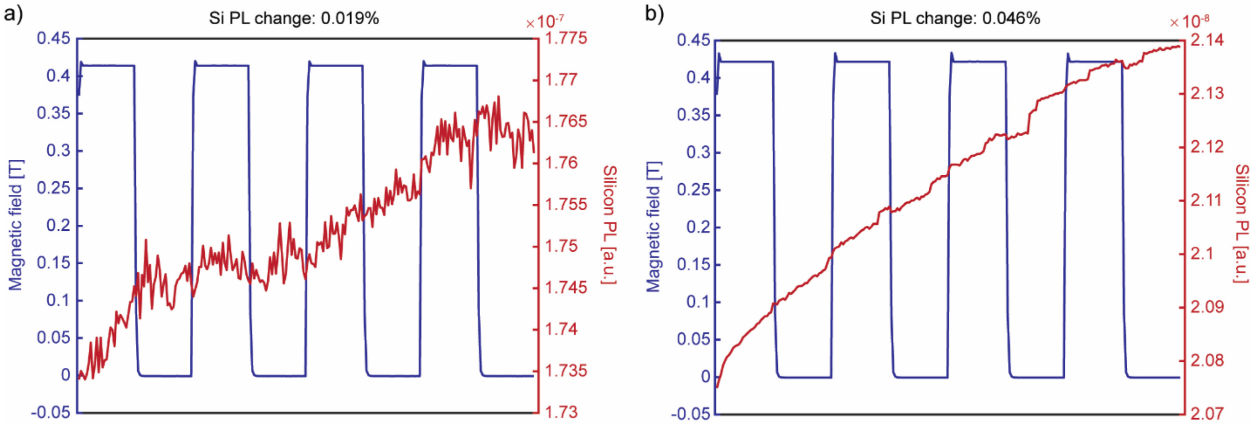

Figure 5-3. Magnetic field-dependent measurements of control samples measured at a field strength of approximately 0.4 T. a) Tc/ZnPc/HfO_x/Si excited with 1064 nm which only excites the silicon. b) Tc/PtOEP/HfO_x/Si excited with 532 nm.

5.3.2. Nature of charging at the interface

The magnetic field-dependent measurements point to the presence of charges at the interface. For there to be effective electric field-effect passivation of the n-Si surface, we expect the holes to be located near the silicon surface such that the minority carriers in the n-Si are repelled away.

Ultraviolet photoelectron spectroscopy (UPS) measurements can be used to inform the expected field direction at the interface. UPS measurements of ZnPc on n-doped silicon[167] (see also Chapter 7) reveals that formation of the charge-separated state from the triplet exciton in ZnPc is accessible only if the hole is located in ZnPc while the electron is in silicon. Swapping the silicon doping to a highly p-doped silicon surface (Chapter 7) actually shifts the alignment such that the opposite is favored (hole in silicon and electron in ZnPc). However, our colleagues at Princeton have mentioned that only the p-doped measurements showed very clear signs of organic layer degradation when collecting the UPS measurements of these structures. Our hypothesis is that the ZnPc does not appear to favor charging negatively and would prefer to donate electrons, which is consistent with literature reports of its electron-donating ability[166].

To actually probe the nature of the charges at the surface and the direction of the electric field, we recommend performing surface photovoltage measurements as a function of excitation wavelength (red vs green excitation), building up the sample stack from n-Si upwards.

5.4. Passivation enhancements

5.4.1. Excitation wavelength-dependent silicon photoluminescence

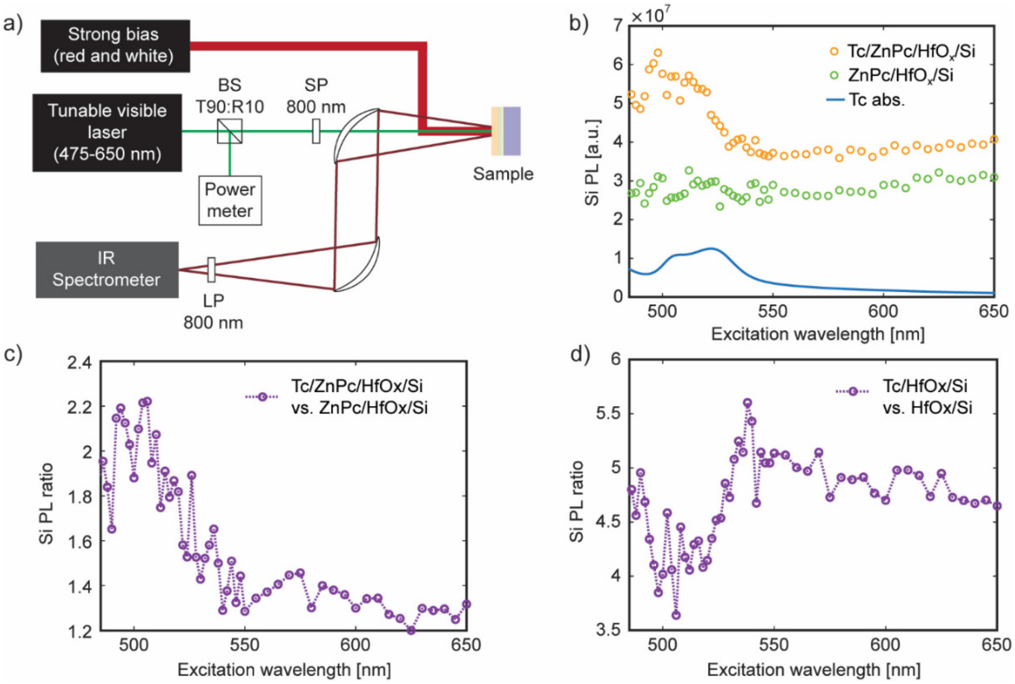

Figure 5-4. a) Diagram of the experimental setup used for the excitation wavelength-dependent silicon photoluminescence measurements. b) Excitation wavelength-dependent silicon photoluminescence measured from Tc/ZnPc/HfO_x/Si (orange) and ZnPc/HfO_x/Si (green) with the tetracene absorption spectra in blue for guidance. c) Ratio of the measured excitation wavelength-dependent silicon photoluminescence from b). d) Ratio of the measured excitation wavelength-dependent silicon photoluminescence for sample stacks without the ZnPc donor layer. All measurements were performed with both a red and white bias.

To investigate the passivation property of the triplet-induced passivation scheme, we perform excitation wavelength-dependent silicon photoluminescence measurements as shown in Figure 5-4a. As the silicon photoluminescence signal is low, we apply a strong red bias, and sometimes also a white bias, to enhance signal-to-noise ratio by increasing the silicon photoluminescence quantum yield. This strong bias is also significantly higher in power compared to the tunable visible laser output; as a result, we can assume that the measured silicon photoluminescence scales linearly with the tunable visible laser power at each wavelength, as demonstrated in Figure 5-5.

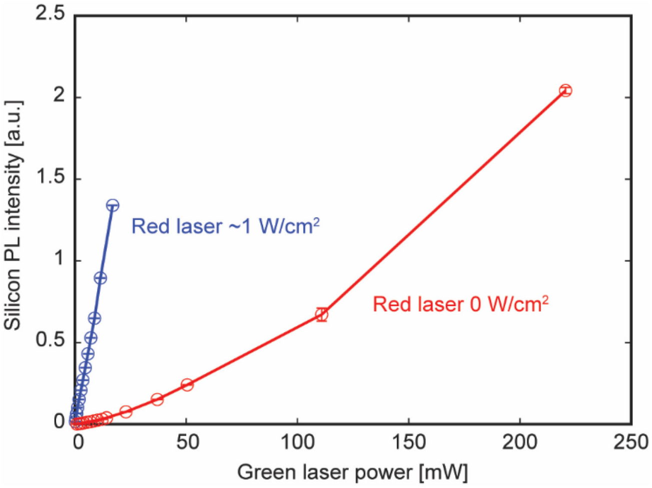

Figure 5-5. Integrated silicon photoluminescence as a function of tunable green laser excitation power, with and without the 660 nm red biasing laser.

Figure 5-4b shows the excitation wavelength-dependent silicon photoluminescence for Tc/ZnPc/HfO$_x$/Si and ZnPc/HfO$_x$/Si samples. We observe that adding the tetracene layer provides an overall enhancement in the silicon photoluminescence at all wavelengths, with notably higher enhancements in the region corresponding to the absorption spectrum of tetracene where the triplet sensitization is expected to occur.

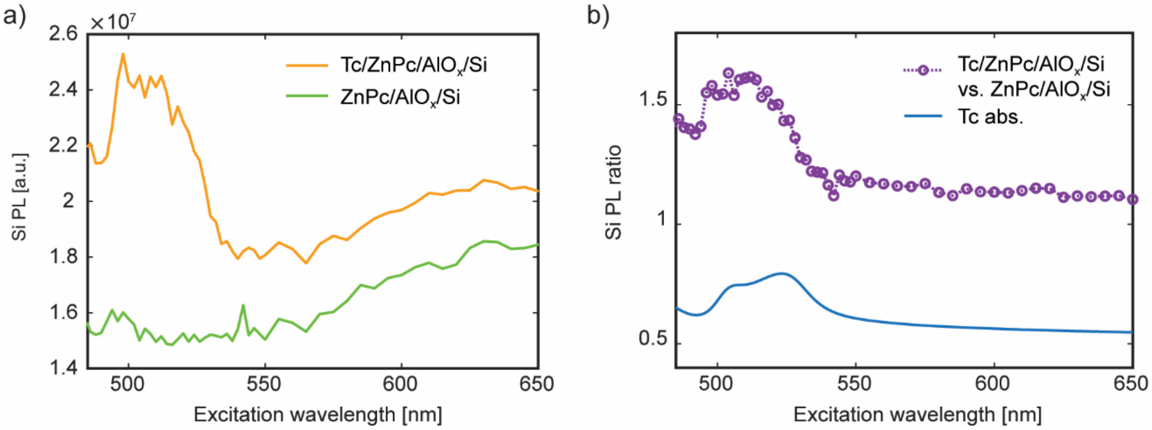

Figure 5-6. a) Excitation wavelength-dependent silicon photoluminescence measured for sample stacks of Tc/ZnPc/AlO_x/n-Si (orange) and ZnPc/AlO_x/n-Si (green). b) Ratio of the spectra plotted in a) (purple) and the tetracene absorption spectra in blue for reference. All measurements were performed with a red bias.

As an aside, Figure 5-6 shows the same excitation scan measurements taken for the samples using AlO_x instead of HfO_x. While we measured differences in the shape of the spectra, particularly in the red-wavelength region (> 550 nm), the overall trend showing a positive enhancement from tetracene is the same regardless of swapping between the AlO_x and HfO_x layers; as a result, we hypothesize that the 2 Å-thick layers are serving purely a chemical passivation role. As the increase in the red wavelength region is observed for both samples, this may be an issue with either the measurement power calibration (had just transitioned to a new SuperK tunable laser excitation system) or a slightly thicker than expected layer of ZnPc might have been deposited for these samples. In theory, any good quality chemical passivation layer should also work (including SiO_x). At the time that these experiments were carried out, we attempted to grow thin Si_3N_4 and amorphous silicon (a-Si) using plasma-enhanced chemical vapor deposition (PECVD) as alternative chemical passivation layers that have been reported for silicon solar cell use[171,172]. However, the PECVD tool was not able to grow the ideal conformal quality of layers that we desired at ultra-thin thicknesses (~1-2 nm), so we did not proceed further with these layers. Future studies may be interesting if good quality, uniformly-thick, ultra-thin layers of these materials can be grown.

To quantify the photoluminescence enhancement from triplet sensitization, we take the ratio of the silicon photoluminescence for the sample with tetracene and without. This ratio is plotted in Figure 5-4c. Transfer matrix method simulations[173] of the sample stack can be performed to estimate the relative absorption of each layer (Figure 5-7). We see from Figure 5-7b that of the total absorption by the sample stack, tetracene absorbs at most 21 % of the absorbed light at 523 nm. From the internal quantum efficiency (IQE) simulations in Figure 5-7d, if only triplet transfer from tetracene to silicon is occurring, this would suggest a maximal boost of 121% for the silicon photoluminescence. Hence, observing an enhancement greater than this in both Figure 5-4c and Figure 5-6b is indicative of triplet-driven passivation of the silicon surface[35].

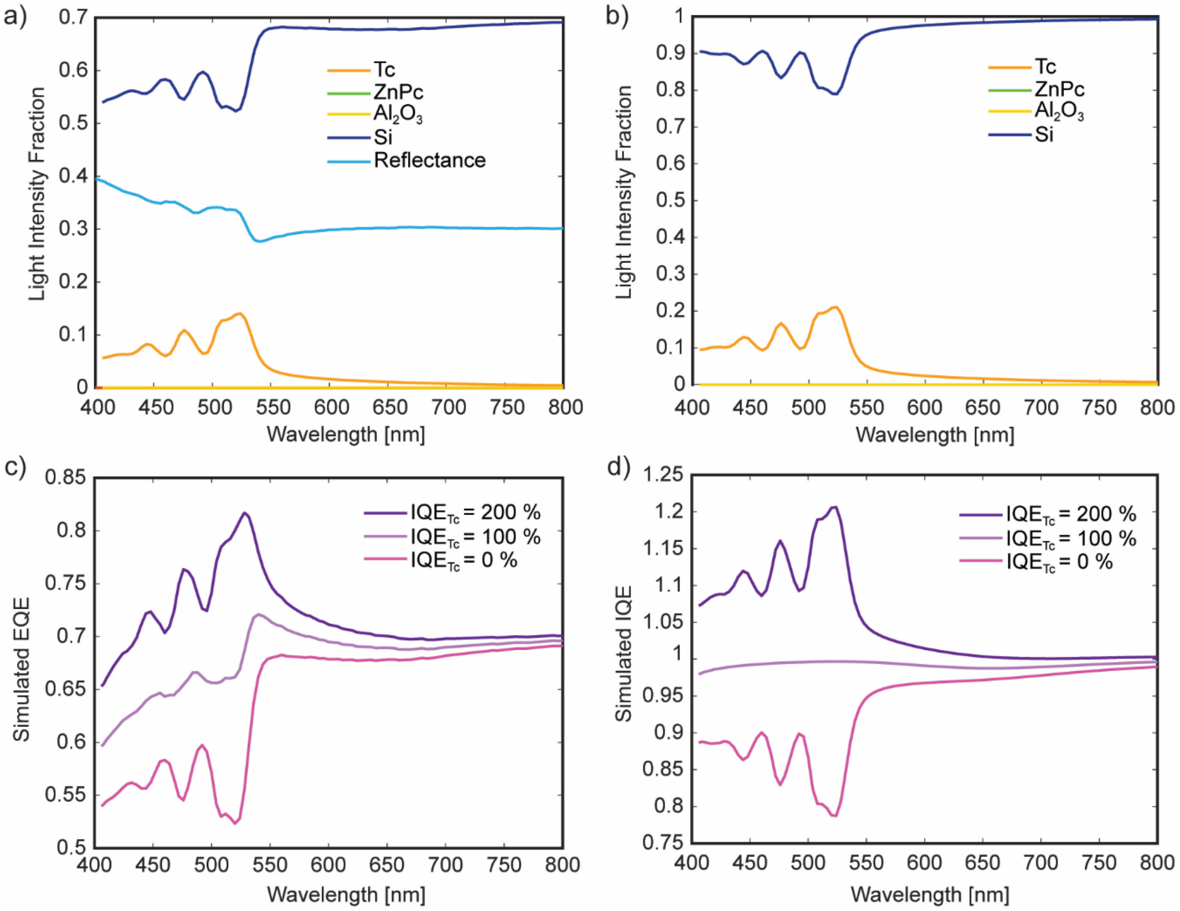

Figure 5-7. Transfer-matrix method[173] simulations for a sample stack with 30 nm Tc/1.5 nm ZnPc/1 nm Al_2O_3/180 µm Si. a) Calculated absorption of each layer, as well the as the overall reflectance from the sample. b) Calculated fractional absorption of each layer, dividing out reflectance. c) Simulated external quantum efficiencies of the device using the calculated absorption of each layer at different tetracene quantum efficiencies using the following formula: $EQE = \alpha_{Si} + IQE_{Tc} \times \alpha_{Tc}$. d) Simulated internal quantum efficiencies of the device using the calculated absorption of each layer at different tetracene quantum efficiencies using the following formula: $IQE = (\alpha_{Si} + IQE_{Tc} \times \alpha_{Tc})/(1 - R)$.

As another aside, it is interesting to see that the external quantum efficiency (EQE) simulations in Figure 5-7c suggest that even if tetracene were able to transfer 100 % of the energy that it absorbed, the performance of the cell is still worse than without tetracene, as evidenced by the dips. Hence, the triplet exciton yield and triplet exciton transfer must be very efficient in order to observe actual peaks contributing to the EQE. We also notice an interesting wavelength red-shifting most likely caused by changes in the tetracene refractive index.

We perform further control experiments by blocking the triplet-driven passivation process using a sample stack without ZnPc. In these structures, the Tc energy level alignment with the silicon valence band edge is such that the triplet-driven electric field cannot be formed. Indeed, performing the same excitation wavelength-dependent silicon photoluminescence measurements for structures with and without the tetracene layer results in the ratio calculated in Figure 5-4d. Unlike in Figure 5-4c, we see dips corresponding to the absorption spectrum of tetracene, indicating a degradation in the passivation quality of the silicon surface from the tetracene layer present.

We also perform similar measurements for samples with no HfO_x chemical passivation layer, as well as samples with a 20 nm-thick ZnPc layer (Figure 5-8). Both measurements also show dips corresponding to the absorption spectrum of tetracene. The lack of chemical passivation results in triplet exciton quenching at the interface and an ineffective triplet-driven passivation. For the thicker ZnPc layer sample, the exciton diffusion length in ZnPc has been reported to be around 10 nm[174]; as a result, the excitons from tetracene cannot diffuse to the interface for the passivation process. While triplet-driven passivation through triplet excitons formed in ZnPc *via* intersystem crossing should be possible for the thicker ZnPc layer sample, studying its effect would require the ratio between a sample with and without the ZnPc layer.

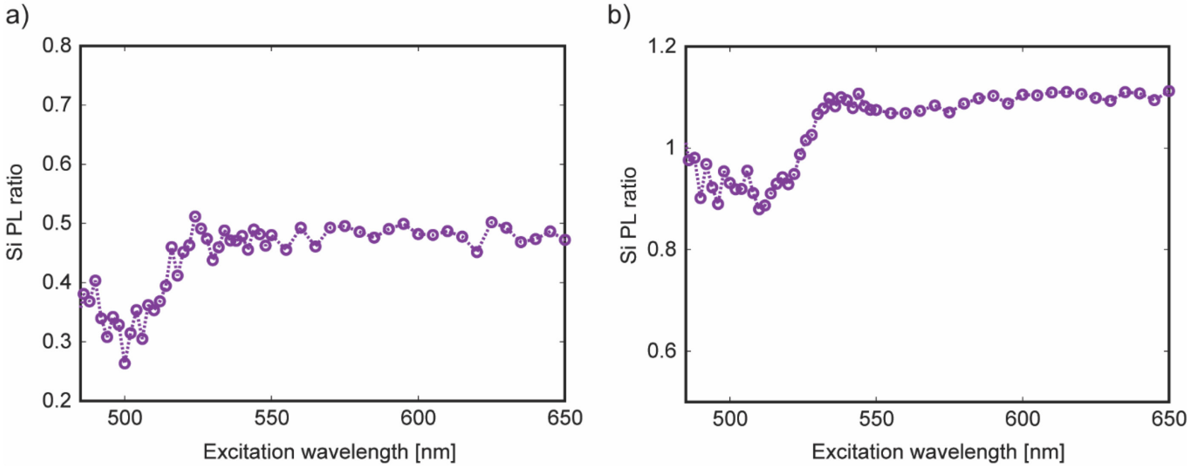

Figure 5-8. Excitation wavelength-dependent silicon photoluminescence ratios obtained for a) Tc/ZnPc/n-Si vs ZnPc/n-Si and b) Tc/20 nm ZnPc/HfO$_x$/n-Si vs 20 nm ZnPc/HfO$_x$/n-Si. All measurements were performed with a red bias.

Finally, we add an aside about the role of the white light bias. The excitation wavelength-dependent silicon photoluminescence ratios in Figure 5-4c-d were obtained using both a red and white bias. We also measure the same samples without a white bias in Figure 5-9 and Figure 5-10. We notice that the samples with the donor ZnPc layer show qualitatively the same peaks near the tetracene absorption region in both biasing conditions, but the samples without the donor ZnPc layer show remarkably different behavior, going from peaks without the white bias, to dips with the addition of the white bias. To better understand the origin of this difference, we turn to the time-dependent response of the silicon photoluminescence without the white bias in Figure 5-11. We notice that the Tc/ZnPc/HfO$_x$/Si sample shows a long timescale increase in the silicon photoluminescence signal with the red bias, and a relatively instantaneous increase with the weak green excitation (Figure 5-11a). For the Tc/HfO$_x$/Si sample, we observe instead an extremely slow long timescale increase in the silicon PL with the introduction of the weak green excitation, which decreases at an even slower rate upon removing the green excitation. Returning to the excitation scan of the Tc/HfO$_x$/Si samples, with the red bias + green excitation, we interpret the peaks as evidence of some kind of tetracene-induced electric field-effect passivation, with the slow dynamics suggesting that the formation of this field is quite rare, potentially as they originate from tail states of the molecular orbital of tetracene. The green excitation in this case is probing both passivation and triplet exciton transfer. Whereas with the white bias + red bias + green excitation, the white bias can set up the slow charging in advance, and the green excitation in this case is probing more of the transfer process, and we see dips that can be correlated with inefficient transfer. In the samples with ZnPc, the red bias already plays the important role of starting the slow charging by excitation of ZnPc and intersystem crossing, and so we see minimal qualitative difference between the experiments with and without the white bias.

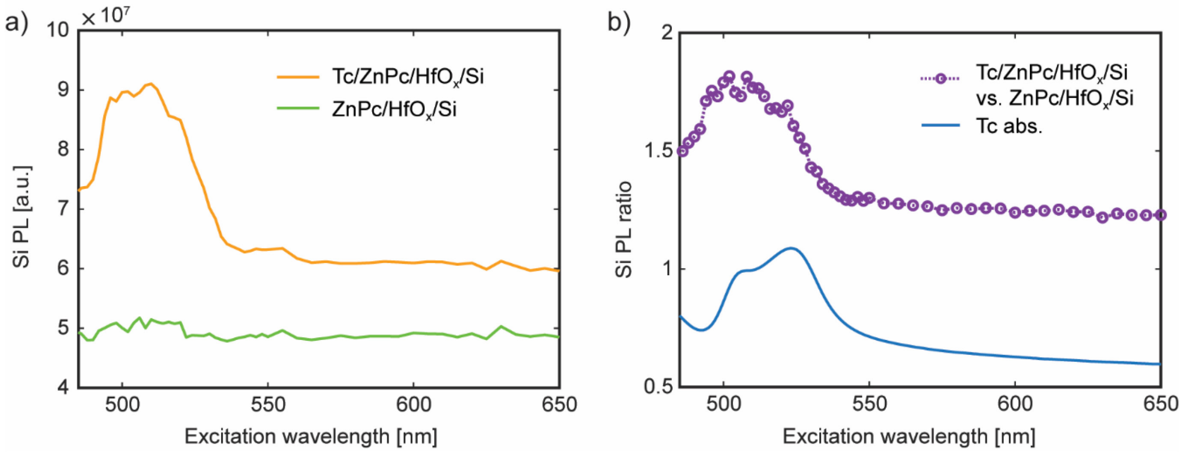

Figure 5-9. Excitation wavelength-dependent silicon photoluminescence measurements for samples with the ZnPc layer and with only a red bias (no white LED bias). a) Excitation wavelength-dependent silicon photoluminescence spectra for Tc/ZnPc/HfO$_x$/n-Si (orange) and ZnPc/HfO$_x$/n-Si (green). b) Ratio of spectra plotted in a) (purple) with tetracene absorption in blue for comparison.

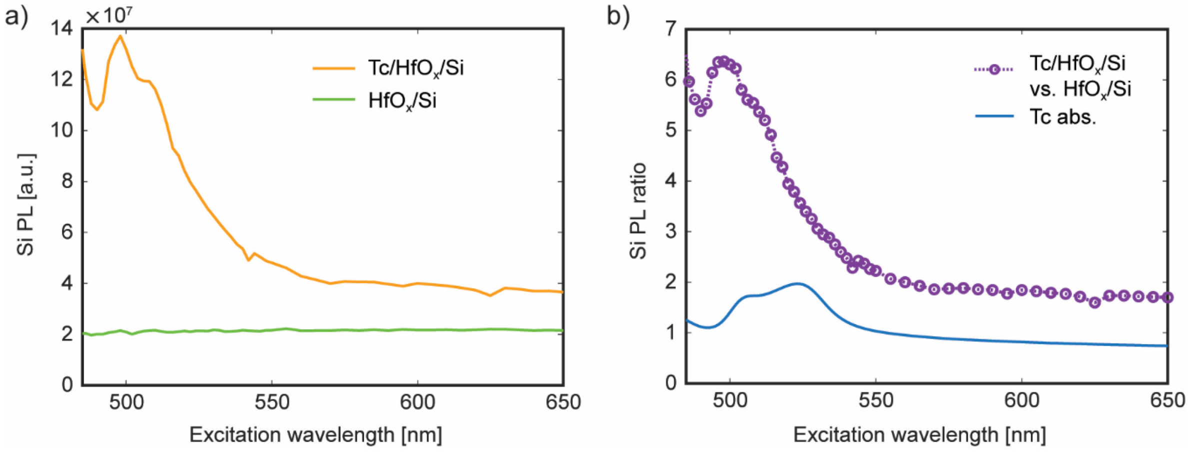

Figure 5-10. Excitation wavelength-dependent silicon photoluminescence measurements for samples without the ZnPc layer and with only a red bias (no white LED bias). a) Excitation wavelength-dependent silicon photoluminescence spectra for Tc/HfO$_x$/n-Si (orange) and HfO$_x$/n-Si (green). b) Ratio of spectra plotted in a) (purple) with tetracene absorption in blue for comparison.

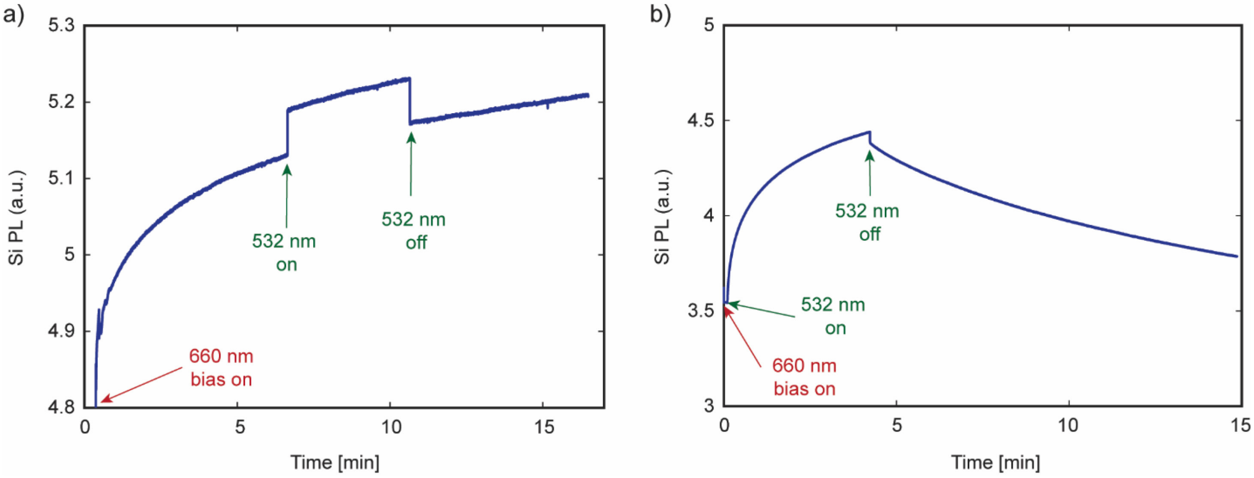

Figure 5-11. Silicon photoluminescence increase over minutes-long time scales upon excitation using the 660 nm red biasing laser, with the effect of a weaker excitation at 532 nm for a) Tc/ZnPc/HfO$_x$/n-Si, and b) Tc/ HfO$_x$/n-Si.

We also note that the excitation ratios all appear to be slightly blue-shifted from the absorption spectrum of tetracene measured on glass. The origin is not entirely clear, and could be an interesting area of further study.

Additional probes of passivation quality include building devices out of the proposed structure and measuring the EQE and surface recombination velocities (SRV). Silicon has a wavelength-dependent absorption coefficient (α_{Si})[175], which corresponds to absorption depth through an inverse relationship: $absorption\ depth = 1/\alpha_{Si}$. Hence, lower wavelength light tends to be absorbed closer to the surface of silicon, making the carriers generated more sensitive to surface recombination. Additional SRV measurements can help quantify the improvements in passivation from the triplet-driven mechanism by measuring Tc/ZnPc/AlO$_x$/n-Si and ZnPc/AlO$_x$/n-Si excited using red and green light.

Transient dynamics could also be measured using a transient surface photovoltage configuration[176,177]. Based on the responses observed in Figure 5-11, the dynamics of the triplet-induced passivation could turn out to be quite slow while the triplet transfer process is much faster.

5.5. Conclusion

Singlet fission-sensitized silicon solar cells require ultrathin passivation layers for carrier tunneling of the triplet excitons, however, these layers cannot provide electric field-effect passivation, which is beneficial for triplet exciton sensitization. We demonstrate a new bilayer interfacial design that uses a donor layer with a HOMO level that supports formation of a charge-separated state between this layer and n-silicon that can act both as an intermediate to triplet exciton transfer, as well as provide an electric field that can induce electric field-effect passivation for the silicon surface. We also use an ultrathin passivation layer to chemically passivate the silicon surface defect states. With zinc phthalocyanine as the donor layer and aluminum oxide/hafnium oxide as the chemical passivation layer, we show through magnetic field-dependent measurements that there are triplet excitons and charges in the system, with triplet excitons contributing positively to the silicon photoluminescence. Excitation wavelength-dependent silicon photoluminescence measurements show that the triplet-driven passivation comes hand-in-hand with successful triplet exciton enhancement of silicon, implying that this bilayer interface is a great candidate for implementation in silicon photovoltaic devices.

Chapter 6.
Heterojunction & interdigitated-back-contacted (IBC) solar cells for singlet fission sensitization

This chapter contains data that was collected in conjunction with Collin F. Perkinson.

6.1. Introduction

Singlet exciton fission has the potential to enhance crystalline-silicon photovoltaic efficiencies beyond the Shockley-Queisser limit[26,28,34]. However, despite promising optical results[35,46,47], evidence of triplet exciton sensitization in the photocurrent quantum efficiencies has yet to be observed. As the exact mechanism for the transfer of the triplet exciton is not known very well, different solar cell structures have been proposed for singlet-fission-sensitized solar cells, such as silicon-tetracene heterojunction cells[46,120], and interdigitated-back-contacted (IBC) cells[35,47]. The former is designed primarily for triplet dissociation at the silicon-tetracene interface, but can also function if the full triplet exciton is transferred, with the hole transporting through the tetracene layer to the top contact. The latter works best for full triplet transfer, as the electrodes are located on the back side of the cell and requires the carriers to travel through the thickness of the silicon wafer. The benefit of the back-contacted cells compared to the heterojunction cells is the similarity of the top surface with the optical devices presented in Chapter 5.

In this work, we incorporate tetracene as the singlet fission layer, and use zinc phthalocyanine and aluminum oxide as the interfacial layers to sensitize silicon solar cells with triplet excitons from tetracene. We fabricate silicon-tetracene heterojunction solar cells and IBC cells, and characterize their electrical performance. Our results show that targeted silicon solar cell design is necessary for observing triplet exciton sensitization effects in the photocurrent, and form the basis of the choice of silicon solar cell architecture presented in Chapter 7.

6.2. Methods

6.2.1. Materials

For the heterojunction solar cells, 295 μm-thick prime grade silicon wafers were purchased from PureWafer (n-Phos, <100>, 1-5 Ωcm, 2 sp). m-MTDATA (sublimed > 99%) and zinc phthalocyanine (sublimed > 99%) were purchased from Luminescence Technology Corp. and used without further purification. Molybdenum(VI) oxide (99.97% trace metals basis) and tetracene (sublimed grade, 99.99% trace metals basis) were purchased from Sigma Aldrich. Tetracene was purified once using a sublimation and recondensation process in a three-zone tube furnace before deposition.

6.2.2. Process flow of heterojunction cell fabrication

The overall process flow followed for fabricating the heterojunction tetracene-silicon solar cells are detailed in Figure 6-1.

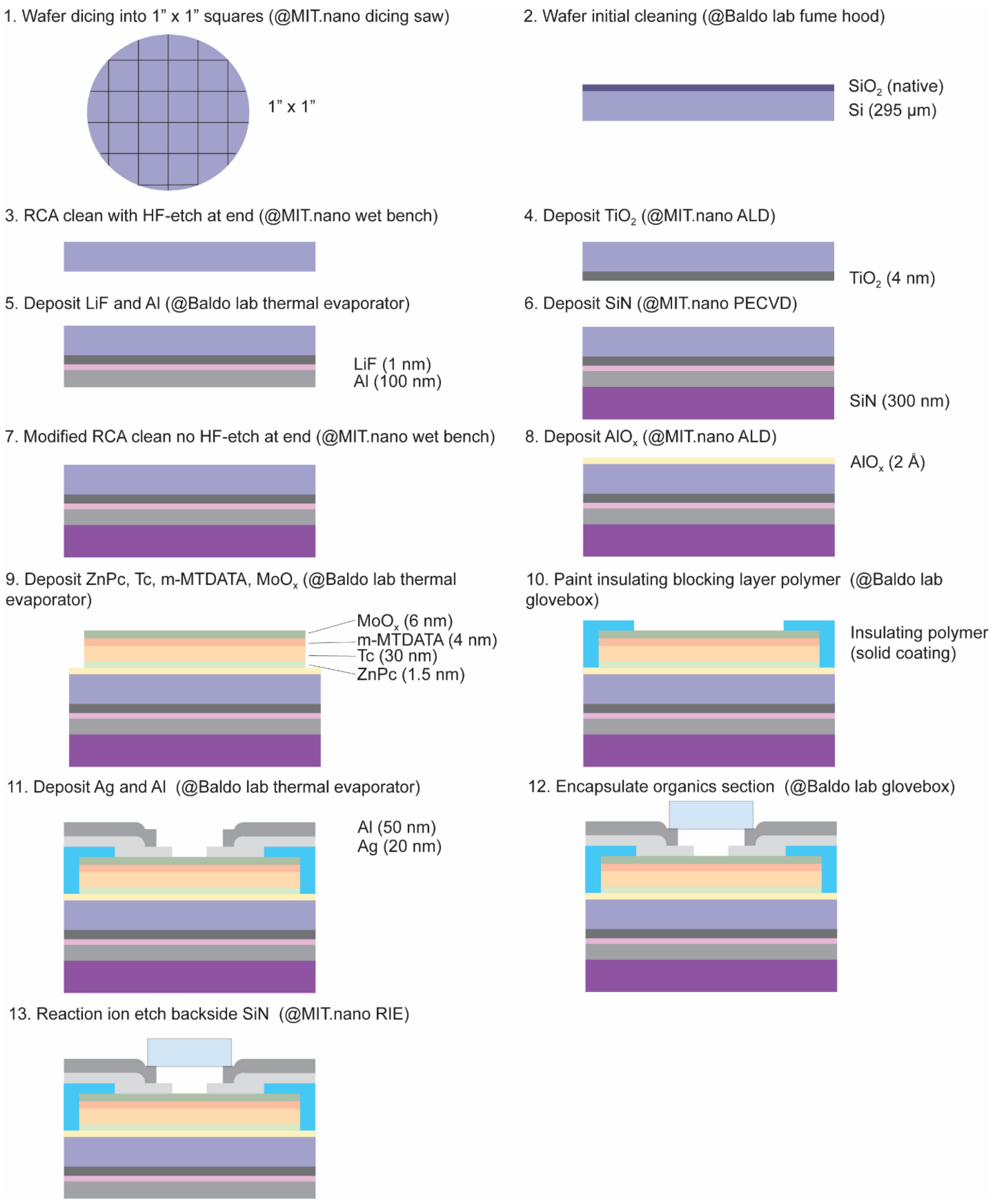

Figure 6-1. Process flow detailing the steps taken to fabricate the silicon-tetracene heterojunction solar cells. Nominal layer thicknesses are presented. Note that the schematics are not to scale.

6.2.2.1. Wafer initial clean

The silicon wafers were diced into 1-inch squares and cleaned by sonicating in detergent solution (Micro-90), deionized water, and acetone, followed by immersion in boiling isopropanol. The wafers were then dried with pressurized nitrogen and transferred to a clean room.

6.2.2.2. Radio Corporation of America (RCA) clean

The diced wafers were loaded into a sample holder and briefly submerged in deionized water (DIW). Then, they were submerged in a 5:1:1 (volumetric ratio) solution of DIW:NH_4OH:H_2O_2 (SC1) at 80 °C for 15 minutes, followed by another rinse in DIW. The sample holder was then lowered into a 25:1 (volumetric ratio) solution of DIW:HF (HF etch) for 60 s, followed by another rinse in DIW. Then, the sample holder was submerged in a 6:1:1 (volumetric ratio) solution of DIW:HCl:H_2O_2 (modified SC2) at 80 °C for 15 minutes, followed by a rinse in DIW. A second HF etch step was performed at the end to remove any oxide layers on the silicon and leave a H-terminated silicon surface. A final double rinse in DIW was performed, and the samples were dried under a stream of nitrogen gas.

6.2.2.3. Modified RCA clean

Most of the steps in this process are the same as the regular RCA clean detailed in section 6.2.2.2. However, the SC2 bath is replaced by a 6:1 (volumetric ratio) solution of DIW:H_2O_2, due to the silicon nitride (SiN) layer being susceptible to degradation in the regular SC2 bath containing HCl, as shown in Figure 6-2. This corrosion of the SiN layer by HCl was observed to be SiN-thickness-independent, and also occurred at room temperature.

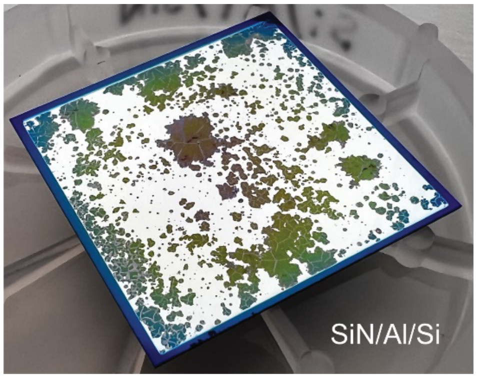

Figure 6-2. Photograph showing the corrosion of a 300 nm-thick SiN layer deposited on top of an aluminum layer on silicon, after submersion in SC2 solution (6:1:1 volumetric ratio of DIW:HCl:H_2O_2).

6.2.2.4. Atomic layer deposition (ALD)

4 nm of titanium oxide (TiO_2) was deposited using the standard recipe (Cambridge Nanotech Savannah) to passivate the back surface of the silicon. 2.2 Å of aluminum oxide was deposited using the Baldo lab-modified recipe (Cambridge Nanotech Savannah) to passivate the top surface of the silicon. Note that because the aluminum oxide layer is thin, this passivation only works if the silicon surface is −OH terminated (end RCA clean with either SC1 or SC2).

6.2.2.5. Plasma-enhanced chemical vapor deposition (PECVD)

300 nm of silicon nitride (SiN) was deposited using PECVD (Surface Technology Systems, multiplex CVD). Low frequency, high frequency and mixed frequency recipes were tested for the silicon nitride layer, although all of them were susceptible to degradation by HCl in regular SC2 solution. Ultimately, mixed frequency silicon nitride was used for the device results presented in this chapter.

6.2.2.6. Thermal evaporation

For layers deposited through thermal evaporation, the samples were transferred to a vacuum chamber at a pressure of $< 1 \times 10^{-6}$ torr. 1 nm of lithium fluoride (LiF) was deposited at a rate of 1 Å/s as an electron-selective contact. 100 nm of aluminum (Al) was deposited at a rate of 2–5 Å/s for the back contact. For the singlet fission top surface, after ALD of AlO_x, the samples were double-bagged in nitrogen and transferred to a dry nitrogen glovebox. Minimizing wait time, 1.5

nm of zinc phthalocyanine (ZnPc) was immediately deposited at a rate of 0.5 Å/s, followed by 30 nm of tetracene (Tc) using a shadow mask that blocked the outer edges of the device. The same shadow mask was also used to deposit 4 nm of m-MTDATA (triplet-blocking layer), followed by 6 nm of molybdenum oxide (MoO_x, hole transport layer). For the top contact, to avoid shorting of the device through direct electrical contact between the top contact and the silicon surface, a continuous but thin layer of insulating blocking polymer was painted on the corners of the device. Then, after drying of the polymer for 30 minutes, the devices were transferred back into the evaporator for masked deposition of 20 nm of silver (Ag). This thickness of Ag was chosen for its semi-transparent properties, so that light could still excite the device area under the pad of Ag. Finally, 50 nm of Al was deposited using a separate mask to cover the corner ends of the pads for electrical contacting. The 50 nm of Al was necessary because the Ag was found to be stripped during the RIE removal step of the silicon nitride layer. Following evaporation of all the layers, a 1 cm x 1 cm quartz piece edge-lined with UV-curable epoxy was used to encapsulate the organic layers at the center of the device, while still enabling contacting through the exposed electrode corners. The final top surface of the device is shown in Figure 6-3.

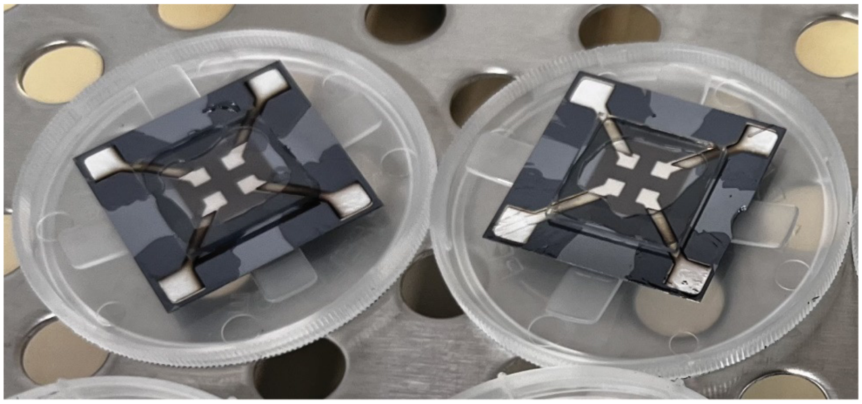

Figure 6-3. Optical image showing the top surface of the silicon-tetracene heterojunction solar cells.

6.2.2.7. Reactive ion etching (RIE)

A silicon nitride layer was deposited to protect the back-side electrode during the second RCA cleaning step. For electrical measurements, the silicon nitride layer was removed through a reactive ion etching process for contacting access to the back electrodes. Prior to the etching step, the chamber was cleaned using a NF3 cleaning step, followed by chamber priming with SF6. The thickness of the final device stack (with the encapsulating quartz) and the thin silicon did result in some degree of warping when the chamber was pumped down to vacuum.

6.2.3. Fabrication of interdigitated-back-contacted solar cells

Interdigitated-back-contacted solar cells were obtained from collaborators at UNSW. To protect the back contacts during RCA clean, we deposited 300 nm of SiN on the back side and performed a modified RCA clean. Then, we deposited a 2 Å-thick AlO_x passivation layer. ZnPc and Tc layers were thermally evaporated in a vacuum chamber at a pressure of $< 1 \times 10^{-6}$ torr. 1.5 nm of ZnPc was deposited at a 0.2 Å/s rate, followed by 30 nm of Tc deposited at a 1 Å/s rate. Thickness calibrations were obtained from ellipsometry measurements. The samples were then encapsulated in a dry nitrogen atmosphere (< 1 ppm O_2) with a glass slide and ultraviolet curable epoxy. A small piece of foil was placed to protect the active area during the UV exposure for the curing step. For electrical contacting, a custom weighted-shadow mask was applied during the RIE process for removing the back side SiN so that only the electrode pads were exposed.

6.2.4. Electrical device measurements

6.2.4.1. Electrical measurements

Current-voltage characteristic curves were obtained using a Newport Orel class A solar simulator (Model 91159) under AM 1.5G illumination. The incident flux was calibrated using a reference Si solar cell from Newport (Model 91150-KG5). The solar cells were measured from –1.0 to 1.0 V at 25 °C in air. External quantum efficiency measurements were performed using a 150 W xenon lamp coupled to a Newport monochromator. The light output from the monochromator was mechanically chopped at a frequency of 330 Hz and the photocurrent from the device was measured through a lock-in amplifier. The light input intensity was measured using a Newport photodetector, responsivity calibrated by Newport. Reverse bias measurements were performed by adding a Keithley 2400 Source Meter in the circuit.

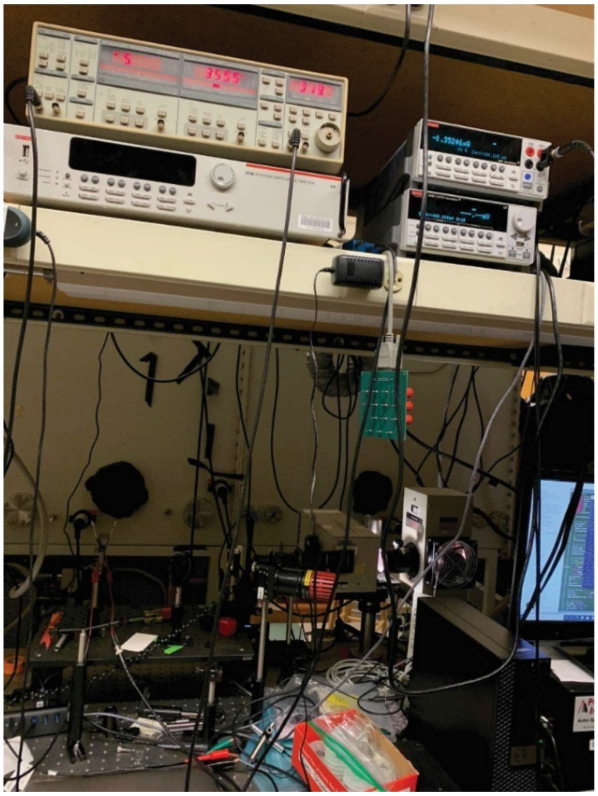

Figure 6-4. Experimental setup of reverse bias measurement. Note the electrical connections and configuration of the lock-in amplifier, the Keithley source meter, the metal contacting for grounding the circuit and the device in the sample holder.

6.2.4.2. Magnetic field-dependent measurements

Magnetic field-dependent measurements were obtained by mounting the solar cell between two poles of an electromagnet. The cell was excited using a frequency-chopped 200 mW 532 nm continuous wave laser (Coherent Verdi G18) and the frequency input was connected to a lock-in amplifier (Stanford Research Systems). For photoluminescence measurements, the silicon emission was collected using a Newport 818-IR detector, with 900 nm and 1000 nm longpass filters in front of the detector to ensure collection of only the silicon photoluminescence. For photocurrent measurements, the solar cell was connected to the lock-in amplifier in voltage-mode using a 50 Ω resistor in parallel to avoid saturation of the signal on the amplifier. The electromagnet was periodically switched on and off at different field strengths for 4-cycle loops at each field strength to obtain the measurements. The magnetic field strengths were measured by a gaussmeter (Lakeshore HMMT-6J04-VF).

6.2.5. Transmission Electron Microscopy (TEM) cross-sections

For cross-sectional TEM imaging of the layers in the device stack for the heterojunction cell, an equivalent device stack sample was prepared without any shadow masks and encapsulation. A layer of platinum was deposited on top of the solar cell just before preparation of the lamella cross-section cut from the device to protect the layers. To analyze the chemical composition of the device structure, energy-dispersive X-ray spectroscopy (EDS) was performed along the device cross-section.

TEM cross-sections were also attempted to be collected for planar shallow junction silicon samples tested in Chapter 7 of this thesis (similar in structure to the samples shipped to Princeton for UPS). For those samples, as there were no top-contacts above the tetracene layer, 30 nm of gold (Au) was deposited on the sample surface to ensure good electrical conductivity for FIB/SEM preparation of the cross-section cutting. However, there was insufficient protection of the organic layers, even with the additionally deposited platinum layer, and the cross-section revealed pockets of space where the organic layers were wicked away during the FIB process (Figure 6-5 and Figure 6-6). Thus, any future attempts to collect TEM cross-sections on non-device structures will need a protective layer above the tetracene, or a different technique to prepare the cross-sections that does not damage the organic layers.

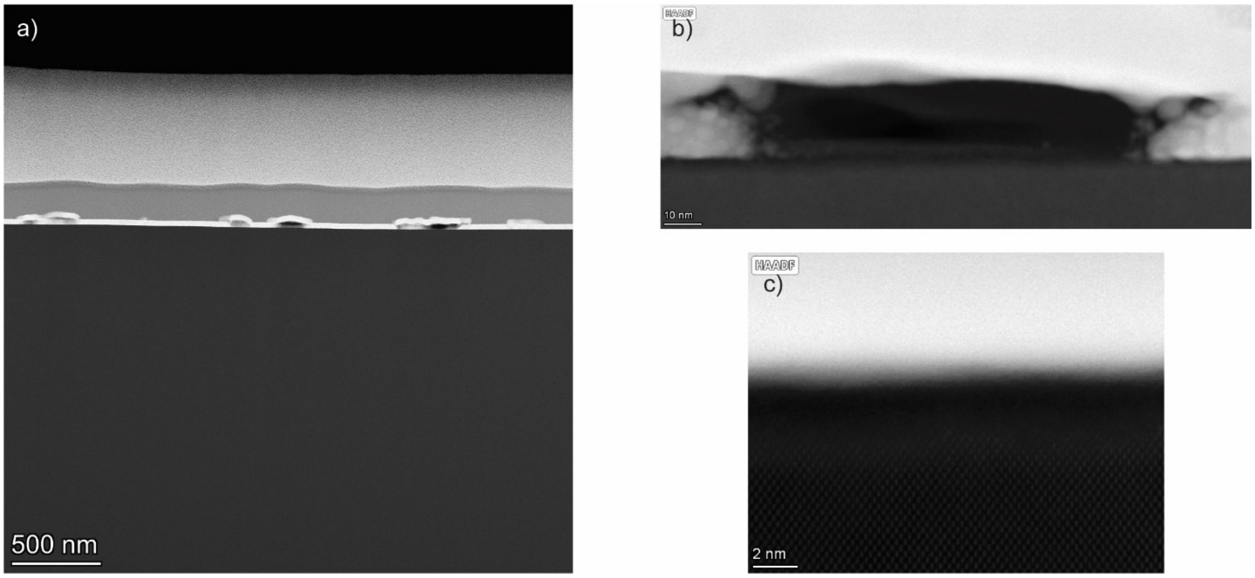

Figure 6-5. Cross-sectional TEM images obtained for structures of silicon/1 nm AlO_x/1.5 nm ZnPc/30 nm Tc/30 nm Au/thick Pt. b) and c) are close up images of the pocket and flat regions respectively.

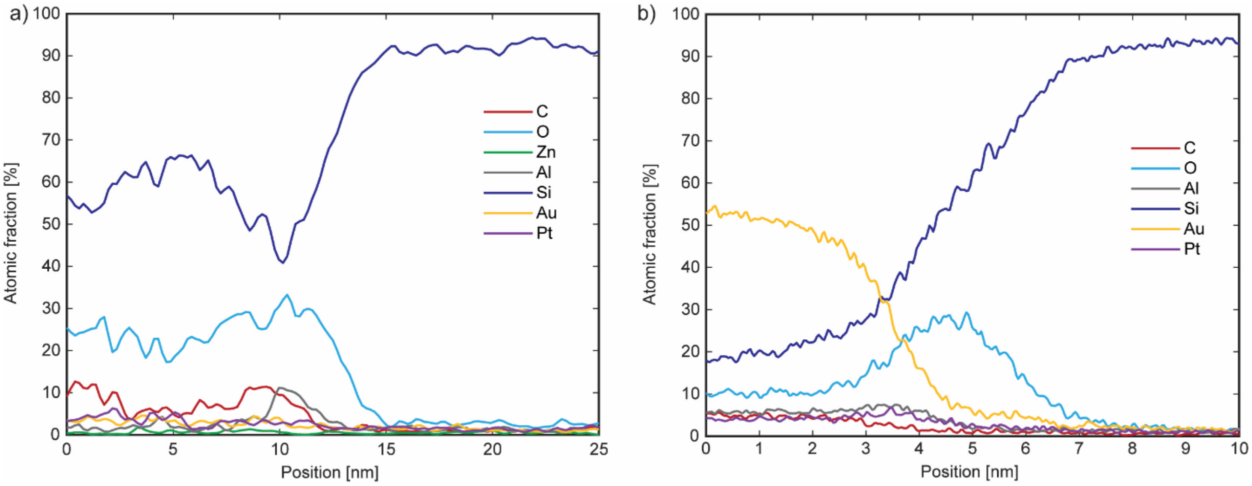

Figure 6-6. Cross-sectional elemental composition profiles obtained from the TEM cross-sections corresponding to the a) pocket and b) flat regions imaged in Figure 6-5.

6.3. Results and discussion

Observing peaks that correspond to the absorption spectrum of tetracene in electrical device measurements (external quantum efficiency, internal quantum efficiency) are unambiguous indications of triplet exciton transfer to the silicon. Depending on the doping concentration of the silicon, the exact alignment of the silicon band edge and zinc phthalocyanine molecular orbital levels may align differently. For example, the alignment may be such that the electron can transfer from the triplet exciton to silicon but the hole encounters an energetic barrier for transfer to silicon. In this case, instead of relying on full triplet transfer to silicon, using a silicon-tetracene heterojunction cell structure where the triplet exciton is dissociated at the interface, with the electron being transported through silicon to the bottom contact and the hole transported through the top organic layers to the top contact may be more ideal for extracting the carriers from the triplet exciton[46,120]. In this cell, the p-n junction is formed across the tetracene-silicon interface. The cell structure used in this work is presented in Figure 6-7a.

On the other hand, if the energy level alignment is such that transfer of the full triplet exciton to silicon is favored, applying the tetracene layer as an optical coating to an existing cell is preferred. One possible solar cell configuration where deposition of the singlet fission enhancement layers is simple is the interdigitated-back-contacted cell structure, shown in Figure 6-7b[35,47]. In this cell, the top surface of the silicon is as close to the optical devices presented in Chapter 5, and the electrodes are all located on the back side, resulting in minimal shadowing losses from the top surface[178,179]. The p-n junction is lateral relative to the plane of the device, and is located on the back-side of the cell. Hence, a thin silicon wafer is preferred for collecting carriers absorbed in the surface of the silicon layer.

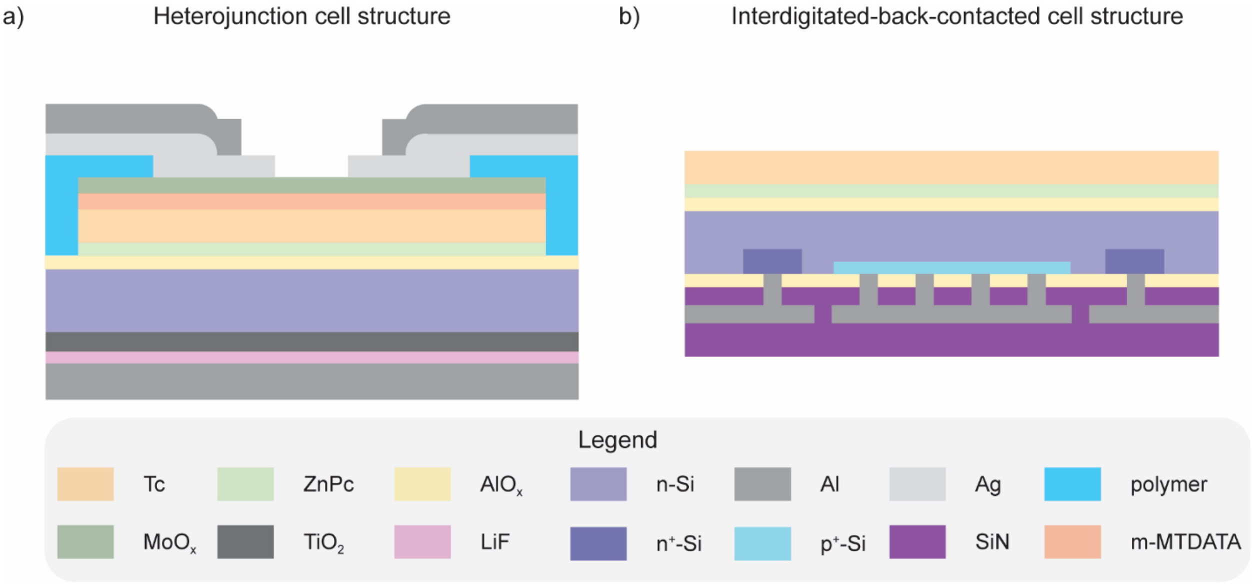

Figure 6-7. Solar cell architectures tested in this work. a) A heterojunction cell structure where the p-n junction is formed between the silicon and tetracene layers. b) An interdigitated-back-contacted cell structure where the contacts are on the back side and the tetracene acts as a top coating for the cell. The p-n junction is formed towards the back side of the cell.

6.3.1. Heterojunction cell studies

We fabricate silicon-tetracene heterojunction cells as detailed in Section 6.2 and measure their electrical characteristics, as presented in Figure 6-8.

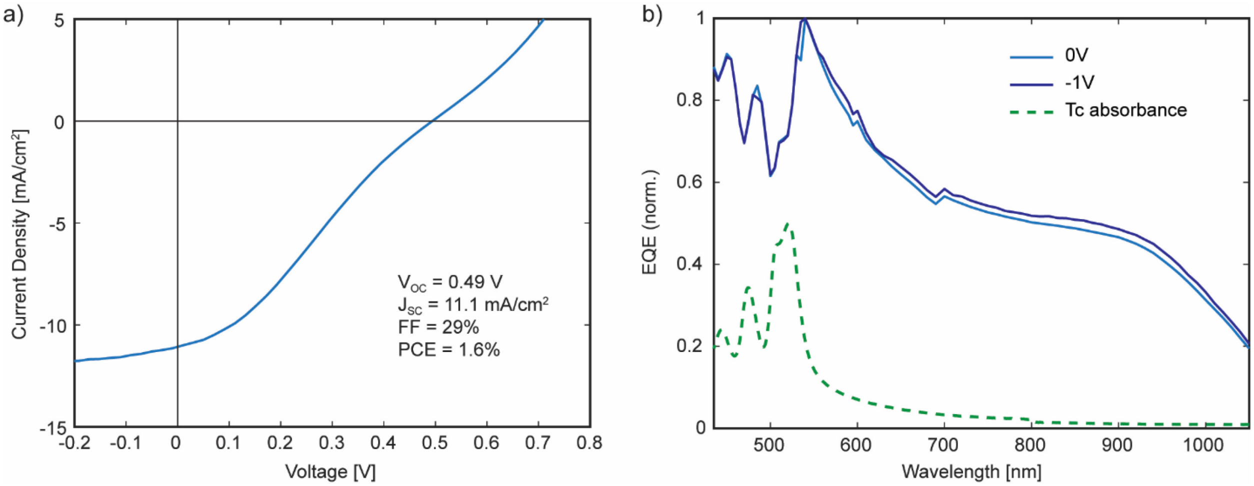

Figure 6-8. a) Measured J-V characteristic curve of a silicon-tetracene heterojunction cell with the zinc phthalocyanine and aluminum oxide interlayer structure. Calculated solar cell parameters are also listed nested within the plot. b) Normalized EQE curves measured for silicon-tetracene heterojunction cells with different applied voltages to the cell. The tetracene absorption spectrum is also plotted alongside for reference in dashed green.

Notably, we observe poor fill factor performance of the heterojunction cell and a “S-kink” type curvature in the device J-V curve. The curvilinear feature in J-V curves has previously been attributed to defects and band edge misalignment between the hole transport layer and perovskite junction for $CsPbI_3$ perovskite solar cells[180], and high conduction band offset in CdTe solar cells[181]. In our system, it is likely that the band alignment of the layers is not completely favorable for normal operation as a standard solar cell, although further measurements of the actual alignment of material energy levels using ultraviolet photoelectron spectroscopy will be necessary to confirm this.

Additionally, in the EQE measurements, we observe dips in the spectrum that correspond to the absorption spectrum of tetracene in Figure 6-8b. This indicates that the tetracene is parasitically absorbing the light, providing no benefit to the silicon device performance through fission. Applying a reverse bias to a solar cell can increase extraction of carriers; previous work has shown a switch from triplet-charge annihilation characteristics to fission characteristics upon application of a reverse bias[79]. However, our normalized EQE spectra with and without a reverse bias show minimal differences in the tetracene absorption region.

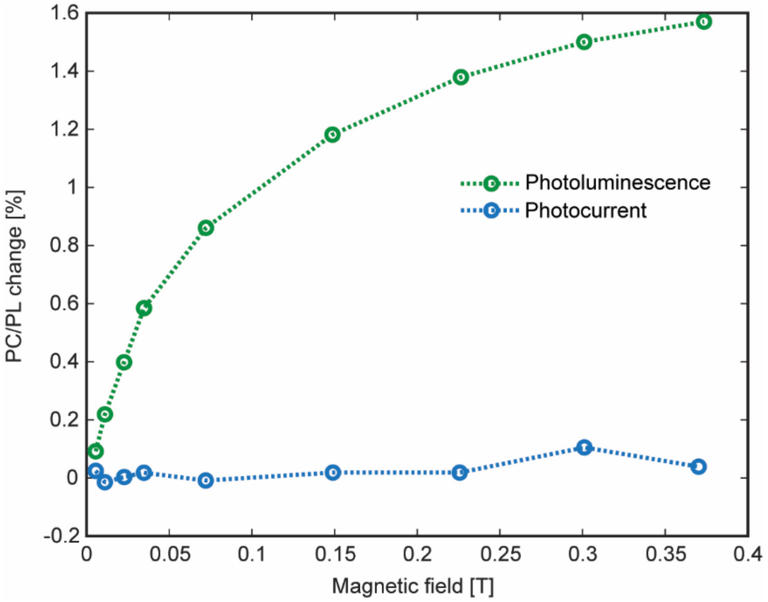

Figure 6-9. Magnetic field-dependent photoluminescence change (green) and photocurrent change (blue) measured in the silicon-tetracene heterojunction devices.

We also measure magnetic field-dependent photocurrent change and photoluminescence change of the devices, as shown in Figure 6-9. While the photoluminescence tracks the previously measured triplet-charge annihilation-like curves in the optical devices presented in Chapter 5, we note a lack of any clear features in the photocurrent measurements.

The electrical device measurements point to a lack of tetracene triplet-sensitization of the silicon cell in the heterojunction device. We perform cross-sectional TEM imaging of the heterojunction device to investigate the morphology and deposition of all the layers in the device stack (data courtesy of Collin F. Perkinson). In Figure 6-10a, we observe very large island-type growth of most-likely the tetracene layer, going from 0 to 60 nm in height, and around 400 nm in lateral size. Significantly, we also see regions where there is no tetracene at all (Figure 6-10c), with the top electrode making direct contact with the ZnPc/AlO_x/Si surface. The islanding (Volmer–Weber-type growth) has been previously reported for various silicon surfaces[120,182,183].

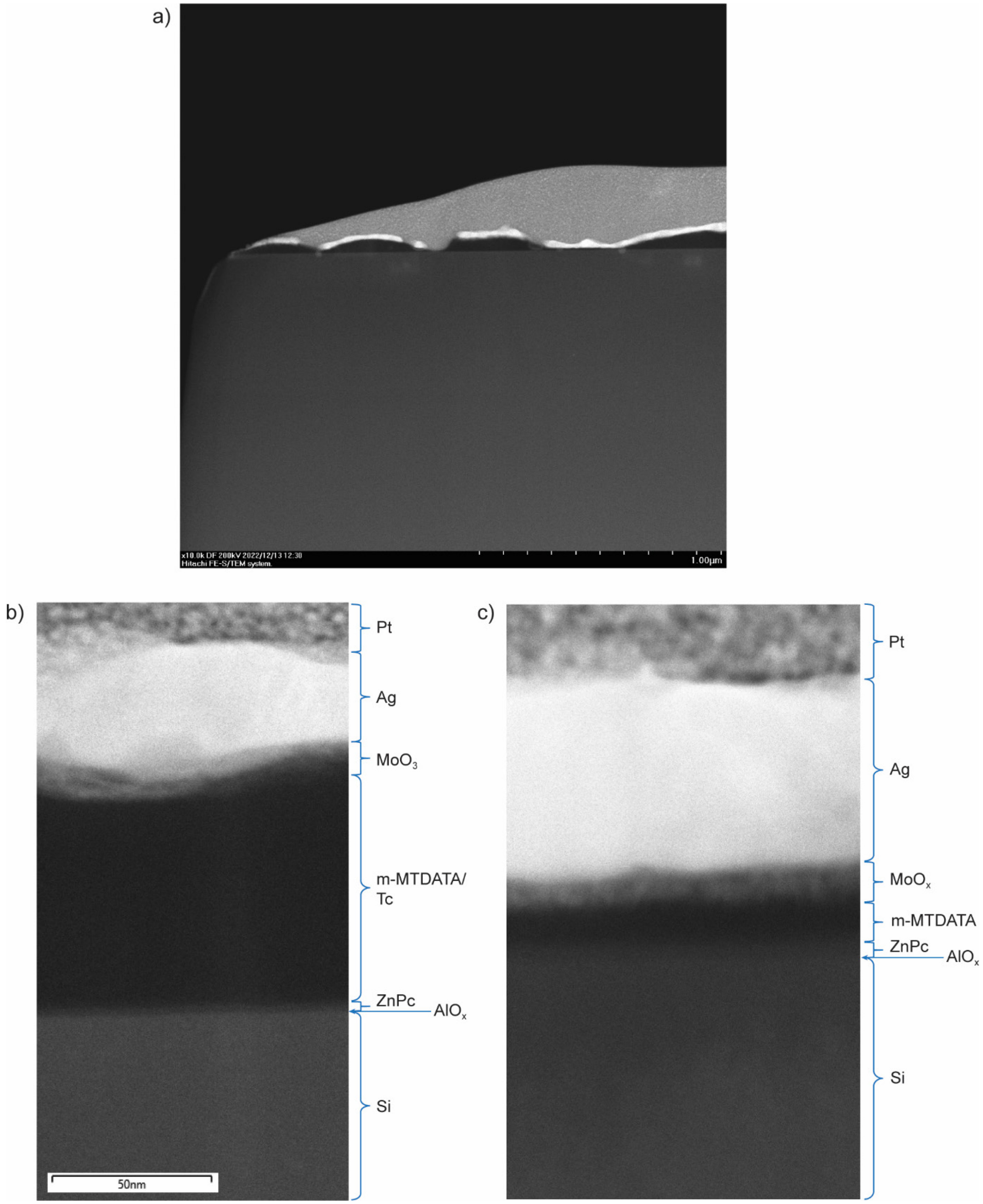

Figure 6-10. Cross-sectional TEM images obtained for the heterojunction solar cell. a) Visible uneven island-growth of tetracene. b) Close-up cross-section of tetracene island region. c) Close-up cross-section of region with no island. Layers were determined from composition analysis obtained through EDS measurements.

From these observations, we can make several comments regarding the ZnPc/AlO_x interface for silicon-tetracene heterojunction cells. First, the silicon-tetracene heterojunction structure is very sensitive to the morphology of the tetracene layer in the cell. Since this device relies on formation of the p-n junction between the tetracene and silicon layers, regions in the vertical stack with no tetracene may dominate the electrical characteristics of the device performance, which we see in the J-V characteristic curves (more akin to a Schottky diode formed between silver and silicon).

Second, applying a reverse bias to extract charge carriers more effectively did not appear to change the tetracene sensitization effect, as observed in the EQE. Magnetic field-dependent photocurrent measurements also show no feature of triplets in the device. One possible explanation is that the triplet excitons are getting quenched significantly at the silicon surface with large recombination losses. Due to the modifications in the RCA cleaning step introduced to process the top and bottom sides of the cell, the very thin aluminum oxide layer may not provide sufficient passivation of the silicon surface defects. The p-n junction formed between the silicon and organic layers may also not be sufficient to drive operation of the heterojunction cell as a good solar cell. Indeed, previous studies with singlet fission heterojunction cells[46,120] used a PEDOT:PSS layer that has been used for high efficiency silicon heterojunction cells[184,185]. However, our attempts at incorporating PEDOT:PSS into our device structure were unsuccessful, as the water-based solvent was incompatible with the tetracene layer. Additionally, the alignment of the energy levels may be such that the triplet excitons are not dissociating at the interface. In this case, the preferred structure of the cell would use tetracene as a top optical layer. Thus, we move our efforts to interdigitated-back-contacted solar cells as a platform for studying the ZnPc/AlO_x interface.

6.3.2. Interdigitated-back-contacted cell studies

Interdigitated-back-contacted (IBC) cells with the structure shown in Figure 6-7b were fabricated. To avoid previous complications with back-contact protection and surface damage from PDMS as reported previously[35], we deposited an additional 300 nm of SiN to protect the back contacts during the RCA-clean step. We also perform a modified RCA clean as opposed to the regular clean to avoid SiN corrosion. Following deposition and encapsulation of the top-side surface, we use a custom-weighted shadow mask (Figure 6-11) to etch only the electrode pads during the RIE process.

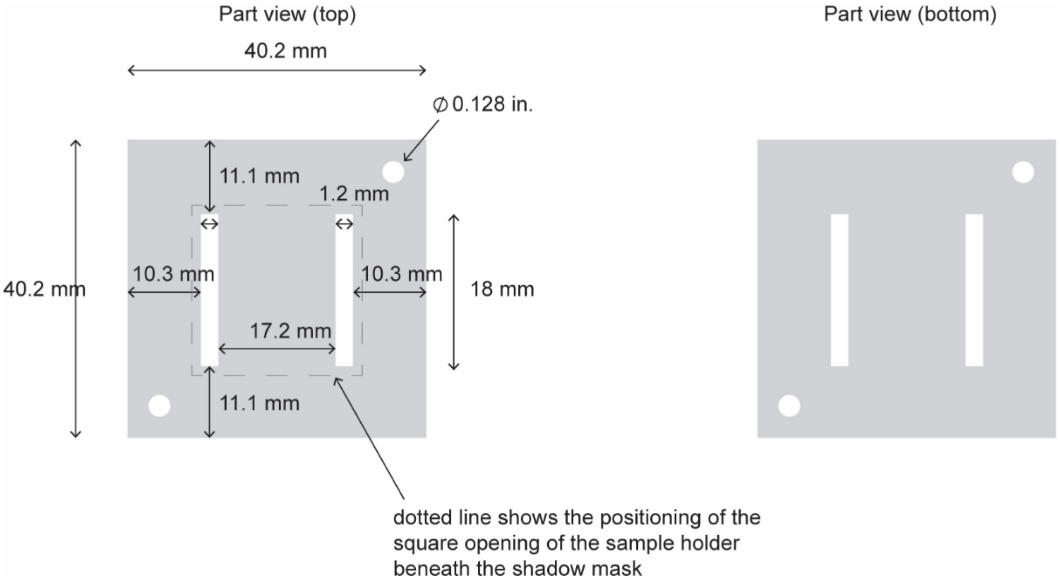

Figure 6-11. Custom designed shadow mask for RIE etching of the back-side SiN protective layer.

Device EQE and magnetic field-dependent measurements were measured, presented in Figure 6-12. The IBC cells with tetracene show clear shadowing in the EQE spectra in the absorption region of tetracene, indicating that the triplet sensitization effect on the photocurrent is minimal. While the optical results presented in Chapter 5 suggest successful triplet transfer from the tetracene to silicon, it is interesting to note the difference in the excitation scan PL measurements from the device photocurrent measurements.

Looking to the magnetic field-dependent studies in Figure 6-12b, we notice that unlike the heterojunction cells, we can recover a triplet-charge annihilation characteristic curve in the photocurrent, although the magnitudes of the change are smaller than in the photoluminescence measured simultaneously from the device surface.

To understand the differences between the photocurrent and photoluminescence measurements, we consider several hypotheses. The first is that the photoluminescence measurements are more sensitive to the surface of the silicon as opposed to the photocurrent measurements for IBC cells specifically. One possible reason for this could be that the contacts for the IBC cells are located on the backside, and because the triplet excitons are expected to transfer primarily to the top region of the silicon wafer, the transferred carriers have to travel to the backside before they are collected by the electrodes.

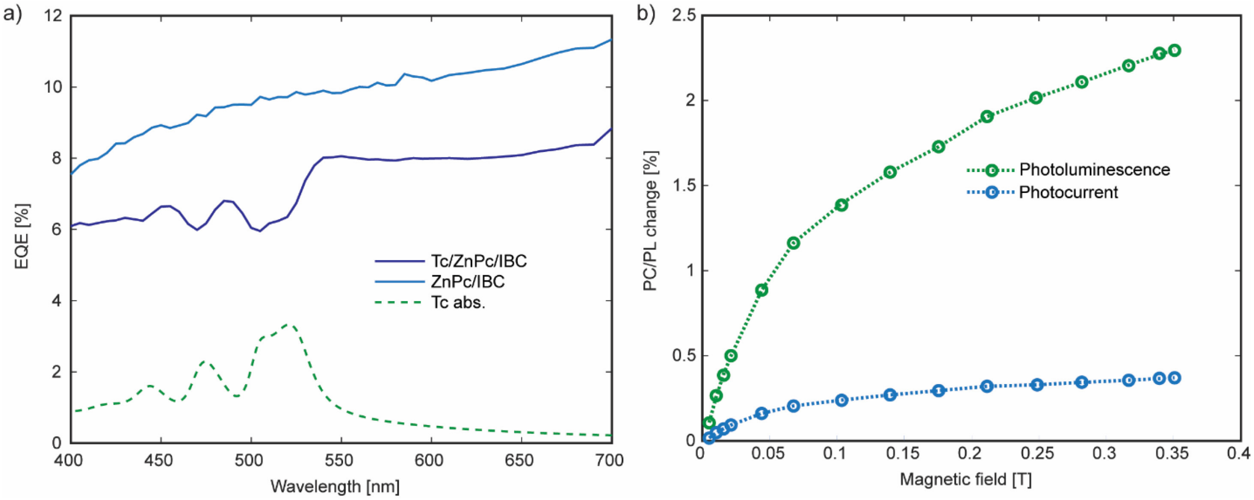

Figure 6-12. a) External quantum efficiency measurements of IBC solar cells with ZnPc (light blue) and Tc/ZnPc (dark blue) deposited on the top surface. The tetracene absorption spectrum is included (dashed green) for comparison. b) Magnetic field-dependent photoluminescence (green) and photocurrent (blue) change measured for the Tc/ZnPc/IBC cells.

Another possible hypothesis for the dips in the EQE spectra could be from poor surface passivation by the AlO_x layer. In the optical devices, the surfaces undergo a full RCA clean, but in order to protect the back contacts, we do a modified RCA clean. We also only use 2 Å of non-stoichiometric AlO_x, and as shown in Chapter 4, oxygen vacancies could result in mid-gap states that are detrimental to the overall silicon solar cell performance.

6.4. Conclusion

In conclusion, we attempt to sensitize silicon solar cells with singlet fission by implementing the ZnPc/AlO_x two-part interface into silicon-tetracene heterojunction cells and interdigitated-back-contacted silicon cells. The heterojunction cells show little evidence of triplet sensitization of the silicon photocurrent, most likely due to the poor p-n junction formed between tetracene and silicon in the device structure as well as the uneven morphology of the tetracene layer. Regardless of full triplet transfer or triplet dissociation, it is recommended to use a device structure that has the singlet fission layer purely as an optical top layer since the p-n junction formed between tetracene and n-Si is not optimal for device performance.

Additionally, the interdigitated-back-contacted cell measurements show that careful solar cell design is necessary for observing triplet exciton enhancement effects in the photocurrent. Instead of a lateral p-n junction located at the back side of the cell, future singlet-fission-sensitized silicon cells should incorporate a vertical p-n junction that lies closer to the surface of silicon with the singlet fission layer, so that the carrier diffusion length can be minimized and overall bulk recombination losses reduced.

Chapter 7.
Exciton fission enhanced silicon solar cells

The basis of this chapter has been adapted from:

Narumi Nagaya†, Kangmin Lee†, Collin F. Perkinson†, Aaron Li, Youri Lee, Xinjue Zhong, Sujin Lee, Leah P. Weisburn, Tomi K. Baikie, Moungi G. Bawendi, Troy Van Voorhis, William A. Tisdale, Antoine Kahn, Kwanyong Seo, Marc A. Baldo. "Exciton Fission Enhanced Silicon Solar Cell." *Submitted* (2024)

† These authors contributed equally.

7.1. Introduction

Silicon solar cells dominate the global photovoltaic market, due to their high efficiencies and low manufacturing costs. It has been proposed that the performance and adoption of silicon solar cells can be further improved by supplementing conventional single-junction cells with singlet exciton fission to generate two electrons from each blue and green photon in sunlight[27]. Singlet fission enhanced silicon solar cells can exceed the efficiency of traditional silicon technologies while exhibiting the simplicity and practical advantages of a single-junction architecture.

Single-junction crystalline-silicon solar cells are rapidly approaching their theoretical efficiency limit of 29%[13]. As in Figure 7-1a, however, there are substantial opportunities to improve performance if thermalization losses can be reduced in the visible and UV spectrum. For example, using singlet exciton fission in Tc to double the available carriers obtained from blue and green sunlight could increase the power conversion efficiency of a single-junction crystalline-silicon solar cell to 35%[28].

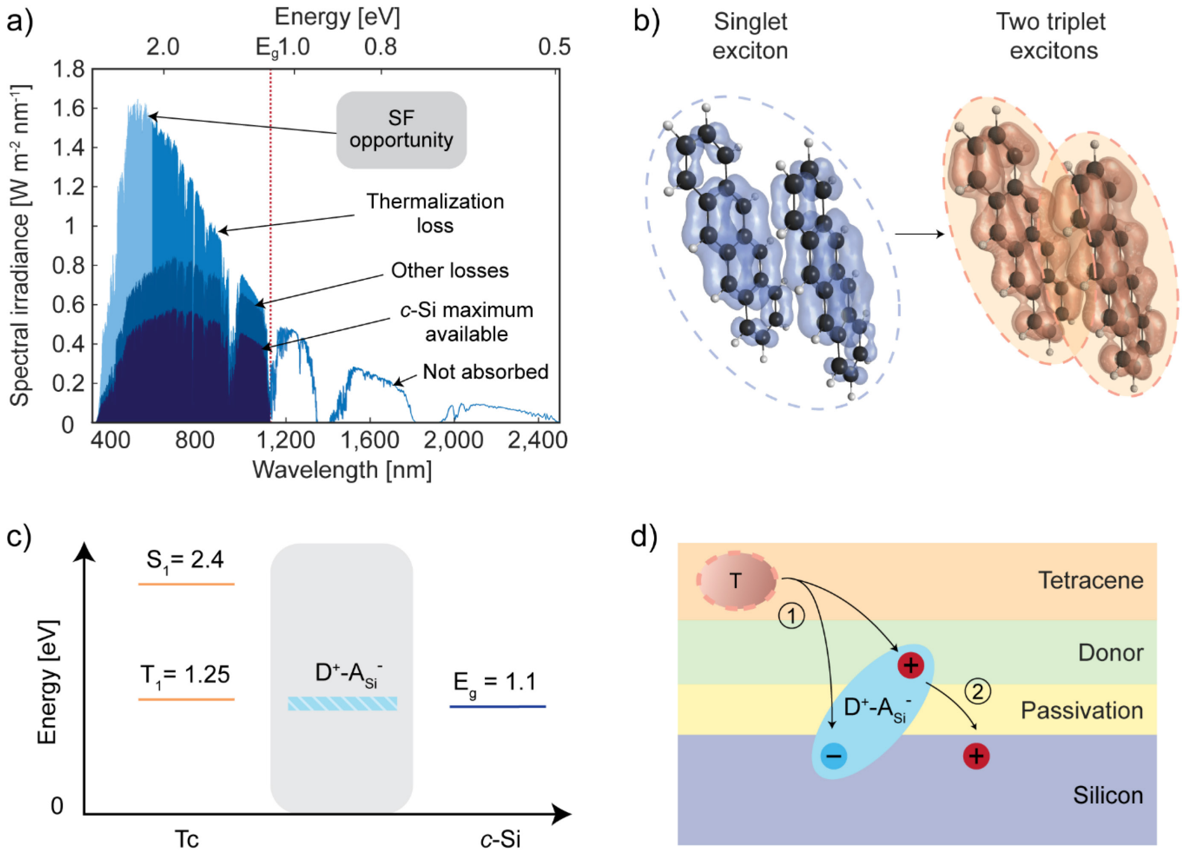

Figure 7-1. Singlet exciton fission and a two-part interface design for coupling to silicon. a) The AM1.5G solar spectrum compared to the optical absorption range of crystalline-silicon (*c*-Si). The red dotted line indicates the bandgap of *c*-Si. The portion of the spectrum to the right of the bandgap is not absorbed. To the left of the bandgap are spectral regions of the solar spectrum that are representative of energy pathways within a single-junction silicon cell at the efficiency limit. These regions correspond to photons that are available to *c*-Si, other losses[2], the thermalization loss, and the opportunity for singlet fission-enhanced *c*-Si devices, respectively shaded from darkest to lightest blue. b) A molecular picture of the singlet exciton fission process, showing the electron density of a delocalized singlet exciton over two Tc molecules in blue, and two product triplet excitons in orange. c) Generalized energetic requirements for the donor-acceptor state (D$^+$-A$_{Si}^-$) for charge injection into silicon. The D$^+$-A$_{Si}^-$ energy should ideally lie between the triplet exciton energy of tetracene (Tc) and the bandgap of silicon. d) The two-part interface design presented in this work. The interface consists of an electron-donating layer (green) and a passivation layer (yellow). The latter passivates silicon surface defects. We propose a sequential charge transfer mechanism: (1) the donor supports an initial electron transfer to silicon, forming D$^+$-A$_{Si}^-$ (light blue oval), followed by (2) a hole transfer from the donor to silicon, ultimately resulting in triplet energy transfer to silicon.

Singlet exciton fission in Tc generates two spin-1 triplet excitons with energies of 1.25 eV from one spin-0 singlet exciton with an energy of 2.4 eV[34]; see Figure 7-1b. Spin conservation opposes the thermalization of a singlet into one triplet exciton, protecting the process against losses and contributing to a near ideal yield in many fission materials, including Tc[34]. The triplet energy of Tc is just above that of the 1.1 eV band gap of crystalline-silicon (*c*-Si), which is ideal for coupling to *c*-Si. However, transferring the energy from the two excitons formed from one high energy photon absorbed in Tc to *c*-Si and observing device enhancements has proven challenging[29]. Depositing Tc directly onto hydrogen-terminated *c*-Si surfaces decreases the external quantum efficiency (EQE) of both silicon-Tc heterojunction solar cells and interdigitated back-contacted (IBC) solar cells[46,47]. Inserting LiF spacers[44,45] and pyrene passivation layers[125] between the Tc and silicon also does not yield efficient triplet energy transfer. Introducing a thin interlayer of HfO_xN_y between Tc and *c*-Si, however, shows sensitization of *c*-Si by triplet excitons, albeit without demonstrating an increase in the photocurrent of an IBC cell[35]. The HfO_xN_y interlayer is hypothesized to play a bifunctional role, acting to passivate some silicon surface defects whilst simultaneously enabling triplet exciton transfer[35].

7.2. Methods

7.2.1. Fabrication of tapered *c*-Si microwire arrays

The photoresist dot arrays (2 μm diameter, 1 μm spacing) were periodically patterned onto the *c*-Si wafer using AZ-nLOF-2035 photoresist (AZ Electronic Materials) *via* a photolithography process. The patterned *c*-Si wafer was then etched by deep reactive ion etching (DRIE, Tegal 200) with 1500 W source power, 100 W stage power, and 45 mTorr gas pressure using SF_6 (250 sccm) and C_4F_8 (150 sccm) as source gases. Following the DRIE process, cleaning was conducted using a piranha solution (3:1 mixture of sulfuric acid and hydrogen peroxide (30% w/w in H_2O)). To fabricate tapered *c*-Si microwires, the *c*-Si microwires were immersed in an $HF/HNO_3/CH_3COOH$ solution (RSE-100, Transene) for ~10 seconds.

7.2.2. Fabrication of tapered *c*-Si microwire solar cells

To fabricate n^+-p-type MWs, after the fabrication of the tapered p-type *c*-Si microwire array on the *c*-Si wafers, a back surface field (BSF) layer was formed in a tube furnace under a mixed atmosphere of O_2 (250 sccm) and N_2 (1000 sccm) at 980 °C using a boron spin-on-dopant source (B155, Filmtronics). Following the BSF layer formation, a SiO_2 layer was thermally grown on the wafer in a furnace. This SiO_2 layer was removed from the front of the substrate with a buffered oxide etchant (BOE) after the backside was protected with photoresist (AZ4330, AZ Electronic

Materials). Subsequently, an additional 200-nm-thick SiO_2 diffusion barrier was deposited on the rear side of the wafer via plasma-enhanced chemical vapor deposition (PEH-600). Next, an emitter layer was formed in a tube furnace under a mixed atmosphere of O_2 (125 sccm) and N_2 (500 sccm) at 800 °C using a phosphorus spin-on-dopant source (P509, Filmtronics). Then, after removing the oxide layer using BOE, SC1 and SC2 cleaning processes were conducted. An AlO_x passivation layer with a thickness of 1 nm was deposited on the front side of the wafer, while a 10-nm-thick Al_2O_3 layer was deposited on the rear side of the wafer via ALD (Lucida D100, NCD) and annealed under 500 sccm of a mixed gas of Ar/H_2 (v/v = 96:4) at 500 °C in a tube furnace. Patterns for the microgrid electrodes and localized back contact surface were formed on the front and rear sides of the wafer, respectively, via photolithography, using AZ4330 photoresist. For electrode fabrication, the wafer was immersed in a BOE solution, and 600 nm thick Al films were deposited on both sides of the wafer via thermal evaporation.

To fabricate p^+-n-type MW, after fabricating the tapered n-type *c*-Si microwire array on the *c*-Si wafers, the process was the same as for n^+-p-type MW, except for the BSF and emitter formation conditions. A BSF was formed in a tube furnace under a mixed atmosphere of O_2 (125 sccm) and N_2 (500 sccm) at 860 °C using a phosphorous spin-on-dopant source (P509, Filmtronics). Then, an emitter layer was formed on the front surface of the wafers under a mixed atmosphere of O_2 (250 sccm) and N_2 (1000 sccm) at 880 °C using a boron spin-on-dopant source (B155, Filmtronics).

7.2.3. Singlet fission top-side fabrication

Before deposition, the samples were dipped in acetone for 5 minutes, and then in IPA for 5 minutes at a low sonication power. Afterwards, the samples were dried with N_2 gas.

After cleaning, the samples were transferred into a nitrogen glovebox for deposition of the organic layers. ZnPc was purchased from Luminescence Technology Corp (sublimed grade, >99% purity) and used as received. Tc was purchased from Sigma Aldrich (sublimed grade, 99.99% trace metal basis) and purified once through a sublimation and recondensation process in a three-zone tube furnace before deposition. The organic layers were deposited by thermal evaporation in a vacuum chamber at a pressure of $< 1 \times 10^{-6}$ torr. 1.5 nm of ZnPc was deposited at a 0.2 Å/s rate, followed by 30 nm of Tc deposited at a 1 Å/s rate. Thickness calibrations were obtained from ellipsometry measurements performed on planar substrates. The surface area of the microwire substrates is much larger. Thus, the true area density of ZnPc (1.5 nm nominal thickness) and Tc (30 nm nominal thickness) in the microwire devices is expected to be lower. The samples were then encapsulated in a dry nitrogen atmosphere (< 1 ppm O_2) with a glass slide and ultraviolet curable epoxy. A small piece of foil was placed to protect the active area during the UV exposure for the curing step.

7.2.4. Photoelectron spectroscopy

Tc and ZnPc layers were deposited on AlO_x-silicon surfaces by thermal evaporation in an ultrahigh-vacuum chamber (10^{-9} Torr) connected to the analysis chamber. 1.5 nm of ZnPc was deposited at a rate of about 0.1 Å/s, followed by 20 nm of Tc at a deposition rate of about 1 Å/s. Then, ultra-violet and X-ray photoemission spectroscopy (UPS, XPS) measurements were conducted under ultrahigh vacuum conditions (10^{-10} Torr) at room temperature. UPS utilized He I photons (21.22 eV) emitted by a discharged lamp to determine the work function of the sample and the energy position of the ZnPc and Tc HOMO with respect to the Fermi level. The experimental energy resolution for UPS is typically 0.10 eV. The position of the Si valence band maximum (E_V), hidden by the organic and AlO_x overlayers in UPS, was determined from the position of the Si 2p core level following the Kraut method[186]. XPS was performed using non-monochromatized Al Kα X-rays (1486.70 eV). The Fermi level reference for all measurements was determined on a clean Au surface.

7.2.5. Device measurements

The current density–voltage curve of the fabricated solar cells was measured using a Newport Orel class A solar simulator (Model 91159) under AM 1.5G illumination. The incident flux was calibrated using a calibrated reference Si solar cell certified by Newport (Model 91150-KG5). The solar cells were measured from –1.0 to 1.0 V at a temperature of 25 °C in air. External quantum efficiency measurements were performed using a 150 W xenon lamp coupled to a Newport monochromator. The light output from the monochromator was mechanically chopped at a frequency of 330 Hz and the photocurrent from the device was measured through a lock-in amplifier. The light input intensity was measured using a Newport photodetector, responsivity calibrated by Newport. The surface morphology of the solar cells was characterized by SEM (Zeiss Merlin High-resolution SEM).

7.2.6. Modeling

The absorption of light by each of the layers in the complete device stack and the total reflection is simulated using the transfer matrix method[173]. The optical absorption of each layer in the Tc/ZnPc/n$^+$-p device is calculated for a stack with 30 nm of tetracene ($Abs_{Tc,Tc=30}$), 1.5 nm of zinc phthalocyanine ($Abs_{ZnPc,Tc=30}$), 1 nm of Al_2O_3 ($Abs_{Al_2O_3,Tc=30}$), and 180 µm of silicon ($Abs_{Si,Tc=30}$). As the control, we also calculate the optical absorption in each layer of an unsensitized n$^+$-p device consisting of 1 nm of Al_2O_3 ($Abs_{Al_2O_3,Tc=0}$), and 180 µm of silicon ($Abs_{Si,Tc=0}$).

To obtain the efficiency of tetracene sensitization, we analyze the percentage differential external quantum efficiency (EQE) ($\Delta EQE/EQE_0$) that results from coupling to tetracene. We define $\frac{\Delta EQE}{EQE_0} = \frac{EQE_{Tc} - EQE_0}{EQE_0}$, where EQE_0 is the silicon cell EQE before Tc and ZnPc deposition and EQE_{Tc} is the silicon cell EQE after Tc and ZnPc deposition.

Microwire cells are especially effective at absorbing incident light[133]. Consequently, we assume that total device reflection losses are negligible in the microwire cells such that device EQEs are approximately equivalent to the device internal quantum efficiencies (IQEs): $\frac{\Delta EQE}{EQE_0} \approx \frac{\Delta IQE}{IQE_0}$ with the subscripts as defined previously.

We assume IQE_0 can be described by:

$$IQE_0(\lambda) = \eta_{Si,Tc=0}(\lambda)\phi_{Si,Tc=0}(\lambda) \tag{7-1}$$

where $\eta_{Si,Tc=0}$ is the internal quantum efficiency of the silicon without the deposited organic layers and $\phi_{Si,Tc=0}$ is the simulated fractional absorption of the silicon layer relative to the total device stack absorption without the deposited organic layers, $\phi_{Si,Tc=0} = \frac{Abs_{Si,Tc=0}}{\sum Abs_{l,Tc=0}}$. All optical absorption simulations are performed in a planar geometry using optical constants experimentally determined in the planar geometry.

Next, we assume that IQE_{Tc} can be described by:

$$IQE_{Tc}(\lambda) = \eta_{Si,Tc=30}(\lambda)\phi_{Si,Tc=30}(\lambda) + \eta_{Tc}\phi_{Tc,Tc=30}(\lambda), \tag{7-2}$$

where $\eta_{Si,Tc=30}(\lambda)$ is the internal quantum efficiency of the silicon with the deposited organic layers, η_{Tc} is the tetracene sensitization efficiency (ranging from 0 to 200%, encompassing efficiency of singlet fission, triplet exciton transport, triplet exciton transfer, and extraction of transferred carriers to silicon), $\phi_{Si,Tc=30}$ and $\phi_{Tc,Tc=30}$ are the simulated fractional absorption of the silicon and tetracene layers, respectively. We treat the tetracene contribution to the IQE as a separate additional term, because we expect the extraction of carriers absorbed by the silicon cell directly to differ from the extraction of transferred carriers from tetracene.

Then, we arrive at the expression:

$$\frac{\Delta EQE(\lambda)}{EQE_0(\lambda)} \approx \left(\frac{\eta_{Si,Tc=30}(\lambda)\phi_{Si,Tc=30}(\lambda)}{\eta_{Si,Tc=0}(\lambda)\phi_{Si,Tc=0}(\lambda)} + \frac{\eta_{Tc}\phi_{Tc,Tc=30}(\lambda)}{\eta_{Si,Tc=0}(\lambda)\phi_{Si,Tc=0}(\lambda)}\right) - 1. \tag{7-3}$$

Since we are interested in the relative effect of adding the organic layers to the device stack, we set $\eta_{Si,Tc=0} = 1$. Then, to obtain a lower bound for η_{Tc}, we also assume $\eta_{Si,Tc=30}(\lambda = 520\ nm) = 1$ (*i.e.* that the deposition of organic layers does not affect the passivation quality of the silicon surface). Finally, we fit for η_{Tc} at λ = 520 nm. The simulated $\frac{\Delta EQE(\lambda)}{EQE_0(\lambda)}$ is presented for different η_{Tc} values in the main text Fig. 4c, showing an optimal fit for $\eta_{Tc} = 138\%$. As noted in earlier, the material optical constants and experimental thickness calibrations are obtained from ellipsometry measurements performed on planar substrates. Consequently, the true area density of ZnPc (1.5 nm nominal thickness) and Tc (30 nm nominal thickness) in the microwire devices is substantially lower, leading to an overestimate of $\phi_{Tc,Tc=30}$ and an interpretation of fits for η_{Tc} as a lower bound.

A similar analysis can be carried out for the other microwire device structures that are studied in this work. Table 7-1 summarizes the obtained fit parameters for η_{Tc} in different device structures. Uncertainty ranges are calculated from the maximum and minimum fit values for η_{Tc} across the tetracene absorption region (λ = 415 – 545 nm).

Table 7-1. Fitted tetracene sensitization efficiency values for each microwire device structure investigated in this work.

Device structure	**η_{Tc} (%)**
n^+-p Si MW (1 nm AlO_x)	138 ± 6
p^+-n Si MW (1 nm AlO_x)	25 ± 42
n^+-p Si MW (10 nm Al_2O_3)	47 ± 45
n^+-p Si MW (1 nm AlO_x, no ZnPc)	74 ± 28
p^+-n Si MW (1 nm AlO_x, no ZnPc)	28 ± 43

We observe that the assumption of a wavelength-independent internal quantum efficiency for silicon ($\frac{\eta_{Si,Tc=30}(\lambda)}{\eta_{Si,Tc=0}(\lambda)} = 1$) only yields good fits for the n^+-p Si MW (1 nm AlO_x) devices. Allowing $\frac{\eta_{Si,Tc=30}(\lambda)}{\eta_{Si,Tc=0}(\lambda)}$ to vary results in the following values for $\frac{\eta_{Si,Tc=30}(\lambda)}{\eta_{Si,Tc=0}(\lambda)}$, presented in Figure 7-2. The apparent reduction in silicon quantum yield at shorter wavelengths is consistent with a deterioration in silicon passivation. This suggests that adding the organic layers may degrade the passivation quality for the devices that do not show transfer.

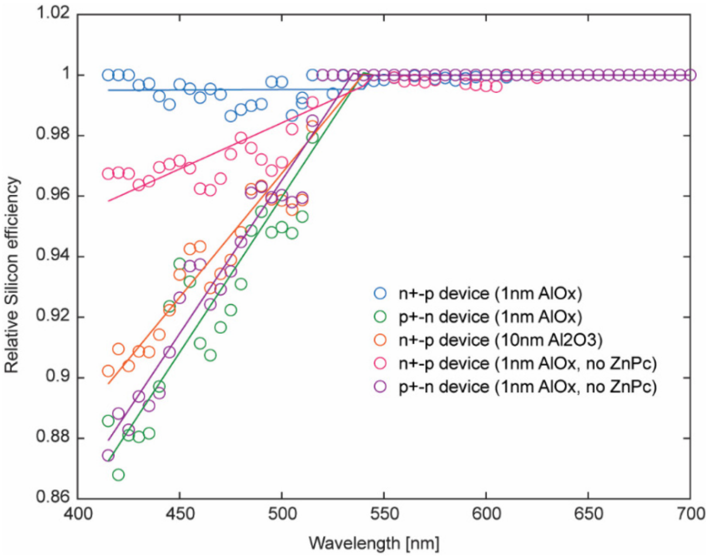

Figure 7-2. The circles show the relative silicon efficiencies $\frac{\eta_{Si,Tc=30}(\lambda)}{\eta_{Si,Tc=0}(\lambda)}$ obtained from fitting the model to the data and setting η_{Tc} to a fixed value presented in Table SC1. A piecewise linear fit from λ = 415 – 545 nm, and from λ = 550 – 700 nm is used to obtain the lines.

We also notice that the device passivation quality is degraded in the blue-green wavelength region when silicon doping is shifted. This drop in passivation quality for three different control silicon solar cells is presented in Figure 7-3, where the functional form of $a(wavelength - b)^c$ was used to fit alongside the tetracene absorption spectrum. The fits are negative as the device EQE shows dips corresponding to absorption from tetracene. We use the swapped doping control (p^+-n Si), the 10 nm Al_2O_3 control and the no ZnPc layer control. The first device has a state in the middle of the gap of silicon. This is most detrimental to the passivation of the device as the mid-gap state can quench the silicon carriers. As a result, we see the curve decays the most at low wavelengths (closer to the surface). The second device should in theory have the best traditional passivation quality, however it is unsuitable for a tunneling process, and has the wrong type of fixed charge for n-doped silicon. Additionally, carriers cannot tunnel from the triplet exciton in ZnPc to form the dynamic passivation. Finally, the device with no ZnPc should have less triplet-driven passivation compared to the device with ZnPc due to the non-ideal energy level alignment. Hence, we also see a corresponding decay at low wavelengths, although to a lesser degree compared to the other control devices.

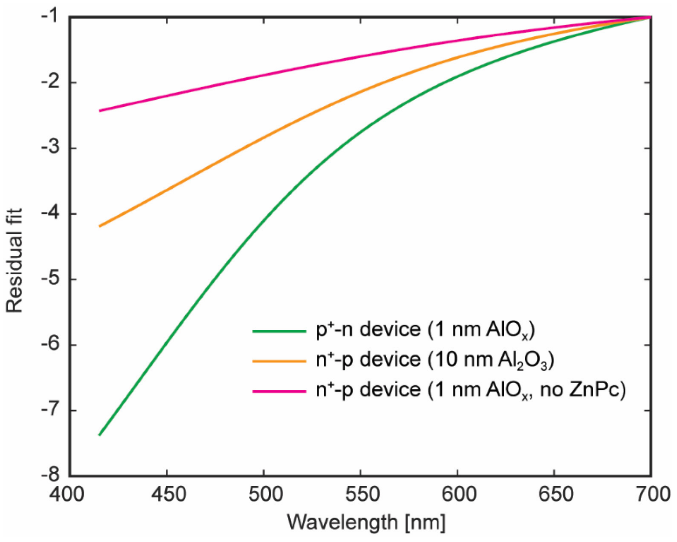

Figure 7-3. Fits obtained for $a(wavelength - b)^c$ of three different control devices where $a(wavelength - b)^c \times Tc\ absorption$ is fitted to the change in EQE with added organic layers (ΔEQE).

7.3. Results and discussion

7.3.1. Zinc phthalocyanine as a donor material

Here, we propose a two-component interface for efficient triplet exciton sensitization of *c*-Si. Our approach is guided by the apparent ineffectiveness of previous efforts to directly transfer triplets from Tc to *c*-Si via a Dexter mechanism[44,45]. We instead design our cells based on the observed coupling between Tc and *c*-Si across thin HfO_xN_y interfaces[35]. We correlate evidence of triplet transfer with the presence of midgap defect states in HfO_xN_y, suggesting the possibility of sequential charge transfer via an intermediate charge-separated state supported by HfO_xN_y (as presented in Chapter 4). Consequently, we propose to mediate sensitization with an initial charge transfer to silicon[35,120], followed by a sequential transfer of the remaining charge carrier. The energy of the intermediate charge-separated state must lie between the triplet energy of Tc (1.25 eV) and the bandgap of silicon (1.1 eV). Tc itself is an electron donor[68], but at least in previously studied interfaces, its highest occupied molecular orbital (HOMO) is too deep to support a charge-separated state within the necessary energy range. Therefore, we propose to insert an additional electron donor at the interface with silicon that supports a state D^+-A_{Si}^- with the appropriate energy, where D^+ represents the charged electron donor and A_{Si}^- describes the electron accepting role of silicon as in Figure 7-1c.

The second component of our interface is a thin passivation layer necessary to prevent the transferred charge carriers from immediately recombining at the silicon surface, while still enabling carrier tunneling; see Figure 7-1d. Aluminum oxide (AlO_x) is commonly used to passivate silicon solar cells[187]. In this work, we use approximately 1-nm-thick layers of AlO_x to both passivate the silicon surface and maintain charge tunneling across the interface.

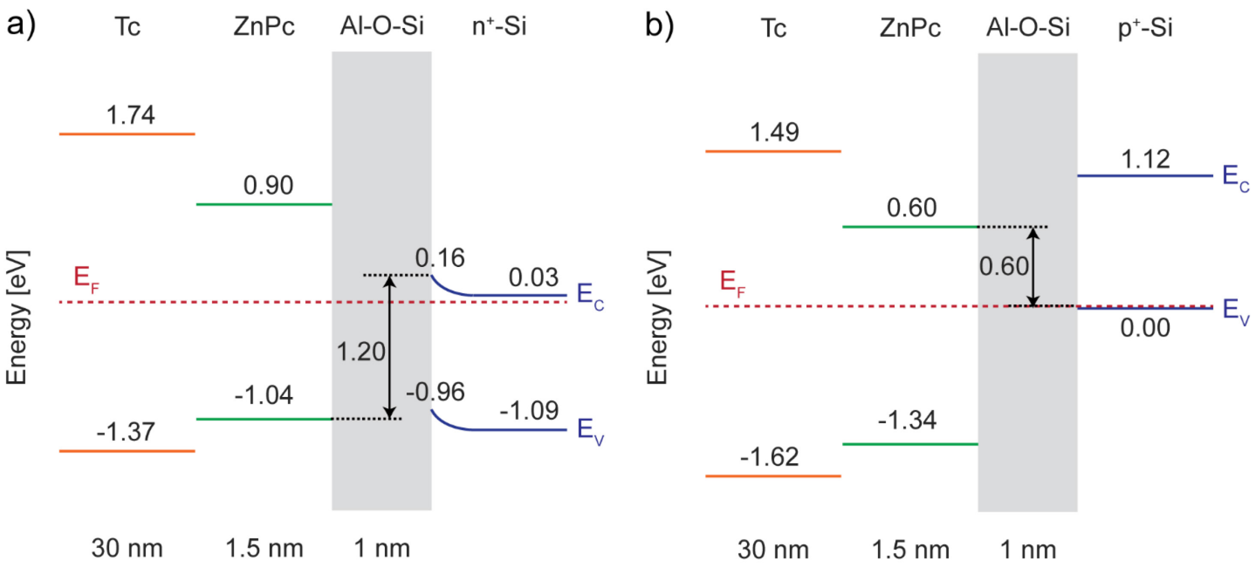

Figure 7-4. Energetic alignments of Tc/ZnPc interfaces on n^+-doped and p^+-doped *c*-Si. Summary of band alignments for tetracene (Tc), zinc phthalocyanine (ZnPc) and aluminum oxide (AlO_x) deposited on a) a highly n-doped silicon surface (n^+-Si), and b) a highly p-doped silicon surface (p^+-Si). The red-dashed line indicates the position of the Fermi level (E_F) of the system. The valence band maximum (E_V) and highest occupied molecular orbital (HOMO) positions with respect to E_F were measured using ultraviolet photoelectron spectroscopy. The conduction band minimum (E_C) and lowest unoccupied molecular orbital (LUMO) positions were calculated using the electronic band gaps from previous UPS and inverse photoemission spectroscopy measurements[35,167]. The experimental energy resolution for measurements is typically 0.10 eV. The bulk E_C and E_V positions of the doped silicon were calculated from the doping concentration. The black-dashed lines show the energy of the lowest-lying state at the interface between the ZnPc layer and *c*-Si: in a), the electron is located on E_C and the hole is located on the HOMO of ZnPc; in b), the electron is located on the LUMO of ZnPc and the hole is located on E_V. Nominal deposited thicknesses for the Tc, ZnPc and AlO_x layers are listed.

We study zinc phthalocyanine (ZnPc) as a candidate donor material at the Tc-Si interface. ZnPc is a common donor with a reported HOMO above that of Tc[167]. Our time-dependent functional theory (TDDFT) calculations and literature[188] show that the excited Tc triplet state is 0.1−0.2 eV higher in energy than the ZnPc triplet, potentially enabling triplet harvesting at the interface prior to the formation of a charge-separated state. Further calculations show that the Tc HOMO is 0.2 eV deeper than the ZnPc HOMO. We perform ultraviolet photoelectron spectroscopy to determine the energetic alignment of ZnPc at interfaces between Tc and *c*-Si. In Figure 7-4a, we summarize the alignments for a highly n-doped Si surface (n^+-Si). The difference between the *c*-Si conduction band minimum and the HOMO level of ZnPc is approximately 1.20 eV, within the allowed energetic range for the D^+-A_{Si}^- state, as depicted in Figure 7-1c. We neglect binding energy in the determination of the energy of the charge-separated state D_{ZnPc}^{+}-A_{Si}^{-} due to expected charge screening and delocalization in silicon[137,138]. Furthermore, there is minimal barrier for subsequent hole transfer to the bulk valence band of silicon, within measurement error. We observe a negligible difference in the Tc-Si energy alignment with and without the ZnPc layer. This confirms that the presence of the ZnPc layer lowers the energy of a donor-acceptor state with silicon, thereby enabling sequential charge transfer to silicon following triplet exciton formation (see Figure 7-5). In contrast, the energetic alignment with a highly p-doped silicon surface (p^{+}-Si) shown in Fig. 2b exhibits a significant electron transfer barrier, and the charge-separated state is the lowest energy state in the system, hindering overall energy transfer from Tc to silicon. Thus, we suspect that the energy levels of Tc/ZnPc enable sequential charge transfer to n^{+}-doped *c*-Si. The energetic alignment, however, is unfavorable for p^{+}-doped *c*-Si.

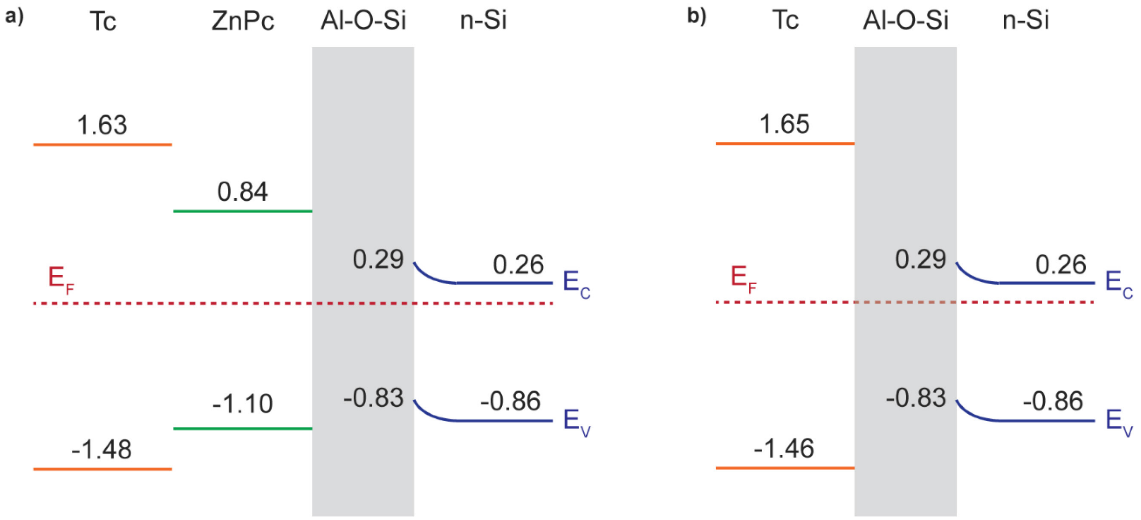

Figure 7-5. Summary of band alignments for **a)** tetracene (Tc), zinc phthalocyanine (ZnPc) and AlO_x deposited on an n-doped silicon surface (n-Si), and **b)** tetracene (Tc) and AlO_x deposited on the same n-doped silicon surface (n-Si). The red-dashed line indicates the position of the Fermi level of the system. The valence band maximum and highest occupied molecular orbital (HOMO) positions were measured using ultraviolet photoelectron spectroscopy. The conduction band minimum and lowest unoccupied molecular orbital (LUMO) positions were calculated using the electronic band gaps from previous UPS and inverse photoemission spectroscopy measurements[35,167]. The bulk values for the conduction band (E_C) and valence band (E_V) of the doped silicon were calculated from the doping concentration.

7.3.2. Silicon solar cell design for singlet fission sensitization

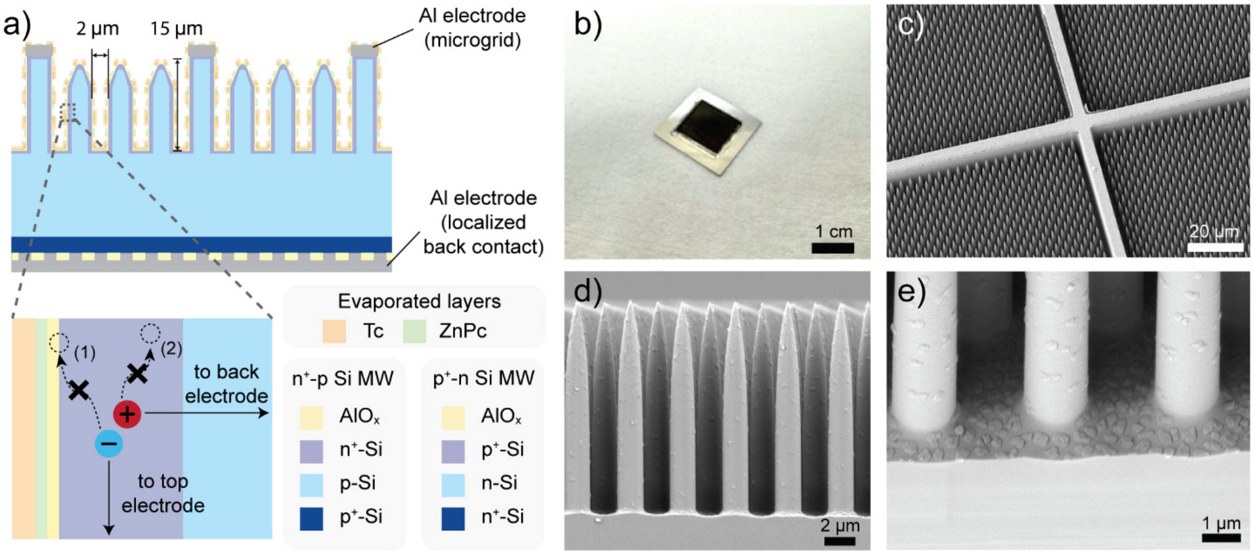

Figure 7-6. Microwire c-Si solar cells. a) Schematic depicting layers of the microwire (MW) solar cells used in this work. MW inset shows that the solar cells are designed to extract carriers from the surface region of silicon: (1) Surface recombination losses are reduced by depositing an AlO_x passivation layer; (2) bulk recombination losses are reduced by employing shallow radial p-n junctions through the microwire architecture, as well as a microgrid array for the top aluminum electrode. b) Photograph of a fabricated n^+-p Si MW cell with deposited Tc and ZnPc layers, with encapsulating glass on the active area. c) Scanning Electron Microscopy (SEM) image of the Tc/ZnPc/n^+-p Si MW cell showing a section of the microgrid array of the top electrode. d) Transverse SEM image of the Tc/ZnPc/n^+-p Si MW cell, showing the deposition on the microwires. e) SEM image of the Tc/ZnPc/n^+-p Si MW cell showing the deposition of the Tc/ZnPc layers focusing on the base of the microwire cell.

Charge injection at the surface of silicon demands a solar cell design with efficient surface carrier collection. Here, we employ shallow p-n junctions, both in conventional planar geometries and microwire (MW) solar cells that employ shallow radial junctions. Shallow junctions efficiently extract charge carriers transferred to the surface of *c*-Si by reducing the propagation distance of minority carriers[133]. The microwire structure also exhibits enhanced light absorption[133,189], particularly in the short wavelength region, reducing reflection losses.

Figure 7-6a shows a schematic of the fabricated devices. Following a previously reported protocol[190,191], we fabricate tapered *c*-Si microwire arrays with a spacing of 2 µm and a length of 15 µm. A radial junction is formed on the p-type tapered *c*-Si microwire arrays with an n-type emitter junction depth of 300 nm (see Figure 7-7) through a spin-on-dopant-based thermal doping process. To minimize recombination on the rear side, a back surface field (BSF) layer with a junction depth of 1 μm and a localized back contact is added. Then, a 1-nm-thick AlO_x layer is formed using Atomic Layer Deposition (ALD) on the front side of the solar cell. A microgrid electrode is applied as the front electrode to efficiently collect carriers[192]. This microgrid electrode covers only 2% of the active area (1 cm²), thereby reducing shading losses from the top electrodes, while also increasing the deposition area of Tc/ZnPc on the AlO_x/*c*-Si surface. Nominally 1.5 nm of ZnPc followed by 30 nm of Tc is then thermally evaporated onto the front surface of the microwire cells. To investigate the role of ZnPc, we also prepare a control device through an identical method on a p^+-n device where we only swap the doping of the base microwire device structure (Figure 7-6a). Figure 7-6d-e show scanning electron microscopy (SEM) images of the Tc/ZnPc/n^+-p Si MW. Island-type growth is observed on the sides of the MWs, with similar but denser growth on the bottom region of the microwire arrays. Since thermal evaporation is a directional deposition technique, increased deposition is expected to occur on the horizontal surface (bottom region) than on the sidewalls of the MWs perpendicular to the deposition sources[193].

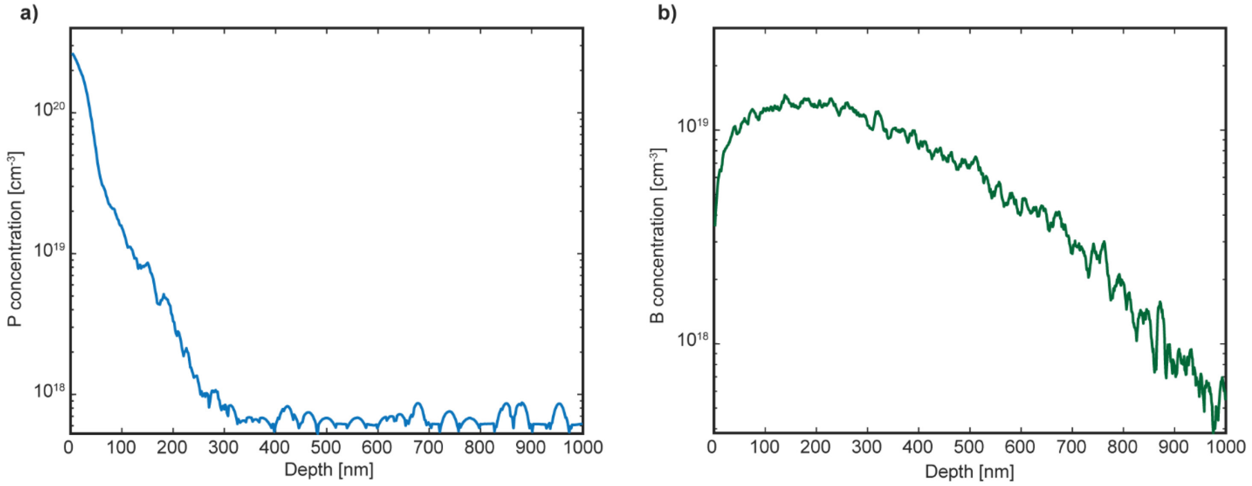

Figure 7-7. Time-of-flight secondary ion mass spectrometry (ToF-SIMS) depth profiles of n^+-p Si. a) The junction depth of the emitter region (n^+) is approximately 300 nm. b) The junction depth of the back surface field region (p^+) is approximately 1000 nm.

7.3.3. Device characterization

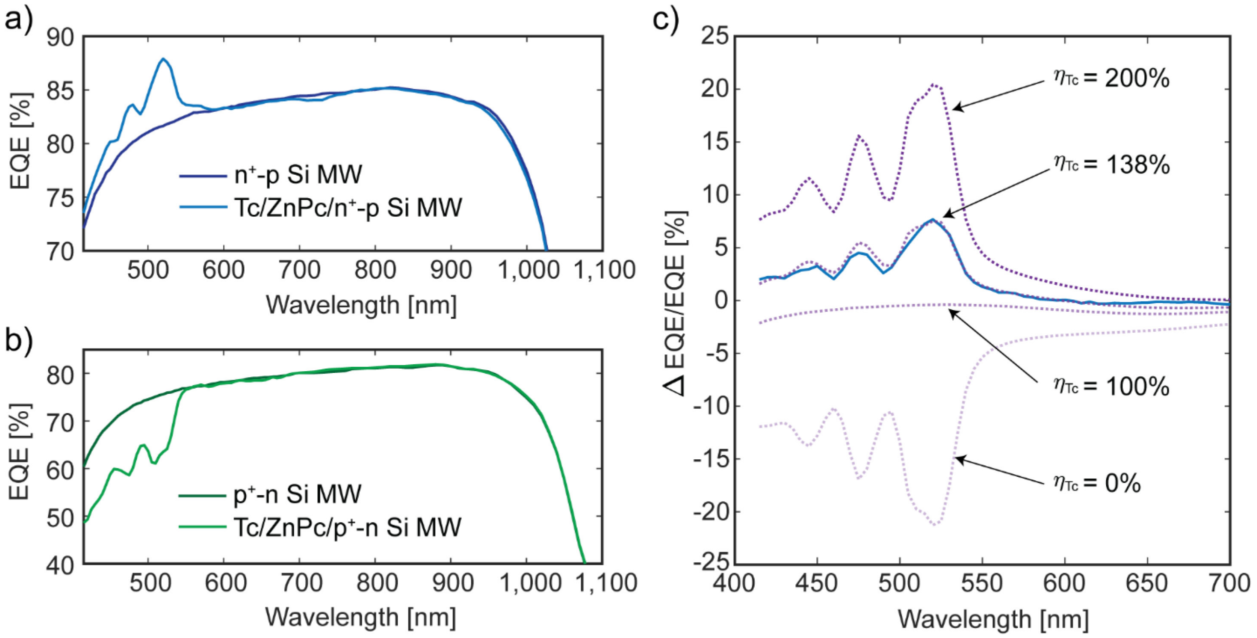

Figure 7-8. Device External Quantum Efficiencies. a) Measured external quantum efficiency (EQE) spectra of n^+-p Si MW cells before and after Tc and ZnPc deposition. b) Measured EQE spectra of p^+-n Si MW cells before and after Tc and ZnPc deposition. c) Simulation fits of the percentage difference enhancement after organic deposition (ΔEQE/EQE) of the n^+-p Si MW cells presented in a). The dotted lines represent simulated differential EQE at different Tc sensitization efficiencies (η_{Tc}). The solid line is data for the Tc/ZnPc/n^+-p Si MW device shown in a).

The measured EQE spectra of the n^+-p MW device before and after Tc and ZnPc deposition are presented in Figure 7-8a. After deposition of Tc/ZnPc, we see a positive contribution corresponding to the absorption spectrum of Tc, with a maximum EQE increase from 81.6% to 87.9% at 520 nm. The measured J-V curves of the devices also show that depositing ZnPc and Tc on the n^+-p MW devices results in an enhancement in the short-circuit current density, with negligible decrease in the open-circuit voltage and fill factors, resulting in an overall enhancement in power conversion efficiency, see Figure 7-9 and Table 7-2. It is notable that the introduction of molecular materials does not degrade the electrical characteristics of the silicon solar cell. Our results suggest that the role of the molecular materials in this cell architecture is primarily excitonic in nature, and other than increased charge injection, decoupled from the operation of the junction itself.

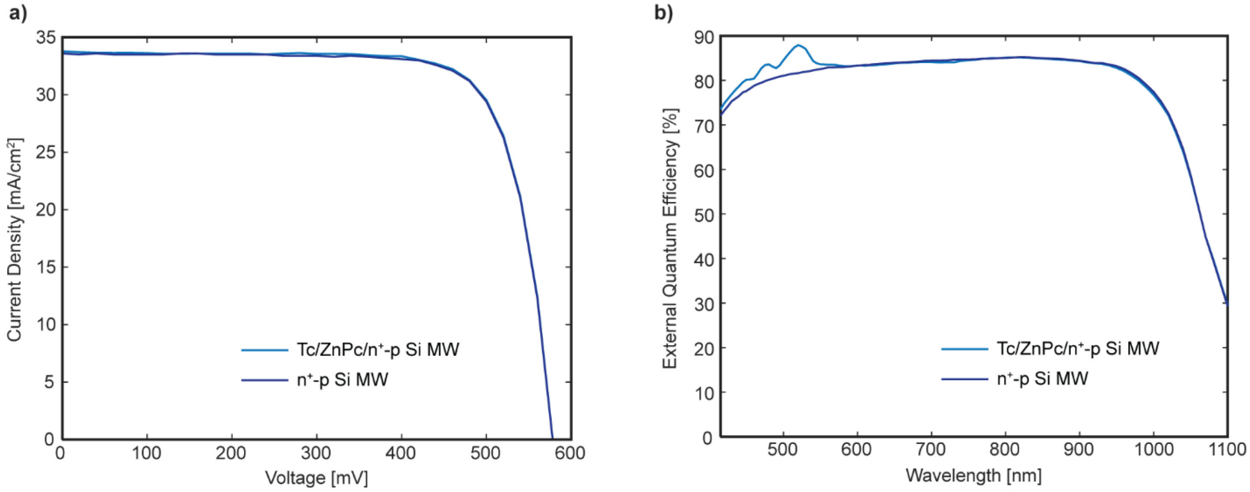

Figure 7-9. Photovoltaic performance of n^+-p Si MW devices. a) *J-V* characteristics of the n^+-p Si MW with and without Tc/ZnPc when illuminated under AM 1.5 G spectral conditions at 25 °C. b) Full-scale external quantum efficiency spectra (EQE) of the n^+-p Si MW with and without Tc/ZnPc.

Table 7-2. Photovoltaic properties of n^+-p Si MW solar cells with and without Tc/ZnPc

Microwire	J_{sc} **(mA/cm²)**	V_{oc} **(mV)**	***FF*** **(%)**	***PCE*** **(%)**
n^+-p Si	33.57	578.1	77.05	14.95
Tc/ZnPc/n^+-p Si	33.79	578.0	76.85	15.01

As expected from the interfacial measurements summarized in Figure 7-5, p^+-n MW devices exhibit dramatically different behavior when coupled to Tc. The measured EQE spectra before and after Tc and ZnPc deposition are shown in Figure 7-8b and Figure 7-10. Unlike the case with the n^+-p MW device, we instead observe shadowing in the EQE spectra from absorption of Tc, dropping from 75.6% to 63.5% at 520 nm. This also confirms that the device performance enhancements observed in the n^+-p devices are not solely from enhanced antireflective effects of adding the additional organic layers.

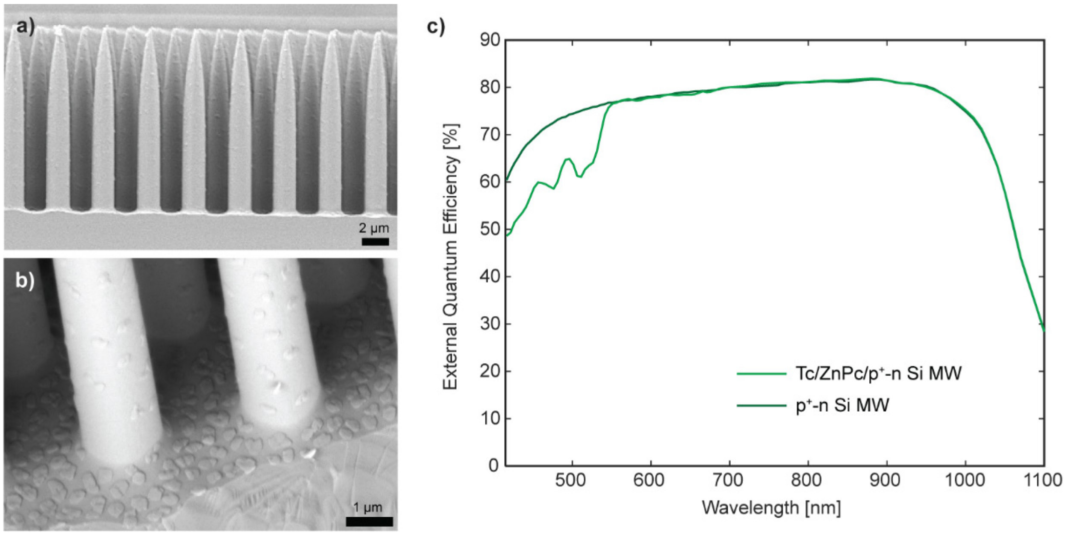

Figure 7-10. Characterization of p^+-n Si MW devices. a-b) SEM images of the Tc/ZnPc/p^+-n Si MW, and c) full scale EQE of the p^+-n Si MW with and without Tc/ZnPc.

We also fabricate n^+-p and p^+-n type planar devices with random surface pyramidal texturing, which is extensively utilized in the *c*-Si solar cell industry for its antireflective properties. The effects on the EQE spectra are consistent with the observations in the MW solar cells presented above, although the magnitude of the enhancement is slightly decreased (see Table 7-3 and Figure 7-11).

Table 7-3. Photovoltaic properties of pyramidal-textured planar n^+-p Si device with and without Tc/ZnPc

Pyramidal-textured planar	J_{sc} (mA/cm^2)	V_{oc} (mV)	*FF* (%)	*PCE* (%)
n^+-p Si	30.50	518.6	50.81	8.0
Tc/ZnPc/n^+-p Si	30.61	518.7	50.52	8.0

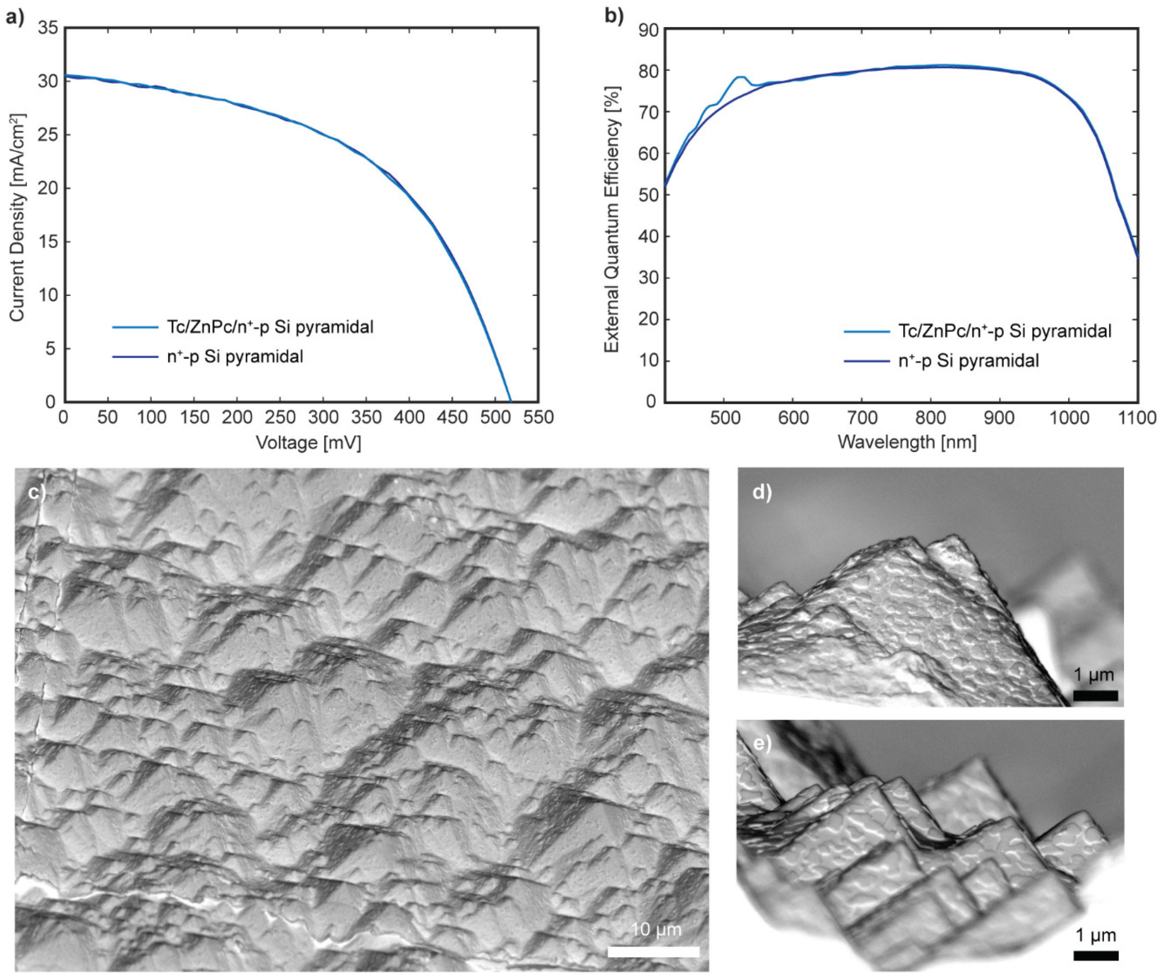

Figure 7-11. Pyramidal-textured planar n^+-p Si device characterization. a) *J-V* characteristics of the n^+-p Si pyramidal cells with and without Tc/ZnPc when illuminated under AM 1.5 G spectral conditions at 25 °C. **b)** External quantum efficiency spectra (EQE) of the n^+-p Si MW with and without Tc/ZnPc. **c-e)** SEM images of the Tc/ZnPc/n^+-p Si pyramidal cells.

The role of charge tunneling in the formation of the D^+-A_{Si}^- state is verified by replacing the 1-nm-thick AlO_x passivation layer on an n^+-p MW solar cell with a 10 nm-thick Al_2O_3 passivation layer. On the thicker sample, we observe Tc shadowing in the EQE spectra, demonstrating that coupling to *c*-Si is disrupted (see Figure 7-12a). We verify that ZnPc is essential by fabricating control devices without the ZnPc donor layer on both n^+-p and p^+-n MW devices, where we again observe Tc shadowing in the EQE spectra (see Figure 7-12b-c). We note that while both n^+-p and p^+-n solar cells fabricated without the ZnPc layer exhibit shadowing from Tc, the shadowing is less in the n^+-p MW device. This suggests that there may be a small number of triplet states from Tc that are able to undergo Dexter transfer or sequential charge transfer to *c*-Si, potentially via charge-separated states incorporating the tail of the Tc density of states.

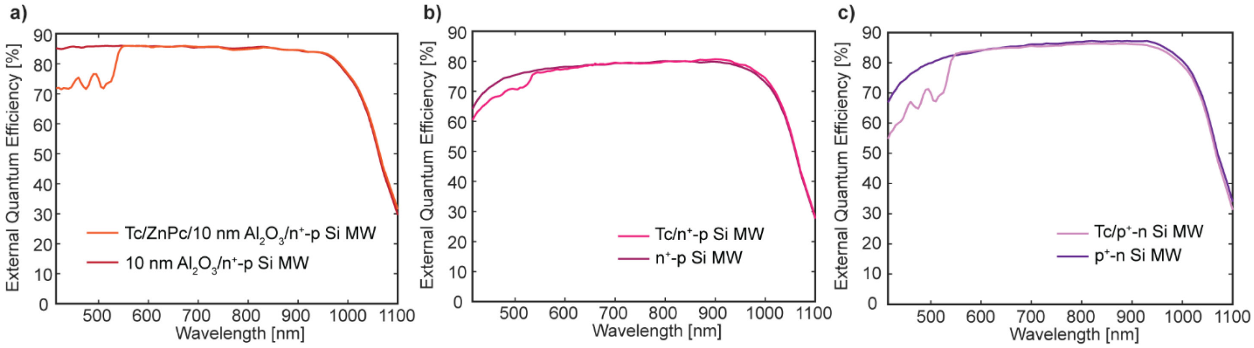

Figure 7-12. Control silicon microwire device characterization. a) EQE spectra of n$^+$-p Si MW with 10 nm Al_2O_3 with and without Tc/ZnPc. b) EQE spectra of n$^+$-p Si MW with and without Tc. c) EQE spectra of p$^+$-n Si MW with and without Tc.

The overall Tc sensitization efficiency, η_{Tc}, encompasses singlet fission efficiency in Tc, transport of triplets to the interface with silicon, triplet transfer efficiency at the interface, and extraction efficiency of charge carriers transferred to silicon. We emphasize that singlet exciton transfer alone from Tc to *c*-Si in the n$^+$-p MW device yields a maximum sensitization efficiency η_{Tc} = 100%. Indeed, it is not possible to observe Tc peaks in the EQE of the silicon solar cell unless there is efficient (η_{Tc} > 100%) coupling to triplets generated by singlet exciton fission. To evaluate η_{Tc} we perform a transfer matrix model of the layers in our solar cell[173]. Figure 7-8c shows the fitting results to the EQE percentage differential ($\Delta EQE/EQE_0$) where $\Delta EQE = EQE_{Tc} - EQE_0$ and EQE_{Tc} and EQE_0 are the efficiencies of the Tc and control devices, respectively, (see Figure 7-8a). The fit yields a sensitization efficiency of η_{Tc} = (138 ± 6)%, where 200% is the maximum theoretical enhancement possible for a photocurrent doubling process.

Based on our results, we expect that it is possible to significantly improve the performance of singlet exciton fission enhanced solar cells and photodetectors toward a peak quantum yield of two electrons per photon and an overall power efficiency that exceeds the conventional single-junction limit. First, technologies from advanced-node field-effect transistors can be adopted to improve the performance of the thin passivation layer. Second, conformal coating and optimized Tc growth could substantially improve the coverage of sensitizing materials on the silicon surface. Finally, although it has long been the archetype fission material for coupling to silicon, Tc has poor photostability[76] and will need to be replaced with a photostable analog.

In conclusion, we demonstrate efficient coupling between a silicon solar cell and singlet exciton fission in Tc, finally realizing the solar cell concept first proposed by D.L. Dexter in 1979[27].

Control over the crucial interface between Tc and silicon is established by assuming sequential charge transfer mediated by a thin layer of ZnPc. The resulting observation of more than one electron per photon in a silicon solar cell provides the foundation for a new solar photovoltaic technology capable of accelerating the global adoption of renewable energy.

Part II: Spectroscopy technique and data analysis development

Chapter 8.
Theoretical framework for spectroscopy techniques for bulk material and interfacial carrier transport

In Part I of this thesis, we covered the interfacial materials and device architecture studies for singlet fission-sensitized silicon photovoltaics. From these studies, we were able to demonstrate the importance of interlayer material selection and device design for observing enhancements in silicon photovoltaic performance from singlet fission. To probe the transport of the carriers in these solar cells both in the bulk materials and across the interface, as well as obtain information on the transient dynamics, we need advanced spectroscopy techniques. In Part II of this thesis, we present the work done on development of data analysis tools and setup building for advanced spectroscopy techniques that can probe carrier transport laterally within bulk semiconductors, and perpendicularly across interfaces. We also include some preliminary transient measurements of singlet fission-sensitized silicon samples to probe the exciton dynamics in these materials and begin to piece together a kinetic picture of the carriers in these samples. In this chapter, we introduce some of the theoretical background to support the remainder of Part II of this thesis, including transient photoluminescence (with spatial resolution), transient second harmonic generation, and transient absorption.

8.1. Transient photoluminescence

Transient dynamics of excited states in bulk materials, such as in tetracene, can be studied using transient photoluminescence. Unlike the other two techniques introduced in this chapter, the time resolution of transient photoluminescence measurements carried out using time-correlated single photon counting (TCSPC) are usually limited by the detector timing uncertainty, excitation pulse duration, and timing jitter of electronic components involved, the combination of which is referred to as the instrument response function (IRF)[194]. In the TCSPC configurations used in this thesis with an avalanche photodiode detector, the timing resolution is about 80 ps.

As noted in section 3.3.2, transient photoluminescence measurements of tetracene show prompt and delayed fluorescence components. The prompt fluorescence is often used to extract the singlet exciton lifetime (of the initially generated population) and the delayed fluorescence is often used to extract the triplet exciton lifetime.

In Part II of this thesis, we perform transient photoluminescence characterization of tetracene fluorescence in different material stack combinations introduced in Part I of this thesis. By probing the changes in the delayed fluorescence, we can confirm consistency with our expectations for the triplet excitons based on our interfacial material studies and device results.

8.1.1. Adding spatial resolution to study bulk transport

In addition to time-resolved information on the fluorescence, it is possible to image the transport process of excitons and free carriers in bulk materials by incorporating spatial resolution into the measurement through transient photoluminescence microscopy[65,195,196]. A sample is excited using a pulsed laser on a microscope setup. Then, using the objective lens of the microscope and external optics, the fluorescence spot from the sample can be magnified and the avalanche photodiode detector raster-scanned across the image plane to obtain 3-dimensional data that collects the fluorescence intensity as a function of both position on sample and time.

Transient photoluminescence microscopy (TPLM) has been used to study exciton transport in tetracene by Akselrod *et al.*[196] Additional ultrafast studies of exciton transport have been subsequently performed by Wan *et al.*[197] using transient absorption microscopy. The studies indicate that the triplet excitons diffuse normally through the crystal until they encounter traps, resulting in subdiffusive transport[196]. Cooperative singlet-triplet transport is observed, where the equilibrium between singlets and triplets through singlet fission and triplet-triplet annihilation results in enhanced effective diffusion constants[197].

For analysis of TPLM measurements, the type of species (excitons or free carriers) determines the method required to model the energy transport. In the particular case of free carriers, which dominate transport in bulk semiconductors such as silicon, the analysis is more involved. In this thesis, we present a detailed numerical framework for analysis of TPLM data collected on materials where transport is dominated by free carriers.

8.2. Transient second harmonic generation

While studying lateral carrier transport is possible through spatially-resolved microscopy techniques, most devices also involve carrier transport in the perpendicular direction, across multiple interfaces. As a result, there is great interest in spectroscopic techniques that can probe interfacial charge transport. Additionally, understanding the temporal dynamics of these charge transfer processes can be useful for designing better optoelectronic devices. Depending on the system of interest, charge transport across interfaces can occur from femtosecond to picosecond time scales[198,199]. Pump-probe spectroscopy techniques are a useful way to obtain the temporal resolution necessary to study these processes: by using one beam to excite the sample and a second beam at a set time delay from the first to probe the sample, the resolution of the technique is not limited by any electronic components that are part of the measurement setup. The time resolution is instead set by the convolution of the temporal width of the two pulses, which with the latest developments in ultrafast laser systems coupled with pulse compression techniques, can reach up to as narrow as 10s of fs[200].

To probe charge transfer across material interfaces, second harmonic generation (SHG) is a powerful nonlinear optical phenomenon that is particularly sensitive to regions of symmetry breaking, *i.e.* surfaces and interfaces. We start with an explanation for the theory for SHG, introduce the special case of electric field-induced second harmonic generation (EFISHG), and extend towards previous examples of transient SHG used to study ultrafast charge transfer and silicon-dielectric surfaces.

8.2.1. SHG principles

This section closely follows the discussion in Boyd[201], which we recommend to the reader for further reading. When an electric field $\tilde{E}(t)$ (*e.g.* light) is incident on a material, the electric field interacts with the charged particles in the material (usually electrons and nuclei). The coulombic force imparted by the electric field causes the charged particles to be displaced from their equilibrium positions, generating electric dipole moments. The polarization of a material $\tilde{P}(t)$ is defined as the dipole moment per unit volume, and depends on the strength of $\tilde{E}(t)$[201]. When the intensity of $\tilde{E}(t)$ is weak, the induced polarization $\tilde{P}(t)$ depends linearly with $\tilde{E}(t)$, described as follows:

$$\tilde{P}(t) = \epsilon_0 \chi^{(1)} \tilde{E}(t), \tag{8-1}$$

where ϵ_0 is the permittivity of free space, and $\chi^{(1)}$ is the linear susceptibility. Because of the linear relationship between $\tilde{P}(t)$ and $\tilde{E}(t)$, such responses fall under the field of linear optics, which includes optical phenomena such as scattering, reflection and (linear) absorption.

When the incident light is strong (*e.g.* laser excitation), $\tilde{P}(t)$ starts to depend nonlinearly with the incident field, such that it can be approximated as follows:

$$\begin{aligned}\tilde{P}(t) &= \epsilon_0\left[\chi^{(1)}\tilde{E}(t) + \chi^{(2)}\tilde{E}^2(t) + \chi^{(3)}\tilde{E}^3(t) + \cdots\right] \\ &\equiv \tilde{P}^{(1)}(t) + \tilde{P}^{(2)}(t) + \tilde{P}^{(3)}(t) + \cdots,\end{aligned} \tag{8-2}$$

where $\chi^{(2)}$ and $\chi^{(3)}$ are the second- and third-order nonlinear susceptibilities, respectively, and $\tilde{P}^{(2)}$ and $\tilde{P}^{(3)}$ are the second- and third-order nonlinear polarization responses, respectively. As electric fields can be described as vectors, $\chi^{(1)}$ is a second-rank tensor, $\chi^{(2)}$ is a third-rank tensor, and so on.

Second Harmonic Generation (SHG) is a special case of the second-order nonlinear polarization response. An incident field with frequency ω can interact with a material to induce a nonlinear second-order polarization at twice the incident frequency 2ω.

The wave equation in nonlinear optical media can be described as:

$$\nabla^2\tilde{E} - \frac{n^2}{c^2}\frac{\partial^2\tilde{E}}{\partial t^2} = \frac{1}{\epsilon_0 c^2}\frac{\partial^2\tilde{P}^{NL}}{\partial t^2}, \tag{8-3}$$

where n is the linear refractive index, and c is the speed of light in vacuum. As a result of the induced nonlinear polarization in the material, for a non-zero $\chi^{(2)}$, radiation (typically emission) at the second harmonic frequency 2ω is generated. This process can be pictured by a photon exchange process, where two photons of frequency ω are converted to one photon of frequency 2ω, as depicted in Figure 8-1. The energy of the transitions does not necessarily need to match real electronic transitions in the material.

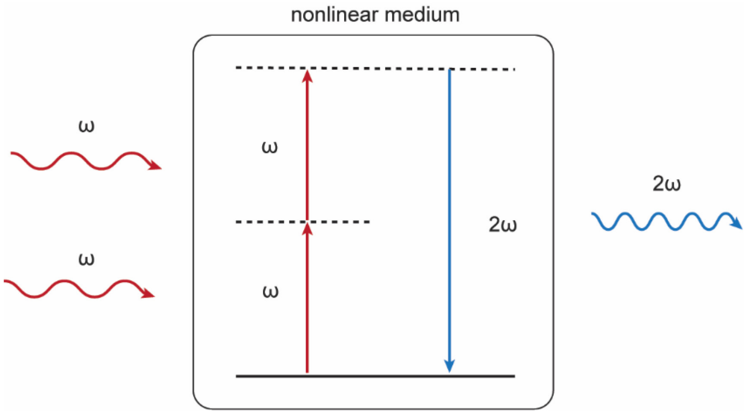

Figure 8-1. Schematic of the process of second harmonic generation (SHG). Two incident photons of frequency ω are converted to one incident photon of frequency 2ω by a nonlinear medium. The energy levels of the transitions in the medium do not necessarily correspond to real energy states in the material.

Other contributions to the second-order polarization include sum-frequency generation (SFG), $\omega_3 = \omega_1 + \omega_2$ and difference-frequency generation (DFG), $\omega_3 = \omega_1 - \omega_2$.

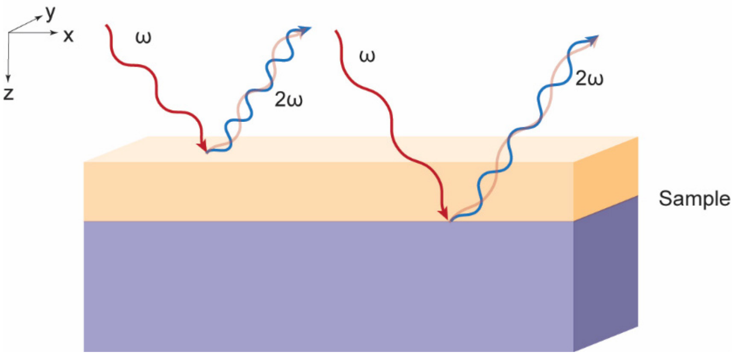

Figure 8-2. Schematic of SHG generated in reflection mode from the sample surface and sample interface. The generated SHG is collinear with the reflected incident fundamental beam.

In addition to generation by passing through the nonlinear medium, SHG can also be generated from reflection off of a surface or interface. For the experiments conducted in this thesis, the SHG signal was probed in reflection mode from various sample surfaces and interfaces, as shown in Figure 8-2. In reflection mode, the intensity of reflected SHG is given by[202]:

$$I^{(2\omega)} \propto \left|\chi^{(2)}\right|^2 \left(I^{(\omega)}\right)^2 |F^{NL}|^2 |F^L|^4, \tag{8-4}$$

where $I^{(2\omega)}$ is the intensity of the SHG, $I^{(\omega)}$ is the intensity of the incident fundamental beam, F^{NL} is the nonlinear Fresnel factor and F^L is the linear Fresnel factor. The Fresnel factors include changes in the refractive index which could result from changing temperature, among other factors.

As shown in the expression, the measured SHG intensity has a *quadratic power dependence* with the incident fundamental light. This property can be used to confirm if the measured signal is a second-order signal.

8.2.1.1. Centrosymmetry

In Cartesian coordinates, the nonlinear induced polarization for SHG is described as:

$$P_i^{(2)} = \epsilon_0 \chi_{ijk}^{(2)}(2\omega, \omega) E_j(\omega) E_k(\omega), \tag{8-5}$$

where $i, j,$ and k are defined by the Cartesian coordinates $x, y,$ and z. The $\chi_{ijk}^{(2)}$ tensor consists of 27 Cartesian components. Due to lattice symmetry and considering that E_j and E_k are degenerate, the number of nonzero distinct components in the $\chi_{ijk}^{(2)}$ tensor can be reduced. For convenience, $\chi_{ijk}^{(2)}$ is sometimes expressed in contracted notation:

$$d_{il} = d_{ijk} = \frac{1}{2}\chi_{ijk}^{(2)}, \tag{8-6}$$

where the subscripts are correlated by the following prescription:

$$\begin{array}{lcccccc} jk: & 11 & 22 & 33 & 23, 32 & 31, 13 & 12, 21 \\ l: & 1 & 2 & 3 & 4 & 5 & 6 \end{array} \tag{8-7}$$

Then, the tensor can be expressed as a 3 × 6 matrix:

$$d_{il} = \begin{bmatrix} d_{11} & d_{12} & d_{13} & d_{14} & d_{15} & d_{16} \\ d_{21} & d_{22} & d_{23} & d_{24} & d_{25} & d_{26} \\ d_{31} & d_{32} & d_{33} & d_{34} & d_{35} & d_{36} \end{bmatrix}, \tag{8-8}$$

and the nonlinear polarization can be expressed in matrix notation:

$$\begin{bmatrix} P_x(2\omega) \\ P_y(2\omega) \\ P_z(2\omega) \end{bmatrix} = 2\epsilon_0 \begin{bmatrix} d_{11} & d_{12} & d_{13} & d_{14} & d_{15} & d_{16} \\ d_{21} & d_{22} & d_{23} & d_{24} & d_{25} & d_{26} \\ d_{31} & d_{32} & d_{33} & d_{34} & d_{35} & d_{36} \end{bmatrix} \begin{bmatrix} E_x(\omega)^2 \\ E_y(\omega)^2 \\ E_z(\omega)^2 \\ 2E_y(\omega)E_z(\omega) \\ 2E_x(\omega)E_z(\omega) \\ 2E_x(\omega)E_y(\omega) \end{bmatrix}. \tag{8-9}$$

Depending on the symmetry of the crystal structure, the number of non-zero distinct components of the matrix can simplify even further. The d_{il} matrix for different crystal classes can be found in Boyd[201].

An interesting feature occurs with SHG (and other even nonlinear optical processes) in materials that possess inversion symmetry, also known as centrosymmetric materials: the $\chi^{(2)}$ term vanishes for these materials, $i.e.\ d_{il} = 0$. 11 of the 32 crystal classes possess inversion symmetry, including silicon, described by the cubic centrosymmetric *m3m* point group[203], and single crystal tetracene, described by the triclinic centrosymmetric $\underline{1}$ point group[204,205]. Additionally, amorphous materials, which is the structure expected for thin deposited layers, as well as air, also constitute as centrosymmetric media. Consequently, SHG is forbidden in the bulk of centrosymmetric materials under the electric-dipole approximation.

This can be seen from a simple analysis of the polarization. Recalling Equation (8-2), the sign of the induced polarization must change with the sign of the applied electric field:

$$\begin{aligned} -\tilde{P}(t) &= \epsilon_0 \left[\chi^{(1)}\left(-\tilde{E}(t)\right) + \chi^{(2)}\left(-\tilde{E}(t)\right)^2 + \chi^{(3)}\left(-\tilde{E}(t)\right)^3 \ldots\right] \\ &= \epsilon_0 \left[-\chi^{(1)}\left(\tilde{E}(t)\right) + \chi^{(2)}\left(\tilde{E}(t)\right)^2 - \chi^{(3)}\left(\tilde{E}(t)\right)^3 \ldots\right] \end{aligned} \tag{8-10}$$

However, we see that only odd-order terms in this expression have changed their sign. For the second-order term, $\tilde{P}^{(2)}(t) = -\tilde{P}^{(2)}(t)$ is implied, which can only be true if $\chi^{(2)} = 0$.

In practice, the SHG signal from centrosymmetric materials is non-zero due to electric-quadrupole and magnetic-dipole contributions, although they are quite negligible. As a result, SHG is a powerful tool for studying surfaces and interfaces because it is very sensitive to these regions where inversion symmetry is broken[201]. Single wavelength and spectral studies can give information on the crystal structure and resonance energy states of surfaces and interfaces[206], whilst time-resolved optical SHG responses can be used to study electron transfer dynamics at semiconductor interfaces[207], including the tetracene-silicon interface.

There are many advantages of SHG compared to other techniques available for studying interfaces. It can be conducted under ambient pressures without any special large vacuum systems and does not invoke any damage to the sample associated with using charged particle beams, contrary to

UPS/XPS measurements. Insulating samples can also be studied without worrying about charge buildup, and thanks to the large penetration depth of the optical field, it is possible to study buried interfaces[206]. Both wavelength-dependent SHG and time-dependent SHG can give insight into understanding interfaces. SHG signals can also display resonance enhancement if the wavelength happens to match an optical transition in the material at either the fundamental frequency or the second-harmonic frequency[208]. The phase is particularly relevant when there are multiple contributions to the overall SHG signal, since out-of-phase contributions can lead to destructive interference[209].

8.2.1.2. Phase-matching

The electric field of traveling waves can be described as:

$$E_j(x,t) = A_j e^{i(k_j x - \omega_j t)} + c.c., \tag{8-11}$$

where A_j is the amplitude, k_j is the wave vector defined by $k_j = n_{\omega_j}\omega_j/c$, with n_{ω_j} as the refractive index of the material at frequency ω_j, c is the speed of light, and $c.c.$ is the complex conjugate. Note, in the above expression we simplify to a one-dimensional treatment.

Considering the case of sum frequency generation of two beams at ω_1 and ω_2, the second-order polarization at frequency $\omega_3 = \omega_1 + \omega_2$ is expressed as:

$$P^{(2)}(x,t) \propto A_1 A_2 e^{i|(k_1+k_2)x - \omega_3 t|} + c.c.. \tag{8-12}$$

We also note that the electric field of the emitted wave at ω_3 is defined as:

$$E_3(x,t) = A_3 e^{i(k_3 x - \omega_3 t)} + c.c.. \tag{8-13}$$

Constructive interference, corresponding to a high intensity of the ω_3 field, will be observed when a condition known as phase-matching occurs, that is, when:

$$\Delta k = k_1 + k_2 - k_3 = 0. \tag{8-14}$$

In a microscopic picture, when phase-matching occurs, the individual atomic dipoles in the material system induced by the fields are all in phase with each other such that the emitted field adds coherently.

For SHG induced by collinear beams, the phase-matching condition becomes:

$$n(\omega_1) = n(2\omega_1). \tag{8-15}$$

In typical materials that exhibit normal dispersion, the above expression cannot be upheld. However, in special materials that exhibit *birefringence*, such as barium borate (BBO), phase matching can be achieved. As a result, these nonlinear crystals are often used for SHG frequency doubling of laser excitation.

8.2.1.3. Electric field-induced second harmonic generation (EFISHG)

The theory for surface SHG was developed by Bloembergen and Pershan[202,210]. We detail some of the important points, and direct the reader towards other reviews from Y. R. Shen for further details[211,212]. To model surface SHG, we treat the surface region as an infinitesimally thin film with a nonlinear susceptibility $\chi_{ijk}^{(2)\,surf}$ assigned to this region. Then, the total second-order polarization for SHG reflected off the surface can be expressed as[213]:

$$P_i^{(2)}(2\omega) = \chi_{ijk}^{(2)\,bd} E_j(\omega)E_k(\omega) + \chi_{ijk}^{(2)\,bnl} E_j(\omega)\nabla_k E_l(\omega) + \chi_{ijk}^{(2)\,surf} E_j(\omega)E_k(\omega), \tag{8-16}$$

where the first term is the bulk dipole term which vanishes in centrosymmetric materials, the second term is the bulk non-local term (includes electric quadrupole and magnetic dipole contributions, often small), and the third term is the surface dipole term. We note that phase matching considerations are usually ignored for surface reflected SHG because this surface region volume is much thinner than the coherence length of the substrate.

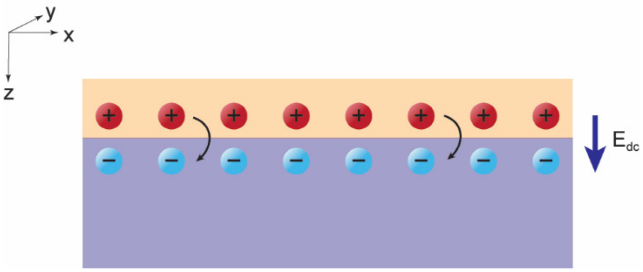

Figure 8-3. When the top donor layer donates an electron to the bottom acceptor material, an electric field E_{dc} in the z-direction is formed at the interface due to the charge separation temporarily, before the hole recombines with the electron. This electric field can be probed using SHG.

When we have a two-layer system where the top donor layer donates an electron to the bottom acceptor material, a positively-charged hole can be left behind in the electron-donating material.

The separation of charge that occurs results in formation of an electric field perpendicular to the sample surface normal (as shown in Figure 8-3), which can affect the symmetry and therefore be observed using SHG. This is referred to as electric field-induced second harmonic generation (EFISHG).

Mathematically, the EFISHG contribution can be described as a third-order nonlinear process with a fourth-rank nonlinear susceptibility tensor where E_{dc} mixes with the incident optical field. Then, the total second-order polarization for SHG reflected from the surface becomes:

$$P^{(2)}(2\omega) = P^{(2)}(2\omega, \boldsymbol{E_{dc}} = 0) + \chi^{(3)}_{EFISHG} : \boldsymbol{E_{dc}} \boldsymbol{E}(\omega) \boldsymbol{E}(\omega), \tag{8-17}$$

where $P^{(2)}(2\omega, \boldsymbol{E_{dc}} = 0)$ is defined in (8-16), which includes the bulk dipole, bulk non-local and surface contributions when there is no electric field at the interface.

The sensitivity of SHG to interfacial electric fields makes it very attractive for monitoring the evolution of this field over time. If we come in with an extra pulsed excitation beam (pump beam) and excite the material system at a certain controlled time delay before the beam used to generate the SHG signal (probe beam), varying the time delay between the pump and the probe beams will allow us to piece together the progression of this field, and consequently the charge transfer dynamics over time, depicted in Figure 8-4. As a result, transient SHG has been used to understand silicon and silver surfaces[214], as well as electron transfer from quantum dots to semiconductors[199,207].

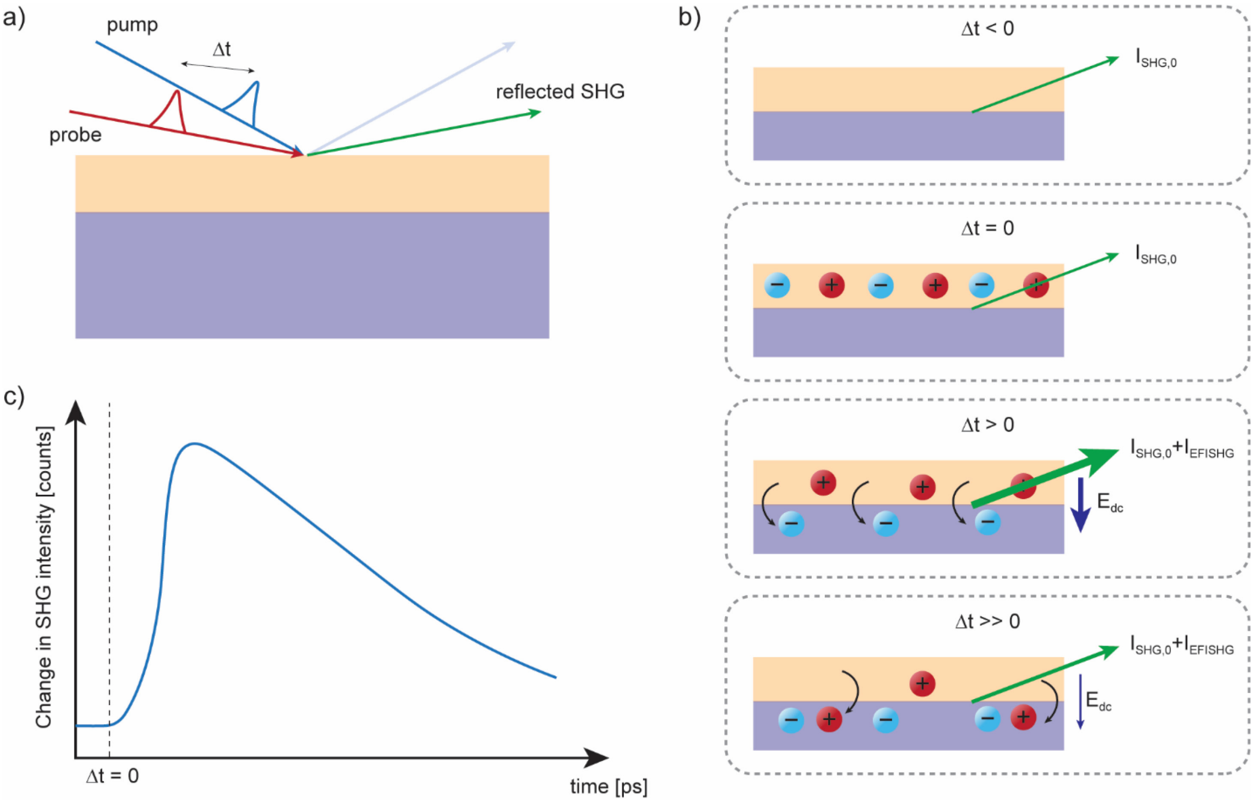

Figure 8-4 Schematic of transient SHG. a) Experimental setting for pump-probe transient SHG experiments. The time difference between the pump pulse and the probe pulse is referred to as the time delay Δt. b) Schematic of electron transfer events occurring in the sample at different time delays. c) Depiction of measured SHG signal for system presented in schematic b).

Charge transfer dynamics can be extracted directly from the SHG experiments by choosing careful combinations of geometry and polarizations of both incident and measured light to make certain contributions negligible. In particular, by manipulating the experimental setup such that $\chi_{surf}^{(2)} \gg \chi_{EFISHG}^{(3)}, \chi_{bnl}^{(2)}$, electron transfer dynamics can be directly extracted from the measured time-resolved SHG signal. We write the corresponding expression of the intensity of reflected SHG:

$$\begin{aligned} I^{(2\omega)} &\propto \left|P^{(2)}(2\omega)\right|^2 \\ &= \alpha\left|\chi_{surf}^{(2)}\right|^2\left(I^{(\omega)}\right)^2 + \beta\left(\chi_{surf}^{(2)*}\chi_{EFISHG}^{(3)} + \chi_{surf}^{(2)}\chi_{EFISHG}^{(3)*}\right)\left(I^{(\omega)}\right)^2 E_{dc} \qquad (8\text{-}18) \\ &= I_0^{(2\omega)} + \theta\left(I^{(\omega)}\right)^2 E_{dc}, \end{aligned}$$

where α, β are geometric constants. As shown above, the measured time-resolved SHG varies linearly with the strength of the interfacial electric field. Treating the charge-separated interface as a parallel plate capacitor:

$$E_{dc} = \frac{1}{\varepsilon_r \varepsilon_0} \frac{2Q^{sep}}{A}, \tag{8-19}$$

where Q^{sep} is the amount of separated charge. Thus, the change in the SHG signal can be directly used to extract the dynamics of electron transfer at the interface.

8.2.2. Previous studies of time-resolved second harmonic generation of surfaces and interfaces

Due to its high sensitivity to surfaces, SHG has been used to probe various surface phenomena in a variety of different materials[211]. We highlight some of the studies of silicon surfaces and thin dielectric films on silicon of relevance to the singlet fission-sensitized silicon materials.

Steady-state SHG studies on Si/SiO_2 surfaces report differences depending on the treatment and growth conditions of the SiO_2 layer[215]. Additionally, SHG measurements were found to be very sensitive to adsorption of oxygen and other molecules onto the surface[213]. Many former reports of transient SHG on Si/SiO_2 were conducted over long timescales, where an increase in the SH signal was observed on the order of 100 s, and was attributed to oxygen traps in the silicon oxide being filled, generating an electric field[216]. For thin oxides, blocking the pump laser resulted in a decrease in the signal, attributed to charge detrapping and subsequent recombination at the interface[217].

Time-resolved SHG has also been used to study charge trapping and defect densities in high-k dielectrics deposited on silicon, including Al_2O_3, ZrO_2 and HfO_2[218]. Information on trap density, type of charge trap (by altering silicon doping type) and trapping/detrapping dynamics were extracted from the SHG measurements.

In addition to time-dependent data, wavelength-dependent SHG has been used to identify interfacial[219]/surface states or even inferring the band-offset between the semiconductor and the oxide[217].

One other interesting feature that has been observed with transient SHG for studying electron transfer is the observation of oscillations in the time-dependent signal, which can be correlated to phonon modes involved in the electron transfer process[199,207].

In this thesis, we work on building a transient SHG setup with the goal of studying the temporal dynamics of interfacial charge transfer from tetracene to silicon with various interlayers.

8.3. Transient absorption

Transient absorption is another pump-probe spectroscopy technique that offers complementary information about excited state dynamics in materials to transient SHG. While transient SHG is exclusively probing the surface, transient absorption can provide information on the excited state dynamics in the bulk of the materials in the system. Additionally, unlike time-resolved fluorescence measurements, we analyze the change in the absorption spectrum of the material system, which enables probing of non-emissive dark states which can be relevant to singlet fission-sensitized silicon, such as triplet excited states.

A schematic of the experimental process is depicted in Figure 8-5. A monochromatic pump pulse excites the sample, and a broadband probe pulse arrives at the sample at a controlled time delay Δt from the pump pulse. The absorption of the broadband probe by the sample affects the transmitted (in the transient absorption (TA) configuration) or reflected (in the transient reflection (TR) configuration) spectra which is collected by a spectrometer. The TA experiment measures how the absorption of the sample changes as a result of the pump excitation over time, with 10s of fs time resolution. The time resolution of the experiment is determined by the cross-correlation of the pump pulse and the probe pulse.

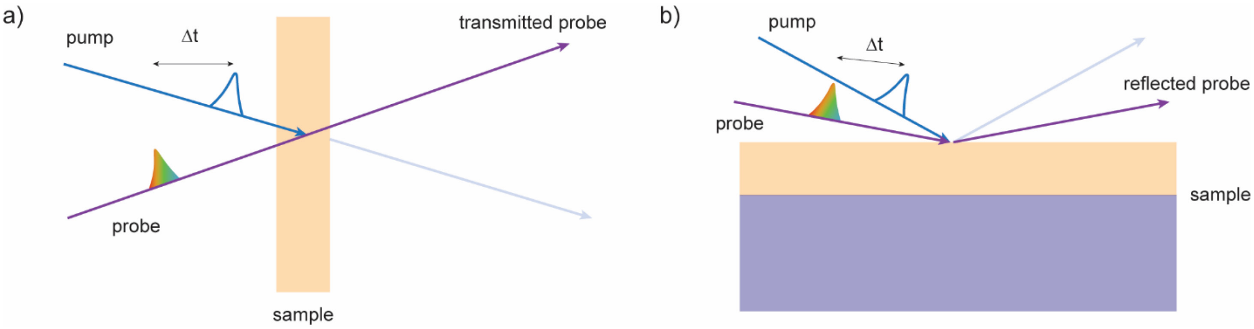

Figure 8-5. Schematic of transient absorption measurements. a) The measurement can be conducted in transmission mode through semi-transparent samples, or b) in reflection mode for non-transmitting materials, *e.g.* silicon. A pump pulse (blue) excites the sample, and the broadband probe pulse (purple) is introduced after a time delay Δt.

8.3.1. Explanation of features

The TA signal that is measured in the experiments is described by:

$$\Delta OD_{TA}(\lambda,t)[\text{mOD}] =- 1000 \times \log_{10}\left(\frac{I_{TA,pumped}(\lambda,t)}{I_{TA,not\ pumped}(\lambda,t)}\right), \tag{8-20}$$

where OD is the optical density, $I_{TA,pumped}(\lambda,t)$ is the transmitted intensity (for absorption experiments) when the sample is pumped and $I_{TA,not\ pumped}(\lambda,t)$ is the transmitted intensity when the sample is unpumped.

There are different kinds of contributions we can expect to see in the TA spectrum. We list some of the features we expect to see in our material systems of interest: ground state bleach (GSB) , stimulated emission (SE), and photo-induced absorption (PIA), depicted in Figure 8-6[220].

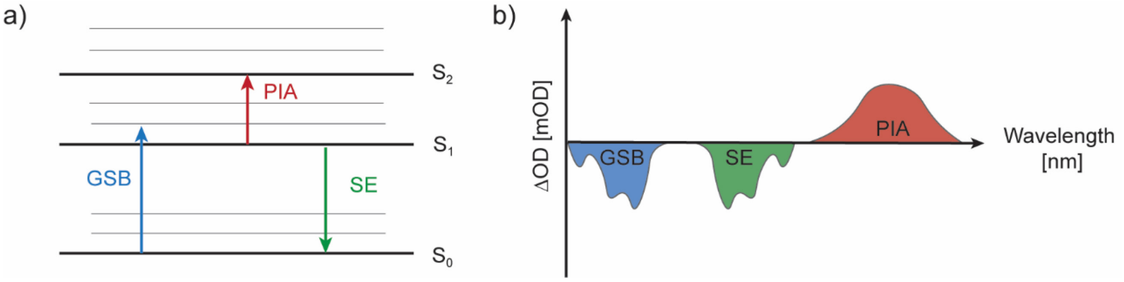

Figure 8-6. Types of features that can be observed in a transient absorption measurement. a) Ground state bleach (GSB), stimulated emission (SE) and photo-induced absorption (PIA) transitions depicted on a molecular energy level diagram. b) Examples of GSB, SE and PIA spectra measured at a time slice.

For the ground state bleach, when the pump pulse excites the sample, the material absorbs the light and molecules are promoted from the ground state to the excited state. As a result, there are less available molecules in the ground state to absorb the probe light compared to the sample that has not been excited by the pump pulse. The GSB appears as a negative signal, since the transmitted intensity $I_{TA,pumped} > I_{TA,not\ pumped}$. The spectral features of the ground state bleach will track the steady-state (ground state) absorption spectrum of the material.

For stimulated emission, this occurs when a photon from the probe beam interacts with the excited molecule, inducing emission of a photon with the same energy as the excited state. SE can only occur for optically allowed transitions (no dark states, *e.g.* triplet excited states) and will usually track the fluorescence spectrum of the excited material. SE appears as a negative signal, since the emitted photon from stimulated emission is in the same direction as the probe photon, so the measured intensity of the pumped sample will be higher than the unpumped sample $I_{TA,pumped} > I_{TA,not\ pumped}$.

Photo-induced absorption (or excited state absorption) occurs when an excited molecule absorbs certain wavelengths of the probe beam and are excited to higher energy excited states. PIA can also occur when a transient excited state (*e.g.* triplet excited states, charge-transfer states) is formed as a result of the excitation by the pump beam, and absorbs the probe beam. PIA appears as a positive signal, since the absorption by the material with the pump on is larger, resulting in reduced detected transmission $I_{TA,pumped} < I_{TA,not\ pumped}$.

In a reflective configuration, changes in reflectivity can be related to changes in the dielectric function. The dielectric function consists of a real and imaginary component, and processes can contribute to changes in both. However, for our materials of interest (silicon) and with the experimental conditions we use, we only consider the change in the real component of the dielectric function, as the real contribution is much larger than the imaginary contribution[221]. Consequently, we only consider the effect of change in the real component of the refractive index to the reflection.

With transient reflectance measurements of silicon specifically, there are three contributions to reflectance changes that have been considered in previous works: free-carrier contributions, state-filling, and lattice temperature contributions[222]. The free-carrier contribution is often described using a Drude model[223]:

$$\Delta n_{FC}(N, T_e) = -\frac{2\pi e^2}{n_0 \omega^2} \frac{\Delta N}{m_{opt}^*(T_e)}, \qquad (8\text{-}21)$$

where Δn_{FC} is the change in the real part of the refractive index from free-carrier contributions, e is the electron charge, n_0 is real part of the square root of the dielectric function, ω is the frequency of the probe, N is the excited carrier density, m_{opt}^* is the carrier effective optical mass at carrier temperature T_e. The dielectric constant decreases with an increased number of carriers; the effect of this is a decrease in reflectivity, and consequently a positive signal in $\Delta OD_{TA}(\lambda, t)$. As the carrier density decreases, through processes such as recombination, the magnitude of this signal will decrease.

The second contribution is the so-called state-filling contribution, which is similar in concept to the ground-state bleach. After excitation, less electrons can be excited from the valence band and less states in the conduction band can be filled, which decreases the absorption coefficient. Using the Kramers-Kronig relationship, we can calculate the change in the real part of the refractive index from the change in the absorption coefficient as a function of the probe wavelength. However, unlike the case of GSB, the effect of excited state saturation results in a decrease in the real part of the refractive index, resulting in reduced reflectivity and also a positive signal in $\Delta OD_{TA}(\lambda, t)$.

The final contribution is the lattice-temperature contribution that includes the dependence of the refractive index on temperature:

$$\Delta n_{LT} = \frac{dn}{dT_L}\Delta T_L, \tag{8-22}$$

where T_L is the lattice temperature. We see that an increase in lattice temperature from recombination of carriers should result in an increase in the refractive index contribution, and a consequent increase in reflectivity, which should result in a negative signal in $\Delta OD_{TA}(\lambda, t)$. Most of the time, the lattice temperature effect is only apparent at later time scales where recombination dominates the dynamics ~ 100 ps, and is important to consider at high pump fluences: ~ 10s of mJ/cm^2.[222]

The main challenge with TA/TR is the interpretation of data. A good understanding of the material being studied is necessary to come up with a sound kinetic model to fit the collected data.

Transient absorption measurements can be used to investigate the evolution of singlet fission dynamics in materials such as tetracene, particularly because this method enables probing of triplet excited states, which are typically optically dark states that cannot be observed directly in transient photoluminescence measurements. In this thesis, we perform magnetic field-dependent transient absorption measurements on tetracene to probe its effect on the fission process. Additionally, we measure transient reflection on tetracene/zinc phthalocyanine/aluminum oxide/silicon films to investigate the transient dynamics of the singlet and triplet excitons in these structures.

Chapter 9.
Robust estimation of charge carrier diffusivity using transient photoluminescence microscopy

The basis of this chapter has been reproduced from:

Narumi Nagaya Wong, Seung Kyun Ha, Kristopher Williams, Wenbi Shcherbakov-Wu, James W. Swan & William A. Tisdale. "Robust estimation of charge carrier diffusivity using transient photoluminescence microscopy" *J. Chem. Phys.* 157, 104201 (2022),

with the permission of AIP publishing.

9.1. Introduction

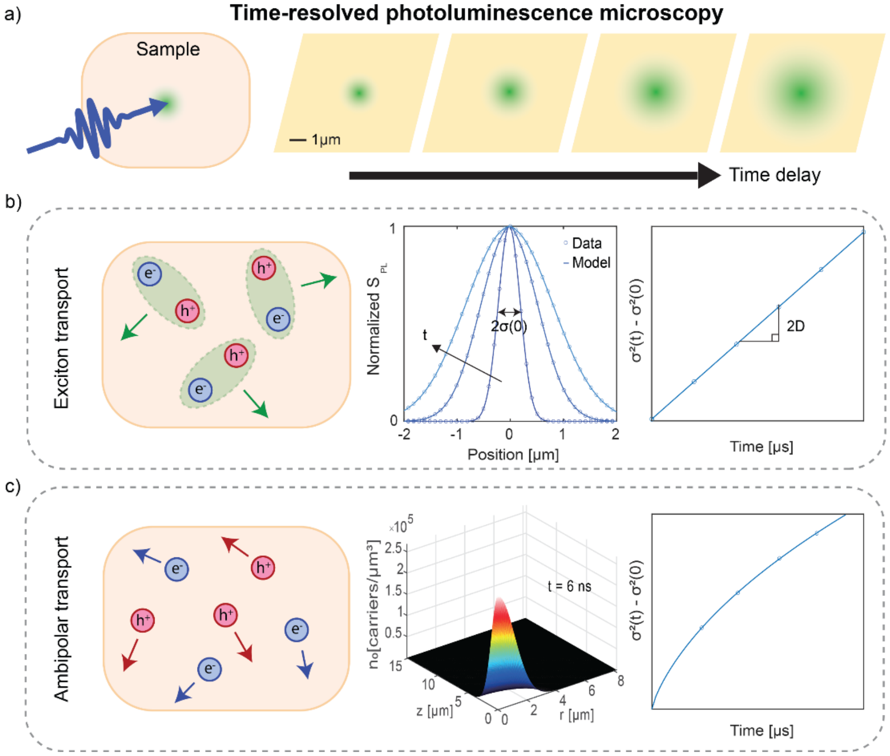

Figure 9-1. a) Schematic of the time-resolved photoluminescence microscopy (TPLM) experiment, providing spatial and temporal information. b) For materials where charge carriers move as bound electron-hole pairs, a simplified technique for extracting exciton diffusivity from the slope of TPLM data can be used. c) For materials where excitons dissociate into free carriers, the correlated movement of charge carriers can be described using the framework of ambipolar transport. In the center panel, we highlight the importance of charge carrier density modeling as opposed to simply normalizing the measured PL signal S_{PL}. On the right, we show that the same slope-based method can no longer be used to extract diffusivities when the signal intensity scales nonlinearly with the local excited state population density.

Understanding electronic energy transport properties such as carrier diffusivity in materials can enhance optimization of optoelectronic device performance, including solar cells[224], displays[225], and sensors[226]. A variety of techniques have been used to study the movement of free charge carriers or excitons (bound electron-hole pairs) in emerging semiconductor materials[65], such as Hall-effect measurements[227,228], field-effect transistors[229–231], terahertz spectroscopy[232,233], and photoluminescence quenching[234–236]. However, in many materials, the nanoscale morphology and structural inhomogeneities have an impact on transport behavior[195,237–240]. Recent studies look to observe both the temporal and spatial movement of charge carriers in optoelectronic materials, including transient-grating techniques[241,242], transient absorption microscopy[243,244,239], transient scattering microscopy[240], and time-resolved photoluminescence microscopy[245–253].

Time-resolved photoluminescence microscopy (TPLM) is particularly attractive for luminescent materials because it is a background-free technique that usually requires lower fluence than other approaches[65]. In this technique, a diffraction-limited population is excited in the sample by a pulsed laser, and an avalanche photodiode is raster scanned across a magnified image plane to collect temporal and spatial photoluminescence (PL) data (Figure 9-1a).

A complete description of carrier dynamics in semiconductors depends sensitively on a range of materials parameters and experimental conditions, including photo-excited carrier density, doping density, exciton binding energy, temperature, band gap, and electronic and vibrational band structure, among other factors, as described in detail by others[254–256]. Here, we highlight a couple limiting examples to illustrate the impact of the nature of carrier dynamics on interpretation of TPLM data.

In one extreme, electrons and holes move together as bound pairs and the local PL signal is proportional to the local density of excitons. As a result, the measured data can be directly analyzed to obtain the diffusivity (Figure 9-1b). For example, applying a 1D diffusion model enables the collected spatiotemporal data (S_{PL}) to be normalized at each time point and fit using a Gaussian or related convolution function[245]. The diffusivity can then be extracted using the mean squared displacement: $MSD(t) = \sigma^2(t) – \sigma^2(0) = 2Dt^{\alpha}$ where $\sigma^2(t)$ is the variance at time t, D is the scaling factor and α is the diffusion exponent. Under normal diffusion conditions ($\alpha = 1$), D is the exciton diffusivity within the material.

In materials where transport is dominated by free charge carriers, a more complex approach is required (Figure 9-1c). In many cases, the measured photoluminescence signal is no longer proportional to the local population density. If the photo-generated carrier density is sufficiently high, the PL signal is expected to have a quadratic dependence on the charge carrier density. Accordingly, the measured PL signal is not directly proportional to the charge carrier density and additional steps are required in data analysis. In particular, bimolecular and higher-order recombination processes can contribute to spatial broadening in a TPLM experiment – even in the absence of carrier diffusion – because of the nonlinear dependence of PL signal decay rate on local carrier density[247,251,253]. Hence, trying to fit the time-normalized spatial data to a Gaussian function and extracting the mean squared displacement in the same manner as the excitonic materials results in a curve instead of a straight line, even under normal diffusion conditions (Figure 9-1c).

Previous works have developed detailed models to describe the behavior of charge carriers in TPLM experiments[247,251,253]. Sridharan *et al.* presented a 3D model for fitting diffusion and recombination coefficients and applied that model to carrier transport in thin film perovskites[247]. In addition to accounting for potential artifacts in such measurements along with photon recycling effects, they performed a time-dependent fit of the diffusion coefficient, which suggested evidence for non-diffusive transport. Recently, deQuilettes *et al.* presented an analytical framework for modeling lateral excitonic and free carrier transport[253]. The effects of photon recycling and grain boundaries were considered, and modified mean-squared displacement formulae for extracting diffusivities were derived for specific dominant recombination pathways.

Herein, a detailed framework for numerical 3D modeling of the free charge carriers in TPLM experiments is presented. We begin with established models relating diffusivity to unimolecular and bimolecular recombination of charge carriers. We then devote particular attention to conversion between the experiment and model frame and outline the process for determining the initial condition for the solver. We describe the numerical implementation of the model in MATLAB, employing a Strang splitting algorithm[257], vectorization, dimension reduction and sparse matrix techniques[258] to speed up the solution time while maintaining reasonable accuracy. We then demonstrate the analysis capabilities enabled by faster solving speed by performing parameter analysis using a Markov Chain Monte Carlo sampler as part of the fitting algorithm on TPLM data collected from methylammonium lead bromide ($MAPbBr_3$) single crystals and bulk CdS. Using the results of these analyses, we conclude that TPLM can be used to obtain statistically confident estimates of ambipolar charge carrier diffusivities but should be coupled with other independent techniques to obtain accurate estimates for unimolecular and bimolecular recombination constants. Furthermore, depending on the experimental conditions chosen (charge carrier densities) and relative magnitudes of materials parameters, reductions can be made to the model to simplify analysis. With our open-source code for the model and the fitting algorithm (see Online Supporting Material for the paper listed at the beginning of the chapter), we present a toolbox that can be used by other members of the community to apply to their material systems.

9.2. Methods and materials

9.2.1. $MAPbBr_3$ single crystal synthesis

Methylammonium lead bromide ($MAPbBr_3$) single crystals were synthesized following the method of Saidaminov *et al.*[259] with slight modifications. 1M solution of $MABr/PbBr_2$ (1:1 molar ratio) was prepared in N,N-dimethylformamide (DMF). The solution was filtered using a 0.2 μm PTFE filter, and 2 mL of the filtered solution was placed in a 5 mL vial. The solution in the vial was immersed in an oil bath preheated to 50 °C. The temperature was increased at 10 °C/20 min until 100 °C and left for 2 hours. The solution was discarded and the crystals were collected. Then, the crystals were dried under vacuum and stored under inert atmosphere.

9.2.2. Characterization (PL, Abs, XRD) sample preparation

The characterization sample was prepared by crushing and grounding $MAPbBr_3$ crystals between two glass substrates. Grounded crystals on a glass substrate were used for downstream characterization steps.

9.2.3. Photoluminescence & Absorption Spectra

For the photoluminescence spectra, a 365 nm fiber-coupled LED (Thorlabs) was used to excite the grounded perovskite crystal sample on a glass substrate. PL spectrum was collected using an Avantes fiber-optic spectrometer. The absorption spectrum was collected by a Cary 5000 UV–vis spectrophotometer. Both were collected in air at room temperature.

9.2.4. X-ray Diffraction (XRD)

Powder XRD was performed using a PANalytical X'Pert Pro operating at 45 kV and 40 mA with a copper radiation source. HighScore software was used for background subtraction. To confirm the crystal structure, collected XRD pattern was compared with cubic $MAPbBr_3$ XRD pattern in crystal structure database (ICSD 268785).

9.2.5. CdS single crystal

Bulk CdS single crystal was purchased from MTI corporation (Richmond, CA). The <0001> oriented crystals were 5 mm x 5 mm square, 0.5 mm thick, and single-side polished. TPLM was performed on the polished surface.

9.2.6. Power-dependent photoluminescence

Power-dependent photoluminescence was measured by spectrally integrating the steady-state photoluminescence spectrum under varying excitation laser power. A 405 nm diode laser (LDH-D-C-405M, continuous wave mode) was used and its incident intensity was varied using neutral density filters (Thorlabs). The excitation beam was directed to an inverted microscope (Nikon, Ti-U Eclipse) and focused onto the surface of the crystals using an objective lens (Nikon, 40X, 0.6 numerical aperture). During experiments, all samples were mounted inside an evacuated microscope cryostat to protect from degradation due to air and water. The photoluminescence was collected in the epi configuration and filtered by a dichroic mirror and longpass filter. The emission was then directed into a spectrograph (Princeton Instruments, SP-2500), mounted with a cooled charge-coupled detector (Princeton Instruments, Pixis).

9.2.7. Time-resolved photoluminescence microscopy

Time-resolved photoluminescence microscopy (TPLM) was performed using a home-built microscope. The samples were mounted on a piezo stage (attocube, ANC350) under vacuum inside a microscopy cryostat (Montana Instruments) to protect the samples from degradation due to air and water exposure. Free carriers were generated using a 405 nm pulsed laser source (PDL 800-D, < 100 ps pulse width) that was focused down to a near diffraction-limited spot onto the surface of the crystals through an objective (Zeiss EC Epiplan-Neofluar 100X/0.85 NA). Epifluorescence from the sample was collected by the same objective lens and filtered by a dichroic mirror

(Semrock, Di02-R405) and a longpass colored glass filter (Thorlabs, FGL435M). The emission then passed through a tube lens (Thorlabs, TTL200-S8) and a telescope (Thorlabs, AC254-030-A and AC254-125-A), resulting in a 495x magnified image plane after the telescope. An avalanche photodiode (APD, Micro Photon Devices, timing resolution ~50 ps, 50 µm sensor width) was raster scanned across the image plane in one dimension. The APD was mounted on stepper-motor stages (Thorlabs) for controlling the x-y position and connected to timing electronics (PicoQuant PicoHarp 300) such that time-correlated single-photon counting measurements could be taken at each position, providing spatiotemporal photoluminescence data.

9.3. Modeling the TPLM experiment

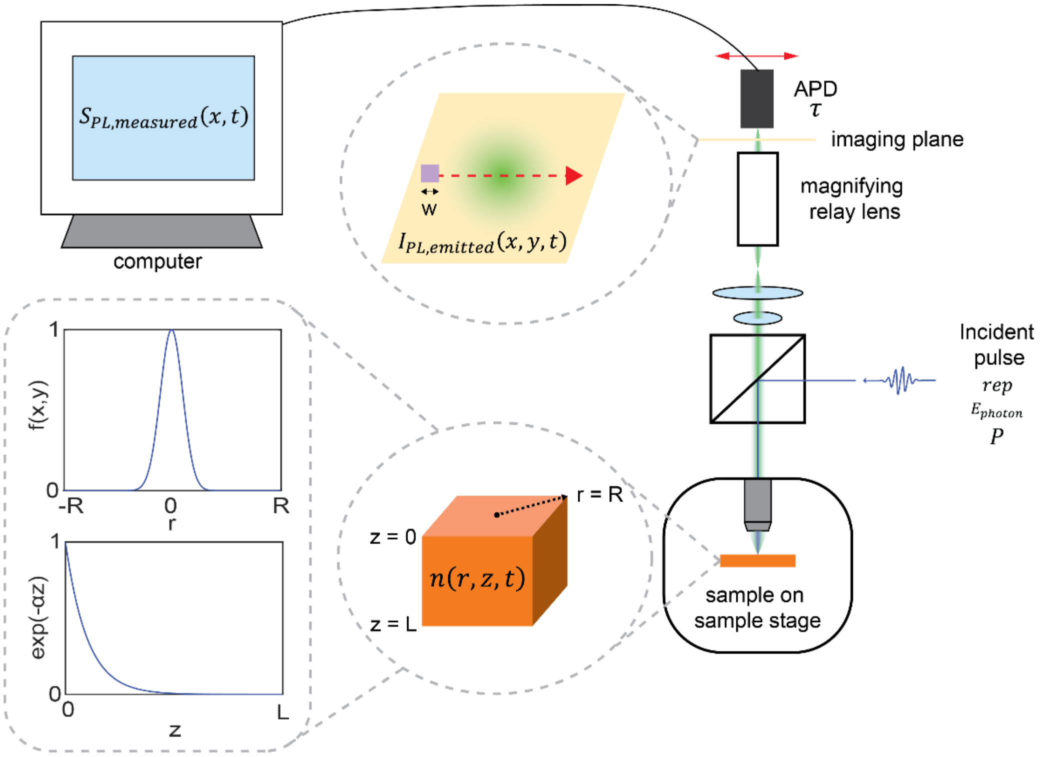

Figure 9-2. Schematic of the time-resolved photoluminescence microscopy (TPLM) experiment. An incident pulsed laser excites a sample of thickness L and lateral size R, generating a charge carrier density distribution $n(r, z, t = 0)$. The emitted photoluminescence $I_{PL,emitted}$ is enlarged to an image plane $\times$ 495, and an avalanche photodetector with sensor width w is used to scan across the image plane, giving the measured PL signal $S_{PL,measured}$ used for analysis.

A schematic of the experimental setup, along with model coordinates is shown in Figure 9-2. The incident pulsed laser is focused to a diffraction-limited spot on the sample and the emitted photoluminescence is detected by raster-scanning an avalanche photodiode (APD) across the magnified image plane to provide the temporal and spatial dimension to the data.

To extract charge carrier diffusivities from TPLM, the experimental data can be modeled using the following partial differential equation (PDE)[247,251,253]:

$$\frac{\partial n}{\partial t} = D\nabla^2 n - An - Bn^2 - Cn^3, \tag{9-1}$$

where $n = n(x, y, z, t)$ is the charge carrier density as a function of space and time [cm^{-3}], D is the diffusion constant [cm^2 s^{-1}], A is the first order recombination constant (including trapping effects) [s^{-1}], B is the second order recombination constant (including radiative recombination effects) [cm^3 s^{-1}], and C is the third order recombination constant (including Auger recombination effects) [cm^6 s^{-1}]. To simplify calculations, it is possible to neglect the third order term by experimentally choosing an incident power that is sufficiently low such that Cn^3 is negligible.

Additionally, anisotropy may be incorporated by defining different diffusivities along each spatial direction. If knowledge of electron and hole behavior is known *a priori,* Eq. (9-1) may be replaced by separate PDEs modeling the electron and hole density separately. In the absence of specific information about the nature of charge carriers within a material, we make the simplifying assumption that electrons and holes behave similarly, in which case the diffusivity D in Eq. (9-1) represents the isotropic ambipolar diffusivity, $D = \frac{2D_e D_h}{D_e + D_h}$, where the subscripts e and h denote the electron and hole respectively.

To go from the experimental frame to the model frame, we must develop equations that relate the measured PL signal $S_{PL,measured}$ to the local charge carrier density n, within the material.

From the laser power and repetition rate, we can calculate the total number of charge carriers photoexcited in the sample per laser pulse, $N_{0,total}$, as

$$N_{0,total} = \frac{P}{rep \cdot E_{photon}}(1 - \gamma), \tag{9-2}$$

where P is the laser power [W], rep is the laser repetition rate [s^{-1}], E_{photon} is the energy of the photon [J], and γ is the fraction of reflected light at the surface. This total number of charge carriers is spatially distributed in the sample at time $t = 0$ such that

$$N_{0,total} = \iiint_0^V n(x, y, z, t = 0)\, dV, \tag{9-3}$$

with V as the total volume of the sample [cm^3]. We assume that the absorbed charge carrier density at $t = 0$ can be approximated using some function that describes the distribution of charge carriers in the (x, y)-plane which depends on the shape of the laser excitation pulse used (often Gaussian), and Beer's law in the z-dimension,

$$n(x, y, z, t = 0) = n_0 \cdot f(x, y) \cdot \exp(-\alpha z), \tag{9-4}$$

where n_0 is the maximum local charge carrier density in the sample at $t = 0$ [cm^{-3}] and α is the absorption coefficient of the sample at the excitation wavelength [cm^{-1}].

An expression for the PL emitted across the sample surface can be written as

$$I_{PL,emitted}(x, y, t) = C \int_0^Z n(x, y, z, t)^2 \, exp(-\bar{\alpha} z) \, dz, \tag{9-5}$$

where C is a constant relating charge carrier density to emitted PL signal (obtained from fitting the initial time point signal), and $\bar{\alpha}$ is the absorption coefficient at the sample emission wavelength [cm^{-1}]. The actual signal that is measured from the sample $S_{PL,measured}$ at each time point is related to $I_{PL,emitted}$ by

$$S_{PL,measured}(x, t) = \int_{x-\frac{w}{2}}^{x+\frac{w}{2}} \int_{\frac{w}{2}}^{\frac{w}{2}} \int_{t}^{t+\tau} I_{PL,emitted}(x', y, t') \, dx' dy dt', \tag{9-6}$$

where w is the APD sensor width [cm], and τ is the integration time used [s]. Using these equations and fitting to the initial time data measured $S_{PL,measured}(x, t = 0)$, the initial condition for the model PDE can be obtained.

Along with the initial condition, boundary conditions also need to be specified to solve the PDE. A point of symmetry at the center of the focal plane yields

$$\left.\frac{\partial n}{\partial x}\right|_{x=0} = \left.\frac{\partial n}{\partial y}\right|_{y=0} = 0. \tag{9-7}$$

As for the edges of the sample, a general boundary condition can be used to account for

$$\left.\frac{\partial n}{\partial z}\right|_{z=0} = \frac{v_s}{D} n(x, y, 0, t), \left.\frac{\partial n}{\partial z}\right|_{z=L} = -\frac{v_s}{D} n(x, y, L, t), \tag{9-8}$$

where v_s is the surface recombination velocity. A reflective boundary can be obtained by setting the surface recombination velocity to zero. Thick samples where the absorption depth is much thinner than the thickness of the sample can be considered as semi-infinite.

Photon recycling may affect the lateral energy transport, particularly in excitonic materials that have short radiative lifetimes – or when considering very long-range transport[260]; additional details have been discussed by deQuilettes *et al*[253]. Due to the length and time scales considered for the materials of interest in this study (3D perovskites, bulk semiconductors), the effect was considered negligible in our analysis.

9.4. Numerical implementation

9.4.1. Explicit finite difference

The PDE in equation (9-1) requires an accurate but fast solver to perform detailed parameter analysis and estimation. Numerical finite differencing techniques can be used to solve the model at discrete space and time points by approximating the derivatives as finite differences.

Using an explicit finite differencing scheme, the derivatives in the PDE can be replaced by the following algebraic expressions:

$$\frac{\partial n}{\partial t} = \frac{n_{i,j,k}^{t+1} - n_{i,j,k}^{t}}{\Delta t}; \quad \frac{\partial^2 n}{\partial x^2} = \frac{n_{i+1,j,k}^{t} - 2n_{i,j,k}^{t} + n_{i-1,j,k}^{t}}{(\Delta x)^2}, \tag{9-9}$$

where the superscript t denotes the timepoint discretization and the subscripts i, j, k denote the x, y, z spatial discretization respectively. Dimensional analysis comparing the different length scales in the problem can be used to determine the best spatial step scale $\Delta x, \Delta y, \Delta z$ to use. From a fast-numerical solving standpoint, choosing Δx to match the experimental length scale avoids inaccuracies from interpolation without increasing the PDE solution time. For Δz, the relevant length scale is $\frac{1}{\alpha}$, and depending on the material and experimental wavelength used, Δz should be just under $\frac{1}{\alpha}$ to adequately capture the Beer's law decay in the z-dimension without excessively increasing the solution time.

As for the simulation time scale Δt, the relevant physical time scales in the problem include $\frac{1}{A}, \frac{N_{0,total}}{B}, \frac{(2R)^2}{D}, \frac{Z^2}{D}, \frac{Z}{v_s}$ and $\frac{1}{D\bar{\alpha}^2}$, the relative magnitudes of which are dependent on the material system being studied and experimental conditions used. However, another important factor that needs to be considered when choosing Δt is the Courant-Friedrichs-Lewy (CFL) condition for an explicit finite differencing scheme[261]. When using explicit solving methods, the condition $\frac{D\Delta t}{(\Delta x)^2} + \frac{D\Delta t}{(\Delta y)^2} + \frac{D_z\Delta t}{(\Delta z)^2} < 0.5$ must be satisfied for the solution to converge. As a result, a small Δt is usually preferred to obtain accurate solutions, but with a tradeoff for long solution times.

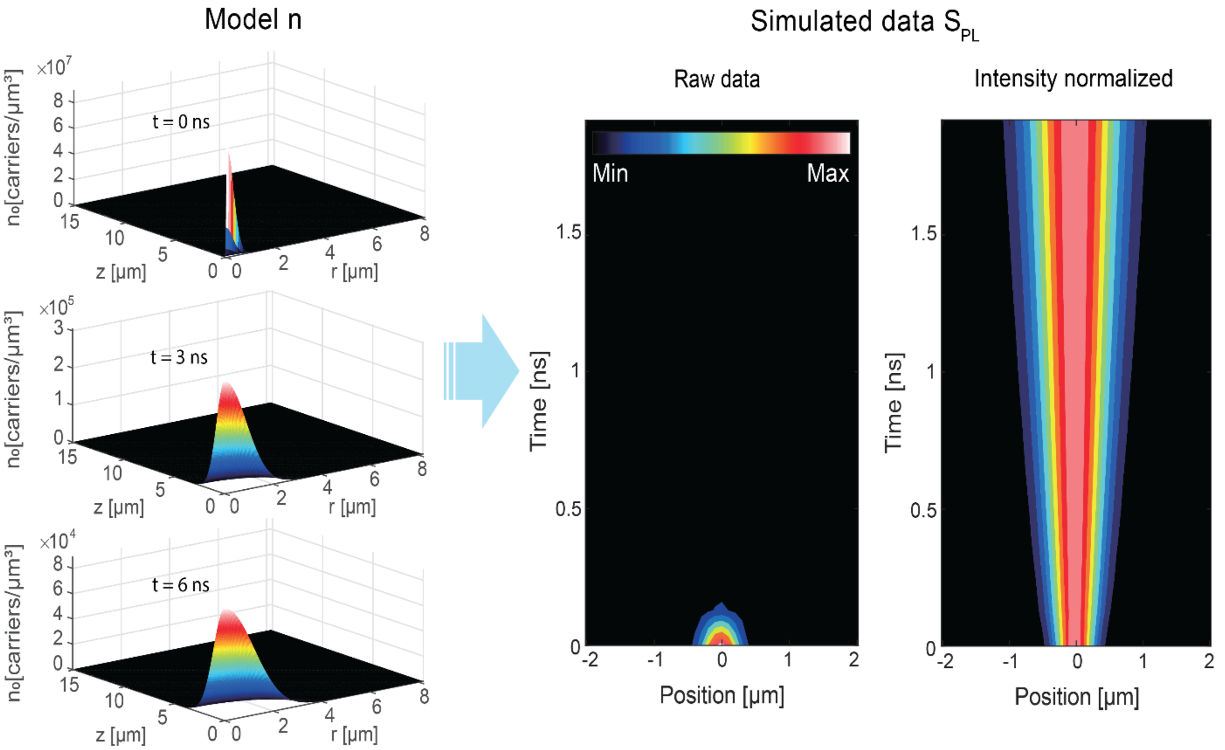

Figure 9-3. Simulated carrier dynamics and the predicted TPLM data arising from those microscopic dynamics. (left) Simulated spatial distributions of $n(r, z, t)$ at different time points using $A = 10^8 s^{-1}, B = 10^{-10} cm^3 s^{-1}, D = 1\ cm^2 s^{-1}$as the inputs for the model, when excited by a laser pulsed focused to 572 nm diameter. (right) Simulated data $S_{PL}(x, t)$ for comparison to experimental TPLM data.

9.4.2. Numerical techniques for speeding up PDE solver

To perform parameter analysis using the numerical model, an accurate but fast solver is required. Using an explicit finite difference method with the full three dimensions led to a PDE single-solve time of more than 2 hours on a typical laptop computer, which is impractical for any statistically robust fitting algorithm. Fortunately, numerical techniques can be used to speed up the solver without compromising accuracy.

For isotropic materials, making the assumption of radial symmetry and transforming to cylindrical coordinates for $n(r,z,t)$ can reduce the solving speed. To go from $n(r,z,t)$ to $S_{PL,measured}(x,t)$, the calculated $I_{PL,emitted}(r,t)$ should be interpolated at the desired x,y points and the rest of the equations introduced above can be used. Figure 9-3 demonstrates an example numerical model 3D solution at different time points and its conversion to the simulated $S_{PL,measured}$ for comparison with experimental data.

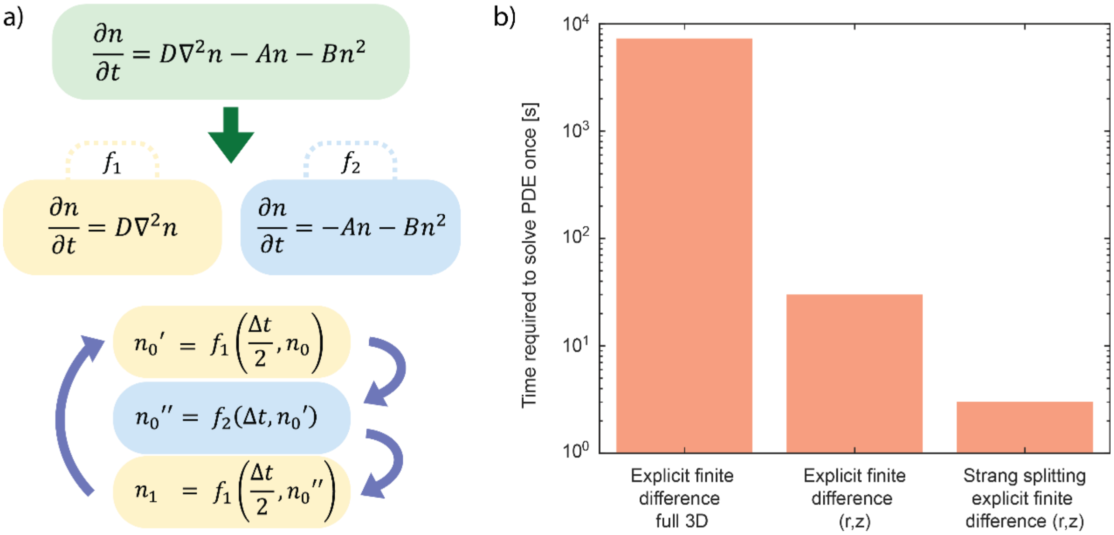

Figure 9-4. Numerical techniques for improving PDE solver speed. a) Illustration of the Strang splitting algorithm used to speed up the solution process. The full PDE can be split into two simpler problems with faster solution methods and combined to speed up the overall solution process. b) Time required to solve the PDE once on a laptop computer, comparing different numerical techniques used to speed up the code.

When a PDE can be represented as a sum of differential operators, the Strang splitting technique[257] may be beneficial. Strang splitting is particularly effective at increasing solution speed when the time scales of the two operators differ greatly. As shown in Figure 9-4a, the PDE introduced in Eq. (9-1) can be split into two separate problems f_1 and f_2, each of which can be solved faster individually than in the combined problem. f_1, which represents the diffusion problem, can be solved using finite differencing schemes, while a direct analytical solution for f_2 (the recombination problem) can be used instead. By combining the faster solvers for f_1 and f_2 in the presented scheme, a solution of error $\sim\mathcal{O}(\Delta t)$ is obtained so long as the CFL stability condition is met.

Other finite differencing schemes were also investigated for the f_1 solver, including implicit finite difference and Crank-Nicolson schemes. The advantage of these methods relative to the explicit finite difference method is that there are no stability conditions limiting the choice of Δt. However, the accuracy of the solution is still affected by the size of Δt, and the solution method requires solving $\boldsymbol{Ax} = \boldsymbol{b}$ type problems involving matrix inversions, which tend to be computationally more expensive than matrix multiplications associated with explicit methods. A comparison of the solution speed with the explicit finite differencing scheme is presented in Figure 9-5. With a combination of Strang splitting, sparse matrix formalisms[258] and vectorization using MATLAB, the fastest solution speed without compromising accuracy was found to involve an explicit finite difference-based solver for f_1 combined with an analytical solver for f_2, as demonstrated in Figure 9-4b and Figure 9-5. Overall, these approaches led to a reduction in PDE solving time from > 2 hours to only a few seconds.

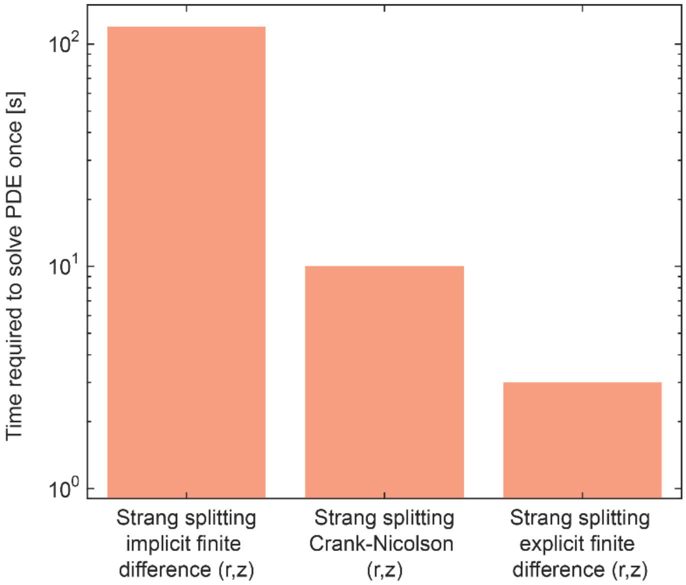

Figure 9-5. Time required to solve the PDE once on a laptop computer, comparing different finite differencing schemes for the diffusion problem using the Strang splitting technique.

9.5. Application to experimental data

With an accurate and fast solver, parameter analyses can be conducted on TPLM data collected from real materials. Lead-halide perovskites have attracted a significant amount of research efforts as a candidate for next-generation photovoltaics, among other optoelectronic devices[262–264].

Consequently, obtaining robust estimates of ambipolar diffusivity is of great interest in this material class.[227,228,235,237,248,251]

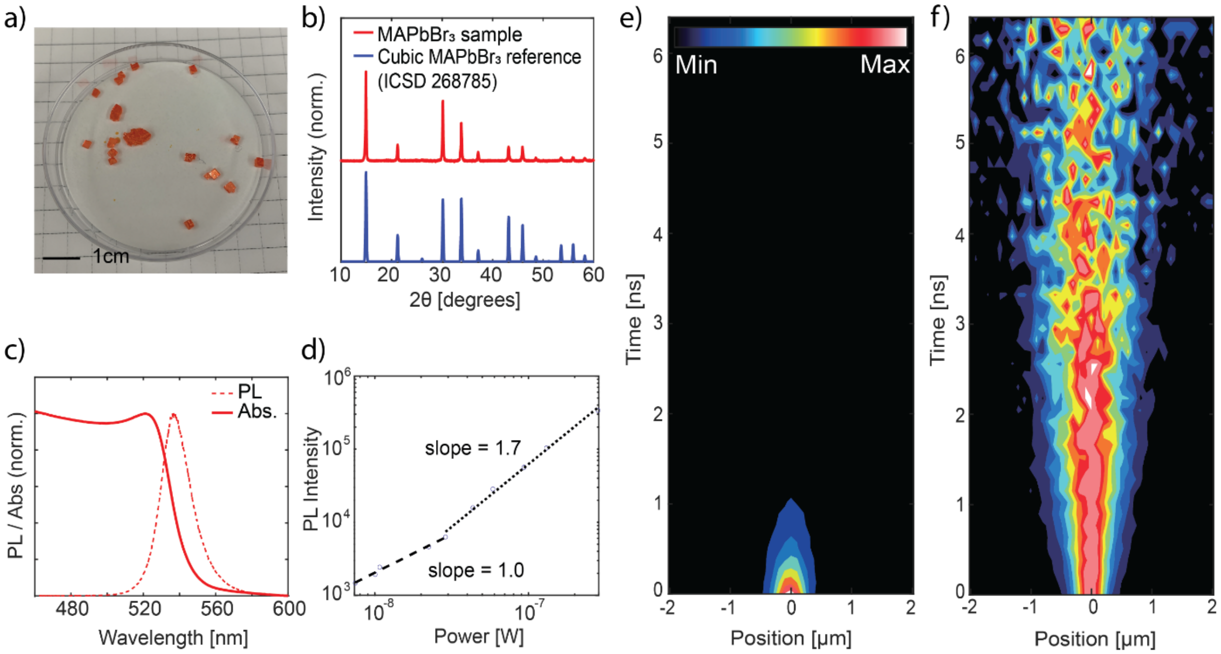

Figure 9-6. Experimental TPLM data from MAPbBr$_3$ crystals. a) Photographic image of grown MAPbBr$_3$ single crystals. b) XRD pattern of MAPbBr$_3$ sample (red) and the comparison to the cubic reference (blue). c) Absorbance (solid line) and photoluminescence (dashed line) spectra of the MAPbBr$_3$ sample. d) Power-dependent photoluminescence intensity measurement of the MAPbBr$_3$ sample. There is a transition in the gradient of the slope from 1.0 to 1.7, indicating a shift from the linear to quadratic regime. e) Raw TPLM data and f) TPLM data that has been intensity-normalized at each time point collected for the MAPbBr$_3$ sample.

Millimeter-sized single crystals of MAPbBr$_3$ were synthesized following the synthetic protocol detailed in Saidaminov *et al.*[259] with slight modifications (Figure 9-6a-c, more details available in Methods and materials section). Power-dependent photoluminescence was measured to determine the transport regime (Figure 9-6d). There is a transition from a linear to quadratic dependence of emitted photoluminescence with input power as free photogenerated charges become the dominant charge carriers within the semiconductor. To avoid sample degradation effects, we chose to excite the sample with incident power just beyond the transition regime.

Figure 9-6e-f shows the obtained TPLM data for single crystal MAPbBr$_3$. Raw data is presented on the left and intensity-normalized data is shown on the right to emphasize broadening of the spatial distribution.

TPLM experiments were also performed on commercially available single crystal CdS (see Figure 9-7 and Figure 9-8).

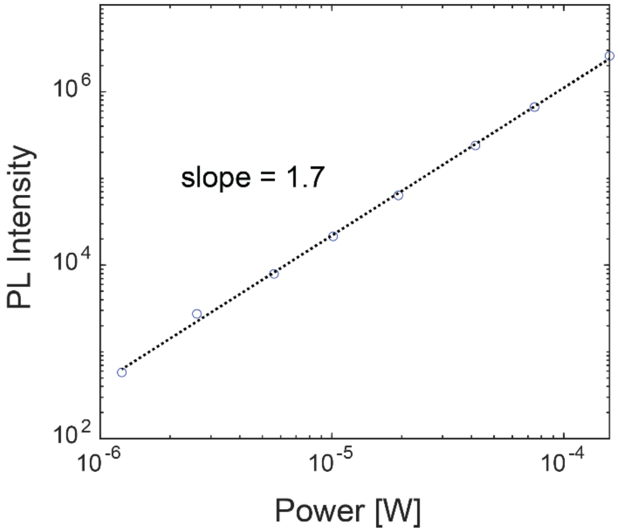

Figure 9-7. Power-dependent photoluminescence intensity measured for purchased CdS single crystal.

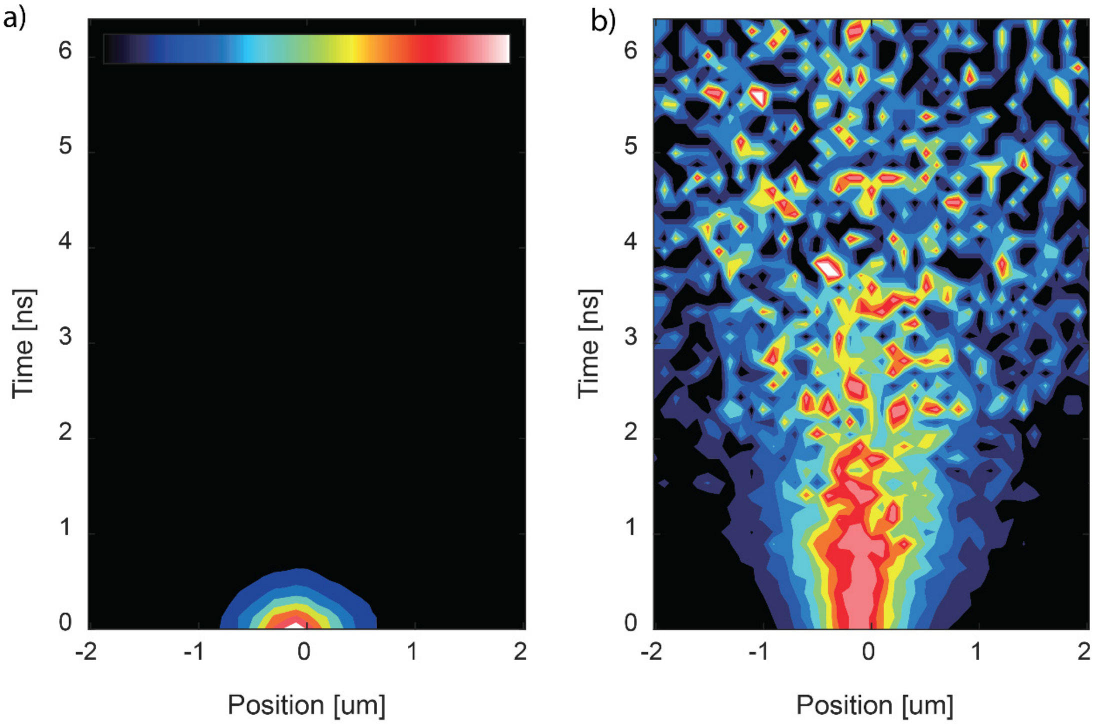

Figure 9-8. a) Raw TPLM data and b) TPLM data that has been intensity-normalized at each time point collected for the CdS sample.

Relevant experimental parameters and materials constants used for numerical solution of the PDE are presented in Table 9-1.

Table 9-1. Simulation model parameters used for single crystal $MAPbBr_3$ and CdS.

Simulation Model Parameters	$\boldsymbol{P}$ [W]	$\boldsymbol{rep}$ [s^{-1}]	$\boldsymbol{\gamma}$	$\boldsymbol{\sigma(t=0)}$ [nm]	$\boldsymbol{\alpha}$ [cm^{-1}]	$\boldsymbol{\bar{\alpha}}$ [cm^{-1}]	$\boldsymbol{\Delta x}$ [μm]	$\boldsymbol{\Delta z}$ [μm]	$\boldsymbol{\Delta t}$ [μs]	**Fitted time range** [ns]
$MAPbBr_3$	4.75×10^{-8}	2.5×10^{6}	0.2	572	2.66×10^{5} [265]	3.25×10^{3} [265]	0.101	0.0505	1.28×10^{-6}	6.4
CdS	1.52×10^{-6}	1.25×10^{6}	0.2 [266]	478	1×10^{5} [266]	3×10^{4} [266]	0.101	0.0505	1.28×10^{-6}	3.2

9.5.1. Markov Chain Monte Carlo sampler fitting algorithm

To obtain statistically robust estimates of carrier diffusivity from TPLM experimental data, we apply a Bayesian framework for parameter estimation[267–269]. This approach has advantages over the more common Levenberg-Marquardt fitting algorithms deployed in commercial fitting software, including robustness to local optima in parameter space. The method is applied here using a Markov Chain Monte Carlo (MCMC) sampler as part of the fitting algorithm. We note that fast solving speed of the model itself is essential for stochastic fitting routines – such as the MCMC sampler used here or for related genetic optimization algorithms[270] – because the PDE must be solved repeatedly using unique parameter combinations (~10^5 times for the statistical analysis presented here). MATLAB code implementing the MCMC sampler and the fast numerical solver is available in the online Supporting Information of the referenced manuscript at the beginning of this chapter.

The MCMC sampling method we applied to analyze TPLM data was adapted from the previously reported methodology by Winslow *et al.*[269] and Ashner *et al.*[271] Briefly, in the defined parameter space, a defined number of "walkers" are initialized at random starting points, with each walker representing a distinct combination of fitting parameters ($i.e.\ A, B,$ and D). Each walker takes random "steps" around the parameter space and the steps are accepted with a probability that depends on the log-likelihood function, which is determined as below.

Using the Bayesian inference framework for the probability distributions, and because we are only interested in the relative probabilities, we use

$$\frac{P\left(\theta_1 \middle| S_{PL,measured}\right)}{P\left(\theta_2 \middle| S_{PL,measured}\right)} = \frac{P\left(S_{PL,measured} \middle| \theta_1\right)}{P\left(S_{PL,measured} \middle| \theta_2\right)} \frac{P(\theta_1)}{P(\theta_2)}, \tag{9-10}$$

where θ is the set of parameters of our model $\{A, B, D\}$. The first term is the ratio of the likelihood functions and the second term is the ratio of the "priors", in which the prior knowledge about the parameter space before obtaining $S_{PL,measured}$ can be included. We assume that the probability of observing a given data point $S_{PL,measured}$ can be described by a normal distribution around the true value from the model such that $P\left(S_{PL,measured} \middle| \theta\right) \sim \prod_{x,t} e^{-\left(\frac{S_{PL}(x,t;\theta) - S_{PL,measured}(x,t)}{\sigma_e(x,t)}\right)^2}$. The natural logarithm of the likelihood function can then be expressed as: $\log\left(P\left(S_{PL,measured} \middle| \theta\right)\right) \sim -\sum_{x,t} \left(\frac{S_{PL}(x,t;\theta) - S_{PL,measured}(x,t)}{\sigma_e(x,t)}\right)^2$. The log-likelihood function includes the variance at $\sigma_e^2(x,t)$ at each of the data points, which can be used to give weightings to different data points. (Note that the variance $\sigma_e^2(x,t)$ in the likelihood function is different from the variance of the spatial distribution obtained experimentally in a transient microscopy experiment). As for the prior, we assume a flat distribution within an upper and lower limit based on both what is physically reasonable for our material system (*i.e.* no negative values for A, B or D), and on order of magnitude estimates for parameters obtained previously from literature.

A two-part search process is applied to find the best combination of model parameters $\{A, B, D\}$ that maximizes the log-likelihood function in the defined parameter space. In the first part, the walkers are initialized randomly throughout the entire parameter space with the goal of searching for the global optimum and narrowing down the parameter space. In the second part, a new set of walkers are randomly dispersed in a ball of parameter space that is near the maximum likelihood estimate (MLE) determined in the first part. The second part provides statistical information about the parameters including their uncertainties and correlations.

Objective function #1: $\log\left(P_1\left(S_{PL,measured} \middle| \theta\right)\right) \sim -\sum_{x,t} \left(\frac{S_{PL}(x,t;\theta) - S_{PL,measured}(x,t)}{S_{PL,measured}(x,t)}\right)^2$

Objective function #2: $\log\left(P_2\left(S_{PL,measured} \middle| \theta\right)\right) \sim -\sum_{x,t} \left(S_{PL}(x,t;\theta) - S_{PL,measured}(x,t)\right)^2$

A key decision in any fitting routine is deciding what should be optimized, known as the objective function. To apply the MCMC sampling method to our model, two different objective functions with different values of $\sigma_e(x,t)$ were considered. For objective functions #1 and #2, we used $\sigma_e(x,t) = S_{PL,measured}(x,t)$ and $\sigma_e(x,t) = 1$, respectively.

Objective function #1 normalizes the error signal by the measured intensity $S_{PL,measured}(x,t)$ at each space and time point, while objective function #2 considers the absolute error. In effect, objective function #1 considers the fractional error such that all time and space points have equal weightings, while objective function #2 gives a greater weighting to the earlier time points where the experimentally measured signal is greatest.

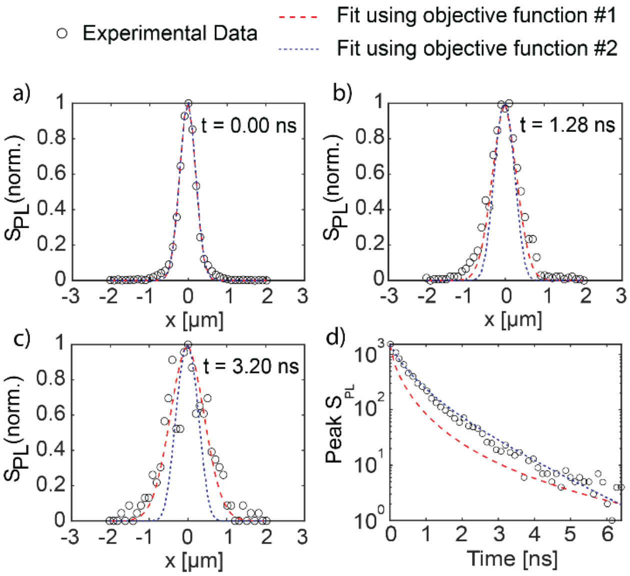

Figure 9-9. Fit comparisons between the spatially-normalized experimental data for the MAPbBr$_3$ crystals (circles) and spatially-normalized simulated data using MLE parameters obtained from the MCMC method with objective functions #1 (red) and #2 (blue) at a) $t = 0.00$ ns, b) $t = 1.28$ ns, c) $t = 3.20$ ns. d) Fit comparisons of the spatial maximum at each time point of the experimental data and the simulated data.

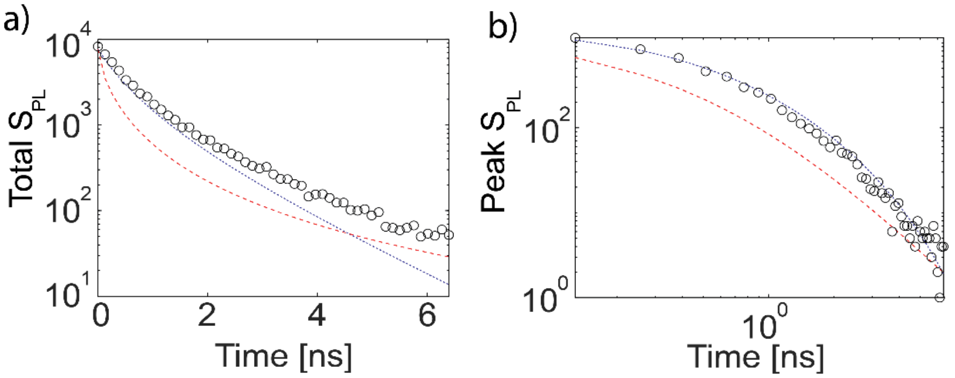

Figure 9-10. Fit comparisons between the spatially-normalized experimental data for the MAPbBr$_3$ crystals (circles) and spatially-normalized simulated data using MLE parameters obtained from the MCMC method with objective functions #1 (red) and #2 (blue) comparing a) the integrated total PL signal S$_{PL}$ and b) the spatial maximum at each time point on a log-log scale. These plots are the same as those plotted in Figure 9-9, but presented in alternate manners.

Figure 9-9 compares the obtained MLE fits for the TPLM data from the $MAPbBr_3$ crystals using each objective function. The fit comparisons between the spatially-normalized data (Figure 9-9a-c) reveal that objective function #1 is better at capturing the spatial broadening that occurs over time. However, objective function #2 is better at capturing the overall signal decay (Figure 9-9d).

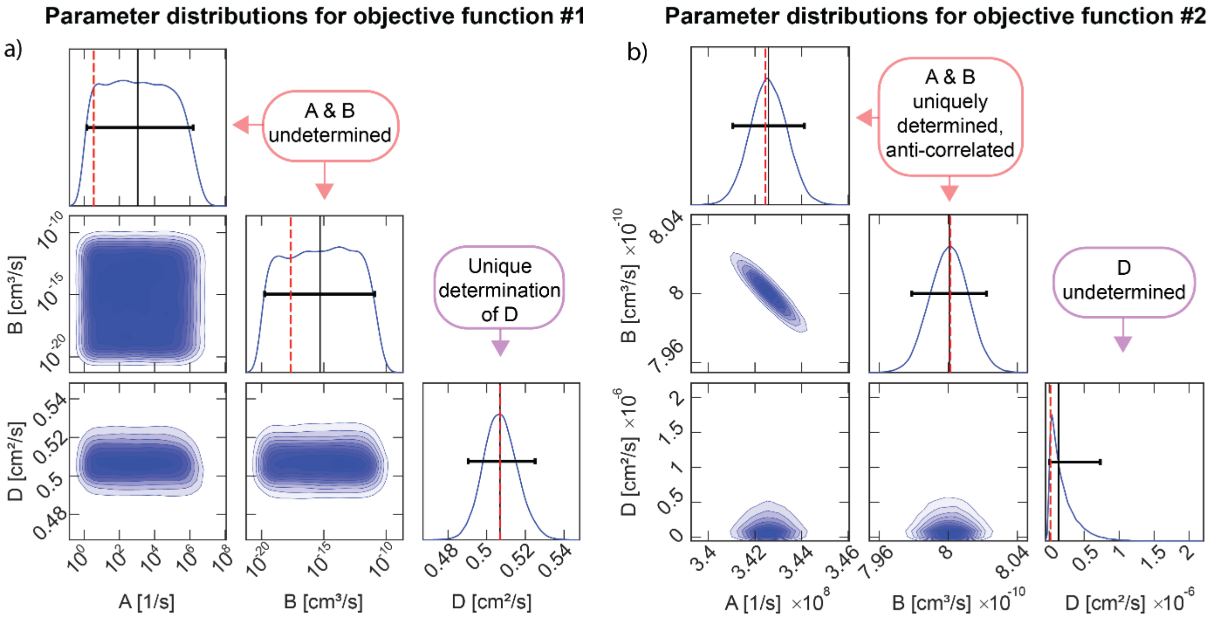

Figure 9-11. Corner plots showing parameter distributions obtained from analysis of $MAPbBr_3$ crystal data for a) objective function #1 and b) objective function #2. The blue curve on the plots along the diagonal demonstrate the uncertainty distributions for each parameter A, B and D. The red dashed line indicates the MLE, the vertical black line shows the median, the horizontal black bar indicates the uncertainty for a 95% confidence interval. The off-diagonal plots show the correlation between the pairs of parameters.

The difference between the two objective functions can be better understood by observing the parameter statistical distributions and cross-correlations obtained from the MCMC analysis (Figure 9-11). In Figure 9-11a, we see that objective function #1 results in flat distributions for A and B, while providing a uniquely determined value of D. The determined MLE with 95% confidence intervals for the uncertainty of $D_{MLE,\#1} = 0.51 \pm 0.02\ cm^2 s^{-1}$, which is consistent with literature reports of ambipolar diffusivities in $MAPbBr_3$ measured using light-induced transient grating experiments[272] and on the same order of magnitude when calculated from mobilities obtained using Hall mobility measurements[273]. The flat parameter distributions for A and B indicate that these parameters are over-specified for the model, resulting in undetermined values. In other words, A and B could be arbitrarily varied within the indicated range without changing the quality of the fit. This makes intuitive sense as parameters A and B are primarily responsible for determining the rate of PL signal decay over time. Since objective function #1 considers the intensity-normalized error at every time point, this objective function is less sensitive to signal decay, as shown graphically in Figure 9-9d.

Using objective function #2, we find that A and B are uniquely determined and anti-correlated. The obtained MLE values with 95% confidence intervals for the uncertainty were $A_{MLE,\#2} = (3.42 \pm 0.01) \times 10^{8}\ s^{-1}$ and $B_{MLE,\#2} = (8.00 \pm 0.02) \times 10^{-10}\ cm^{3}s^{-1}$. B is on the same order of magnitude with literature measurements using transient photoluminescence[272] and transient absorption techniques[274], however, A is 3-4 orders of magnitude larger than the values obtained from the same literature measurements. Since A includes the effects of trap recombination, it is sample-dependent and dependent on the growth conditions. However, the obtained MLE D value approaches zero and is undetermined. Again, these results make intuitive sense given the choice of objective function. Objective function #2 emphasizes the overall signal intensity, which is most sensitively determined by parameters A and B. However, this accuracy in tracking the overall signal decay (Figure 9-9d) is obtained at the expense of accuracy in predicting the spatial broadening of the PL signal at later times (Figure 9-9c), which is mostly determined by the diffusivity D. The negative correlation between A and B can also be understood intuitively – since increasing either A or B both results in faster signal decay, a greater value of A would result in a smaller value of B for the fit, and vice versa. A D value near zero could also explain the unreasonably large A value found by objective function #2: diffusion acts to lower the local carrier density, leading to a transient decay in the total photoluminescence signal; if $D \approx 0$, then A must increase to account for signal decay.

We also applied the MCMC fitting algorithm to TPLM data experimentally obtained for CdS single crystals (see Figure 9-12 to Figure 9-15). Similar to the $MAPbBr_3$ analyses, unique determination of $D_{MLE,\#1} = 1.61\ \pm 0.03\ cm^{2}s^{-1}$ was obtained when using objective function #1. This value is again comparable with literature reported values of ambipolar diffusivities obtained using light-induced transient grating[275,276] or calculated from Hall mobilities[277,278]. Interestingly, with objective function #2, unlike in the case for $MAPbBr_3$, B was undetermined for CdS. Given the experimental conditions used, it is likely that the contribution from bimolecular recombination is negligible relative to the other terms. The obtained estimates for the 'determined' parameters were $A_{MLE,\#2} = (1.27 \pm 0.01) \times 10^{9}\ s^{-1}$ and $D_{MLE,\#2} = (1.20\ \pm 0.08) \times 10^{-2}\ cm^{2}s^{-1}$; the estimate for A is also larger than the literature reported value using single-beam Z-scanning[279], while D is underestimated by objective function #2. The analysis reveals a negative correlation between A and D for objective function #2 – intuitively, both A and D contribute to decay of the measured PL signal, hence a larger A would result in a lower D estimate, and vice versa. A summary of the obtained maximum likelihood estimates of the parameters and a comparison against literature values is provided in Table 9-2.

Table 9-2. Maximum likelihood estimates of parameters A, B and D obtained from objective function #1 and #2 for $MAPbBr_3$ single crystal and bulk CdS. The uncertainties were obtained using 95% confidence intervals. Comparisons to literature are provided. *The ambipolar diffusivity for CdS from Hall mobility measurements were obtained by first calculating the electron and hole diffusivities from the respective mobilities obtained through Hall mobility measurements using $D_{e/h} = \mu_{e/h}k_BT/q$, where μ is the mobility, k_B is the Boltzmann constant, T is the temperature and q is the charge of the electron. Then, they were inserted into $D = \frac{2D_eD_h}{D_e+D_h}$. For $MAPbBr_3$, the reported charge carrier mobility was used directly. **The unimolecular recombination constant was obtained from recombination lifetimes τ using $A = 1/\tau$.

Model parameters	**$MAPbBr_3$**			**CdS**		
	A [s^{-1}]	***B*** [$cm^3\ s^{-1}$]	**D** [$cm^2\ s^{-1}$]	***A*** [s^{-1}]	***B*** [$cm^3\ s^{-1}$]	**D** [$cm^2\ s^{-1}$]
Objective function #1 (this work)	-	-	$0.51\ \pm 0.02$	-	-	$1.61\ \pm 0.03$
Light-induced transient grating	-	-	0.45 ± 0.08 [272]	-	-	1.6 [275] 1.7 ± 0.2 [276]
Hall mobility measurements *			≈ 0.26 [273]	-	-	1.75 [277,278]
Objective function #2 (this work)	$(3.42 \pm 0.01) \times 10^{8}$	$(8.00 \pm 0.02) \times 10^{-10}$	-	$(1.27 \pm 0.01) \times 10^{9}$	-	$(1.20\ \pm 0.08) \times 10^{-2}$
Transient PL	$(7 \pm 1) \times 10^{5}$ [272]**	$(6 \pm 1) \times 10^{-10}$ [272]	-	-	-	-
Transient Absorption	$(3.7 \pm 0.2) \times 10^{4}$ [274]**	$(4.9 \pm 0.2) \times 10^{-10}$ [274]	-	-	-	-
Single-beam Z-scan technique	-	-	-	$(2.8 \pm 0.7) \times 10^{8}$ [279]**	-	-

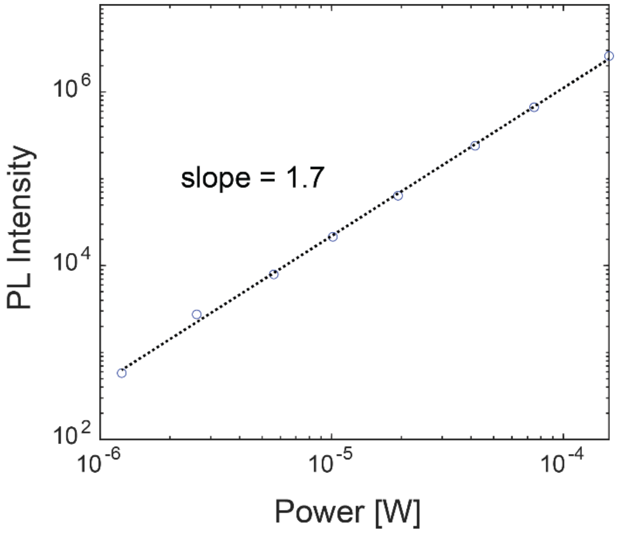

Figure 9-12. Power-dependent photoluminescence intensity measured for purchased CdS single crystal.

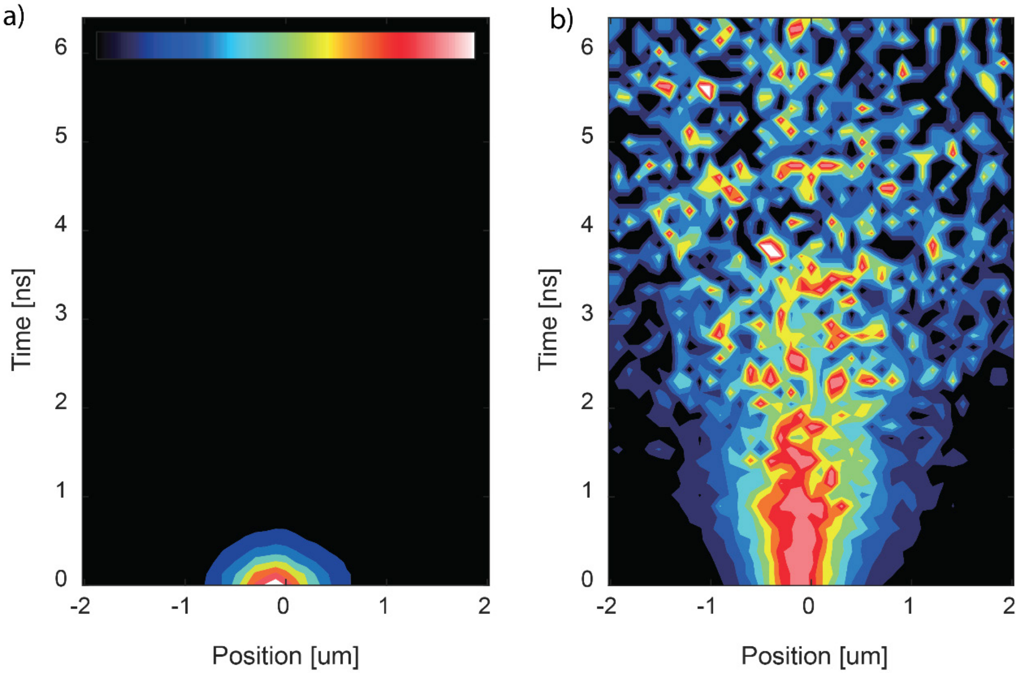

Figure 9-13. a) Raw TPLM data and b) TPLM data that has been intensity-normalized at each time point collected for the CdS sample.

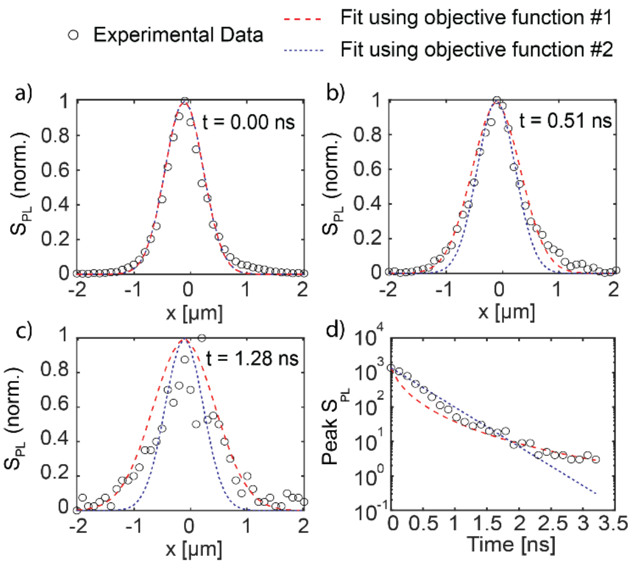

Figure 9-14. Fit comparisons for the CdS sample between the spatially-normalized experimental data (circles) and spatially-normalized simulated data using MLE parameters obtained from the MCMC method with objective functions #1 (red) and #2 (blue) at a) $t = 0.00$ ns, b) $t = 0.51$ ns, c) $t = 1.28$ ns. d) Fit comparisons of the spatial maximum at each time point of the experimental data and the simulated data.

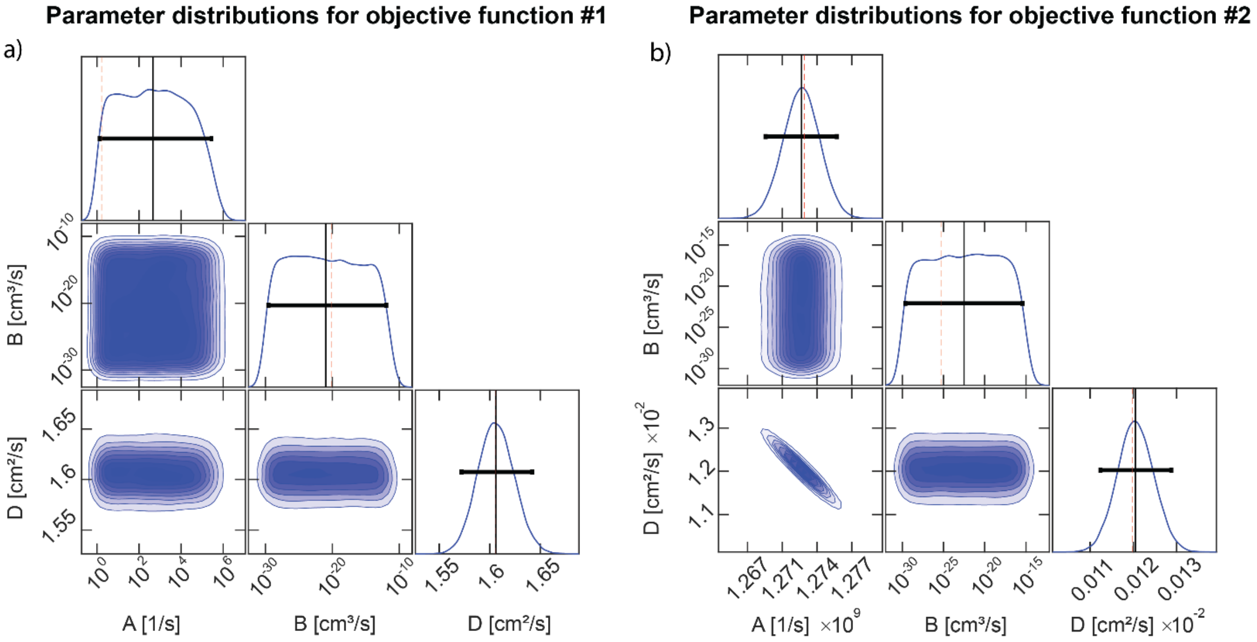

Figure 9-15. Corner plots showing parameter distributions of the CdS sample for a) objective function #1 and b) objective function #2. The blue curve on the plots along the diagonal demonstrate the uncertainty distributions for each parameter A, B and D. The red dashed line indicates the MLE, the vertical black line shows the median, the horizontal black bar indicates the uncertainty for a 95% confidence interval. The off-diagonal plots show the correlation between the pairs of parameters.

9.6. Considerations when using the model

It is important to note that compared to a Levenberg-Marquardt (LM) fitting technique, the MCMC sampling analysis identifies undetermined parameters where the LM fitting technique returns a single best-fit value even if the parameters are truly undetermined for the specific objective function. To demonstrate, two built-in functions using the LM algorithm from MATLAB were used to determine the 'best fit' parameters for $MAPbBr_3$ and compared to the MCMC sampling method. The LM fitting technique returned 'best fit' values for all parameters; however, these values depended on what initial guess was provided to the solver, settling on local optima instead of finding the true global optimum parameter values. Parameter variances and cross-correlations could also be obtained from the LM method by calculating the variance-covariance matrix; however, some of the results were unphysical. Nevertheless, the LM fitting algorithms present significant speed benefits over the MCMC fitting algorithm, and can provide useful estimates of materials parameters if sufficient prior knowledge of the material exists to generate accurate initial guesses.

9.6.1. Comparison between built-in MATLAB fitting algorithms and the MCMC fitting algorithm

MATLAB has two built-in nonlinear fitting algorithms 'lsqcurvefit' and 'nlinfit'. The algorithm can be set to Levenberg-Marquardt for 'lsqcurvefit' as one of the input settings for the function while 'nlinfit' uses a Levenberg-Marquardt algorithm by default.

Using an initial guess of $A = 10^8\ s^{-1}$, $B = 10^{-10}\ cm^3s^{-1}$ and $D = 1\ cm^2s^{-1}$ resulted in 'best fit' parameter values presented in Table 9-3 (with comparisons to the MCMC predicted values provided).

Table 9-3. 'Best fit' parameter values obtained from MATLAB's lsqcurvefit and nlinfit built-in functions using $A = 10^8\ s^{-1}$, $B = 10^{-10}\ cm^3 s^{-1}$ and $D = 1\ cm^2 s^{-1}$ as the initial guess, with comparisons to the maximum likelihood estimate parameter values obtained using the Markov Chain Monte Carlo analysis using objective functions #1 and #2 from the main text.

Model parameters	**MAPbBr$_3$**		
	A [s^{-1}]	***B*** [cm^3 s^{-1}]	***D*** [cm^2 s^{-1}]
lsqcurvefit	2.15×10^7	2.34×10^{-14}	0.2
nlinfit	1×10^8	9.16×10^{-12}	0.24
Objective function #1 (MCMC)	-	-	0.51 ± 0.02
Objective function #2 (MCMC)	$(3.42 \pm 0.01) \times 10^8$	$(8.00 \pm 0.02) \times 10^{-10}$	-

Changing the initial guess results in different 'best fit' values:

Table 9-4. 'Best fit' parameter values obtained from MATLAB's lsqcurvefit and nlinfit built-in functions using different values for A, B and D for the initial guess.

Initial Guess			**lsqcurvefit**			**nlinfit**		
A [s^{-1}]	***B*** [cm^3 s^{-1}]	***D*** [cm^2 s^{-1}]	***A*** [s^{-1}]	***B*** [cm^3 s^{-1}]	***D*** [cm^2 s^{-1}]	***A*** [s^{-1}]	***B*** [cm^3 s^{-1}]	***D*** [cm^2 s^{-1}]
10^8	10^{-10}	1	2.15×10^7	2.34×10^{-14}	0.2	1×10^8	9.16×10^{-12}	0.24
10^6	10^{-12}	0.5	5.57×10^5	2.34×10^{-14}	0.21	1×10^6	-6.98×10^{-11}	0.76
10^{10}	10^{-8}	5	1.58×10^8	3.47×10^{-14}	0.1	1×10^{10}	-4.96×10^{-8}	-114.04

Note that nlinfit does not allow input of bounds on the parameters, therefore resulting in unphysical solutions for the best fit values in certain cases.

Parameter variances and cross-correlations can be obtained by calculating the variance-covariance matrix. The resultant matrices obtained from lsqcurvefit and nlinfit using the initial guess of $A = 10^8\ s^{-1}$, $B = 10^{-10}\ cm^3 s^{-1}$ and $D = 1\ cm^2 s^{-1}$ are presented below:

$$VCV_{lsqcurvefit} = \begin{bmatrix} 2.51 \times 10^{17} & 3.78 & -1.76 \times 10^8 \\ 3.78 & 1.30 \times 10^{-16} & -3.93 \times 10^{-9} \\ -1.76 \times 10^8 & -3.93 \times 10^{-9} & 0.15 \end{bmatrix}$$

$$VCV_{nlinfit} = \begin{bmatrix} 7.00 \times 10^{-61} & 9.88 \times 10^{-42} & 1.23 \times 10^{-51} \\ 9.88 \times 10^{-42} & 1.39 \times 10^{-22} & 1.74 \times 10^{-32} \\ 1.23 \times 10^{-51} & 1.74 \times 10^{-32} & 2.17 \times 10^{-42} \end{bmatrix}$$

The diagonal elements of the variance-covariance matrix give the individual parameter variances, while the off-diagonal elements give the parameter cross-correlations, with the parameter ordering set to A, B followed by D. The variances may be compared against the 95% confidence intervals obtained from the MCMC analysis – we see hugely varying differences in the orders of magnitudes between the two built-in functions and our analyses, most likely as the built-in functions cannot capture the undefined nature of some of the parameters.

As for the cross-correlations, lsqcurvefit suggests negative correlations between parameters that make physical sense, however, nlinfit does not.

9.6.2. Alternative objective functions for MCMC analysis

Given the strong dependence of the fitting results on the choice of objective function, alternative values for the estimated experimental error $\sigma_e(x,t)$ were also considered. To estimate experimental error, a combination function for $\sigma_e(x,t)$ involving the sum of the measurement shot noise, $\sqrt{S_{PL,measured}(x,t)}$ which scales as the square root of the measured signal, and the detector noise signal (≈1 dark count per bin per acquisition period), was used such that $\sigma_e(x,t) = \sqrt{S_{PL,measured}(x,t)} + 1$. This places a greater weighting on early time data whilst also accounting for broadening effects. The resulting parameter analyses led to the similar results as with objective function #2, with both A and B determined for MAPbBr$_3$, but D undetermined. Alternative scalings for $\sigma_e(x,t)$ were also tested, the most interesting of which $\sigma_e(x,t) = \left(S_{PL,measured}(x,t)\right)^{0.75} + 1$ resulted in unique estimates for both A and D, but B remained undetermined for MAPbBr$_3$. While B has been shown to contribute to the broadening[247,251,253], it is likely that with the experimental conditions used for this sample, the contribution from B is less significant than D.

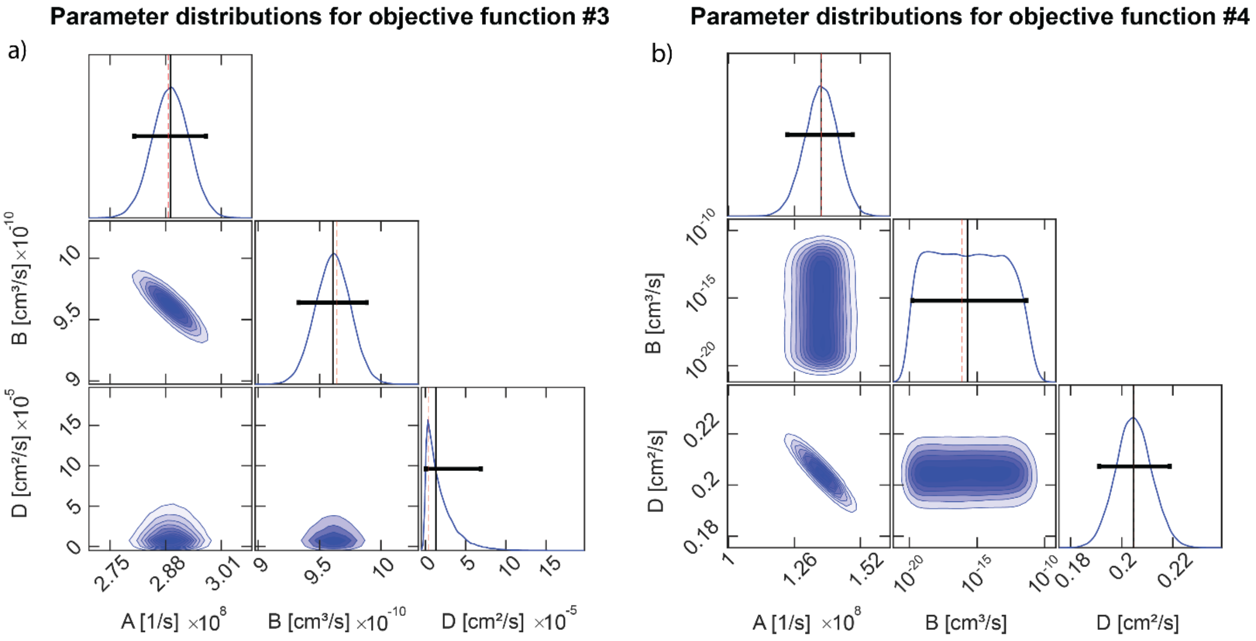

Figure 9-16. Corner plots showing parameter distributions of the MAPbBr$_3$ sample for a) objective function #3 and b) objective function #4. The blue curve on the plots along the diagonal demonstrate the uncertainty distributions for each parameter A, B and D. The red dashed line indicates the MLE, the vertical black line shows the median, the horizontal black bar indicates the uncertainty for a 95% confidence interval. The off-diagonal plots show the correlation between the pairs of parameters.

9.6.3. Simplifications to the model

While unique estimates of D from TPLM data were possible, the parameter analyses suggest that A and B are over-specified if using objective function #1. Indeed, performing an order of magnitude analysis reveals that, based on the experimental and material conditions used, the $D\nabla^2 n$ term in the PDE dominates over the other two terms. In fact, for many material systems of interest, simplifications to the fitting model can be made by judiciously selecting a desirable n_0 *via* the laser power used for the experiment.

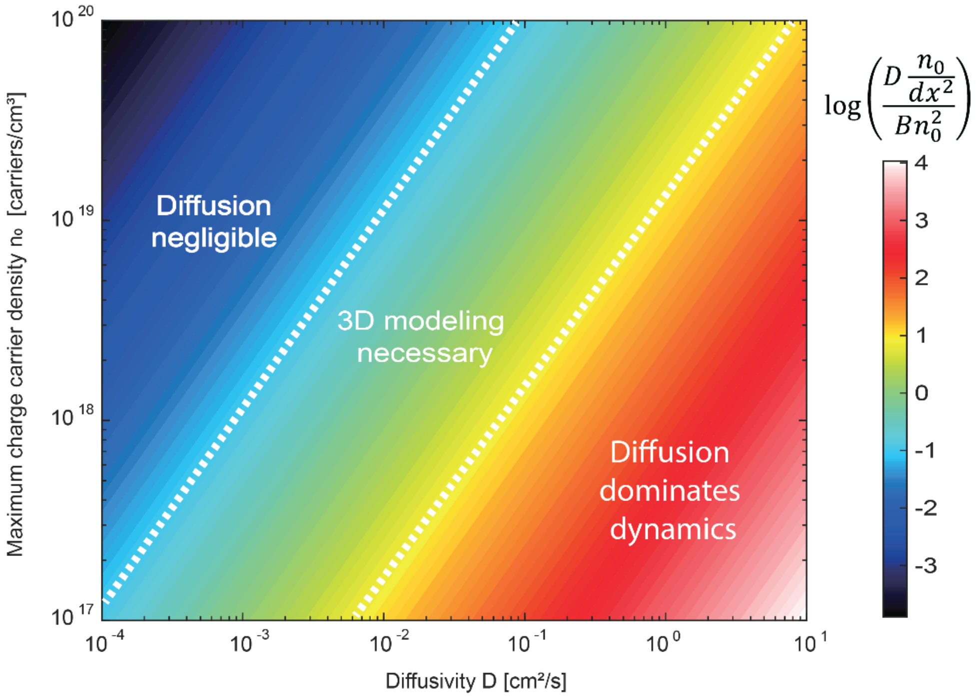

Figure 9-17. Color plot showing how the logarithm of ratio between the diffusivity term and the bimolecular recombination term $log\left(\frac{D\frac{n_0}{dx^2}}{Bn_0^2}\right)$ varies depending on the maximum charge carrier density n_0 and the diffusivity D. This plot was obtained using $B = 5.5 \times 10^{-10} cm^3 s^{-1}$ and $dx = 1/\alpha$ using the α for MAPbBr₃. The region in the upper left corner is where diffusion can be considered negligible in the model. The bottom right region is where diffusion dominates the dynamics such that the recombination terms can be considered negligible. The central region is where 3D modeling including all three parameters is necessary.

Figure 9-17 shows that depending on the value of the ratio between the diffusivity and the bimolecular recombination terms $\frac{D\frac{n_0}{dx^2}}{Bn_0^2}$, it is possible to make simplifications to the model. For example, if the diffusion term dominates (over an order of magnitude), such as in $MAPbBr_3$ and CdS single crystals, the model can be simplified to $\frac{\partial n}{\partial t} = D\nabla^2 n$ and the diffusivity may be obtained from TPLM data without having to consider the effects of recombination on the charge carrier density. This is consistent with the conclusions drawn by deQuilettes *et al*[253]. On the other hand, if the diffusion term is negligible, then a unique determination of the diffusivity from TPLM data will be challenging. For materials where the diffusion and bimolecular recombination terms are of similar magnitude, it is recommended to use the full model approach as detailed in this chapter with the code provided in the online supporting information of the paper referenced at the beginning of this chapter.

In the case of new material systems where relative estimates of the orders of magnitudes of A, B and D are unknown, it is recommended to first use alternative techniques, such as thickness-dependent transient photoluminescence with a defocused laser beam[280,281,247], to obtain estimates of A and B, before using TPLM and the full model to estimate D.

Chapter 10.
Transient second harmonic generation setup development

10.1. Introduction

For the singlet fission-sensitized silicon samples, we hypothesize that the mechanism of triplet exciton sensitization from tetracene is through a sequential charge transfer process, where the electron is donated first to silicon by the donor layer, followed by a hole tunneling process, as detailed in Chapter 7. For a deeper mechanistic understanding of the sensitization process and obtaining rate information for the carrier tunneling steps, ultrafast pump-probe spectroscopy techniques with 100s of fs resolution can be used. Later in Chapter 11, we use transient absorption and reflection measurements to study early time dynamics, and transient photoluminescence to study later time dynamics of the singlet fission-sensitized silicon samples. Both of these techniques are dominated by the signals from the bulk materials involved in the sample stack. As we are interested in studying the interfacial charge transfer from tetracene to silicon, we use transient second harmonic generation (tr-SHG) to study the charge transfer dynamics across the interface. In particular, we are interested in using the sensitivity of the SHG signal to formation of interfacial electric fields which can greatly amplify the second harmonic signal observed through an electric field-induced second harmonic (EFISH) contribution[214,198]. The resulting electric field may also induce coherent phonon vibrations in silicon depending on energy alignments in the structure, which can be observed through oscillations in the tr-SHG data[198].

Tetracene and silicon are both centrosymmetric materials[282]; thus, we expect most of the measured SHG signal to come from the interface between these two layers. The other thin interfacial layers are expected to be amorphous.

While charge transfer is expected to occur over fast timescales (~ps), we also observe evidence of charge trapping over very long timescales (~ mins, see Chapter 5) in our samples. SHG can also be used to study this charge trapping phenomena, as demonstrated on oxide-silicon surfaces[216,217,283].

In this chapter, we detail the process, decisions made and challenges encountered when building the z-polarized SHG microscopy setup and the tabletop ultrafast pump-probe tr-SHG setup for studying the interfacial charge transfer for singlet fission-sensitized silicon.

10.2. Z-polarized second harmonic generation microscopy

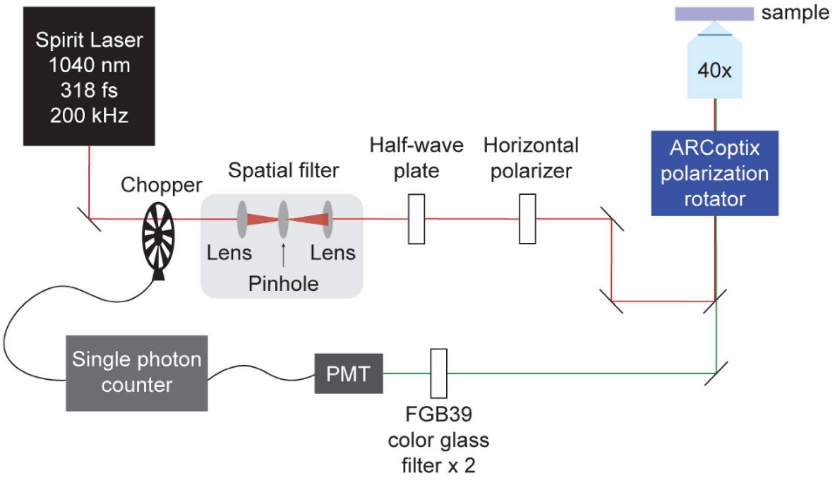

Figure 10-1. Schematic of the z-polarized second harmonic generation microscopy setup built for this work.

Building a second harmonic generation setup using a microscope provides the ability to obtain spatially-resolved SHG image maps of the sample, which may have potential applications for devices which have interesting lateral features[284,285], as well as imaging biological samples[286]. The additional focus provided by microscope objective lenses can also enable achievement of high excitation power densities which are necessary for observing SHG signals.

In the existing SHG microscopy setup, the polarization of the laser beam entering the microscope is linearly polarized. After the beam passes through the objective lens, the polarization of the beam focused on the sample will be in the x-y plane, parallel to the sample surface, as shown in Figure 10-2a. In order to study charge transfer across interfaces in the sample stack, we are most interested in probing the electric field formed across the interface, *i.e.* the polarization of the probe beam should have a longitudinal component to probe the plane perpendicular to the sample surface.

This can be achieved by using a beam that is radially polarized, which results in an output beam through the objective lens with a strong z-polarized component (Figure 10-2b)[287–289].

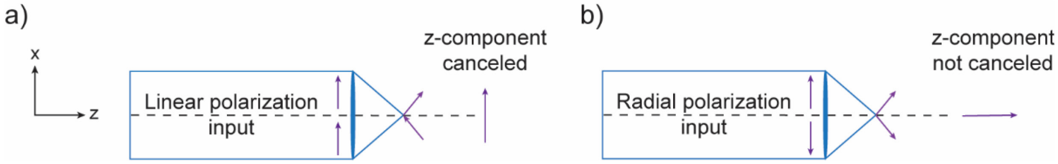

Figure 10-2. Polarization of light after passing through the objective lens in a microscope. a) Using a beam with linear polarization results in an output beam with no z-component. b) Using a beam with radial polarization results in an output beam with some z-component.

10.2.1. Radial polarization converter

Conversion of a beam of linearly polarized light to radially polarized light can be achieved by using a liquid-crystal radial polarization converter[290]. In our setup, we used the ARCoptix radial polarization converter with an electrically controlled polarization rotator that enables switching between azimuthal and radial polarization outputs.

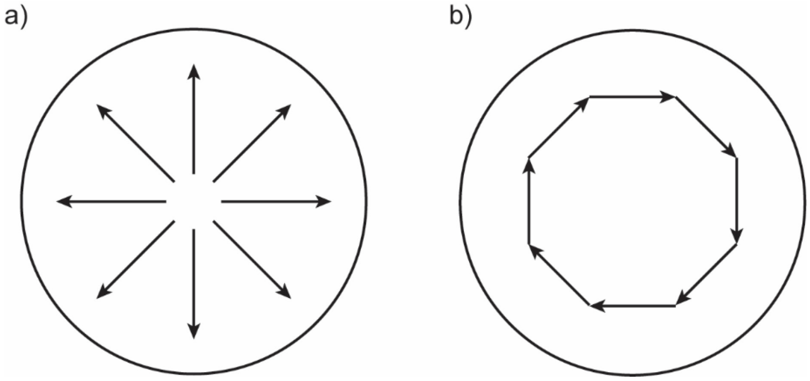

Figure 10-3. Polarizations of light achievable by the ARCoptix radial polarization converter. a) Radially polarized light. b) Azimuthally polarized light.

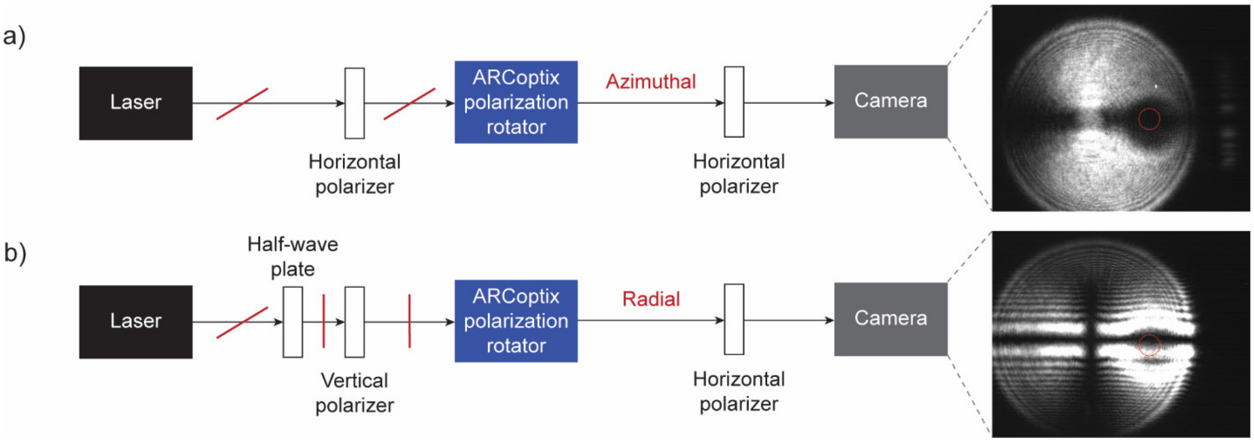

Figure 10-4. Optical setup used to test polarization outputs from the ARCoptix polarization rotator. a) Using a horizontally polarized input beam generates a pattern on the camera (right) that is brighter in the center top and bottom regions of the beam, indicating an azimuthal polarization output. b) Using a vertically polarized input beam generates a pattern on the camera (right) that is darker in the center top and bottom regions of the beam, indicating a radial polarization output.

We verify radial polarization output from the ARCoptix radial polarization converter by using the setup depicted in Figure 10-4 and imaging the beam on a camera. Careful positioning of linear polarizers before and after the polarization rotator enables confirmation of the beam polarization, and is necessary to confirm as both the radial and azimuthally-polarized beams have the same ‘doughnut’ shape[288].

10.2.2. Selection of a good control sample

To probe whether there is sufficient z-component polarization in the beam through the objective lens on the microscope, we choose a control sample that has large SHG signals when probed in the z-direction, and nominally no SHG signal when probed in the x-y plane.

This is because the SHG signal that we measure involves various tensor element contributions[201], as shown in Equations (10-1) and (10-2).

$$\begin{bmatrix} P_x \\ P_y \\ P_z \end{bmatrix} = 2\epsilon_0 \begin{bmatrix} d_{11} & d_{12} & d_{13} & d_{14} & d_{15} & d_{16} \\ d_{21} & d_{22} & d_{23} & d_{24} & d_{25} & d_{26} \\ d_{31} & d_{32} & d_{33} & d_{34} & d_{35} & d_{36} \end{bmatrix} \begin{bmatrix} E_x^2(\omega) \\ E_y^2(\omega) \\ E_z^2(\omega) \\ 2E_y(\omega)E_z(\omega) \\ 2E_x(\omega)E_z(\omega) \\ 2E_x(\omega)E_y(\omega) \end{bmatrix} \tag{10-1}$$

$$I(2\omega) \propto |\boldsymbol{P}(2\omega)|^2 \tag{10-2}$$

Depending on the crystal structure of some materials, it is possible to reduce the number of elements in the χ tensor (in d-matrix form in Equation (10-1))[201]. Ideally, we should choose a control sample that has very different magnitudes of SHG response when excited with z-polarization compared to x–y-polarization, and with as few tensor elements as possible (*i.e.* a material with subscripts for the χ tensor: $ijk = izz \neq ixx, iyy$ and $izz \gg ixx, iyy$ or $ixx, iyy = 0$). However, no single crystal materials that are easily obtainable meet these criteria. Even wurtzite materials such as collagen[286] and cubic materials such as ZnSe (110)[291], which were previously studied using z-polarization SHG microscopy, are not expected to show large differences on our setup depending on the excitation beam polarization when collecting the total SHG signal from the sample. This is because we still expect some x–y-polarization in the input even with the radial polarization input, primarily due to the lower numerical aperture of our objective lens[287].

Instead, we settle on a metal-semiconductor control sample, consisting of a silicon wafer that has a gold layer thermally evaporated on the surface, as studied by Biss & Brown[289]. This is an ideal control sample because silicon is centrosymmetric, and no bulk SHG is expected[292]. Additionally, thermally evaporated films of metals also tend to be amorphous – for sputtered thin films of gold, the SHG signal was found to be dominated by surface SHG compared to bulk SHG[293]. Thus, we expect the interface between the silicon and the gold in the z-direction to dominate the SHG signal, which can be probed exclusively using z-polarized microscopy.

10.2.3. Gold/silicon studies

To test whether we have z-polarized light at the output of the objective lens, we prepare a control sample of silicon with 80 nm of thermally-evaporated gold. To prepare the sample, the silicon was sonicated in detergent solution, water, acetone and immersed in boiling IPA. The silicon wafer was dried with compressed nitrogen and transferred to a glovebox for thermal evaporation of 80 nm of gold. Different polarization inputs were tested and the power-dependent spectra was measured. In Figure 10-5, we show the integrated intensity of the peak at 520 nm as a function of excitation power for the three different polarization inputs tested. We observe a quadratic power dependence of the 520 nm signal using a laser excitation wavelength of 1040 nm, indicating strong evidence for SHG. Additionally, we observe that the SHG intensity is highest when using a radial polarization input, decreasing as we switch to linear and finally an azimuthally-polarized input beam. This is consistent with previous work[289], as well as the expected trend in decreased magnitude of z-polarized component out of the objective lens.

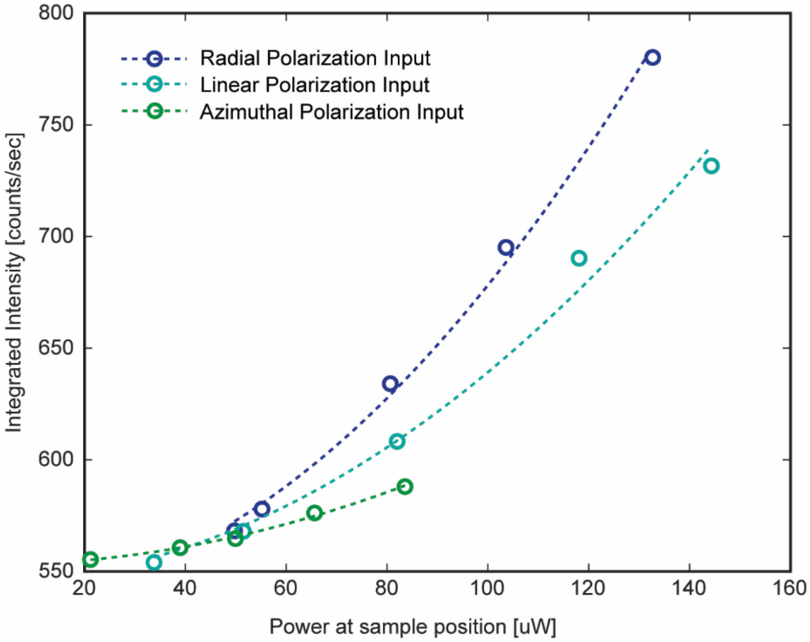

Figure 10-5. Integrated intensity of the SHG peak centered at 520 nm as a function of incident laser power measured from a gold/Si sample with different polarization inputs. All points show a roughly quadratic power-dependence, supporting evidence that the 520 nm peak corresponds to the SHG from the sample.

Given the excitation wavelength used (1040 nm), there were some concerns that the light was not probing the silicon-gold interface (80 nm deep). Some quick back-of-the-envelope calculations using optical constants for gold[294] suggest an absorption depth of:

$$L_{incident} = \frac{1}{\alpha_{1040}} = \frac{\lambda}{4\pi k} = \frac{1040}{4\pi \times 6.8167} = 12.14\, nm. \tag{10-3}$$

Thus, we also prepare a sample with 10 nm of gold on silicon. The measured spectrum is presented in Figure 10-6. Although the SHG peak is visible, it is notable that there are spectral features present in the 400–750 nm range (wavelengths beyond this range were filtered out by the FGB39 color glass filters). The shape of the spectral features share some similarities with the two-photon luminescence observed from gold nanorods and nanowires[295,296], and could be dominating the signal as the 10 nm evaporated gold film may not be completely smooth and/or continuous.

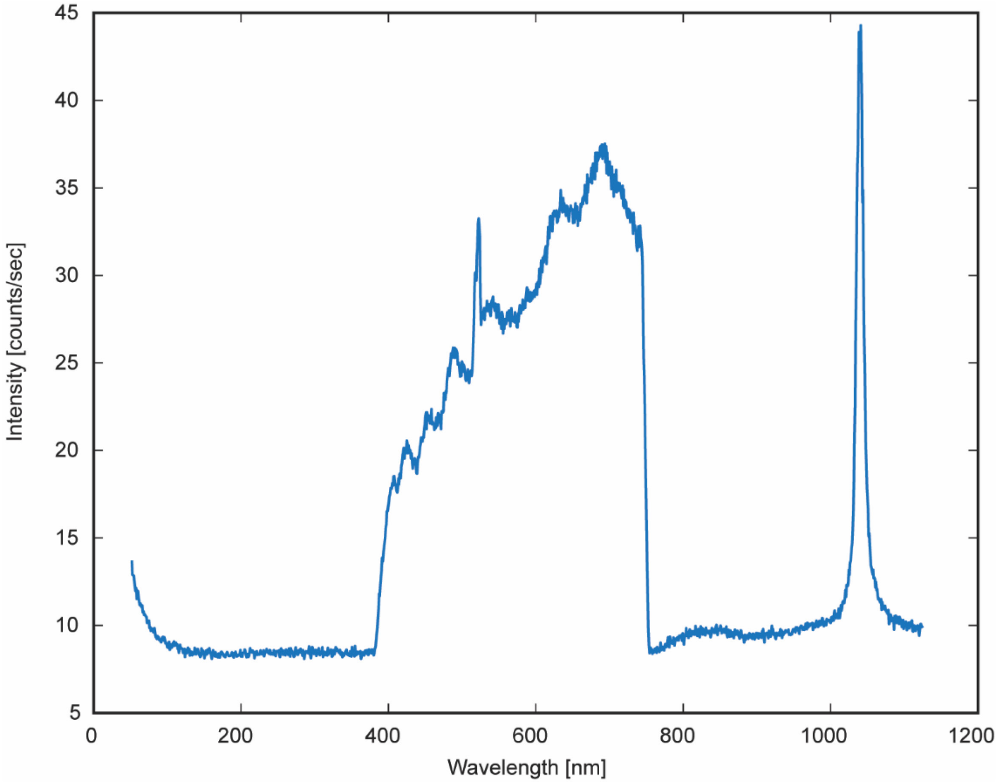

Figure 10-6. Measured spectrum from a 10 nm-thick gold film thermally evaporated on silicon upon excitation by 4 mW 1040 nm laser excitation. The SHG peak is visible, but additional features can also be observed from 400–750 nm.

Even though there were some concerns regarding the laser absorption depth and probing of the gold-silicon interface, the 80 nm-thick gold on silicon sample can still be considered a good control sample, as the air/gold surface is expected to be sensitive to z-polarized inputs as well, yielding clean spectra of just the SHG signal. We see clear indication that a radially-polarized input provides some z-component in the output beam from the objective lens. Hence, we move on to more interesting samples, such as the HfO_xN_y/silicon surface.

10.2.4. HfO_xN_y/silicon studies

Using a radial polarization input, we test the SHG signal from various silicon samples relevant for singlet fission-sensitized silicon as described in Chapter 4. We prepared the following samples to measure: 1.1 nm HfO_xN_y/n-Si, 30 nm Tc/1.1 nm HfO_xN_y/n-Si, RCA-cleaned n-Si, and RCA-cleaned and H-terminated n-Si. We notice that compared to the gold/Si control sample, these samples showed considerably less SHG signal. In fact, we notice that the onset of distinguishable

SHG signal beyond the noise floor (~ > 150 counts/sec) is right when the sample exhibits evidence of burning, as seen in Figure 10-7.

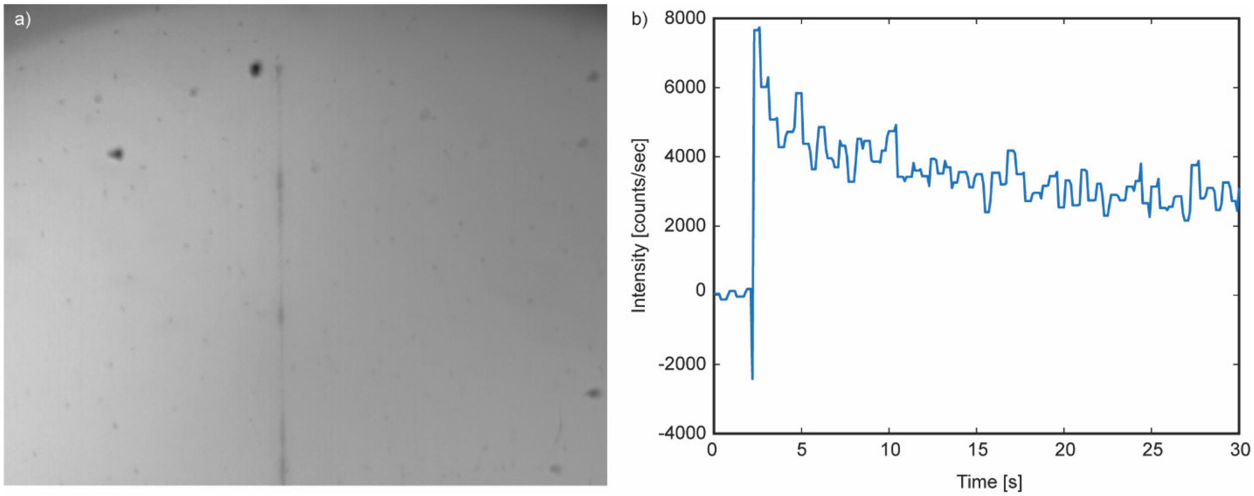

Figure 10-7. Evidence of burning of the Tc/HfO_xN_y/silicon samples. a) Image taken using the optical microscope, showing a line of burnt sections on the sample as the sample was translated upwards with the 1040 nm laser excitation at 1 mW excitation power. b) SHG counts measured as a function of time, showing an initial sharp rise when the laser is first unblocked, followed by a rapid decay in the SHG signal over the course of several seconds, indicating burning of the sample.

To avoid burning, we try using lower excitation densities, however, the spectra measured from the samples at these densities (Figure 10-8) show that the SHG signal is so low that it is comparable to the signal of setup artifacts. Note that the silicon-only samples did not exhibit burning so higher excitation powers could be used to measure better SHG signals.

We conclude that for obtaining SHG signal from singlet fission-sensitized silicon samples, a different SHG setup needs to be built where we can leverage higher input power while using configurations that can potentially prevent sample burning to obtain higher SHG signals. However, the z-polarized SHG microscopy setup can still be useful for samples that are expected to have very high z-component SHG.

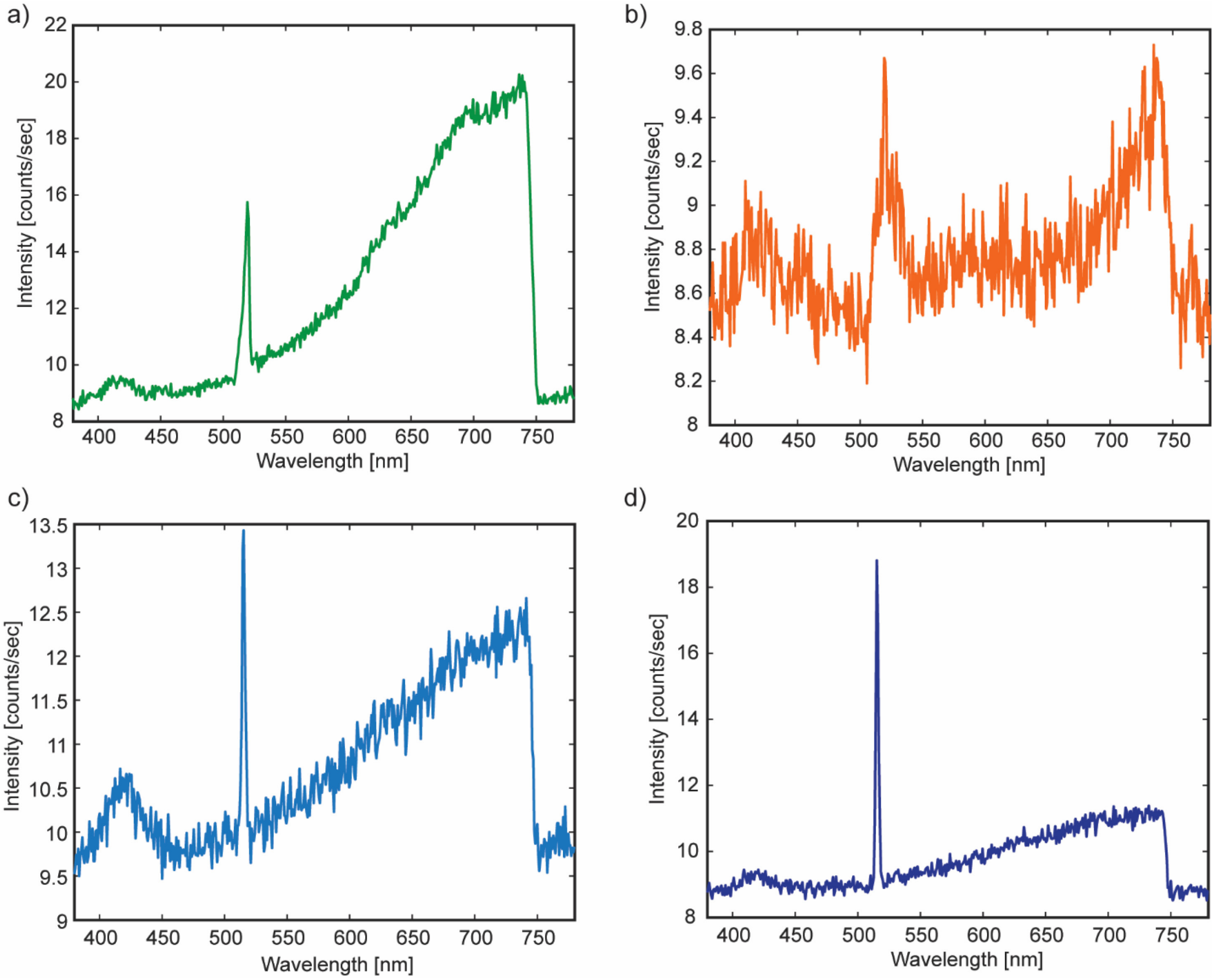

Figure 10-8. a) Spectra obtained from exciting 1.1 nm HfO_xN_y/Si with 507 µW excitation. b) Spectra obtained from exciting 30 nm Tc/1.1 nm HfO_xN_y/Si with 507 µW excitation. c) Spectra obtained from exciting RCA-cleaned Si with 1 mW excitation. d) Spectra obtained from exciting RCA-cleaned H-Si with 1 mW excitation. The peak observed at 520 nm is most likely the SHG signal from the samples.

10.3. Tabletop pump-probe setup

Another way to probe the z-direction of vertical devices is to excite the sample at an angle using horizontally-polarized light. To achieve this, an on-table SHG setup was built with the pump and probe beams exciting the sample at an angle to probe the z-component. In this section, we detail the key design decisions made when building the on-table transient SHG (tr-SHG) setup.

10.3.1. Transient second harmonic generation setup design

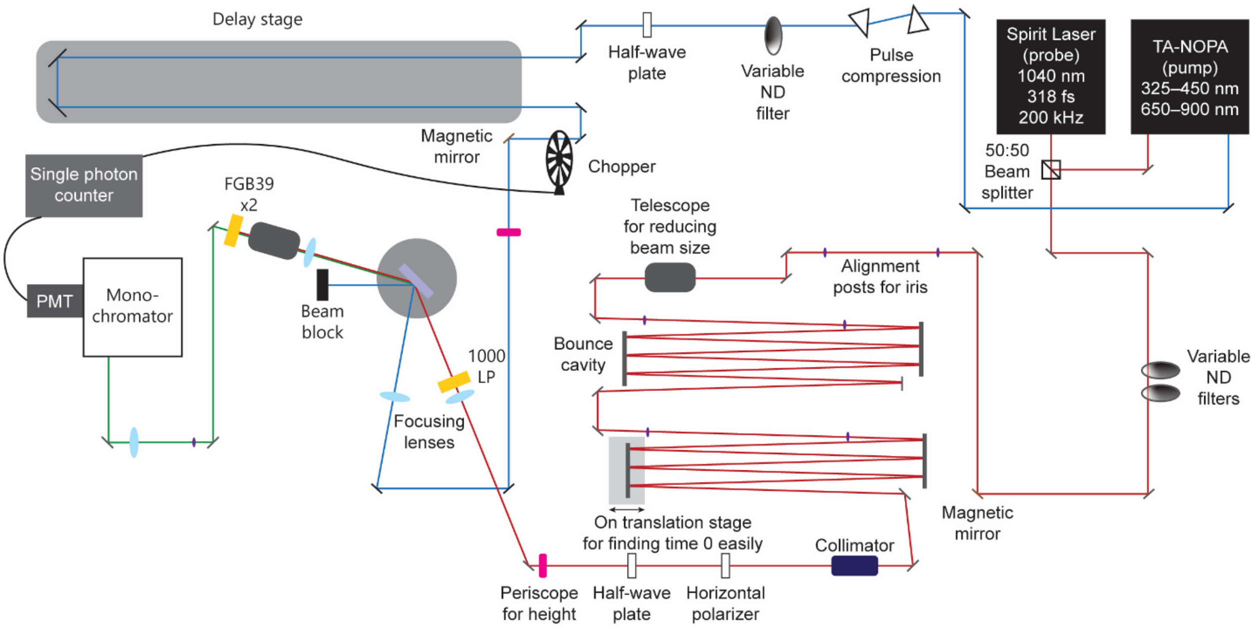

Figure 10-9. Illustration of the key components in the pump-probe SHG setup. Schematic is not to scale and does not exactly reflect the positions of all the optical components. LP = longpass filter, ND = neutral density filter, FGB39 = bandpass color glass filter (Thorlabs), PMT = photomultiplier tube.

The full pump-probe SHG setup is depicted in Figure 10-9. The 1040 nm output from the Spirit laser is split and half of the light is sent to the non-collinear optical parametric amplifier (NOPA, Spectra-Physics). In the NOPA, the laser input is split to generate the pump and seed beams for the difference frequency generation process that enables output light of tunable frequency (not to be confused with pump and probe beams in the tr-SHG experiment). The pump seed is generated by frequency doubling of the laser input to generate 520 nm light. The seed beam is generated by passing the 1040 nm input through a sapphire crystal for supercontinuum generation. The seed and pump beams are then passed through two nonlinear crystals (BBO) such that a specific wavelength in the seed beam is amplified (signal beam) by weakening of the pump beam. For the tr-SHG setup, the signal beam is then frequency-doubled through a third BBO crystal to generate the tr-SHG pump beam at 450 nm.

After the 450 nm pump beam exits the NOPA, the beam undergoes pulse compression to reduce the duration of the pump pulse to ~10s of fs. This is important for achieving the ultrafast temporal resolution for tr-SHG experiments. The pump path also contains a half-wave plate for selection of polarization, along with a delay stage which provides the time delay between the pump and probe beams. The delay stage consists of a corner cube mirror mounted on a motorized translation stage. With < 10 µm step sizes and a total path length of 1200 mm (round-trip), we can probe a 4 ns time window of our samples' dynamics. After the delay stage, the pump beam is focused through a mechanical chopper connected to a gated single photon counter so that the pump-induced change in SHG signal can be collected. After the chopper, a magnetic mirror picks off the pump line and directs it towards the sample. The height of the beam is raised using a periscope and the beam is focused onto the sample surface to overlap with the probe beam. Most of the pump beam path is the same as the pump line in the Tisdale lab transient absorption setup, and the magnetic mirror allows easy switching between the two setup configurations.

The probe beam path was designed and built from scratch. We detail some of the key setup design decisions made for the probe beam path. For most of the probe beam path, silver mirrors were used due to its increased reflectivity in the infrared compared to aluminum mirrors.

10.3.1.1. Bounce cavity

The pump beam travels a significant distance within the NOPA – the probe beam path needs to be increased to compensate the additional distance so that the pump and probe pulses arrive at the sample surface at the same time. As it is difficult to measure the path length within the NOPA, we use the distance traveled by the probe beam of the transient absorption setup until the sample position to obtain the 'time zero' distance of the transient absorption pump beam. A rough estimate of the distance can be measured using a piece of string. Initial measurements suggested that ~12 m of additional path length is needed for the tr-SHG setup probe beam. We introduce this extra distance using two bounce cavities.

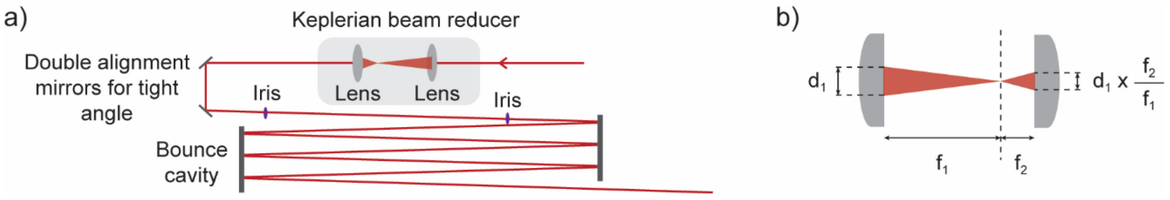

Figure 10-10. Detailed view of the first bounce cavity, including the Keplerian beam reducer, the alignment mirrors and the alignment irises.

A more detailed schematic of the first bounce cavity is presented in Figure 10-10a. First, the beam passes through a Keplerian beam reducer. This consists of two plano-convex lenses with focusing lengths selected specifically to reduce the beam diameter by the ratio of the focusing lengths (Figure 10-10b). The beam size was reduced as the beam coming from the laser is not perfect and diverges when traveling through the ~12 m of added path length, making it difficult to align through the bounce cavity.

Additionally, to simplify the alignment process of the bounce cavity and increase the number of bounces achievable on the square mirrors of the cavity, we set up two mirrors behind one of the square mirrors to achieve a tight angle entry into the cavity. Finally, there are two iris posts to guide the re-alignment process, and ensure the beam is traveling at a constant height through the cavity.

Specific mirror mounts for the square mirrors (Thorlabs Kinematic Grating Mounts) were purchased instead of gluing the mirrors with epoxy onto the optical posts, as epoxy can deform over time. The cavities were mounted onto Polaris® low-drift kinematic mirror mounts and specialized optical posts to reduce drift effects as the bounce cavity requires precise alignment to operate.

One of the mirrors on the second bounce cavity is mounted on a linear translation stage; this allows for additional adjustment of the probe beam path when finding time zero (see Section 10.3.3). After leaving the second bounce cavity, the beam is collimated and spatially filtered using a pinhole placed between two plano-convex lenses. Then, it is directed towards the sample position.

10.3.1.2. Fiber couple idea

To increase flexibility with space, passing the probe beam through a 12 m-long optical fiber was also considered. However, as the beam travels through a fused silica fiber core, the fiber is expected to broaden the pulse duration due to dispersion, which results in reduced time resolution for the tr-SHG experiments. Using material constants for fused silica fiber to calculate the group velocity dispersion parameter D_λ[297], we obtain an expected material dispersion of 2.23 ps, as detailed in Equation (10-4), which is approximately 6 times longer than the pulse duration of the probe beam exiting the Spirit laser.

$$\Delta t_g = |D_\lambda| \Delta\lambda l = 31.770 \times 5.9 \times \frac{11.9}{1000} = 2.23\, ps. \qquad (10\text{-}4)$$

$\Delta\lambda$ is the spectral width of the beam and l is the path length of the fiber.

To counter the effects of dispersion, there are some tricks that can be used. For example, one could consider the same pulse compression prism method to reduce the pulse temporal width. However, as the beam is generated directly from the laser, the spectral width of the beam is quite narrow. As a result, the calculated inter-prism distance for SF10 prisms using Equation (10-5)[298,299] is 83 cm, which undermines the space flexibility provided by the optical fiber.

$$GDD_{prism} = GVD\ \times l \approx \frac{\lambda^3}{2\pi c^2}\left[-4L\left(2\left(\frac{dn}{d\lambda}\right)^2\right) + 4\left(\frac{d^2n}{d\lambda^2}\right)\left(2D_{\frac{1}{e^2}}\right)\right]. \qquad (10\text{-}5)$$

Here, GDD_{prism} is the group delay dispersion of the prism compression system, GVD is the group velocity dispersion of the fiber, l is the path length of the fiber, $\lambda = 1040\ nm$, c is the speed of light, L is the prism separation distance, n is the refractive index of the SF10 prisms, and $D_{\frac{1}{e^2}}$ is the diameter of the beam at $\frac{1}{e^2}$.

Alternatively, there are some dispersion-shifted and dispersion-compensating fibers that could be considered. As these need to be designed and made-to-order specifically for the wavelength used, we chose to proceed with a bounce cavity which was simpler to implement instead without significantly increasing pulse duration.

10.3.1.3. Sample stage

The probe beam is passed through a focusing lens and a 1000 nm longpass filter right before the sample position. The filter is placed specifically to remove any second harmonic signal which may be generated from the high power laser passing through any of the optical components in the probe path setup.

To allow for temperature-dependent and low-oxygen measurements, the sample stage was designed with posts to secure a tower cryostat (Janis Research, ST-100). The sample can be mounted at a 45° angle for reflection-mode measurements. Three-dimensional movement is permitted with the combined x-y-z screw-based mechanism translation mounts. The mounts were chosen specifically to handle high-weight loads. The beam height to the sample position was raised for both the pump and probe beams using periscopes as close to the sample position as possible to minimize risk of direct eye exposure. For the collection pathway, the entire path was built elevated to match the height of the beam coming out of the cryostat to reduce complexity.

10.3.1.4. Light collection and signal measurement

For light collection, the pump beam is physically blocked using blackout material in the beam path. The SHG signal coming off a sample surface travels along the same path as the reflected fundamental probe beam, so the collection path can be aligned using the 1040 nm reflection and an IR viewing card as the SHG signal from typical samples is too dim to be seen by eye.

The beam goes through a Keplerian beam reducer, followed by two bandpass color filters (Thorlabs, FGB39) to spectrally filter out the 1040 nm fundamental and allow the 520 nm SHG signal to pass. As the SHG signal is low, a cage system was used for most of the collection path and during experiments, blackout material is used to cover the collection path to improve the signal-to-noise ratio.

For signal detection, the beam passes through a monochromator for increased spectral filtering for 520 nm, and is detected using a photomultiplier tube (PMT). The monochromator also allows collection of the spectral output by scanning the central wavelength setting over a desired wavelength range. The SHG signal from samples is expected to be very low, as a result, the PMT is a good choice for detection[300]. For detailed discussion on operation of PMTs, we direct the reader to other resources[301].

The PMT output is connected to the same gated single photon counter (Stanford Research Systems SR400) which is also connected to the mechanical chopper in the pump line.

10.3.2. GaAs steady state tests

To test the probe beam path, probe-excitation-only SHG signal was collected using a GaAs (100) crystal (purchased from MTI corporation) as the control sample. The assortment of data is presented in Figure 10-11. In Figure 10-11a, we collect the SHG signal from the sample with a half-wave plate in the path to rotate the polarization. We observe a four-fold symmetry that tracks with measurements in literature of the same surface[302], with a slight discrepancy in angles as the starting orientation of the GaAs crystal was not controlled in our measurements. Figure 10-11b shows the SHG spectra collected by the PMT with the monochromator central wavelength scanned, confirming that the signal measured from the sample is at 520 nm. Figure 10-11c-d show the power-dependent SHG signal collected, showing that the data follows the expected quadratic power dependence, until around 60 mW average excitation power at the sample position, at which the power-dependence transitions to linear. This linear dependence is most likely not from sample burning, but instead from fundamental 1040 nm beam leakage through the spectral filters placed in the collection pathway, as we can recover the same power dependence when returning to a lower power after exciting the sample at high powers.

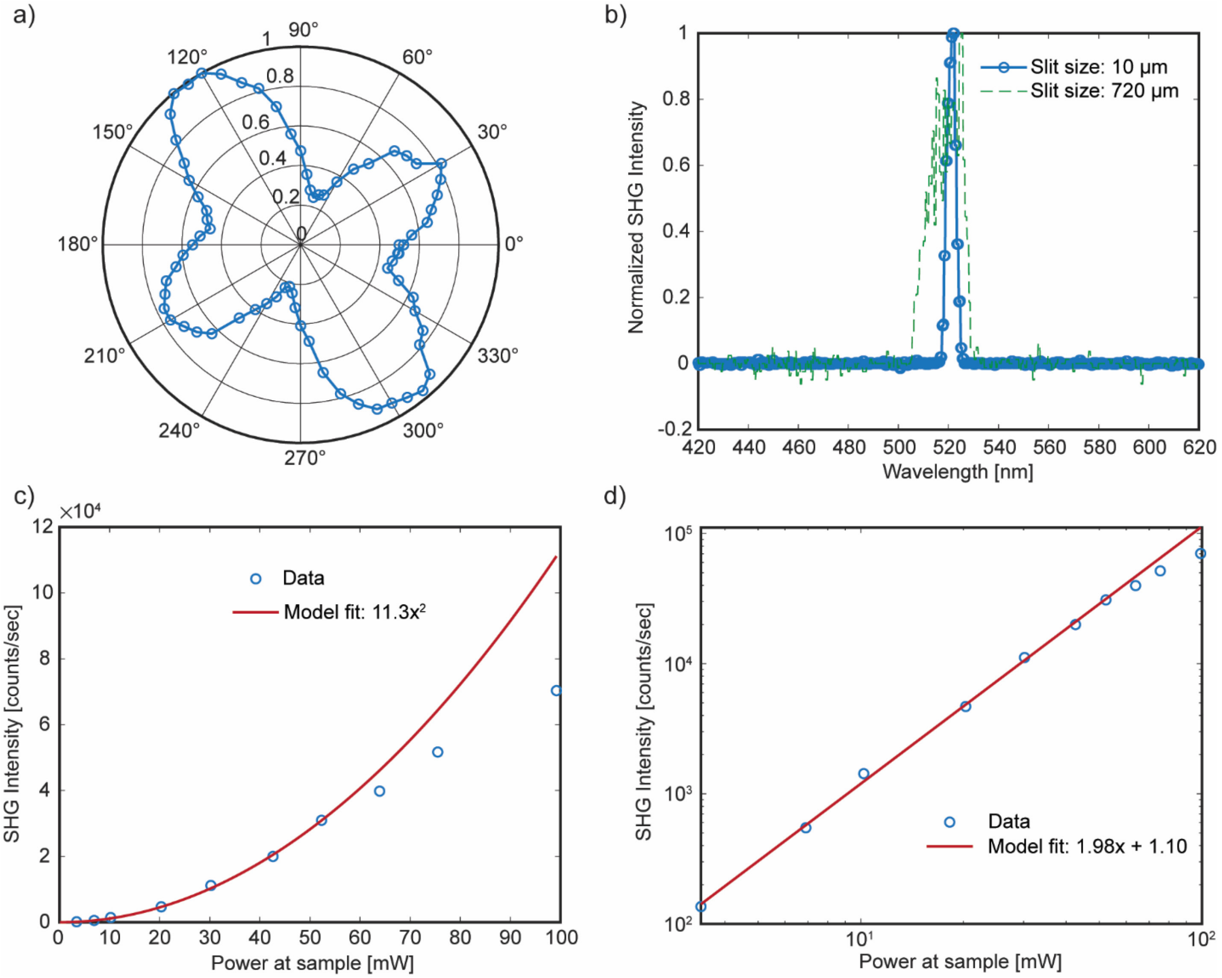

Figure 10-11. Control probe-only measurements collected on GaAs (100) single crystals. a) Polarization-dependent SHG signal collected by placing a motor-controlled half-wave plate to rotate the probe-polarization. b) Measured SHG spectra for different monochromator entrance slit widths. c) Power-dependent SHG intensity, with a quadratic fit. d) Same data as c), but presented logarithmically.

10.3.3. Finding time zero

After confirming successful collection of SHG signal from the probe beam, we incorporate the pump beam and work towards observing spatial and temporal overlap of the two beams in order to perform transient SHG experiments – also referred to as finding ‘time zero’. We start with the same GaAs (100) control sample.

10.3.3.1. Spatial overlap

As one of the beams is in the infrared (probe: 1040 nm), it is difficult to directly observe the pump and probe beam overlap on the sample surface, particularly inside the cryostat. As a first attempt, we position the sample in free space without the cryostat in the center of the mount and use an IR viewing card to roughly align the two spots near the sample surface.

Following rough alignment, we mount the sample in the cryostat and use a Thorlabs CMOS camera (DCC1240M-GL) coupled with a macro-focusing lens (Navitar, Zoom 7000-2 Macro Lens) to image the surface of the sample through the cryostat window. We observe the pump and probe spots in Figure 10-12, and note that the pump spot appears smaller than the probe spot when imaged on the camera, which is not ideal for the tr-SHG measurements, although this may also be due to the wavelength-dependent sensitivity of the camera. We also note the presence of many reflection spots in the image – care should be taken when aligning for spatial overlap to check that the spot moves with steering of the pump beam mirror across the sample surface. Spot reflections off other surfaces will usually show up on the camera as changing in intensity in the same position or moving in a different direction than the expected steering.

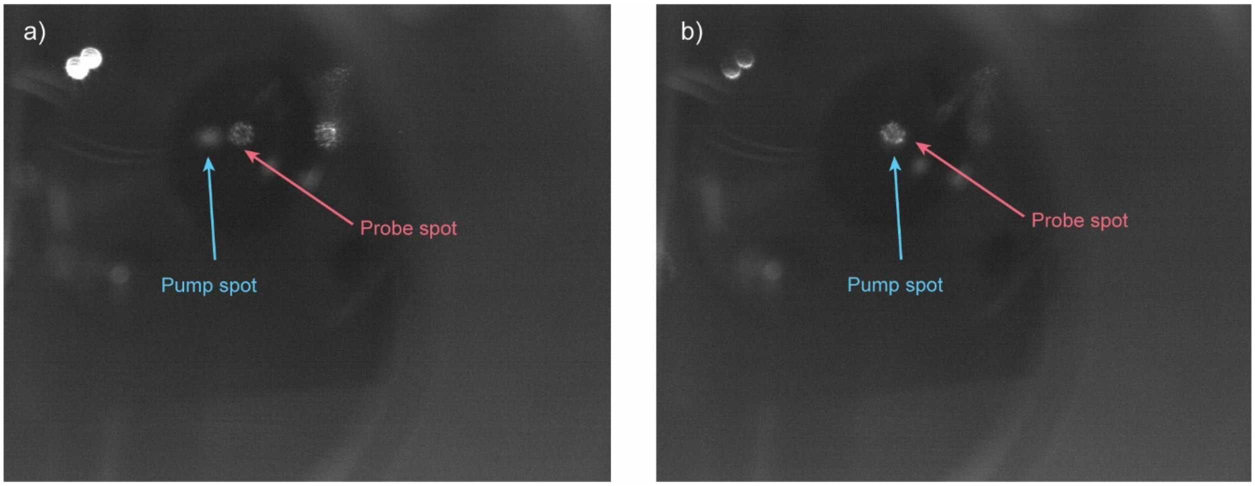

Figure 10-12. Zoom-in of the GaAs (100) sample surface in the cryostat imaged using a Thorlabs CMOS camera (DCC1240M-GL) coupled with a macro-focusing lens (Navitar, Zoom 7000-2 Macro Lens). a) The pump spot and probe spot are not overlapped on the sample surface. b) The pump spot and probe spot are overlapped on the sample surface.

For final alignment, once time zero has been found as detailed in the following sections, finer adjustment of the spot positions can be performed to obtain maximal spatial overlap.

10.3.3.2. Sum frequency generation

When the pump and probe beams are spatially and temporally overlapped, sum frequency generation (SFG) of the two beams can occur, resulting in an output of 314 nm light during the overlap period. The duration of the SFG pulse is a cross-correlation of the pump and probe beams, which also determines the overall time resolution of the tr-SHG setup. The reflection of the SFG photons lies between the reflections of the pump and probe beams from the GaAs surface[198,303,199], as shown in Figure 10-13.

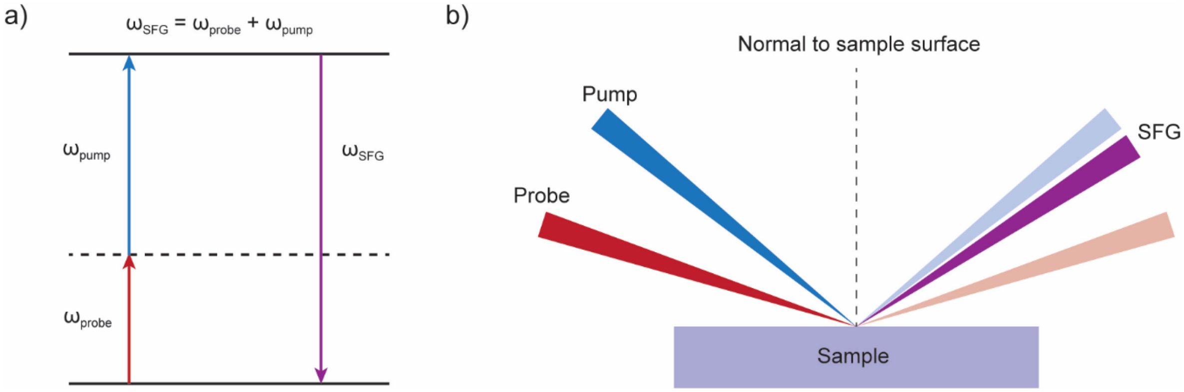

Figure 10-13. Sum frequency generation (SFG) from non-collinear inputs at a surface. a) Sum frequency generation schematic energy diagram. b) Sum frequency generation at a sample surface with the pump and probe beams as non-collinear inputs. By conservation of momentum, the SFG beam lies between the reflected pump and probe beams off the sample surface.

Several attempts were made to obtain the SFG signal from the GaAs sample surface, however, we encountered some challenges. The first is that the SFG signal produced from a 450 nm pump beam and a 1040 nm probe beam is at 314 nm, which is in the UV region. Most shortpass filters on Thorlabs do not let all of the wavelengths of light below the cut-off wavelength through – in fact, they work more like wide-range bandpass filters. Instead, we try colored glass filters (Thorlabs FGUV11M) to block out the pump, probe and SHG wavelengths. Additionally, the monochromator grating has 20% transmission efficiency at 314 nm; as a result, we switch the setting to mirror mode (set center wavelength to 0 nm) to maximize signal. The PMT also has a lower responsivity to 314 nm – although we did not try a different PMT, a PMT with high sensitivity in the UV region may have a better detection likelihood of the SFG.

However, despite the many attempts to observe SFG signal, we were unable to obtain clear evidence of SFG at 314 nm. The most likely reason for this is the low power of the pump beam obtained at the sample surface. Estimating the pump pulse duration to be about 70 fs, and using the average power measured at the sample position of 1 mW, with a 200 kHz laser repetition rate and an estimated beam size of ~250 μm, the peak power density at the sample is 1.45×10^8 W/cm^2. For the 1040 nm probe beam, we find that the average power threshold for SHG signal detection from the surface was around 7 mW. With an expected greater pulse duration of 318 fs, repetition rate of 200 kHz and estimated beam diameter of ~250 μm, the threshold peak power density at the sample is 2.24×10^8 W/cm^2. Even though the SFG signal should scale linearly with the pump beam power (or probe beam power), the peak pump beam power is below the expected threshold to obtain SFG signal. Indeed, increasing the probe beam power by several orders of magnitude did not yield any observable SFG signal. Additionally, in the actual pump probe experiment, the pump beam should illuminate a larger area than the probe beam, which would significantly decrease the peak power density even further. As it was not possible to observe SFG signal from the control sample of GaAs, it is likely that there would be greater difficulty with the silicon-tetracene samples which are expected to show even less SHG signal from the interface.

10.3.3.3. Single wavelength transient absorption

Given the complications with observing the SFG signal, we instead found time zero by performing single wavelength-probe transient absorption.

With the SFG method, the two beams being overlapped are very short (~10s fs and ~100s fs); as a result, the SFG convolution is also expected to be on the order of ~100s of fs, akin to finding a needle in the haystack. Transient absorption signals usually last much longer in duration (~100s ps–ns). Hence, instead of searching for the SFG signal, we replace the sample with a sample that has known strong TA signals upon excitation by the pump beam. In this case, we use a perovskite quantum dot (QD) solution as reference which has a long-lived TA signal at 520 nm. We find time zero by first observing the TA signal using the frequency-doubled probe beam and move the delay stage until the signal is maximized.

While this method works for approximating the position of the delay stage for close to time zero, we still need to be able to find the actual time zero on the sample to be used for the tr-SHG experiments, using the actual probe beam at 1040 nm, as there are expected chirp effects that would shift the position of time zero depending on the probe wavelength used. Using a control sample that has known TA signals at 1040 nm from 450 nm excitation would be useful – in theory, silicon could be a good sample with expected stimulated emission signal near 1040 nm, although there are not many studies of silicon transient reflection measurements with probes in the IR[304]. In practice, this would require coupling to the IR spectrometer, which is present in the Tisdale lab but requires additional maintenance and calibration before use.

10.3.4. Future suggestions for the setup

Although it was difficult to find time zero on the setup, we made some attempts to take transient SHG measurements on GaAs, based on an expected position of time zero from the single-wavelength transient absorption measurements on QD solutions. Unfortunately, there was no clear evidence of successful measurements of transient SHG.

10.3.4.1. Studying the interface of singlet fission-sensitized silicon solar cells

For future measurements on studying the silicon interface with zinc phthalocyanine for singlet fission-sensitized photovoltaics, we propose some modifications. The first is to use a higher wavelength pump. Tetracene absorbs more strongly close to 520 nm, which could induce more changes in the SHG signal – however, 520 nm is also exactly at the wavelength of the SHG signal that we are interested in measuring, which makes distinguishing between the SHG signal from the interface and the pump excitation beam very difficult. Additionally, the NOPA is not able to produce light at this wavelength. Instead, we propose changing the material system of study by replacing the tetracene layer in the Tc/ZnPc/AlO_x/Si stack to platinum tetraphenyltetrabenzoporphine (PtTPBP) or palladium tetraphenyltetrabenzoporphine (PdTPBP). Both PtTPBP and PdTPBP contain heavy metal atoms, resulting in high intersystem crossing efficiencies which can generate a lot of triplet excited states that can transfer to ZnPc[305]. These triplet sensitizing materials also absorb close to 620-640 nm in solution[306], which may be potentially red-shifted in film as is common for some organic molecules[307,308]. The NOPA can output higher power at redder wavelengths (~300 mW at 650 nm, compared to 43 mW at 450 nm), which could help bring the system above the SFG detection threshold. Additionally, the SFG produced with a redder pump wavelength would be closer to the visible region, resulting in higher detection efficiencies, increasing the probability of observing time zero through the SFG method.

Spectroscopy studies introduced in Chapter 11, as well as other studies performed on the singlet fission process suggest that the most interesting time scales for the triplet transfer process is likely in the 10s of ns to 100s of µs region. In addition to finding time zero and studying the early time dynamics of the system, additional pump beam path length may be required to probe the later time dynamics further, although practically, this may not be ideal. There is a possibility that the charge transfer and recombination at the interface may not need ultrafast time resolution. Instead, relying on slower transient measurements where the time resolution is limited by the electronics of detection may be easier to implement.

In addition to obtaining time scales of interfacial charge transfer, optical SHG experiments have been used to identify resonances that correspond to electronic transitions in strained subsurface layers of SiO_2/Si interfaces[283]. By looking at the SHG spectra, Daum et. al. observed direct bandgap transitions corresponding to the thin Si region of the Si-SiO_2 interface that were different from the transitions of bulk Si. Although ruled out as a cause for the specific resonance identified in their paper, it is also possible to use such SHG spectra to identify surface states[283]. Performing additional SHG experiments with a broadband probe could be useful for indicating if there are any interesting interfacial states in our system, such as the D^+-A_{Si}^- charge-separated state.

It may also be interesting to introduce a varying magnetic field to modulate the singlet/triplet populations and observe this effect on interfacial charge transfer dynamics (noting that triplet states cannot be observed directly since SHG can only probe dipole-allowed transitions).

Although tr-SHG measurements on the singlet fission-sensitized silicon samples could not be obtained, it should also be noted that these samples have many interfaces, which could complicate the overall SHG signal. An alternative set of experiments can be conducted to obtain information on the amplitude (sign) and phase of each contribution. This information can be extracted by designing heterodyne-detected SHG (HD-SHG) on each of the individual components contributing to the total SHG signal[309–311]. Here, a reference signal, often referred to as a local oscillator (LO) signal, is spatially overlapped with the SH signal from the sample and the resulting signal is measured. Since information on the phase and amplitude of the LO signal is known, it is possible to extract the phase and amplitude information for the SH signal from the measured signal.

10.3.4.2. Studying charge transfer across other interfaces

The tr-SHG setup can also be used for measurements of other systems with interesting interfacial charge transfer properties. Although we did not have the capability of measuring the time resolution of the system, we expect to be limited by the probe beam pulse duration. Adding some form of pulse compression may be needed, depending on the desired temporal resolution for the system of interest. A regular prism compression system works best when the beam being compressed has a wide bandwidth. Instead, we recommend using some form of narrowband compression, given that the probe beam is coming directly from the laser, with a narrow bandwidth.

In general, for pump-probe experiments, the pump beam spot area should be larger than the probe beam. If the interface being studied permits, it may be interesting to try swapping the pump and probe beams around such that we pump with 520 nm (frequency double the 1040 nm fundamental) and probe with a higher wavelength output from the NOPA (e.g. 800–900 nm). In this case, we may be limited by the power of the beam coming from the NOPA, as SHG scales quadratically with intensity.

Finally, for increased flexibility of wavelength tunability, we suggest setting up a pump-probe tr-SHG setup with both beams coming from two separate NOPAs, although there may be power limitations for reasons mentioned above. This could be circumvented by choosing the probe wavelength to match a specific electronic transition in the material system of interest to increase the measured SHG signal.

Chapter 11.
Transient photoluminescence and transient absorption/reflection studies of singlet fission-sensitized silicon

11.1. Introduction

Singlet exciton fission can be used to enhance silicon solar cell efficiencies beyond the Shockley-Queisser limit[26,28,34]. Prior to this thesis work, singlet fission-sensitization of bulk crystalline-silicon (*c*-Si) by tetracene (Tc), the archetypal singlet fission material, was only observed using hafnium oxynitride (HfO_xN_y) interlayers[35], and the mechanism of the sensitization process was not well understood. As a result of the advancements in understanding of the necessary interfacial material properties and successful demonstration of triplet exciton enhancement of silicon solar cell devices in Part I of this thesis, there are a multitude of optical spectroscopy measurements that can be performed on these samples for supplementary temporal kinetics information. Knowledge of key rates of excitonic processes in the system can help inform material development, particularly for the singlet fission layer, as tetracene is well-known to suffer from photooxidation, making it unsuitable for industrial use[76,106].

In this chapter, we present a variety of transient spectroscopy measurements performed on sample stacks of tetracene/zinc phthalocyanine/aluminum oxide/n-silicon and their variations. We start with ultrafast transient absorption measurements performed with an externally-applied magnetic field on a tetracene film. Our studies of the magnetic field effect on early-time dynamics of the fission process are correlated with magnetic field-dependent transient photoluminescence measurements performed by Burdett *et al.*[127] and previous measurements of transient absorption measurements of tetracene thin films by Wilson *et al.*[129], providing an introduction of the transient absorption technique, data analysis process, and the singlet fission process in tetracene to readers. We then expand to multilayer structures, starting with transient photoluminescence measurements to probe the effect of adding the subsequent layers to tetracene and monitor the decays corresponding to singlet and triplet excitons in tetracene. We finish with ultrafast transient absorption comparison measurements of the multilayer structures, giving insight into transient dynamics that complement our understanding of the exciton interactions at the tetracene-silicon interface.

11.2. Methods and materials

11.2.1. Sample preparation

Organics-only samples were prepared on diced 1” x 1” squares of Borofloat 33 glass (Swift Glass Co. Inc.). Each glass substrate was 1.1 mm thick. Silicon samples were prepared on diced 1” x 1” squares of n-doped silicon wafers purchased from PureWafer (Phosphorus, 1-10 Ωcm, prime grade, single side polished). Glass and silicon substrates were cleaned by sonicating in detergent solution (Micro-90), deionized water, and acetone, followed by immersion in boiling isopropanol. The substrates were dried with pressurized nitrogen. The glass substrates were immediately transferred into a glovebox environment for thermal evaporation of the organic materials. The silicon substrates were transferred to a cleanroom environment for RCA cleaning, with an HF oxide etch step at the end. The silicon substrates were then transferred to an atomic layer deposition tool for deposition of 1 nm or 10 nm of aluminum oxide using the Baldo lab-modified recipe (Cambridge Nanotech Savannah). After the ALD step, the silicon samples were transferred to the glovebox environment for thermal evaporation of the organic layers.

For the organic layers, substrates were transferred to a vacuum chamber at a pressure of $< 1 \times 10^{-6}$ torr. Zinc phthalocyanine (Luminescence Technology Corp., sublimed > 99 %) was deposited at a rate of 0.5 Å/s, and tetracene (Sigma Aldrich, sublimed grade, 99.99 % trace metals basis) was deposited at a rate of 1 Å/s. Due to challenges with setups, in some samples, tetracene was purified once *via* a sublimation-recondensation process in a tube furnace prior to deposition. However, in some samples, we used unpurified tetracene as is after purchase. After deposition of the organic layers, the samples were encapsulated using Borofloat glass with UV-curable epoxy. The active area was protected during the UV curing step.

11.2.2. Magnetic field-dependent transient absorption

A 1030 nm laser output (Light Conversion, PHAROS, Yb:KGW lasing medium, 150 fs duration, 50 kHz repetition rate) was used to seed the transient absorption measurement. The 515 nm pump beam was generated using a harmonic generation unit equipped with a beta-barium borate nonlinear crystal (Light Conversion, HIRO). The pump average power measured just before the cryomagnet was 3.7 mW, which we approximate to an excitation density of 60.6 μJ/cm^2. The probe beam was generated from the seed laser *via* supercontinuum generation in a sapphire crystal. The delay between the pump and probe lines was set by a motor-controlled multi-pass delay stage ranging 8 ns. Before illuminating the sample, the pump was passed through a 100 Hz optical chopper and a beamsplitter/photodiode configuration to differentiate between pumped and unpumped probe signal. The sample was placed in a cryomagnet (Quantum Design, OptiCool) and measurements were taken in Voigt geometry (perpendicular to the magnetic field). The probe signal collected in transmission configuration was passed into a grating spectrograph (Andor Kymera 193i) and recorded using a Si NMOS photodiode array detector (256 pixels). The probe spectrum ranged from ~540–900 nm.

11.2.3. Transient photoluminescence

Transient photoluminescence measurements were collected on an inverted microscopy setup (Nikon, Ti-U Eclipse) in air at room temperature, with encapsulated samples. The sample was excited by a 405 nm pulsed laser (ODL 800-D, < 100 ps pulse width) that was focused onto the surface through an objective (Nikon, CFI S Plan Fluor ELWD, 40x, 0.6 NA). The epifluorescence from the sample was collected by the same objective lens and filtered by a dichroic mirror and a longpass filter. The emission was then directed to a Si avalanche photodiode (APD, Micro Photon Devices, timing resolution ~50 ps, 50 μm sensor width) connected to timing electronics (PicoQuant PicoHarp 300). To reduce after-pulsing artefacts, a neutral density filter was added in the collection pathway.

11.2.4. Transient reflection measurements

Experimental details for the transient reflection measurements are analogous to the transient absorption measurements described previously, except the sample was positioned outside of the cryomagnet and probe signal was collected in reflection mode from the sample surface. As the samples were not constricted to within the electromagnet, a higher pump average power was accessible, 8.6 mW measured at the sample position, corresponding to an excitation density of 141 μJ/cm^2.

11.3. Magnetic field-dependent transient absorption of tetracene

Tetracene is a four-ringed polyacene that has garnered significant interest over the years for its ability to perform singlet fission, with its triplet energy positioned just above the band gap of silicon[34], making it suitable for integrating with silicon solar cells. To better understand the dynamics of singlet and triplet excitons in tetracene, a variety of optical spectroscopy measurements have been performed. In steady-state measurements, the fluorescence signal measured from tetracene can be modulated by applying an external magnetic field, a model for which was presented by Merrifield and is also detailed in Chapter 2.1.5.1 of this thesis[161,82]. Briefly, the presence of the magnetic field modulates the overall rate of the singlet fission process by affecting the wavefunction of the intermediate triplet-triplet pair state of the fission process, which in turn affects the relative population of the singlet and triplet excitons in tetracene, resulting in a magnetic field-dependence of the tetracene fluorescence. The overall fission process is also known to be slightly endothermic due to the respective energies of the singlet and triplet excitons, as a result, both singlet and triplet dynamics can be monitored through transient photoluminescence measurements, signaled by prompt and delayed fluorescence[34,45]. Burdett *et al.* performed magnetic field-dependent transient photoluminescence studies of tetracene, studying its effect on different timescales[127].

Ultrafast pump-probe spectroscopy techniques can yield temporal information on the exciton- and even possibly charge-transfer dynamics in the material system of interest[220]. Transient absorption is one such technique where a pump pulse is used to excite the sample and a probe pulse is introduced at a time delay after the pump pulse to measure the change in the sample's absorption as a result of the pump excitation. As the time resolution is dependent on the convolution of the pump and probe pulse durations, a faster time resolution can be obtained compared to transient photoluminescence measurements. Additionally, information on optically dark states such as triplet excitons can be obtained. Transient absorption measurements have been performed by various groups for tetracene in solution, in single crystal form, and in polycrystalline thin films[129,312–316], due to particular interest in understanding the exact kinetic scheme of the singlet fission dynamics in tetracene. In this section, we study transient absorption of thermally-evaporated polycrystalline thin films of tetracene under application of an external magnetic field.

11.3.1. Transient absorption of tetracene at 0T

We first take a transient absorption measurement of an encapsulated 30 nm-thick polycrystalline film of tetracene thermally-evaporated on glass with no external magnetic field applied. The color map is plotted in Figure 11-1a and time-integrated spectra at different time intervals is plotted in

Figure 11-1b. With a 515 nm excitation, we note that the ground state bleach signal of the sample is likely overlapped with the pump spectra, as a result, we only consider probe wavelengths at 535 nm and above. We observe a strong stimulated emission signal from 540 – 600 nm that corresponds with the steady-state emission spectra collected from tetracene (see Chapter 5). Additionally, we observe broad, likely-overlapped photo-induced absorption from 600–900 nm. The features seen in the transient absorption spectra are similar to what has been previously reported for thin films of tetracene at room temperature[129], with faster dynamics, which we attribute to using a higher pump excitation fluence. In previous experiments, oscillations were observed in transient absorption decay curves at excitation fluences above 8 μJ/cm^2,[129,312] attributed to acoustic modes in tetracene excited by heating from singlet-singlet exciton annihilation. In order to maximize signal-to-noise in our setup for observing the feature at 800-900 nm, we had to use an excitation density that was 7.5x higher, which results in the need to consider singlet-singlet annihilation effects in our kinetic models.

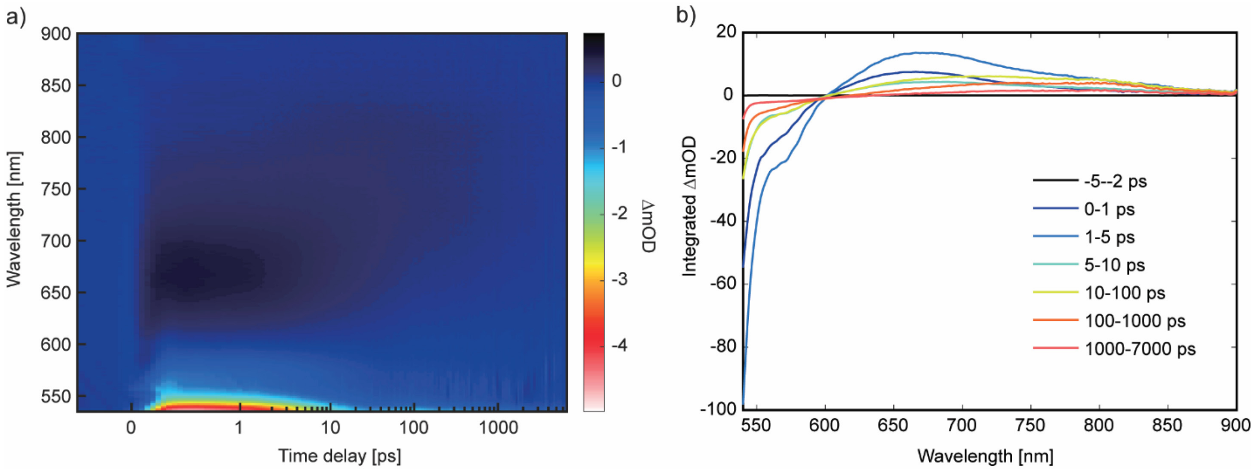

Figure 11-1. Transient absorption measurement collected from a 30 nm tetracene sample evaporated on glass with 0 T of magnetic field applied. The sample was excited with a 515 nm pump at approximately 3.7 mW. a) Color map showing change in optical density as a function of wavelength and time delay. b) Time-integrated spectra at select time intervals.

11.3.1.1. Assignment of spectral features

One of the trickiest parts of transient absorption measurements is the assignment of spectral features, which affects the consequent model developed. Fortunately, as plenty of prior studies have been performed on tetracene, we have a general good understanding of the expected excitonic processes in this material.

We start with the stimulated emission. As triplet excitons are not emissive in tetracene, the stimulated emission should largely track with the singlet population in tetracene. At the expected peak position for fluorescence (535 nm), there are some fluctuations and spectral inversions incurred from the pump beam at 515 nm. As a result, we select the shoulder at 565 nm to monitor the stimulated emission, and consequently singlet exciton decay.

The photoinduced absorption appears to show two partially-overlapped broad features centered at 670 nm and 805 nm that have different dynamics (Figure 11-2). Previous work assigned the 670 nm feature to correspond to the PIA of the photogenerated singlet exciton[129,313], as this feature had similar decay kinetics as the SE feature and the energy matches optical transitions from the first singlet excited state to higher singlet excited states. Interestingly, we notice some differences in the kinetics for the 670 nm feature compared to the 565 nm feature, particularly in the onset, which is different from what was reported in single crystal studies[313]. The onset appears to match the initial growth of the 805 nm feature, and also decays in a similar timescale as the 670 nm feature. Thus, we attribute this feature in our data to include contributions from the 805 nm feature and singlet dynamics matching decay of singlets observed with 565 nm.

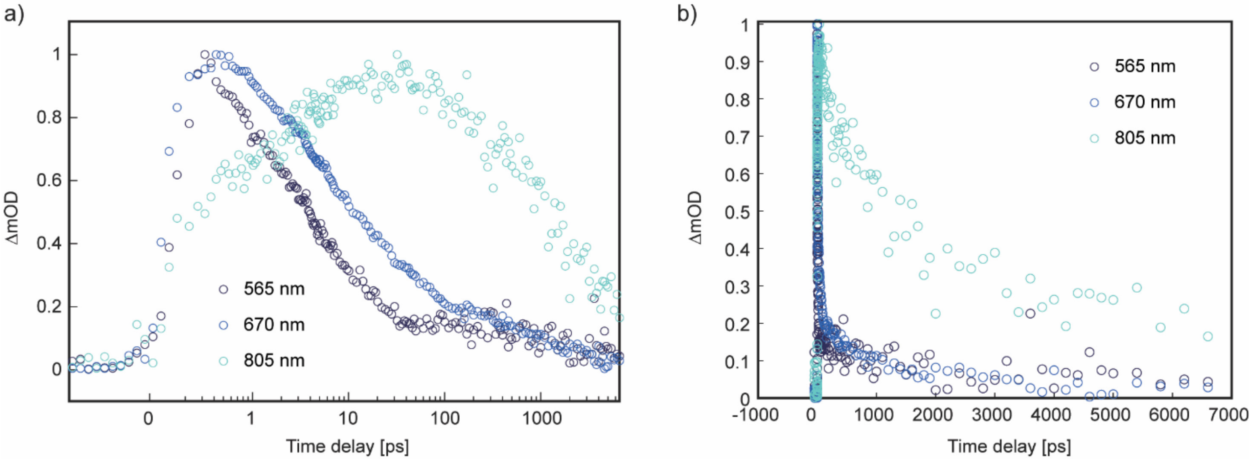

Figure 11-2. Normalized kinetic traces of select wavelength features measured from 30 nm of thermally evaporated tetracene on glass. a) Presented in log-scale for time, b) Presented in linear-scale for time.

As for the 805 nm feature, we notice that it grows in at the same time frame that the 565 nm decays. As with the assignment made by Wilson *et al.*, we attribute this feature to correspond to the triplet excitons in tetracene[129], which matches energies of predicted transitions of the first triplet excited state to higher triplet excited states[317]. We note that the decay of the 565 nm feature exactly corresponds to the rise in the 805 nm feature: this reflects the conversion of singlets to triplets. Additionally, as the timescale of this transition is on the order of < 100 ps, much faster than expected for intersystem crossing, we can attribute this conversion process to singlet fission[34,129].

Because of some uncertainty in exact contributions to the 670 nm feature, we focus the rest of the magnetic field-dependent kinetic studies to just the 565 nm SE feature for the singlet excitons, and the 805 nm PIA feature for the triplet excitons.

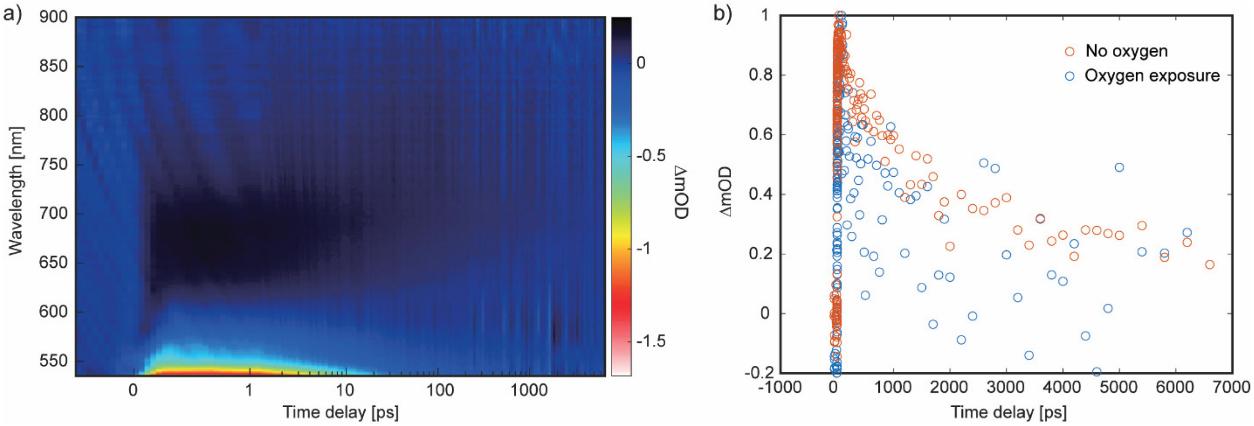

Figure 11-3. Transient absorption measurements collected on a tetracene sample that was encapsulated in an environment with oxygen exposure. a) Color map showing change in optical density as a function of wavelength and time delay. Notably, the positive feature at 805 nm is less pronounced. b) Comparison of measured normalized ΔmOD at 805 nm for a sample that was encapsulated in a glovebox environment at 0.1 ppm oxygen (orange) and for a sample that was encapsulated in an environment with higher concentrations of oxygen (blue).

Incidentally, due to glovebox-related issues, one tetracene sample was also prepared and encapsulated under non-ideal oxygen conditions. The TA measurement of this sample is presented in Figure 11-3. Notably, comparing the feature at 805 nm corresponding to triplet excitons in the samples, we notice quenching of the 805 nm decay for the sample with oxygen exposure, although we note the measurement is also noisier. This is a good control to confirm the assignment of the PIA feature.

11.3.1.2. Kinetic model development

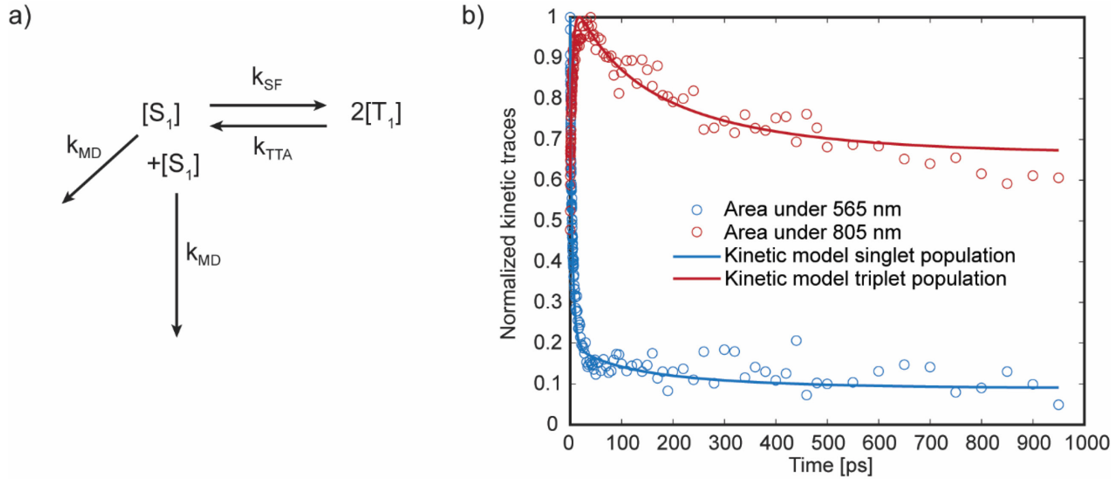

Figure 11-4. Simple proposed kinetic model to fit tetracene kinetic traces for the singlet and triplet populations. a) Schematic of the model, where k_{SF} is the rate of singlet fission, k_{TTA} is the rate of triplet-triplet annihilation, k_{MD} is the rate of monomolecular singlet decay, and k_{BD} is the rate of bimolecular singlet decay. b) Fits of the normalized kinetic traces for the singlet and triplet population (lines), along with the measured kinetic traces at 565 nm and 805 nm (circles).

We fit the kinetic traces at 565 nm and 805 nm to a simple proposed kinetic model for the exciton dynamics in tetracene. Note, we assume that the area under the curve at 565 nm is proportional to the singlet population and the area under the curve at 805 nm is proportional to the triplet population. This may not always necessarily be true, given the previously reported models[129]. Regardless, reasonably good fits were obtained (Figure 11-4b).

Our proposed kinetic model is as follows:

$$\frac{\partial N_{S_1}}{\partial t} =- k_{SF}N_{S_1} + k_{TTA}{N_{T_1}}^2 - k_{MD}N_{S_1} - k_{BD}{N_{S_1}}^2 \tag{11-1}$$

$$\frac{\partial N_{T_1}}{\partial t} = 2k_{SF}N_{S_1} - k_{TTA}{N_{T_1}}^2, \tag{11-2}$$

where N_{S_1} and N_{T_1} are the singlet and triplet populations, k_{SF} is the rate of singlet fission, k_{TTA} is the rate of triplet-triplet annihilation, k_{MD} is the rate of monomolecular singlet decay, k_{BD} is the rate of bimolecular singlet decay. We note that we use a simplified kinetic model with less parameters compared to previous work, but this was sufficient to fit our data[129,316]. The obtained rate constants are presented in Table 11-1.

Table 11-1. Table of fitted rate constants obtained from experimental transient absorption measurements.

k_{SF} [s^{-1}]	k_{TTA} [cm^3 s^{-1}]	k_{MD} [s^{-1}]	k_{BD} [cm^3 s^{-1}]	$N_{T_1,0}/N_{S_1,0}$
5.24×10^{10}	4.91×10^{-10}	3.65×10^{10}	3.44×10^{-9}	0.54

Comparing these values to previously reported rates, we notice that our rates for fission and TTA are on the same order of magnitude as other work on thin films[129,316,318]. Our rate constant for monomolecular decay is higher than other reports, while the rate constant for bimolecular decay is comparable or lower (reports range multiple orders of magnitude)[316,319,320]; we suspect these parameters to be correlated and note that the higher fluences used may cause a faster singlet decay than in other works.

11.3.1.3. Brief aside on global and target analysis attempts

Earlier, we noted that different assignments of the 805 nm feature have been proposed, as the PIA is broad and can overlap with the adjacent 670 nm feature. Indeed, previous work has assigned the 805 nm signal to include contributions from singlet and triplet populations at a ratio determined by their respective oscillator strengths[129]. In this section, we go over some methods that have been reported by other groups for analyzing TA data in general and extracting spectral features.

One of the well-reported methods is through global and target analysis[321]. The term global refers to simultaneous analysis of all measurements, while target refers to probing whether the proposed target model describes the data. Transient absorption data is a function of both wavelength and time. We assume that the absorption data can be separated into a sum of some number of component spectra $s_i(\lambda)$, where i is the number of species in the kinetic model, weighted by a time-dependent concentration of the species $c_i(t)$:

$$\Delta OD(\lambda, t) = \sum_{i=1}^{n_{species}} c_i(t) s_i(\lambda). \tag{11-3}$$

Conveniently, this can be considered in matrix form:

$$\boldsymbol{\Delta OD} = \boldsymbol{C} \cdot \boldsymbol{S}. \tag{11-4}$$

where $\Delta\boldsymbol{OD}$ is the matrix of TA data with dimensions of time delay points × wavelength points, $\boldsymbol{C}$ is the species time-dependent concentration matrix with dimensions of time delay points × number of species, and $\boldsymbol{S}$ is the species spectra matrix with dimensions of number of species × wavelength points.

If knowledge of the detailed kinetic model is known *a priori*, some techniques may be used to extract estimates for the species spectra $\boldsymbol{S}$. For first-order kinetic systems, the kinetics for the components can be described as follows:

$$\frac{d\boldsymbol{C}}{dt} = \boldsymbol{K} \cdot \boldsymbol{C}, \tag{11-5}$$

where $\boldsymbol{K}$ is the matrix of decay rates for the components. If $\boldsymbol{K}$ is non-diagonal (*i.e.* coupled kinetics equations), singular value decomposition can be used to decompose $\boldsymbol{K} = \boldsymbol{UDU^{-1}}$. As we have a linear system, the solution for the components of $\boldsymbol{C}$ are described by linear combinations of exponential functions of the diagonal elements in $\boldsymbol{D}$, and the linear coefficients are defined by the eigenvectors in $\boldsymbol{U}$ and initial conditions. It follows that matrix math can be used to extract $\boldsymbol{S}$.

Simultaneous fitting of $\boldsymbol{C}$ and $\boldsymbol{S}$ to the measured data allows for extraction of kinetic parameters. A Markov Chain Monte Carlo (MCMC) fitting algorithm similar to the one introduced in Chapter 9 can be used to obtain correlations between parameters and evaluate the fitting model being used[271].

For the kinetic model proposed for tetracene, the nonlinear dependence of the reverse triplet-triplet annihilation process and the need to consider bimolecular recombination of the singlet excitons due to the high excitation fluence complicates the mathematics behind the eigenvalue decomposition process. Instead of performing an eigenvalue decomposition, we instead use MATLAB's ode15s solver to solve the nonlinear coupled differential equations to obtain values for the matrix $\boldsymbol{C}$. To extract $\boldsymbol{S}$, we can use the Moore-Penrose pseudoinverse of $\boldsymbol{C}$[322]:

$$\boldsymbol{S} = \boldsymbol{C}^{\dagger}\Delta\boldsymbol{OD}, \tag{11-6}$$

where $\boldsymbol{C}^{\dagger}$ is the Moore-Penrose pseudo inverse of $\boldsymbol{C}$.

However, we find that simultaneous fitting of nonlinear kinetic models to extract $\boldsymbol{C}$ and $\boldsymbol{S}$ were not straightforward as in the linear case. Indeed, minimization schemes for fitting simulated $\Delta\boldsymbol{OD}$ to measured $\Delta\boldsymbol{OD}$ using the MCMC fitting algorithm and MATLAB's fmincon did not yield any success. We note that fitting of nonlinear kinetics *via* this method has been reported to cause convergence issues due to ill-conditioning of the problem, particularly if any decay rate parameters are of comparable magnitude[322,323]. Further numerical schemes for optimization may be necessary if component spectra for the singlet and triplet excitons are desired to be extracted through global and target analysis, but are outside of the scope of this thesis.

11.3.2. Magnetic field-dependent transient absorption measurements

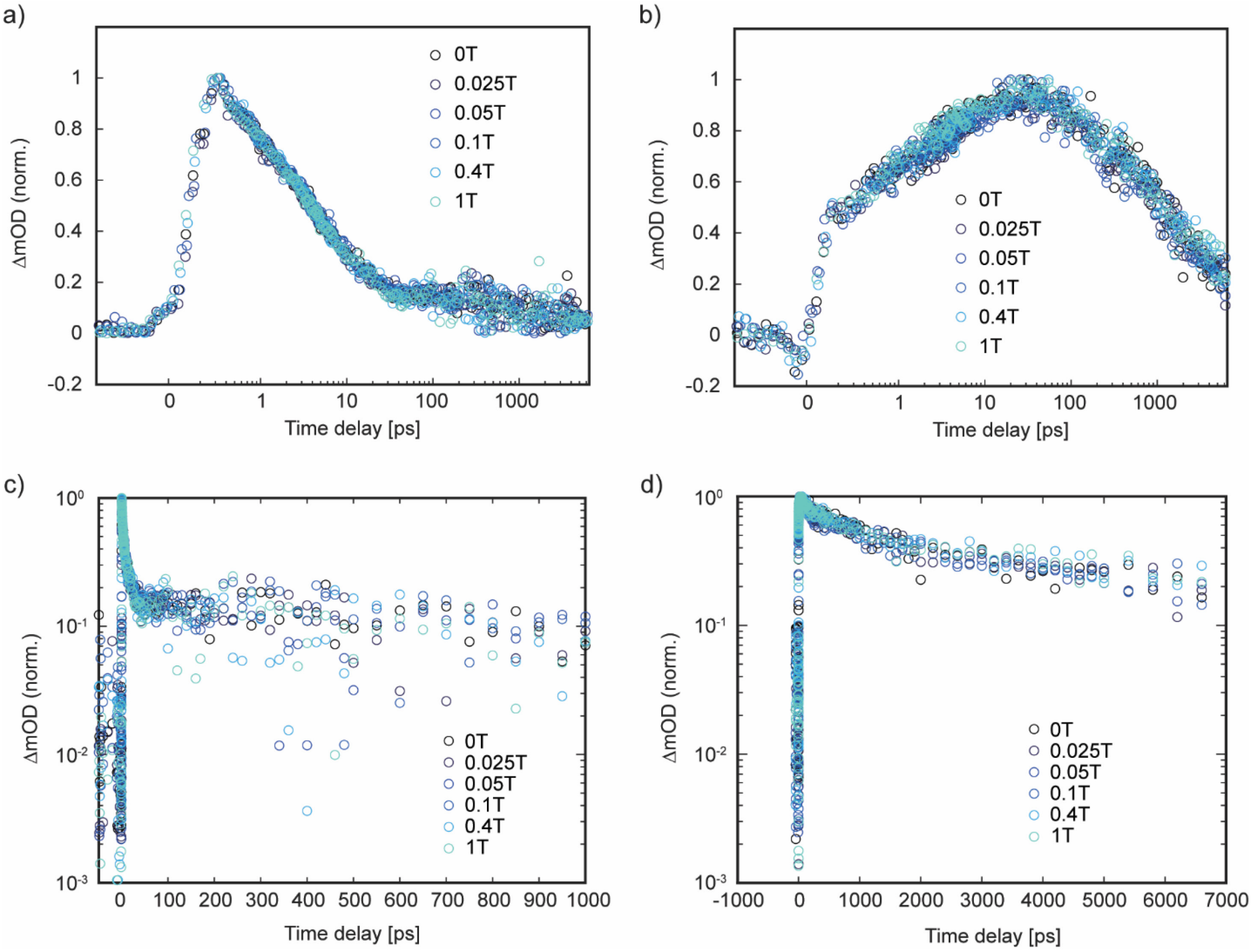

Figure 11-5. Transient absorption traces for a 30 nm thin film of tetracene at different externally applied magnetic fields. a) Normalized trace at 565 nm, logarithmic-scale in time. b) Normalized trace at 805 nm, logarithmic-scale in time. c) Normalized trace at 565 nm, logarithmic-scale in ΔmOD. d) Linear-scale normalized trace at 805 nm, logarithmic-scale in ΔmOD.

Transient absorption measurements for a thermally evaporated 30 nm film of tetracene on glass was measured with different magnetic field strengths applied in Voigt geometry, ranging from 0 T to 1 T. The comparisons of the transient absorption traces at 565 nm and 805 nm are presented in Figure 11-5. By eye, there does not appear to be an appreciable change in the kinetics for the traces obtained at 565 nm and 805 nm, at least in the first 30 ps. We expect this decay in 565 nm/rise in 805 nm at this time scale to correspond to singlet fission of the initial photoexcited population of singlet excitons, based on our earlier kinetic analysis and previous work[129,316]. Burdett *et al.* found that in transient photoluminescence measurements, early-time measurements do not show an appreciable change in dynamics with an applied external magnetic field[127]. This was attributed to the triplet pair states being formed through this initial singlet fission step having primarily singlet character, and in order to observe magnetic field effects, these triplet pair states will need to have a back-and-forth population transfer with another state which has not yet occurred at this time scale.

Table 11-2. Fitted rate constants to transient absorption data collected at different externally applied magnetic field strengths.

Magnetic field [T]	k_{SF} **[s^{-1}]**	k_{TTA} **[cm^3 s^{-1}]**	k_{MD} **[s^{-1}]**	k_{BD} **[cm^3 s^{-1}]**	$N_{T_1,0}/N_{S_1,0}$
0	5.24×10^{10}	4.91×10^{-10}	3.65×10^{10}	3.44×10^{-9}	0.54
0.025	5.29×10^{10}	4.25×10^{-10}	4.04×10^{10}	3.24×10^{-9}	0.57
0.05	5.25×10^{10}	4.08×10^{-10}	4.95×10^{10}	2.50×10^{-9}	0.53
0.1	5.75×10^{10}	4.65×10^{-10}	4.71×10^{10}	2.79×10^{-9}	0.58
0.4	5.37×10^{10}	3.55×10^{-10}	4.32×10^{10}	3.09×10^{-9}	0.64
1	4.28×10^{10}	4.37×10^{-10}	2.88×10^{10}	3.80×10^{-9}	0.52

At later times, where we might expect to see variation with magnetic fields, we note that there are no clear signs of trends with changing magnetic field. This could potentially be due to increased noise with the low signal measurements, and magnetic field-induced changes are expected to be low in magnitude. Additionally, the time scales that we are probing may still be too early to observe larger field effects, as the triplet excitons will need time to dissociate from the pair state and randomize their spin populations, which is expected at the 100 ns timescale[127]. Attempts to extract rates for the kinetic model are presented in Table 11-2. As can be seen from the extracted parameters, there is very little variation in the rates. We note that the magnetic field dependence is on the overall rate of singlet fission, which includes all of these parameters, as well as processes that occur at much longer time scales that were not included in the model as the measurement was probing early time dynamics.

11.3.3. Future considerations for additional studies

At the very least, our initial preliminary studies appear to be consistent with what is expected from the magnetic field-dependent transient PL measurements reported by Burdett *et al.*[127]

For future measurements, we strongly recommend finding ways to improve signal-to-noise ratio so lower excitation densities can be used, and better analysis can be performed on the longer time-scale data. This can be achieved by using thicker samples, lock-in amplification of the signal, and more time-averaging, as well as more measurements on multiple samples. Due to the high pump excitation, we expect some of the noise may also come from temperature-induced oscillations from bulk acoustic modes of the film. Additionally, probing out to longer time scales can be interesting, as many of the triplet exciton dynamics are expected to occur at these time scales. Finally, having a means to evaluate the kinetic model would be useful, especially if any of the parameters are correlated or if the model is over-parametrized. Working on a numerical method to fit the nonlinear kinetics could be applicable to many other systems as well.

11.4. Multilayer measurements

To understand how the exciton dynamics in tetracene changes as we add additional layers to the sample, we can study the multilayer structures using transient reflection since the silicon wafers are not transmissive. We also use transient photoluminescence which can probe dynamics further out in time.

11.4.1. Multilayer measurements: Transient absorption and reflection measurements

From the magnetic field measurements, we observe that the timescales that can be studied in the transient absorption measurements are too early to investigate triplet exciton dynamics in detail. We hypothesize and show through the device external quantum efficiency measurements in Chapter 7 that the boost in silicon photocurrent is a result of transfer of triplet excitons from tetracene. This can be complemented with transient reflection control measurements at early timescales to show that the enhancement is from triplet excitons rather than from a multiabsorption singlet exciton-related process. We can also probe if there are any effects on the tetracene fission process as a result of the additional layers present.

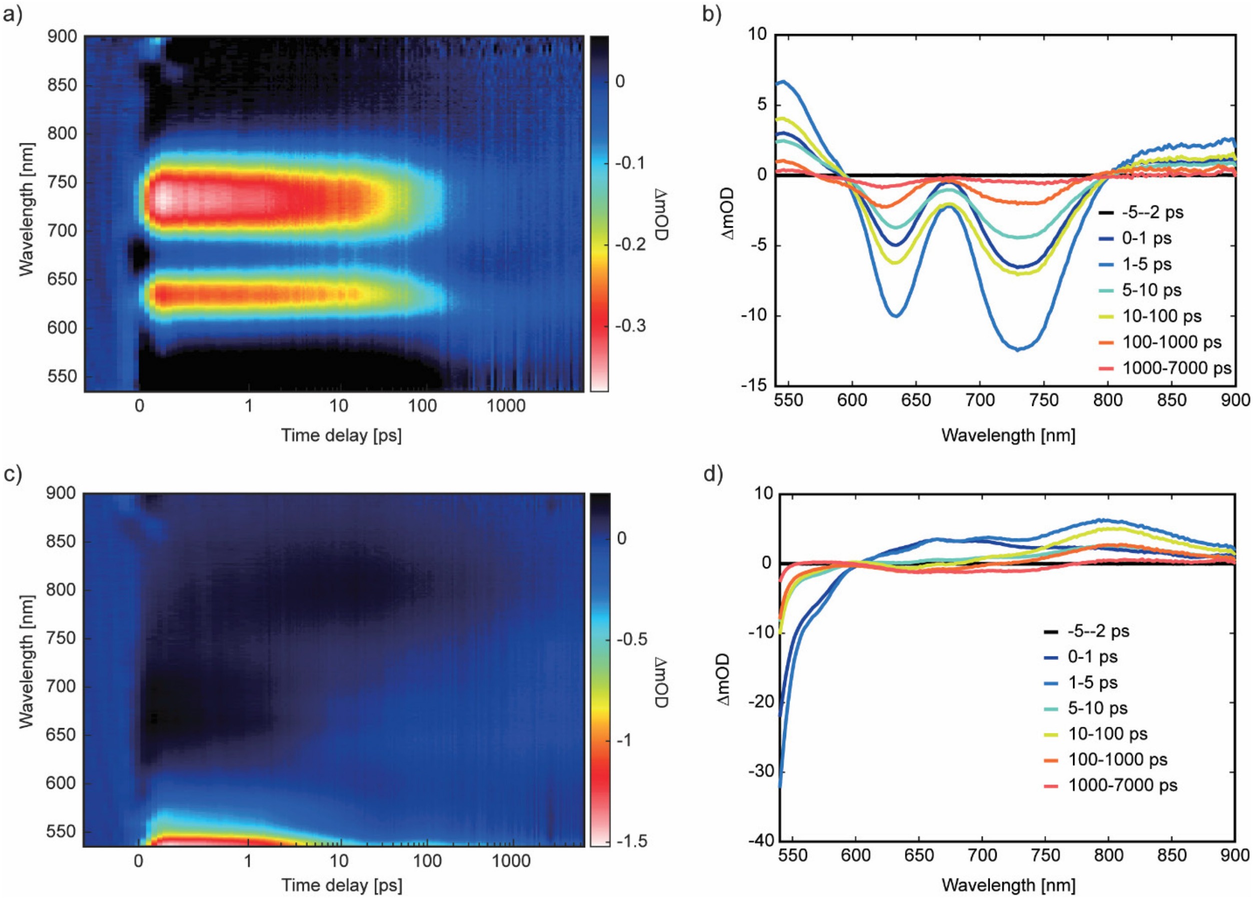

Figure 11-6. a) Transient absorption colormap obtained for a 30 nm-thick sample of zinc phthalocyanine. b) Spectral evolution over time for the 30 nm-thick sample of zinc phthalocyanine. c) Transient absorption colormap obtained for a 30 nm-thick layer of tetracene deposited on a 1.5 nm-thick layer of zinc phthalocyanine. d) Spectral evolution over time for the 30 nm-thick layer of tetracene deposited on a 1.5 nm-thick layer of zinc phthalocyanine. Samples were excited using a pump average excitation power of 8.6 mW.

We start with transient absorption measurements on a 30 nm-thick sample of zinc phthalocyanine, and a combined sample with 30 nm-thick tetracene and 1.5 nm-thick tetracene, presented in Figure 11-6. Note, the tetracene used in this sample was deposited in a different deposition system, New Angstrom, and was not exposed to any oxygen, while the remaining studies with tetracene all had partial dark exposure to oxygen due to glovebox difficulties, resulting in altered kinetics. As a result, direct comparison of this sample cannot be made with the remaining samples presented later in this section. For the zinc phthalocyanine sample, we see the features from 600 to 800 nm correspond to the ground-state absorption spectra of zinc phthalocyanine, which we can assign as the ground state bleach. We also observe photoinduced absorption on either side of the spectral range with similar decay kinetics as the GSB. With the combination film of 30 nm-thick tetracene and 1.5 nm-thick zinc phthalocyanine, most of the features are dominated by tetracene spectral features identified previously, with some visible contributions from zinc phthalocyanine GSB at late times.

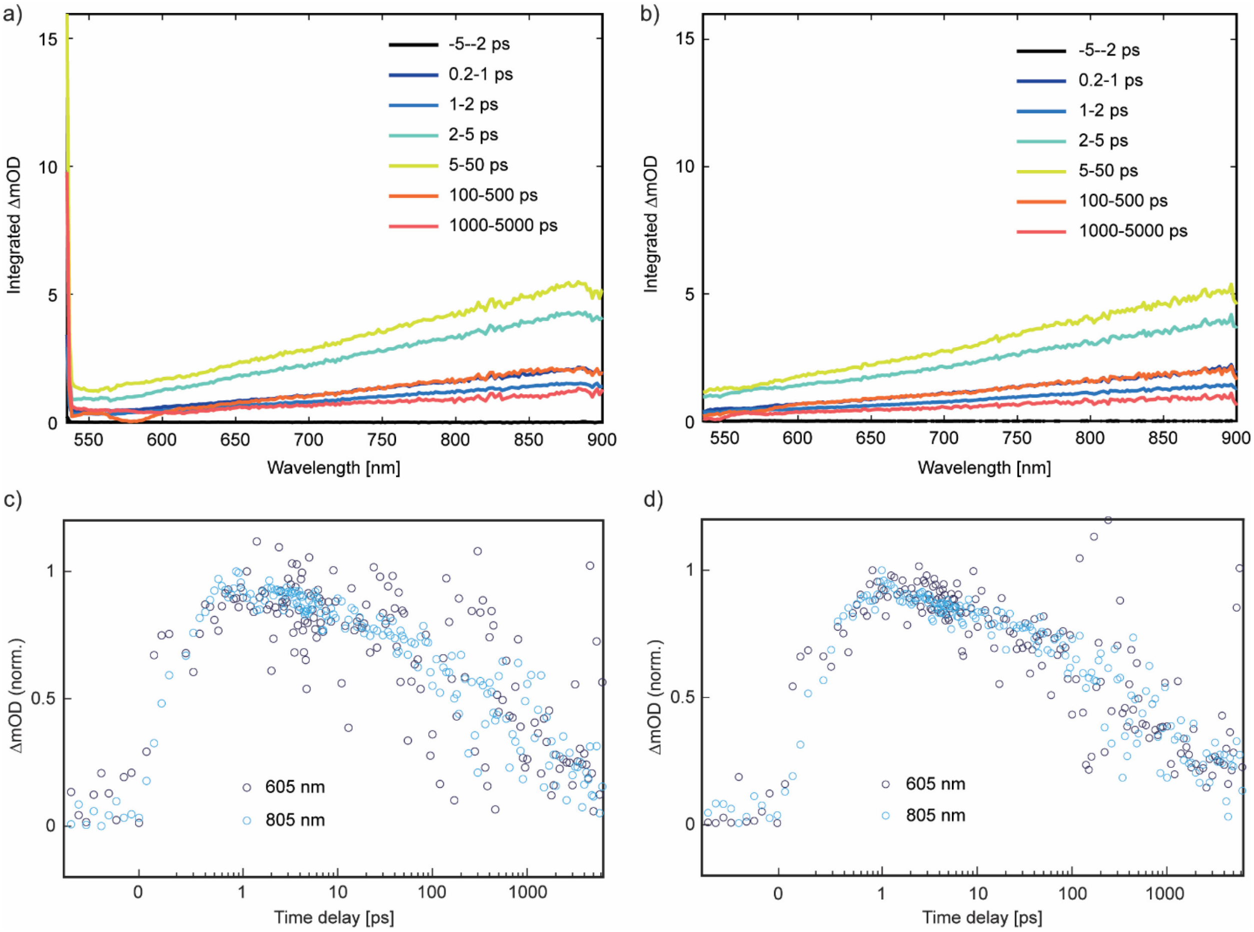

Figure 11-7. Time-integrated transient reflection spectra at different time intervals collected for a) 1 nm AlO_x/n-Si, b) 1.5 nm ZnPc/1 nm AlO_x/n-Si.

Moving on to the samples with silicon, we collect the measurements in reflection mode as silicon is not transmissive. We start with silicon samples with 1 nm of AlO_x, and additionally with 1.5 nm of ZnPc, presented in Figure 11-7. We notice the spectral features appear remarkably similar, indicating that most of the observed features are originating from silicon. As for the origin of the spectral features in silicon, we note that various groups have performed transient silicon reflectivity measurements and used the transient response to probe surface recombination at the surface[324,222,325,304]. Increased ΔmOD is observed from 550–900 nm, consistent with previous observations[304], although we note that our signal in this region has a longer lifetime, most likely as we are using much weaker pump fluences than in previous studies. The wavelength-dependence of the signal in this region has previously been attributed to a combination of the wavelength-dependence of the state-filling effect and free carrier contribution. Simply, we can consider this to reflect the absorption constant (and therefore absorption depth) of silicon. The lifetimes extracted in this region reflect the carrier dynamics, with contributions from carrier diffusion, and recombination. We note that carriers absorbed in the lower wavelength region show similar lifetimes as those absorbed deeper in silicon (Figure 11-7c and d), but note that probes of surface recombination would best be inferred using a probe wavelength near 400 – 450 nm[324].

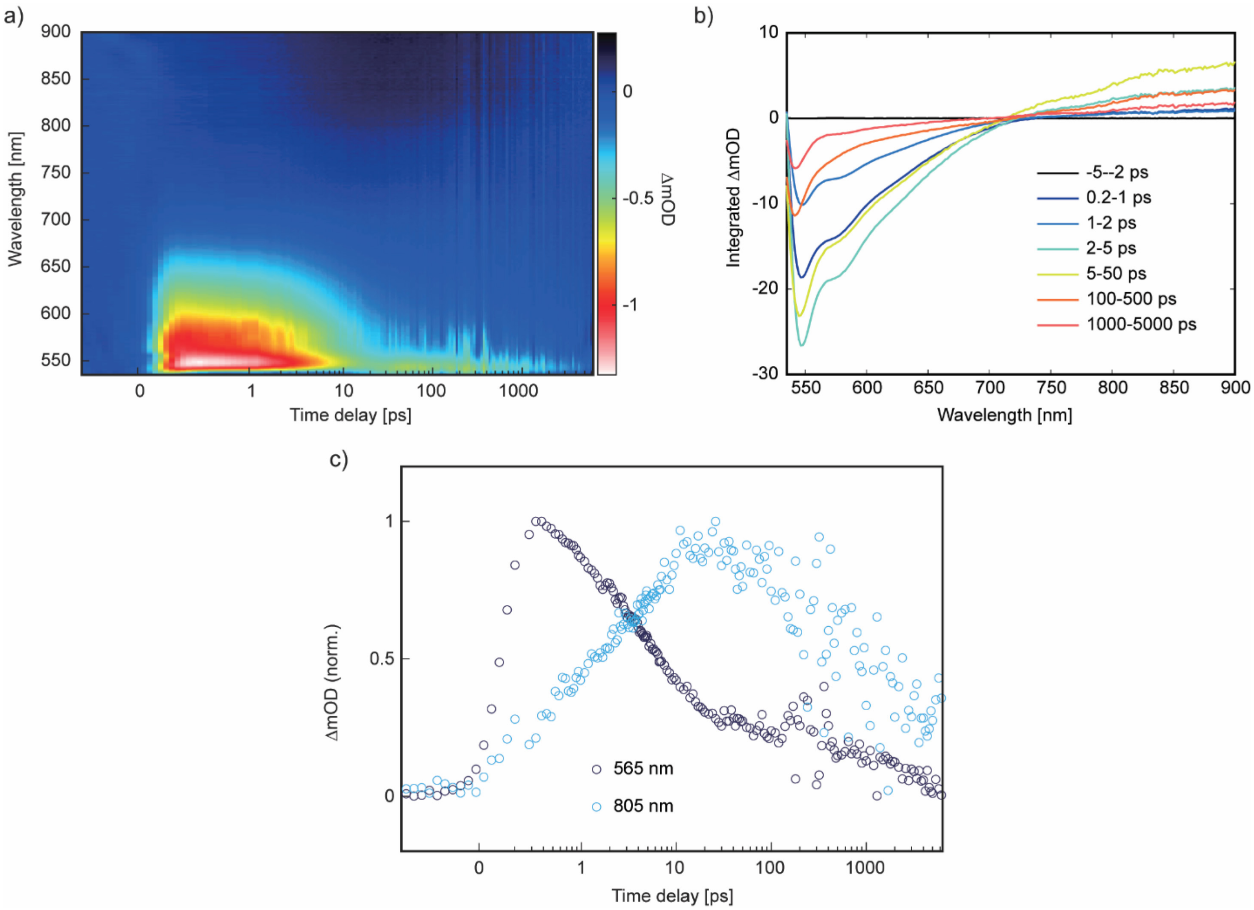

Figure 11-8. Transient reflection measurement of 30 nm tetracene/1.5 nm zinc phthalocyanine/1 nm aluminum oxide/n-silicon. a) Colormap spectra of measurements. b) Time-integrated spectra collected at different time intervals. c) Normalized kinetic traces collected at 565 nm and 805 nm.

Transient reflection measurements collected on a sample stack with 30 nm tetracene/1.5 nm zinc phthalocyanine/1 nm aluminum oxide/n-silicon are presented in Figure 11-8. We observe spectral features that correspond to tetracene, although slightly different from the features identified in the absorption measurements performed on tetracene-only films. We tentatively assign the negative feature from 540–700 nm to correspond to stimulated emission of tetracene, and note that this feature is red-shifted and the tail extends significantly into the red wavelength region from the stimulated emission feature in tetracene-only films. Previous measurements of steady-state tetracene PL on silicon with a 1 nm-thick SiO_2 layer has also shown a long emission tail and a red-shifted 0-0 emission peak, with a tail extending well into the NIR region[326]. The exact origin of this red-shifting and tail is not fully understood, and could be a subject of further study.

As for the feature from 800–900 nm, the shape looks quite similar to the feature that is also present in silicon without the tetracene. However, we notice that the timescale of growth corresponds with the timescale of decay of the SE feature (Figure 11-8c), and is slower than the growth of the feature in the silicon samples (Figure 11-7c and d), which suggests that the signal in this region could correspond to triplet excitons formed from the singlet fission of the singlet excitons contributing to the SE feature.

We also prepare a similar film with 10 nm-thick AlO_x. In this control, the passivation barrier is too thick for any carrier tunneling to occur from the triplet excitons in tetracene. We again notice similar features in the spectral trace from tetracene as identified with the 1 nm-thick AlO_x sample. The stimulated emission is also red-shifted, but notably to a lesser degree than with the 1 nm AlO_x sample. A comparison with tetracene-only transient absorption is provided in Figure 11-9a. Comparing kinetic traces at 565 nm in Figure 11-9b, we notice that the kinetics are identical, showing no change in singlet dynamics between the control and working sample. We also compare kinetic traces at 805 nm in Figure 11-9c and d. Again, the traces are overlapped, within measurement noise, suggesting no change in the initial triplet dynamics (during the initial singlet fission process) between the control and working sample.

We conclude that the singlet and triplet dynamics in the early timescales are unaffected by changing the thickness of the aluminum oxide. This supports our previous results, where we used the 10 nm-thick aluminum oxide to block the tunneling process in Chapter 7; the effects that were measured with the changes in EQE are purely affecting the triplet exciton transfer process, which is occurring at timescales beyond the 8 ns window measured using the transient reflection experiment, and that the observation of dips in the EQE do not correspond to any changes in the rate of the fission process.

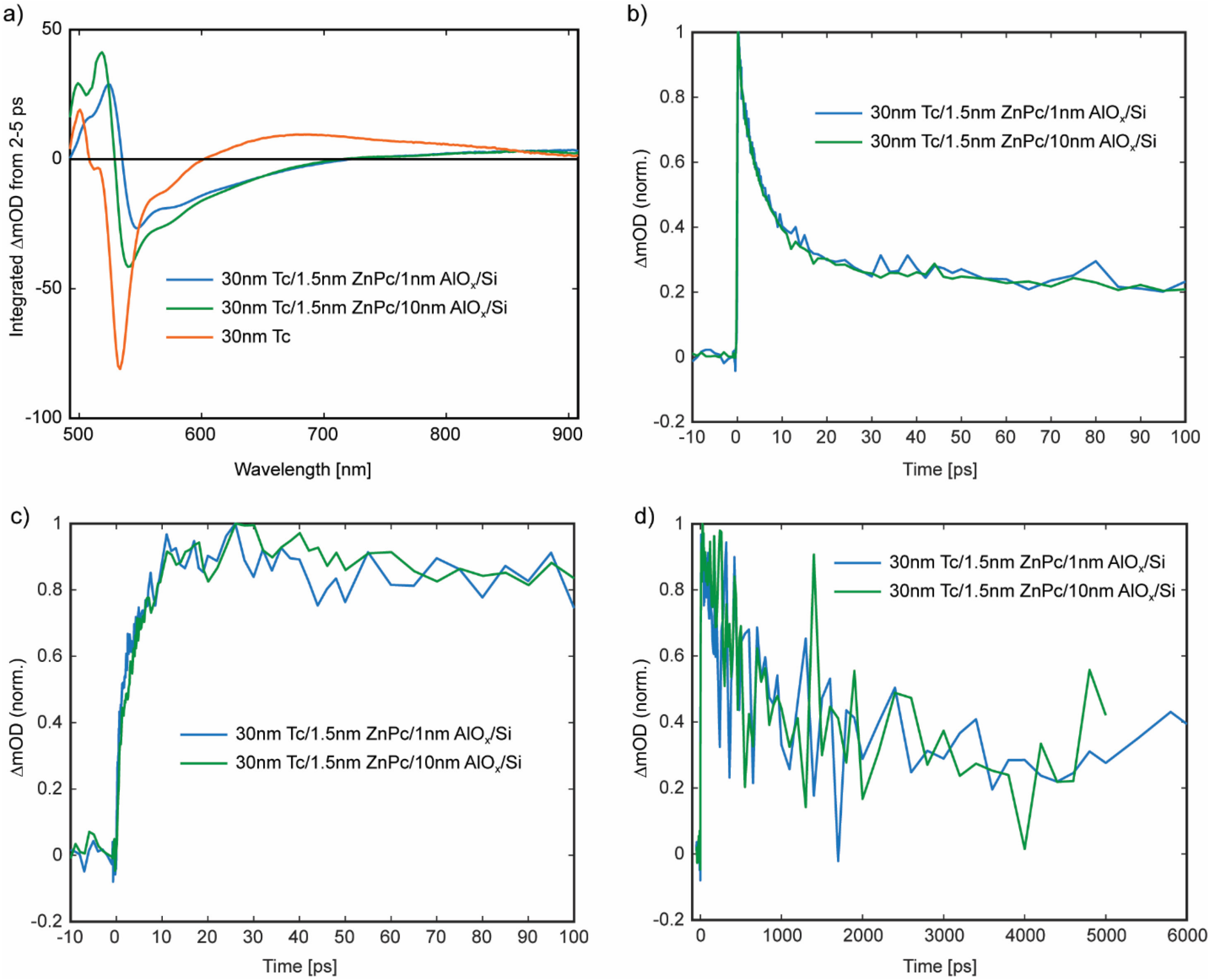

Figure 11-9. a) Comparison of time-integrated transient absorption/reflection spectra over the time-delay interval of 2-5 ps, measured for 30 nm Tc/1.5 nm ZnPc/1 nm AlO$_x$/Si (blue), 30 nm Tc/1.5 nm ZnPc/10 nm AlO$_x$/Si (green), 30 nm Tc (orange). b) Comparison of kinetic traces at 565 nm between 30 nm Tc/1.5 nm ZnPc/1 nm AlO$_x$/Si (blue) and 30 nm Tc/1.5 nm ZnPc/10 nm AlO$_x$/Si (green). c) Comparison of kinetic traces at 805 nm between 30 nm Tc/1.5 nm ZnPc/1 nm AlO$_x$/Si (blue) and 30 nm Tc/1.5 nm ZnPc/10 nm AlO$_x$/Si (green) over the first 100 ps. d) Comparison of kinetic traces at 565 nm between 30 nm Tc/1.5 nm ZnPc/1 nm AlO$_x$/Si (blue) and 30 nm Tc/1.5 nm ZnPc/10 nm AlO$_x$/Si (green) over the full range of measurement to 6 ns.

Finally, we attempt to compare the singlet and triplet dynamics between the transient reflection measurements of the 30 nm tetracene/1.5 nm zinc phthalocyanine/1 nm aluminum oxide/n-silicon and the transient absorption measurements of the 30 nm tetracene film. Assuming that the assignment for the singlet and triplet features are valid for both films, we notice some slight variations in the triplet exciton feature growth in Figure 11-10b. However, the crossover point at around 20-30 ps appears to be the same between the two samples. We note that the tetracene used in the tetracene-only film was purified once, while the one in the silicon samples were unpurified, due to instrument difficulties encountered at this time, so there could be some differences in the kinetics arising from the variation in tetracene. Additional control measurements would be helpful to verify.

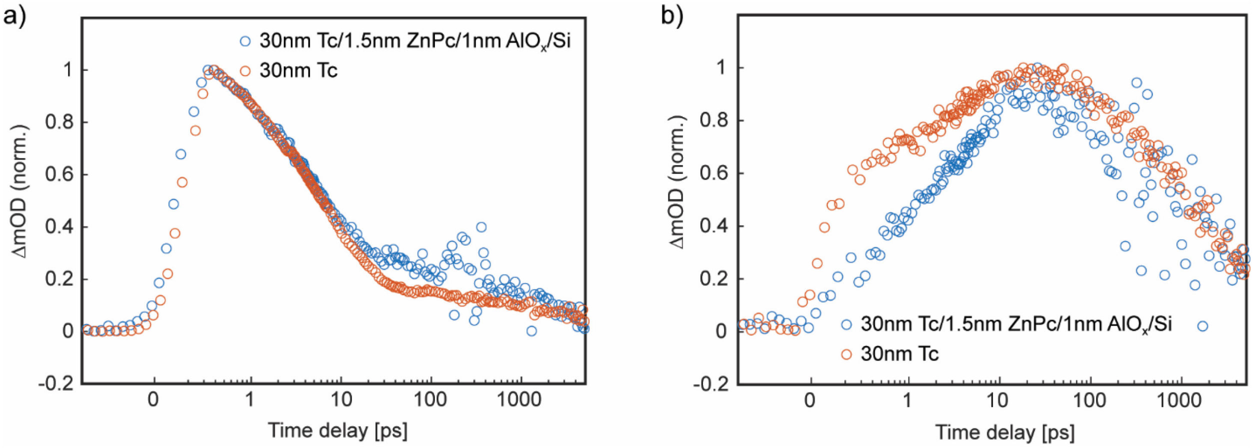

Figure 11-10. Kinetic trace comparison between 30 nm Tc/1.5 nm ZnPc/1 nm AlO_x/Si (blue) transient reflection measurements and 30 nm Tc (orange) transient absorption measurements at a) 565 nm and b) 805 nm. Both samples were measured with 8.6 mW pump pulse excitation power.

A summary of all the rates obtained for every sample is presented Table 11-3. All samples were excited with 8.6 mW pump average power. For samples that involved tetracene kinetics, we assumed that the entire pump excitation was absorbed by the tetracene layer to generate the excitation-induced exciton density for obtaining the triplet-triplet annihilation and bimolecular decay rate constants. For the zinc phthalocyanine sample, no fission and annihilation contributions were included in the model. For silicon, the absorption depth (inverse absorption coefficient) at 515 nm is 1.08 µm[88]. We use this thickness to calculate the excitation-induced carrier density for obtaining the bimolecular carrier recombination rate constant.

Table 11-3. Summary of fitted rate constants for different processes occurring in the samples presented in this section. Samples denoted with * were deposited in the New Angstrom setup with most ideal oxygen conditions. Samples denoted with ** were deposited in the Old Angstrom setup after purification. Samples denoted with no asterisk were deposited in the Old Angstrom setup with no purification of tetracene.

Sample structure	k_{SF} **[s^{-1}]**	k_{TTA} **[cm^3 s^{-1}]**	k_{MD} **[s^{-1}]**	k_{BD} **[cm^3 s^{-1}]**	$N_{T_{1,0}}/N_{S_{1,0}}$
30 nm ZnPc*	-	-	20.25	2.44×10^{-10}	-
30 nm Tc/ 1.5 nm ZnPc*	6.10×10^{10}	3.61×10^{-10}	6.76×10^{10}	2.57×10^{-9}	0.44
30 nm Tc**	5.28×10^{10}	8.61×10^{-11}	5.38×10^{10}	5.53×10^{-10}	1.05
1 nm AlO_x/ Silicon	-	-	-	7.42×10^{-10}	-
1.5 nm ZnPc/ 1 nm AlO_x/ Silicon	-	-	-	7.54×10^{-10}	-
30 nm Tc/ 1.5 nm ZnPc/ 1 nm AlO_x/ Silicon	6.02×10^{10}	5.86×10^{-10}	5.88×10^{10}	3.03×10^{-10}	0.27
30 nm Tc/ 1.5 nm ZnPc/ 10 nm AlO_x/ Silicon	5.76×10^{10}	5.74×10^{-10}	5.79×10^{10}	2.60×10^{-10}	0.16

The results of our initial transient absorption and reflection studies are in agreement with our expectations for what is occurring at the interface. We observe that despite there being some slight batch-to-batch variation, the fission process in tetracene remains largely unchanged even when the subsequent layers are included. As we are most interested in studying the effect on the triplet excitons, we need a measurement that is able to capture dynamics that occur at times beyond the first 10 ns.

11.4.2. Transient photoluminescence measurements of tetracene structures

Transient photoluminescence (PL) of tetracene has been well-studied and shows two distinct features: a prompt decay, attributed to radiative decay of the initially excited singlet population, and a delayed decay, attributed to radiative decay of singlet excitons formed from uncorrelated triplet excitons that encounter each other and undergo triplet-triplet annihilation[45,127,128]. Consequently, quenching of the prompt or delayed fluorescence in transient PL traces is often used as an intermediate probe of singlet or triplet exciton decay, respectively. Population decay pathways could include transfer of the exciton to an adjacent layer, charge transfer by the exciton to an adjacent layer, annihilation of the exciton through encounter with a charge, or other non-radiative decay pathways.

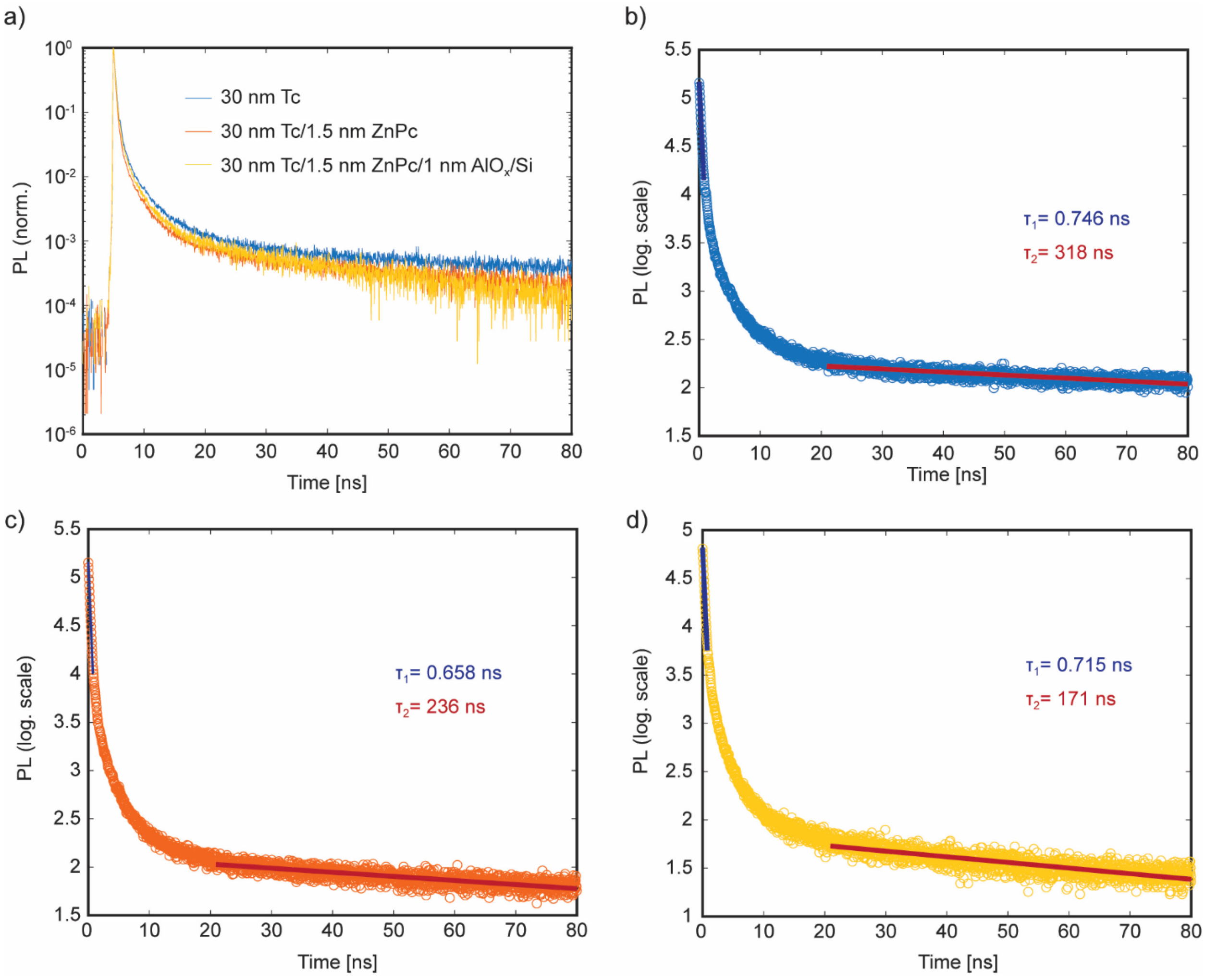

Figure 11-11. Transient photoluminescence measurements of a) 30 nm tetracene (blue), 30 nm tetracene/1.5 nm zinc phthalocyanine (orange), 30 nm tetracene/1.5 nm zinc phthalocyanine/1 nm aluminum oxide/silicon (yellow). b) Transient photoluminescence of 30 nm tetracene with extracted lifetime fits for the early dynamics (dark blue) and late dynamics (red). c) Transient photoluminescence of 30 nm tetracene/1.5 nm zinc phthalocyanine with extracted lifetime fits for the early dynamics (dark blue) and late dynamics (red). d) Transient photoluminescence of 30 nm tetracene/1.5 nm zinc phthalocyanine/1 nm aluminum oxide/silicon with extracted lifetime fits for the early dynamics (dark blue) and late dynamics (red).

We observe quenching of both prompt and delayed fluorescence as zinc phthalocyanine is added to tetracene, as well as with the full structure involving zinc phthalocyanine, aluminum oxide and silicon. We note that the delayed fluorescence is the most quenched with the full structure, consistent with expectations of the triplet exciton transfer to silicon. For the Tc/ZnPc sample, the quenching of the delayed fluorescence could correspond to triplet transfer from Tc to ZnPc, which is expected based on the predicted energy of the triplet exciton state in ZnPc being slightly lower than that of Tc[327]. We also notice slight prompt fluorescence quenching, which could correlate with singlet transfer from tetracene to zinc phthalocyanine, and also to silicon, although we note the lifetime fits for the prompt fluorescence are based on very few data points due to the time resolution of the measurement.

Interestingly, the delayed fluorescence quenching occurring is smaller than expected for these structures. The wafers used in these optical studies were lightly n-doped as opposed to the highly n-doped structures used in Chapter 7. This could result in less optimal alignment for triplet exciton transfer to silicon; further follow-up studies with highly n-doped silicon and also with thicker zinc phthalocyanine layers for the bilayer structures may be useful to study the relative quenching effect of the delayed fluorescence lifetime.

11.5. Future considerations for studying tetracene-silicon structures

Our optical measurements in this chapter are in agreement with our expectations for the triplet excitons formed from fission in tetracene. However, to really probe the dynamics of the transfer process, we need a technique that can directly probe the triplet exciton dynamics from the 10 ns – 100 μs time regime. Absorption measurements are still great candidates for this, and since we do not need the ultrafast time resolution, we can design simpler transient experiments where the resolution is limited by the detection electronics.

The electric field generated at the interface could also introduce a Stark effect (electric field-analogue of the magnetic field Zeeman effect) to the absorption spectrum that can be identified. For example, the effect of surface electric fields on quantum dots has resulted in energetic shifting of the spectrum[328–330], although the actual strength of the field at the silicon interface may not be as strong as in the quantum dot samples.

Even though we have demonstrated that energy level alignment is important for the triplet sensitization process, we still have yet to show that the triplet transfer is occurring through this charge-separated intermediate state. One other theory is that the triplet transfer is possible through Dexter and/or sequential charge transfer, but that there also needs to be an induced electric field near the interface to help prevent the carriers that have transferred to the near-surface region of silicon from recombining immediately. Being able to resolve the timescales of the triplet transfer process, the electric field-effect passivation process and the triplet-charge annihilation would be necessary to put together a complete picture of the processes occurring.

One of the other challenges with spectroscopy of these devices is the difficulty in obtaining measurements with good signal-to-noise ratio (SNR). Higher SNR could be obtained through using thicker organic layers, although this would no longer be representative of the device (due to changes in triplet diffusion length, *etc.*). Using higher excitation power could also achieve better SNR, although as we observed with tetracene, this introduces some oscillations in the data previously attributed to bulk acoustic phonons[312]. Additionally, the contributions of singlet-singlet annihilation, as well as other competing processes become non-negligible, affecting the overall efficiency of the triplet transfer process.

Chapter 12.
Conclusion and outlook

12.1. Conclusion

There is huge potential for solar power to match the growing global energy demand, but we are limited by resources, space, and efficiency losses in the energy conversion process. Crystalline-silicon continues to remain the dominant solar technology, but their efficiencies have only increased incrementally over the recent 20 years as they are starting to approach the theoretical efficiency limit. The main source of losses in crystalline-silicon solar cells are thermalization losses, where energy in excess of the bandgap absorbed by silicon is lost as heat[20]. In 1979, Dexter first proposed combining a silicon solar cell with an organic layer that performs singlet exciton fission enclosing the cell[27]. By having the organic layer absorb the high energy light and transferring the triplet excitons generated from singlet fission to silicon, the photocurrent in this spectral region can be doubled, with the potential of raising the efficiency from the classical limit of 29.4 % to 35-42 %[26,36,28,37,38].

Since then, many groups have worked towards sensitizing silicon with singlet fission, however, the greatest challenge has been to demonstrate an increase in the silicon photocurrent, a necessary condition to show that the technology is viable. Scientifically, there are three main challenges to this problem. The first is to successfully couple the triplet excitons to silicon. Triplet excitons in molecular semiconductors are optically dark states; as a result, direct transfer of triplet excitons across the interface is limited to very short distances, on the order of 1 nanometer for tunneling of the charge carriers. This also limits the passivation layer thickness that can be used on the silicon surface, which is necessary to prevent surface states from quenching the triplet excitons throughout the transfer process. Additionally, simply using a thin chemical passivating layer is insufficient for successful triplet transfer, raising the question about the mechanism of the transfer process. This brings us to the second main challenge with progress in this area, which is that not much is understood regarding the exciton and charge carrier dynamics at this interface. Definitive probes of successful triplet sensitization require fabrication of a full working device, which can show no improvements in silicon photocurrent for reasons other than unsuccessful triplet transfer from the singlet fission layer to silicon. Intermediate probes without building devices exist, but the measurements can be complicated to interpret. Finally, the third main challenge is the design of the silicon solar cell itself. The carriers from the transferred triplet excitons are expected to be located within the top surface region of silicon. As a result, for enhancements to be observed, not only should there be high singlet fission yields, and high triplet transfer efficiencies, we also need a silicon solar cell that is efficient at extracting near-surface carriers.

This thesis tackles these three challenges from an interfacial materials, device architecture and spectroscopy approach.

1. From an **interfacial materials** standpoint (Chapters 4, 5 and 7), we follow up on previously reported hafnium oxynitride (HfO_xN_y) thin films which enabled triplet exciton sensitization of silicon by tetracene[35], but the mechanism for the transfer process was not well understood. We show that the composition of this layer affects the sensitization process, and through a combination of density functional theory calculations and magnetic field-dependent silicon photoluminescence measurements, identify that **defect-induced states** that lie **near the band edge** of silicon are **beneficial for the triplet exciton transfer process**, potentially mediating a sequential charge transfer process. However, our studies also reveal that the HfO_xN_y layer can introduce a variety of mid-gap states that quench the silicon photoluminescence, acting detrimentally to the overall silicon performance. We also identify that **electric field-effect passivation** is beneficial for the triplet sensitization process, preventing transferred carriers from recombining at the interface – as a result, we design a bilayer interface between the tetracene and silicon layers consisting of a **donor layer** which introduces an energy level near the valence band edge of n-doped silicon such that charge separation is energetically supported from the triplet exciton state in tetracene, and an ultra-thin **passivating layer** that chemically passivates dangling bonds on the silicon surface. Using zinc phthalocyanine as the donor layer and either aluminum oxide or hafnium oxide as the passivating layer, we observe evidence for triplet excitons generating electric field-effect passivation, benefiting the silicon photoluminescence.
2. From a **device architecture** standpoint (Chapters 6 and 7), we use our donor-passivation interface and apply it to various silicon solar cell architectures. We find that the silicon-tetracene heterojunction cells face challenges related to morphology of the tetracene layer, resulting in suboptimal device performance. We observe no evidence of enhancements from singlet fission in interdigitated-back-contact cells, suggesting that this device

structure is not sensitive to surface carriers in silicon. Indeed, when we switch to microwire and shallow junction planar solar cells with pyramidal surface texturing, both devices **designed to efficiently extract silicon surface charge carriers**, we observe **enhancements in the silicon device external quantum efficiencies and photocurrent** from tetracene. Additionally, we perform silicon doping dependence studies and interlayer knockout controls, confirming the importance of the **interfacial energy alignment** and the **donor layer**, as well as the **device architecture**.

3. From a **spectroscopy** standpoint (Chapters 9, 10 and 11), we work on techniques that can be used to better understand the exciton and carrier dynamics of the singlet fission-donor-passivation-silicon structure. To better understand **carrier transport in bulk materials**, we detail a **numerical framework for robust estimation of carrier diffusivity**. To better understand **interfacial charge transport**, we build a **transient second harmonic generation spectroscopy** setup. Finally, we probe early timescale dynamics of excitonic processes in tetracene using **transient absorption and reflection**, confirming that the singlet fission process in tetracene is **not affected** by the addition of the various donor, passivation and silicon layers. Our studies also reveal that the triplet transfer and electric field-effect passivation is occurring at **timescales beyond the first 10 ns of excitation**, opening up the studying of these interfaces to slower spectroscopy experiments, not limited to ultrafast time scales.

These results have shown that singlet fission-sensitized silicon solar cells are a viable technology for enhancing silicon solar cell efficiencies beyond the conventional single-junction limit. This interface remains a rich area for fundamental scientific studies, involving coupling between molecular dark states to bulk silicon. We hope that the key findings can help direct research efforts towards scalable implementation of this technology, and stress that the fundamental understanding of the interface also has broad implications to other silicon technologies that can benefit from enhanced quantum yields, including photodetectors.

12.2. Outlook

As my thesis comes to a close, I am once again reminded that the scientific understanding of a problem is never over: with new findings come new questions. In this section, I outline some of the lingering questions that remain, with suggestions for further directions of study.

12.2.1. Industrial viability

We have shown that the triplet states in tetracene can be coupled to silicon solar cells, resulting in an increase in photocurrent. This opens up the path for singlet fission-silicon solar cells as a viable technology for going beyond the conventional single-junction limit.

12.2.1.1. Over 100 % external quantum efficiency

The initial device enhancements that we showed raised the power conversion efficiency of the cell by 0.06 %. However, the maximum benefit from fission is expected to be much higher[26,36,28,37,38], suggesting many opportunities for further improvements.

We observe peaks in the EQE spectra, indicating successful triplet exciton sensitization, however, there is still the question about whether this is from triplet exciton transfer or purely an electric field-effect passivation from tetracene. In practice, these two effects can be hard to separate, especially if the passivation is coming from triplet excitons in tetracene, through a dynamic passivation scheme discussed in Chapter 5. However, there are some measurements that suggest that the peaks in EQE observed in Chapter 7 are not solely from triplet-driven passivation and that the triplet excitons are being transferred to silicon.

From the transfer matrix modeling in Chapter 5 and Chapter 7, we know that tetracene absorbs at most about 20 % of the light at 520 nm, leaving silicon with 80 %. As a result, the photogenerated carriers from just silicon absorption alone is lower with the tetracene present. If tetracene triplets were just passivating the silicon surface and repelling minority carriers to improve carrier collection, the number of photogenerated carriers would not change, only the collection efficiency would be enhanced. It is unlikely for the collection efficiency of carriers alone to be responsible for the 138 % sensitization efficiency as calculated in Chapter 7. We turn to the control microwire device deposited with 10 nm Al_2O_3 as a case study. 10 nm-thick Al_2O_3 should be a high-quality passivation layer, providing slight electrical field effect and strong chemical passivation for silicon solar cells[187]. In comparison to the 1 nm-thick AlO_x devices, we observe the baseline cells with no organic layers deposited, we see that the silicon EQE is enhanced from about 81 % to 85 % at 520 nm, which is a 105 % enhancement. Additionally, we note that the absorption depth of 520 nm light in silicon is approximately 1.14 µm[88]. From space charge region modeling of field-effect passivation on the top surface of silicon, the field effect is most likely to affect the top few 100 nm of silicon[331]. For these reasons, we do not think that the peaks in our EQE in Chapter 7 are from field-effect passivation alone.

Of course, the clearest way to prove triplet exciton transfer is to show a device with greater than 100 % EQE. There are several avenues to achieving this:

1. *Conformal coating of the tetracene layer on the microwire solar cells*: We see in Chapter 7 that tetracene is demonstrating island-type growth on the microwires. Additionally, most of the deposition occurs on the base of the cell compared to the side walls of the microwires. The rates of singlet fission (and potentially triplet exciton transfer) are expected to be morphology-dependent[122]. Improved morphology of the tetracene layer and increased thickness on the side walls could result in enhanced peaks, which could take the cells closer to 100 %. The current thermal evaporation process is a directional deposition technique[193]; as an alternative, we suggest low-pressure, organic vapor-phase deposition as a technique to potentially achieve conformal coating on 3D structures[332].
2. *Anti-reflective coating on the encapsulating glass*: As tetracene is photosensitive[76,77,106], the device active area was encapsulated using a glass slide. Although the microwire solar cells reduce reflection losses[133], the glass itself can introduce additional reflection off the surface. Ideally, we would not encapsulate the cell. However, any singlet fission material that could be viable for industrial applications may still need to be encapsulated due to competitive harvesting of triplet excitons by the oxygen triplet ground state. Instead, antireflective coatings can be applied onto the glass to reduce any additional losses induced by the glass layer.
3. *Further optimizations of device components:* The device presented in Chapter 7 was not completely optimized. Indeed, the actual area density of the organic layers are expected to be lower due to the high surface area of the substrates. The aspect ratio of the microwires could also be tuned to maximize absorption by the tetracene layer.

4. *Alternative passivation layers:* We have found that the quality of the passivation strongly affects the magnitude of the peaks. As a result, getting a high-quality passivation layer is vital for achieving greater enhancements. Interesting candidates for further study include ultra-thin oxides that are used in TOPCon solar cells (such as SiO_x), or in advanced-node field-effect transistors, which could further improve the probability and rate of tunneling across the interface.
5. *Accurate reflectance and absorbance measurements:* To quantify the contribution in losses from reflection, decrease in passivation quality, and absorbance from tetracene, obtaining accurate measurements of reflectance and absorbance on microwire structures is desired to calculate the internal quantum efficiency spectrum. I tried this once using an integrating sphere setup but had some issues with calibrating the sphere as I noticed a strange power-dependence of the reflectance. Finetuning this setup further could be helpful for future calculations of IQE.
6. *Demonstration of sensitization for p^+-n Si:* All demonstrations of triplet sensitization so far have been performed on n-doped silicon. In theory, many of the findings in this thesis can be transferred to p-Si as well by using a suitable donor layer with a LUMO level that is aligned near the conduction band edge of silicon. The challenge is finding an appropriate hole-donating material, as the leading thermally evaporable candidate C_{60} reacts with tetracene through a Diels-Alder reaction, resulting in an unstable interface[333]. Its triplet energy is also higher than tetracene (~1.6 eV[334,335]), which can potentially prevent the sensitization process, depending on whether the triplet excitons transfer to the donor layer or simply dissociate directly from tetracene in the donor layer. Other materials include Y6[336], although its deposition is typically done from solution, which can pose some undesirable reactions between the solvent and the silicon surface passivation.

12.2.1.2. Stable fission materials

The known photosensitivity of tetracene to oxygen[76,77,106] makes it an unattractive material for industrial adoption of this technology. In theory, the results of this thesis suggest that triplet exciton transfer can occur with any singlet fission material similar to tetracene, as long as the donor and passivation interlayers are applied between the material and silicon. Stable alternatives to tetracene include perylene diimides (PDI) and their derivatives[110,337,112], functionalized acenes[338], and potentially aza-cibalackrot[339].

Even better, if there is a singlet fission material with a HOMO level that is similar to ZnPc such that the alignment is near the band edge of silicon, this could lead to a structure that eliminates the ZnPc layer altogether, and the fission material can directly donate the electron across the interface.

12.2.2. Nature of the triplet exciton transfer process

We show the importance of introducing a state near the band edge of silicon for triplet exciton sensitization of silicon. Throughout this thesis, we hypothesize that this state is helping with the triplet exciton transfer process by mediating an intermediate charge-separated state (D^{+}-A_{Si}^{-}) where the electron lies in the silicon and the hole lies in the donor layer. Naturally, the question arises: is triplet exciton transfer only possible through this charge-separated state, or can Dexter transfer still occur between tetracene and silicon?

This is an interesting question to consider. One could consider this through a probability argument. Because we are pushing the limits of carrier tunneling due to the thickness of the passivation layer, Dexter transfer may simply not be favorable compared to the sequential charge transfer mechanism because it requires simultaneous tunneling of both the electron and the hole across the interface. However, it is also entirely possible that the near-band-edge state could just be supporting triplet-driven field-effect passivation, where the triplet excitons are indeed transferring through a Dexter transfer mechanism, but the field-effect passivation is necessary to prevent carrier recombination near the surface. The control sample to look at in particular is the device in Chapter 7 with no ZnPc layer on n^{+}-p Si. Indeed, we notice the magnitude of the dip in this layer is reduced compared to the p^{+}-n Si. The difference between this sample and the one with ZnPc could be explained by both theories: for the sequential charge transfer mechanism, the HOMO level of tetracene is such that there could be a small density of tail states that are still able to form the intermediate charge transfer state, resulting in some triplets transferring completely. For the passivation mechanism, the reduction in the dips may be indicative of a baseline Dexter transfer level, and that the triplet-driven field-effect passivation is insufficient to completely prevent carriers from getting quenched by surface defects. However, we note previous unsuccessful attempts to transfer the triplet exciton to silicon[44,45], for which Dexter transfer should have theoretically been possible.

The question also extends beyond tetracene and silicon, to triplet transfer from any organic molecule to bulk semiconductors in general. Although in the reverse direction, we note that trap-assisted triplet sensitization has been reported for transfer from perovskites to rubrene[340]. It is not clear if the indirect gap of silicon plays a role, as triplet transfer has been shown from molecules to quantum dots[116,117], and a Dexter transfer mechanism was proposed for these systems. In theory, the indirect gap of silicon should not play a role between the two transfer mechanisms. Nevertheless, it can be interesting to pursue this by trying a direct gap replacement to silicon, such as copper indium gallium selenide (CIGS). One other theory for the differences in observations between the quantum dots as acceptors *vs* silicon is related to the quantum confinement effect in the quantum dots, and the large dielectric constant in silicon. A further detailed study into the transfer mechanism can be very interesting, particularly if kinetics can be obtained.

One other structure that I propose for study is a three-terminal device. Although this may be difficult due to the inhomogeneous deposition of the tetracene layer observed in Chapter 6, adding a third electrode on top of the silicon allows for injection of additional charge carriers in tetracene that could also artificially induce an electric field-effect passivation at the silicon surface, which can be used to compare the triplet exciton sensitization effect for a device without an applied electric field.

12.2.3. Spectroscopy of silicon-tetracene samples

Characterizing these samples over the years, I have noticed a couple of observations in the data that may be interesting to probe further.

12.2.3.1. Tetracene optical properties when deposited on silicon

Tetracene's absorption spectrum measured on glass shows a Davydov split in the 0-0 peak, where the lower energy peak is higher in magnitude. However, in all of the excitation wavelength-dependent silicon photoluminescence and silicon EQE measurements in Chapter 5 and Chapter 7, the higher energy peak of the Davydov split is consistently higher in magnitude. The relative ratio of the peaks in the split have been attributed to the presence of two tetracene polymorphs in polycrystalline films[129]. Notably, other reports in literature have seen differences in absorption spectra from our work on glass, where the higher energy peak is higher in magnitude[129,341]. Previous reports in literature suggest that ageing of tetracene results in an increase in a specific tetracene polymorph which they attribute to favorable triplet sensitization[47]. If greater peaks can be observed in EQE such that we can resolve the Davydov split, it may be interesting to probe the morphology theory. We note that previous preliminary collaborations with Helmholtz appeared to suggest minimal differences in orientation of ultrathin tetracene layers grown on HfO_x and HfO_xN_y.

In Chapter 11, we also observe differences in the stimulated emission features measured for tetracene samples on glass compared to on silicon, showing a longer tail and an apparent red-shifting of the emission 0-0 peak. It would be interesting to confirm if this is also observed in the steady-state emission spectra of tetracene on silicon. We note that there have been previous observations of a long tetracene emission tail expanding out to the NIR[326]. Probing further in this region could also be interesting for studying potential charge-separated states across the donor-silicon interface.

Finally, in Chapter 7, and in other measurements not presented in this thesis, we have observed a shoulder in the EQE extending to 600 nm. The origin of this effect is not entirely clear. It could arise from the microwire geometry through some reflective effects, or it could potentially signal some interesting possibilities for sub-bandgap sensitization of silicon. Simulation of absorption beyond the simplified transfer matrix model for more complex 3D structures can be useful.

12.2.3.2. Understanding the silicon-tetracene interface

In this thesis, we show that both the triplet transfer and triplet-driven passivation processes occur at timescales slower than the first 8 ns of excitation. To better understand the transient dynamics at this interface, slower time-resolved spectroscopy studies are desirable.

1. *The interface between tetracene and the donor ZnPc*: Based on the initial transient photoluminescence measurements in Chapter 11, time-dependent density functional theory calculations from our collaborators in Chapter 7, and from reports of the triplet exciton energy in zinc phthalocyanine[188], we expect there to be triplet transfer from tetracene to zinc phthalocyanine, prior to the electron donation step to silicon. Obtaining timescales for this transfer process and the subsequent electron-donating process would be useful. One possible experiment to probe this would be ZnPc thickness dependence studies from 1.5 nm to 10 nm (reported exciton diffusion length[174]). If the triplet excitons were transferring

to ZnPc first before dissociation, there would be a less dramatic thickness-dependence of the sensitization process to ZnPc layer thickness (under the diffusion length).

2. *The interface between the donor ZnPc, the passivation layer and silicon:* This interface remains an area of great spectroscopic interest. The greatest but perhaps most interesting challenge will be resolving the triplet exciton transfer process and the triplet-driven passivation process, although it is highly likely that these two processes are coupled. Hysteresis sweeps can be useful for investigating the minute-long charge trapping processes in these cells. Pump wavelength-dependent transient surface photovoltage measurements can be used to obtain timescales of the charge separation and recombination processes induced by the triplet excitons. Monitoring the carrier dynamics in silicon would also be interesting, but would require an IR detector and high excitation powers.

12.2.3.3. Magnetic field-dependent measurements

In Chapter 5, we see that the devices with ZnPc show magnetic field-dependent characteristics that track with triplet-charge annihilation, whereas in Chapter 4 and previous work[35], we observe magnetic field-dependent characteristics for devices with HfO_xN_y that track with singlet fission and triplet transfer. As we expect there to be some degree of charges present in HfO_xN_y, it is notable that we never see any traces of triplet-charge annihilation. This could be a potentially interesting area for further probing *via* simulations and kinetic modeling.

12.3. Concluding thoughts

The area of singlet fission-sensitized silicon solar cells poses a rich set of interesting research questions. From gaining a fundamental understanding of the interfacial properties and material exciton and charge carrier dynamics through advanced spectroscopy techniques, while simultaneously having the opportunity to work on device engineering to apply what was learnt about the interface to fabricate an actual working device, I have thoroughly enjoyed working on this project. Now that we have shown silicon photocurrent enhancement is possible from fission, there are many more exciting follow up research questions that can be answered. I hope that fission-sensitization of silicon can receive the same excitement from the scientific community as perovskite-tandems, and I look forward to future progress in this field.

Appendix: Assortment of other experimental observations

A. TDMAH-based HfO_xN_y films

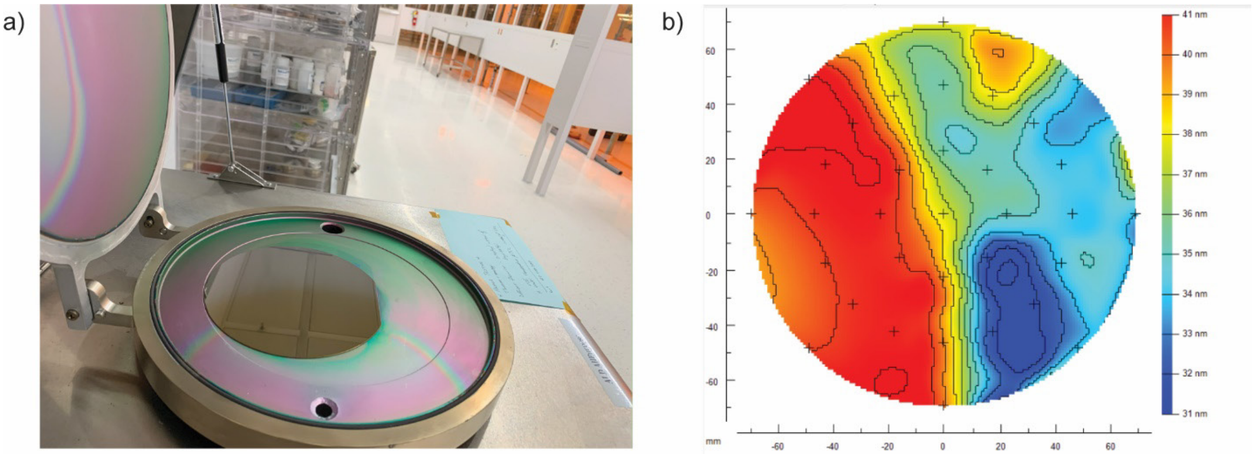

Figure A-0-1. HfO_xN_y films grown using TDMAH. a) Photograph of the grown film. b) Ellipsometer thickness map taken of the entire wafer.

When growing the TDMAH-based HfO_xN_y films on the ALD tool, we noticed that a thickness of 1.6 Å/cycle could only be obtained over part of the wafer. The remainder of the wafer showed a thinner thickness of cycle, suggesting that the films grown using the recipe in Einzinger *et al.*[35] were actually not ALD but CVD.

B. Deposition rate-dependent AFM measurements

In an attempt to obtain better morphological growth of tetracene layers for the heterojunction solar cells, several different processing conditions were attempted for tetracene growth. The AFM measurements for these samples are shown in Figure A-2. We observe that using higher deposition rates results in smaller grains of tetracene. Annealing at high temperatures in a glovebox environment did not result in any obvious morphological changes. Finally, co-evaporating with MTDATA resulted in sparser tetracene grains, although this could have been because of improper calibration of the tooling factors for co-evaporation. The observation of the grain sizes with the changing deposition rate is consistent with previous observations[342].

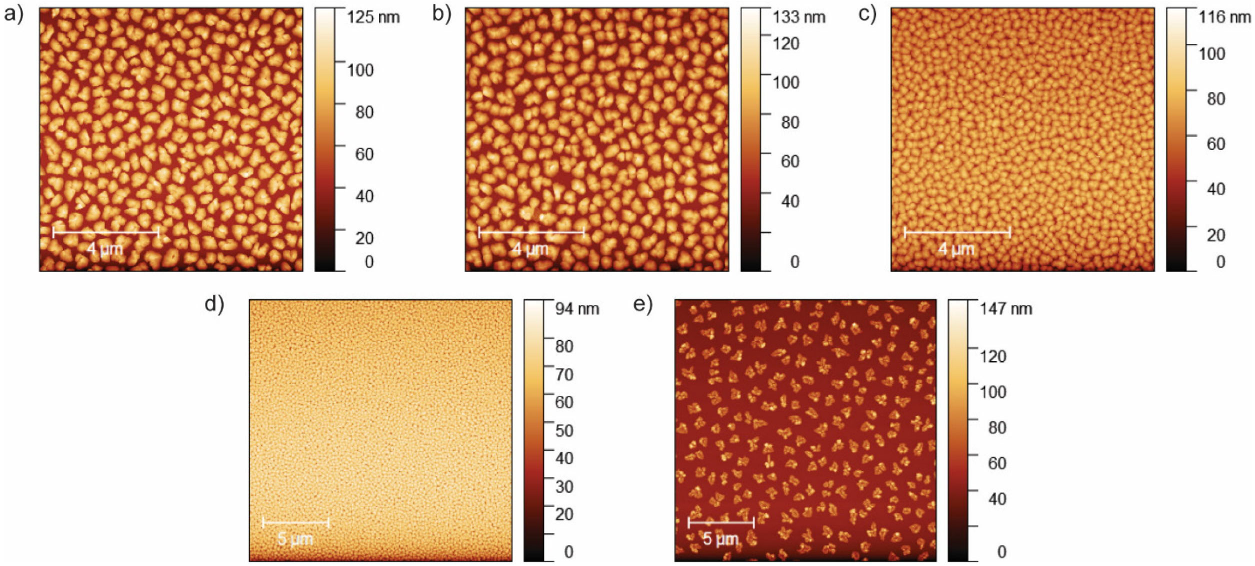

Figure A-0-2. AFM measurements of tetracene films grown with various processing conditions. a) Tetracene grown at 1 Å/s. b) Tetracene grown at 1 Å/s and annealed on a hotplate inside a glovebox for 30 minutes at 125 °C. c) Tetracene grown at 5 Å/s. d) Tetracene grown at 8 Å/s. e) Tetracene co-evaporated with MTDATA. Respective deposition rates are unknown because they were not tooled.

C. Technique for transport of samples from cleanroom to lab glovebox

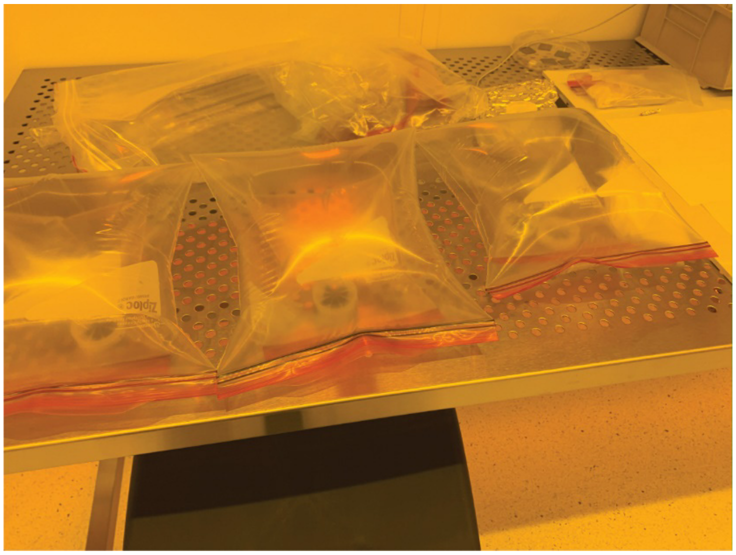

Figure A-0-3. Double-nitrogen-filled Ziploc bag technique used for transporting samples from the cleanroom to the lab glovebox.

The triplet exciton sensitization efficiency was found to be very sensitive to the quality of silicon surface passivation. Particularly with the HfO_xN_y films and the 2 Å-thick ALD films with no annealing, exposure of the films to air resulted in oxygen diffusion that would vary the performance of the sensitization. Various sample transporting techniques were tested, including vacuum sealing and nitrogen-bagging. The best reproducibility was found using double nitrogen-filled Ziploc bags.

D. Artifacts observed in EQE measurements

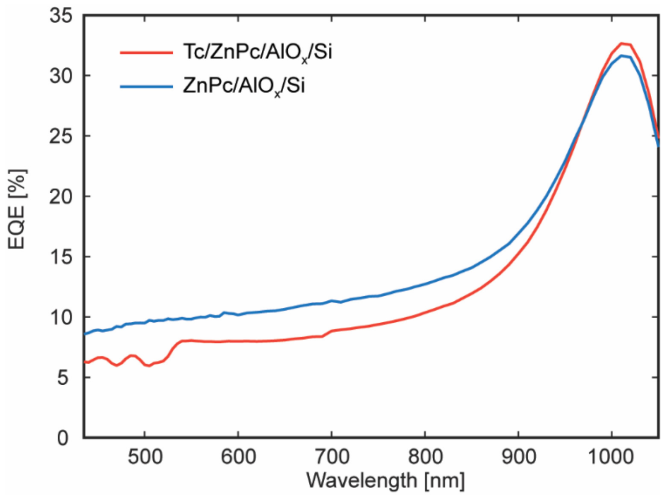

Figure A-0-4. Artifact observed in the EQE measurements for silicon solar cells where the EQE increases dramatically from 900-1000 nm.

There were many instances where artifacts were observed in the EQE measurements. These usually arose from improper calibration using the photodetector. We found the best results were obtained by operating the lock-in amplifier used in voltage mode and measuring the signal with a 50 Ω resistor in circuit. The lock-in amplifier has a much higher range of sensitivity in voltage mode, and will not result in current saturation during the photodetector calibration where the lamp spectrum is high, which is the reason behind the IR artifact.

E. Artifacts observed in magnetic field effects

Artifacts can also be observed in magnetic field-dependent measurements, and are usually easier to identify if full scan measurements are performed. They are most likely to arise from loose screws on any of the optical components in the setup, particularly the sample holder and electrical probe connections on the sample holder which move as the magnetic field is applied.

F. Attempts to diffusion image IR samples in Montana

When I first started transient PL microscopy measurements in the Montana, I attempted to measure diffusion imaging maps on NIR samples, including GaAs and MAPbI$_3$. Unfortunately, neither of them worked. I suspect the setup was not built optimally for samples emitting outside of the visible region. To align the laser spot, we need to be able to image the spot on the camera, however the camera likely has low sensitivity to NIR. Additionally, the APD has low photon detection efficiency in this region. Finally, the objective lens may have low transmission efficiency for NIR photons.

G. Temperature rise from laser modeling

Laser-induced temperature rise in samples can be modeled using:

$$\frac{\partial \Theta(r,z,t)}{\partial t} = D_{thermal} \nabla^2 \Theta(r,z,t), \tag{A-1}$$

where $\Theta(r,z,t)$ is the dimensionless temperature $\Theta = \frac{T(r,t)-T_{initial}}{\Delta T_{max}}$ as a function of radial position r, axial position z and time t, T is the actual temperature in the sample, $T_{initial}$ is the initial temperature that the sample is at before the laser excitation, ΔT_{max} is the maximum temperature rise induced in the sample as a result of the laser excitation, and $D_{thermal}$ is the thermal diffusivity of the material of interest.

We can obtain $D_{thermal}$ using:

$$D_{thermal} = \frac{k}{\rho c_p}, \tag{A-2}$$

where k is the thermal conductivity of the material, ρ is the density of the material, and c_p is the specific heat capacity of the material.

We can calculate ΔT_{max} using the following expression:

$$\Delta E_{photon} \times \langle n \rangle = \rho c_p V \Delta T_{max}, \tag{A-3}$$

where ΔE_{photon} is the photon energy, $\langle n \rangle$ is the average number of photons absorbed per pulse, and V is the volume of the material.

List of publications

Publications

Published

- N. Nagaya Wong, S.K. Ha, K. Williams, W. Shcherbakov-Wu, J.W. Swan, W.A. Tisdale; Robust estimation of charge carrier diffusivity using transient photoluminescence microscopy. *J. Chem. Phys.* 157, 104201 (2022)

Submitted

- N. Nagaya*, K. Lee*, C.F. Perkinson*, A. Li, Y. Lee, X. Zhong, S. Lee, L.P. Weisburn, T.K. Baikie, M.G. Bawendi, T. Van Voorhis, W.A. Tisdale, A. Kahn, K. Seo, M.A. Baldo; Exciton Fission Enhanced Silicon Solar Cell.

In preparation

- N. Nagaya, A. Alexiu, C.F. Perkinson, M.G. Bawendi, W.A. Tisdale, T. Van Voorhis, M.A. Baldo; Triplet Exciton Sensitization of Silicon Mediated by Defect States in Hafnium Oxynitride.
- N. Nagaya, C. F. Perkinson, A. Li, T. K. Baikie, W. P. A. Verheijen, K. Lee, Y. Lee, J. Song, Z. VanOrman, O. M. Nix, M. G. Bawendi, S. Feldman, K. Seo, W. A. Tisdale, M. A. Baldo; Dynamic triplet-driven passivation of silicon surfaces.

Patents

- N. Nagaya, K. Lee, C. F. Perkinson, A. Li, M. A. Baldo; Silicon solar cell design for triplet exciton sensitization (provisional)
- N. Nagaya Wong, C. F. Perkinson, M. A. Baldo; Interlayers for Charge Transfer-Mediated Triplet Exciton Transfer from a Singlet Exciton Fission Material to An Inorganic Semiconductor (decision pending)

Bibliography

1. Energy Institute. Statistical Review of World Energy, 73rd Edition. (2024).

2. Ritchie, H., Rosado, P. & Roser, M. Energy Production and Consumption. *Our World in Data* (2024).

3. Vaclav Smil. *Energy Transitions: Global and National Perspectives*. (Praeger, 2016).

4. Tsao, J., Lewis, N. & Crabtree, G. Solar FAQs. (2006).

5. Fraunhofer Institute for Solar Energy Systems, ISE. *Photovoltaics Report*. https://www.ise.fraunhofer.de/content/dam/ise/de/documents/publications/studies/Photovoltaics-Report.pdf (2024).

6. John Fitzgerald Weaver. Silicon cost per watt down 96% over last two decades. *pv magazine USA* https://pv-magazine-usa.com/2023/01/10/silicon-cost-per-watt-down-96-over-last-two-decades/ (2023).

7. David Feldman *et al. NREL Spring 2024 Solar Industry Update*. https://www.nrel.gov/docs/fy24osti/90042.pdf (2024).

8. Müller, A. *et al.* A comparative life cycle assessment of silicon PV modules: Impact of module design, manufacturing location and inventory. *Solar Energy Materials and Solar Cells* **230**, 111277 (2021).

9. IRENA (International Renewable Energy Agency) & IEA-PVPS (International Energy Agency Photovoltaic Power Systems Programme). *End-of-Life Management: Solar Photovoltaic Panels*. https://www.irena.org/-/media/Files/IRENA/Agency/Publication/2016/IRENA_IEAPVPS_End-of-Life_Solar_PV_Panels_2016.pdf?rev=49a75178e38c46288a18753346fb0b09 (2016).

10. Tao, M. *et al.* Major challenges and opportunities in silicon solar module recycling. *Progress in Photovoltaics: Research and Applications* **28**, 1077–1088 (2020).

11. Best Research-Cell Efficiency Chart. https://www.nrel.gov/pv/cell-efficiency.html.

12. Champion Photovoltaic Module Efficiency Chart. https://www.nrel.gov/pv/module-efficiency.html.

13. Shockley, W. & Queisser, H. J. Detailed Balance Limit of Efficiency of p-n Junction Solar Cells. *Journal of Applied Physics* **32**, 510–519 (1961).

14. Richter, A., Hermle, M. & Glunz, S. W. Reassessment of the Limiting Efficiency for Crystalline Silicon Solar Cells. *IEEE Journal of Photovoltaics* **3**, 1184–1191 (2013).

15. Green, M. A. *et al.* Solar cell efficiency tables (Version 64). *Progress in Photovoltaics: Research and Applications* **32**, 425–441 (2024).

16. LONGi Sets New World-Record for Silicon Solar Cell Efficiency, Launching 2nd Generation Ultra-Efficient BC-Based Module. *Longi* https://www.longi.com/en/news/longi-hi-mo9-bc-world-record//.

17. Energy, Entropy and Efficiency. in *Third Generation Photovoltaics: Advanced Solar Energy Conversion* (ed. Green, M. A.) 21–34 (Springer, Berlin, Heidelberg, 2003). doi:10.1007/3-540-26563-5_3.

18. Max Planck, translated by Morton Masius. *The Theory of Heat Radiation*. (1913).

19. Vos, A. D. Detailed balance limit of the efficiency of tandem solar cells. *J. Phys. D: Appl. Phys.* **13**, 839 (1980).

20. Octavi Semonin, Joseph M. Luther, & Matthew C. Beard. Multiple exciton generation in a quantum dot solar cell. https://spie.org/news/4146-multiple-exciton-generation-in-a-quantum-dot-solar-cell.

21. Sark, W. G. J. H. M. van *et al.* Luminescent Solar Concentrators - A review of recent results. *Opt. Express, OE* **16**, 21773–21792 (2008).

22. Meinardi, F., Bruni, F. & Brovelli, S. Luminescent solar concentrators for building-integrated photovoltaics. *Nat Rev Mater* **2**, 1–9 (2017).

23. van Sark, W. G. J. H. M., Meijerink, A., Schropp, R. E. I., van Roosmalen, J. A. M. & Lysen, E. H. Enhancing solar cell efficiency by using spectral converters. *Solar Energy Materials and Solar Cells* **87**, 395–409 (2005).

24. Khare, A. A critical review on the efficiency improvement of upconversion assisted solar cells. *Journal of Alloys and Compounds* **821**, 153214 (2020).

25. Beery, D., Schmidt, T. W. & Hanson, K. Harnessing Sunlight via Molecular Photon Upconversion. *ACS Appl. Mater. Interfaces* **13**, 32601–32605 (2021).

26. Hanna, M. C. & Nozik, A. J. Solar conversion efficiency of photovoltaic and photoelectrolysis cells with carrier multiplication absorbers. *Journal of Applied Physics* **100**, 074510 (2006).

27. Dexter, D. L. Two ideas on energy transfer phenomena: Ion-pair effects involving the OH stretching mode, and sensitization of photovoltaic cells. *Journal of Luminescence* **18–19**, 779–784 (1979).

28. Rao, A. & Friend, R. H. Harnessing singlet exciton fission to break the Shockley–Queisser limit. *Nature Reviews Materials* **2**, 1–12 (2017).

29. Baldacchino, A. J. *et al.* Singlet fission photovoltaics: Progress and promising pathways. *Chemical Physics Reviews* **3**, 021304 (2022).

30. Lewis, N. S. Research opportunities to advance solar energy utilization. *Science* **351**, aad1920 (2016).

31. Tanabe, K. A Review of Ultrahigh Efficiency III-V Semiconductor Compound Solar Cells: Multijunction Tandem, Lower Dimensional, Photonic Up/Down Conversion and Plasmonic Nanometallic Structures. *Energies* **2**, 504–530 (2009).

32. Polman, A. & Atwater, H. A. Photonic design principles for ultrahigh-efficiency photovoltaics. *Nature Mater* **11**, 174–177 (2012).

33. Akhil, S. *et al.* Review on perovskite silicon tandem solar cells: Status and prospects 2T, 3T and 4T for real world conditions. *Materials & Design* **211**, 110138 (2021).

34. Smith, M. B. & Michl, J. Singlet Fission. *Chem. Rev.* **110**, 6891–6936 (2010).

35. Einzinger, M. *et al.* Sensitization of silicon by singlet exciton fission in tetracene. *Nature* **571**, 90–94 (2019).

36. Lee, J. *et al.* Singlet Exciton Fission Photovoltaics. *Acc. Chem. Res.* **46**, 1300–1311 (2013).

37. Tayebjee, M. J. Y., Gray-Weale, A. A. & Schmidt, T. W. Thermodynamic Limit of Exciton Fission Solar Cell Efficiency. *J. Phys. Chem. Lett.* **3**, 2749–2754 (2012).

38. Daiber, B., van den Hoven, K., Futscher, M. H. & Ehrler, B. Realistic Efficiency Limits for Singlet-Fission Silicon Solar Cells. *ACS Energy Lett.* **6**, 2800–2808 (2021).

39. Søndergaard, R., Hösel, M., Angmo, D., Larsen-Olsen, T. T. & Krebs, F. C. Roll-to-roll fabrication of polymer solar cells. *Materials Today* **15**, 36–49 (2012).

40. Kwon, J. H., Yoo, S., Lampande, R. & Kim, S. Vacuum Deposition. in *Handbook of Organic Light-Emitting Diodes* (eds. Adachi, C., Hattori, R., Kaji, H. & Tsujimura, T.) 1–23 (Springer Japan, Tokyo, 2019). doi:10.1007/978-4-431-55761-6_12-2.

41. Futscher, M. H., Rao, A. & Ehrler, B. The Potential of Singlet Fission Photon Multipliers as an Alternative to Silicon-Based Tandem Solar Cells. *ACS Energy Lett.* **3**, 2587–2592 (2018).

42. Jiang, Y. *et al.* Singlet fission and tandem solar cells reduce thermal degradation and enhance lifespan. *Progress in Photovoltaics: Research and Applications* **29**, 899–906 (2021).

43. Congreve, D. N. *et al.* External Quantum Efficiency Above 100% in a Singlet-Exciton-Fission–Based Organic Photovoltaic Cell. *Science* **340**, 334–337 (2013).

44. Hayashi, T., Castner, T. G. & Boyd, R. W. Quenching of molecular fluorescence near the surface of a semiconductor. *Chemical Physics Letters* **94**, 461–466 (1983).

45. Piland, G. B. *et al.* Dynamics of molecular excitons near a semiconductor surface studied by fluorescence quenching of polycrystalline tetracene on silicon. *Chemical Physics Letters* **601**, 33–38 (2014).

46. MacQueen, R. W. *et al.* Crystalline silicon solar cells with tetracene interlayers: the path to silicon-singlet fission heterojunction devices. *Mater. Horiz.* **5**, 1065–1075 (2018).

47. Daiber, B. *et al.* Change in Tetracene Polymorphism Facilitates Triplet Transfer in Singlet Fission-Sensitized Silicon Solar Cells. *J. Phys. Chem. Lett.* 8703–8709 (2020) doi:10.1021/acs.jpclett.0c02163.

48. Zou, S.-J. *et al.* Recent advances in organic light-emitting diodes: toward smart lighting and displays. *Mater. Chem. Front.* **4**, 788–820 (2020).

49. Hong, G. *et al.* A Brief History of OLEDs—Emitter Development and Industry Milestones. *Advanced Materials* **33**, 2005630 (2021).

50. Huang, Y., Hsiang, E.-L., Deng, M.-Y. & Wu, S.-T. Mini-LED, Micro-LED and OLED displays: present status and future perspectives. *Light Sci Appl* **9**, 105 (2020).

51. Kaur, N., Singh, M., Pathak, D., Wagner, T. & Nunzi, J. M. Organic materials for photovoltaic applications: Review and mechanism. *Synthetic Metals* **190**, 20–26 (2014).

52. Zhang, G. *et al.* Renewed Prospects for Organic Photovoltaics. *Chem. Rev.* **122**, 14180–14274 (2022).

53. Solak, E. K. & Irmak, E. Advances in organic photovoltaic cells: a comprehensive review of materials, technologies, and performance. *RSC Adv.* **13**, 12244–12269 (2023).

54. Liu, K., Ouyang, B., Guo, X., Guo, Y. & Liu, Y. Advances in flexible organic field-effect transistors and their applications for flexible electronics. *npj Flex Electron* **6**, 1–19 (2022).

55. Yuvaraja, S. *et al.* Organic field-effect transistor-based flexible sensors. *Chem. Soc. Rev.* **49**, 3423–3460 (2020).

56. Anna Köhler & Heinz Bässler. Electronic Processes in Organic Semiconductors | Wiley Online Books. https://onlinelibrary.wiley.com/doi/book/10.1002/9783527685172.

57. Strong, S. E. & Eaves, J. D. Tetracene Aggregation on Polar and Nonpolar Surfaces: Implications for Singlet Fission. *J. Phys. Chem. Lett.* **6**, 1209–1215 (2015).

58. Pope, M. & Swenberg, C. E. Semiconductors, Organic—Electronic Properties. in *Encyclopedia of Applied Physics* (John Wiley & Sons, Ltd, 2003). doi:10.1002/3527600434.eap423.

59. Loebbert, G. Phthalocyanine Compounds. in *Kirk-Othmer Encyclopedia of Chemical Technology* (John Wiley & Sons, Ltd, 2000). doi:10.1002/0471238961.1608200812150502.a01.

60. Alvertis, A. M. Organic Semiconductors and Their Properties. in *On Exciton–Vibration and Exciton–Photon Interactions in Organic Semiconductors* (ed. Alvertis, A. M.) 7–23 (Springer International Publishing, Cham, 2021). doi:10.1007/978-3-030-85454-6_2.

61. Köhler, A., Wilson, J. s. & Friend, R. h. Fluorescence and Phosphorescence in Organic Materials. *Advanced Materials* **14**, 701–707 (2002).

62. Felix. Chemical Quantum Images: HOMO-LUMO gaps and excitation energies. *Chemical Quantum Images* https://chemical-quantum-images.blogspot.com/2013/06/why-is-homo-lumo-gap-not-good-guess-of.html (2013).

63. Frenkel, J. On the Transformation of light into Heat in Solids. I. *Phys. Rev.* **37**, 17–44 (1931).

64. Wannier, G. H. The Structure of Electronic Excitation Levels in Insulating Crystals. *Phys. Rev.* **52**, 191–197 (1937).

65. Ginsberg, N. S. & Tisdale, W. A. Spatially Resolved Exciton and Charge Transport in Emerging Semiconductors. *Annual Review of Physical Chemistry* **71**, 1–30 (2020).

66. Pope, M., Geacintov, N. E., Saperstein, D. & Vogel, F. Calculation of the diffusion length, diffusion coefficient and lifetime of triplet excitons in crystalline tetracene. *Journal of Luminescence* **1–2**, 224–230 (1970).

67. Akselrod, G. M. *et al.* Visualization of exciton transport in ordered and disordered molecular solids. *Nat Commun* **5**, 3646 (2014).

68. Wu, T. C. *et al.* Singlet fission efficiency in tetracene-based organic solar cells. *Appl. Phys. Lett.* **104**, 193901 (2014).

69. Förster, T. Ein Beitrag zur Theorie der Photosynthese. *Zeitschrift für Naturforschung B* **2**, 174–182 (1947).

70. Förster, Th. Zwischenmolekulare Energiewanderung und Fluoreszenz. *Annalen der Physik* **437**, 55–75 (1948).

71. Cleave, V., Yahioglu, G., Barny, P. L., Friend, R. H. & Tessler, N. Harvesting Singlet and Triplet Energy in Polymer LEDs. *Advanced Materials* **11**, 285–288 (1999).

72. Kawamura, Y., Brooks, J., Brown, J. J., Sasabe, H. & Adachi, C. Intermolecular Interaction and a Concentration-Quenching Mechanism of Phosphorescent Ir(III) Complexes in a Solid Film. *Phys. Rev. Lett.* **96**, 017404 (2006).

73. Dexter, D. L. A Theory of Sensitized Luminescence in Solids. *J. Chem. Phys.* **21**, 836–850 (1953).

74. Singh, S., Jones, W. J., Siebrand, W., Stoicheff, B. P. & Schneider, W. G. Laser Generation of Excitons and Fluorescence in Anthracene Crystals. *The Journal of Chemical Physics* **42**, 330–342 (1965).

75. Chan, W.-L., Ligges, M. & Zhu, X.-Y. The energy barrier in singlet fission can be overcome through coherent coupling and entropic gain. *Nature Chem* **4**, 840–845 (2012).

76. Dong, S., Ong, A. & Chi, C. Photochemistry of various acene based molecules. *Journal of Photochemistry and Photobiology C: Photochemistry Reviews* **38**, 27–46 (2019).

77. Foote, C. S. Photosensitized oxygenations and the role of singlet oxygen. *Acc. Chem. Res.* **1**, 104–110 (1968).

78. Murawski, C., Leo, K. & Gather, M. C. Efficiency Roll-Off in Organic Light-Emitting Diodes. *Advanced Materials* **25**, 6801–6827 (2013).

79. Thompson, N. J. *et al.* Nanostructured Singlet Fission Photovoltaics Subject to Triplet-Charge Annihilation. *Advanced Materials* **26**, 1366–1371 (2014).

80. Johnson, R. C., Merrifield, R. E., Avakian, P. & Flippen, R. B. Effects of Magnetic Fields on the Mutual Annihilation of Triplet Excitons in Molecular Crystals. *Phys. Rev. Lett.* **19**, 285–287 (1967).

81. Johnson, R. C. & Merrifield, R. E. Effects of Magnetic Fields on the Mutual Annihilation of Triplet Excitons in Anthracene Crystals. *Phys. Rev. B* **1**, 896–902 (1970).

82. Merrifield, R. E. Magnetic effects on triplet exciton interactions. *Pure and Applied Chemistry* **27**, 481–498 (1971).

83. Piland, G. B., Burdett, J. J., Dillon, R. J. & Bardeen, C. J. Singlet Fission: From Coherences to Kinetics. *J. Phys. Chem. Lett.* **5**, 2312–2319 (2014).

84. Merrifield, R. E., Avakian, P. & Groff, R. P. Fission of singlet excitons into pairs of triplet excitons in tetracene crystals. *Chemical Physics Letters* **3**, 155–157 (1969).

85. Ern, V. & Merrifield, R. E. Magnetic Field Effect on Triplet Exciton Quenching in Organic Crystals. *Phys. Rev. Lett.* **21**, 609–611 (1968).

86. Martin Pope & Charles E. Swenberg. *Electronic Processes in Organic Crystals and Polymers*.

87. Saha, M. N. & Fowler, A. On a physical theory of stellar spectra. *Proceedings of the Royal Society of London. Series A, Containing Papers of a Mathematical and Physical Character* **99**, 135–153 (1997).

88. Green, M. A. & Keevers, M. J. Optical properties of intrinsic silicon at 300 K. *Progress in Photovoltaics: Research and Applications* **3**, 189–192 (1995).

89. Goetzberger, A., Knobloch, J. & Voß, B. The Physics of Solar Cells. in *Crystalline Silicon Solar Cells* 67–86 (John Wiley & Sons, Ltd, 2014). doi:10.1002/9781119033769.ch5.

90. Augusto, A., Herasimenka, S. Y., King, R. R., Bowden, S. G. & Honsberg, C. Analysis of the recombination mechanisms of a silicon solar cell with low bandgap-voltage offset. *Journal of Applied Physics* **121**, 205704 (2017).

91. Rein, S. *Lifetime Spectroscopy: A Method of Defect Characterization in Silicon for Photovoltaic Applications*. vol. 85 (Springer, Berlin, Heidelberg, 2005).

92. Goetzberger, A., Knobloch, J. & Voß, B. The Principles of Photovoltaics. in *Crystalline Silicon Solar Cells* 9–48 (John Wiley & Sons, Ltd, 2014). doi:10.1002/9781119033769.ch3.

93. Shockley, W. & Read, W. T. Statistics of the Recombinations of Holes and Electrons. *Phys. Rev.* **87**, 835–842 (1952).

94. Hall, R. N. Electron-Hole Recombination in Germanium. *Phys. Rev.* **87**, 387–387 (1952).

95. Hoex, B. *et al.* Excellent passivation of highly doped p-type Si surfaces by the negative-charge-dielectric Al2O3. *Applied Physics Letters* **91**, 112107 (2007).

96. Benick, J. *et al.* High efficiency n-type Si solar cells on Al2O3-passivated boron emitters. *Applied Physics Letters* **92**, 253504 (2008).

97. Schmidt, J. *et al.* Advances in the Surface Passivation of Silicon Solar Cells. *Energy Procedia* **15**, 30–39 (2012).

98. Glunz, S. W. & Feldmann, F. SiO2 surface passivation layers – a key technology for silicon solar cells. *Solar Energy Materials and Solar Cells* **185**, 260–269 (2018).

99. Allardice, J. R. *et al.* Engineering Molecular Ligand Shells on Quantum Dots for Quantitative Harvesting of Triplet Excitons Generated by Singlet Fission. *J. Am. Chem. Soc.* **141**, 12907–12915 (2019).

100. Perkinson, C. F. *et al.* Discovery of blue singlet exciton fission molecules via a high-throughput virtual screening and experimental approach. *The Journal of Chemical Physics* **151**, 121102 (2019).

101. Wang, X., Tian, X., Chen, X., Ren, L. & Geng, C. A review of end-of-life crystalline silicon solar photovoltaic panel recycling technology. *Solar Energy Materials and Solar Cells* **248**, 111976 (2022).

102. Jørgensen, M., Norrman, K. & Krebs, F. C. Stability/degradation of polymer solar cells. *Solar Energy Materials and Solar Cells* **92**, 686–714 (2008).

103. Ehrler, B. *et al.* In situ measurement of exciton energy in hybrid singlet-fission solar cells. *Nat Commun* **3**, 1019 (2012).

104. Ehrler, B., Musselman, K. P., Böhm, M. L., Friend, R. H. & Greenham, N. C. Hybrid pentacene/a-silicon solar cells utilizing multiple carrier generation via singlet exciton fission. *Applied Physics Letters* **101**, 153507 (2012).

105. Reddy, A. R. & Bendikov, M. Diels–Alder reaction of acenes with singlet and triplet oxygen – theoretical study of two-state reactivity. *Chem. Commun.* 1179–1181 (2006) doi:10.1039/B513597D.

106. Zade, S. S. *et al.* Products and Mechanism of Acene Dimerization. A Computational Study. *J. Am. Chem. Soc.* **133**, 10803–10816 (2011).

107. Nagao, Y. Synthesis and properties of perylene pigments. *Progress in Organic Coatings* **31**, 43–49 (1997).

108. Zhang, F. *et al.* Self-assembly, optical and electrical properties of perylene diimide dyes bearing unsymmetrical substituents at bay position. *Sci Rep* **8**, 8208 (2018).

109. Fukuzumi, S. *et al.* Control of Photoinduced Electron Transfer in Zinc Phthalocyanine−Perylenediimide Dyad and Triad by the Magnesium Ion. *J. Phys. Chem. A* **112**, 10744–10752 (2008).

110. Eaton, S. W. *et al.* Singlet Exciton Fission in Polycrystalline Thin Films of a Slip-Stacked Perylenediimide. *J. Am. Chem. Soc.* **135**, 14701–14712 (2013).

111. Masoomi-Godarzi, S. *et al.* Competitive Triplet Formation and Recombination in Crystalline Films of Perylenediimide Derivatives: Implications for Singlet Fission. *J. Phys. Chem. C* **124**, 11574–11585 (2020).

112. Gao, C. *et al.* Efficient Singlet Fission in Perylenediimide Derivative Nanocrystals. *J. Phys. Chem. C* **126**, 18767–18777 (2022).

113. Korovina, N. V., Pompetti, N. F. & Johnson, J. C. Lessons from intramolecular singlet fission with covalently bound chromophores. *The Journal of Chemical Physics* **152**, 040904 (2020).

114. Casillas, R. *et al.* Molecular insights and concepts to engineer singlet fission energy conversion devices. *Energy Environ. Sci.* **13**, 2741–2804 (2020).

115. Pazos-Outón, L. M. *et al.* A Silicon–Singlet Fission Tandem Solar Cell Exceeding 100% External Quantum Efficiency with High Spectral Stability. *ACS Energy Lett.* **2**, 476–480 (2017).

116. Thompson, N. J. *et al.* Energy harvesting of non-emissive triplet excitons in tetracene by emissive PbS nanocrystals. *Nature Mater* **13**, 1039–1043 (2014).

117. Tabachnyk, M. *et al.* Resonant energy transfer of triplet excitons from pentacene to PbSe nanocrystals. *Nature Mater* **13**, 1033–1038 (2014).

118. Davis, N. J. L. K. *et al.* Singlet Fission and Triplet Transfer to PbS Quantum Dots in TIPS-Tetracene Carboxylic Acid Ligands. *J. Phys. Chem. Lett.* **9**, 1454–1460 (2018).

119. Huang, T. *et al.* Bidirectional triplet exciton transfer between silicon nanocrystals and perylene. *Chem. Sci.* **12**, 6737–6746 (2021).

120. Niederhausen, J. *et al.* Energy-Level Alignment Tuning at Tetracene/c-Si Interfaces. *J. Phys. Chem. C* **124**, 27867–27881 (2020).

121. Köhler, A. & Bässler, H. What controls triplet exciton transfer in organic semiconductors? *J. Mater. Chem.* **21**, 4003–4011 (2011).

122. Piland, G. B. & Bardeen, C. J. How Morphology Affects Singlet Fission in Crystalline Tetracene. *J. Phys. Chem. Lett.* **6**, 1841–1846 (2015).

123. Arias, D. H., Ryerson, J. L., Cook, J. D., Damrauer, N. H. & Johnson, J. C. Polymorphism influences singlet fission rates in tetracene thin films. *Chem. Sci.* **7**, 1185–1191 (2016).

124. Li, X. & Tang, M. L. Triplet transport in thin films: fundamentals and applications. *Chem. Commun.* **53**, 4429–4440 (2017).

125. Daiber, B. *et al.* A method to detect triplet exciton transfer from singlet fission materials into silicon solar cells: Comparing different surface treatments. *J. Chem. Phys.* **152**, 114201 (2020).

126. van den Boom, A. F. J., Ferro, S., Gelvez-Rueda, M., Zuilhof, H. & Ehrler, B. Toward Improving Triplet Energy Transfer from Tetracene to Silicon Using a Covalently Bound Tetracene Seed Layer. *J. Phys. Chem. Lett.* **14**, 4454–4461 (2023).

127. Burdett, J. J., Piland, G. B. & Bardeen, C. J. Magnetic field effects and the role of spin states in singlet fission. *Chemical Physics Letters* **585**, 1–10 (2013).

128. Burdett, J. J. & Bardeen, C. J. The Dynamics of Singlet Fission in Crystalline Tetracene and Covalent Analogs. *Acc. Chem. Res.* **46**, 1312–1320 (2013).

129. Wilson, M. W. B. *et al.* Temperature-Independent Singlet Exciton Fission in Tetracene. *J. Am. Chem. Soc.* **135**, 16680–16688 (2013).

130. Kunzmann, A. *et al.* Singlet Fission for Photovoltaics with 130 % Injection Efficiency. *Angewandte Chemie International Edition* **57**, 10742–10747 (2018).

131. Krenz, M., Gerstmann, U. & Schmidt, W. G. Defect-Assisted Exciton Transfer across the Tetracene-Si(111):H Interface. *Phys. Rev. Lett.* **132**, 076201 (2024).

132. Klymenko, M. V., Tan, L. Z., Russo, Salvy. P. & Cole, J. H. Excitons and Singlet Fission at the Crystalline Tetracene–Silicon Interface. *Chem. Mater.* **36**, 2346–2354 (2024).

133. Um, H.-D. *et al.* Progress in silicon microwire solar cells. *J. Mater. Chem. A* **8**, 5395–5420 (2020).

134. Inomata, Y., Fukui, K. & Shirasawa, K. Surface texturing of large area multicrystalline silicon solar cells using reactive ion etching method. *Solar Energy Materials and Solar Cells* **48**, 237–242 (1997).

135. Kim, M. S., Lee, J. H. & Kwak, M. K. Review: Surface Texturing Methods for Solar Cell Efficiency Enhancement. *Int. J. Precis. Eng. Manuf.* **21**, 1389–1398 (2020).

136. Gavartin, J. L., Shluger, A. L., Foster, A. S. & Bersuker, G. I. The role of nitrogen-related defects in high-k dielectric oxides: Density-functional studies. *Journal of Applied Physics* **97**, 053704 (2005).

137. Giebink, N. C., Wiederrecht, G. P., Wasielewski, M. R. & Forrest, S. R. Ideal diode equation for organic heterojunctions. I. Derivation and application. *Phys. Rev. B* **82**, 155305 (2010).

138. Renshaw, C. K. & Forrest, S. R. Excited state and charge dynamics of hybrid organic/inorganic heterojunctions. I. Theory. *Phys. Rev. B* **90**, 045302 (2014).

139. Lin, F., Hoex, B., Koh, Y. H., Lin, J. J. & Aberle, A. G. Low-temperature Surface Passivation of Moderately Doped Crystalline Silicon by Atomic-layer-deposited Hafnium Oxide Films. *Energy Procedia* **15**, 84–90 (2012).

140. Wratten, A. *et al.* Exploring hafnium oxide's potential for passivating contacts for silicon solar cells. *Solar Energy Materials and Solar Cells* **259**, 112457 (2023).

141. Lei, M., Yum, J. H., Banerjee, S. K., Bersuker, G. & Downer, M. C. Band offsets of atomic layer deposited Al2O3 and HfO2 on Si measured by linear and nonlinear internal photoemission. *physica status solidi (b)* **249**, 1160–1165 (2012).

142. Tan, T. *et al.* Band structure and valence-band offset of HfO2 thin film on Si substrate from photoemission spectroscopy. *Appl. Phys. A* **97**, 475–479 (2009).

143. Bersch, E., Rangan, S., Bartynski, R. A., Garfunkel, E. & Vescovo, E. Band offsets of ultrathin high-$\ensuremath{\kappa}$ oxide films with Si. *Phys. Rev. B* **78**, 085114 (2008).

144. Chikata, Y., Kita, K., Nishimura, T., Nagashio, K. & Toriumi, A. Quantitative Characterization of Band-Edge Energy Positions in High-k Dielectrics by X-ray Photoelectron Spectroscopy. *Jpn. J. Appl. Phys.* **52**, 021101 (2013).

145. Bersch, E. *et al.* Complete band offset characterization of the HfO2/SiO2/Si stack using charge corrected x-ray photoelectron spectroscopy. *Journal of Applied Physics* **107**, 043702 (2010).

146. Staišiūnas, L. *et al.* Silicon Passivation by Ultrathin Hafnium Oxide Layer for Photoelectrochemical Applications. *Front. Chem.* **10**, (2022).

147. Hausmann, D. M. & Gordon, R. G. Surface morphology and crystallinity control in the atomic layer deposition (ALD) of hafnium and zirconium oxide thin films. *Journal of Crystal Growth* **249**, 251–261 (2003).

148. Zheng, J. X., Ceder, G., Maxisch, T., Chim, W. K. & Choi, W. K. First-principles study of native point defects in hafnia and zirconia. *Phys. Rev. B* **75**, 104112 (2007).

149. Takeuchi, H., Ha, D. & King, T.-J. Observation of bulk HfO2 defects by spectroscopic ellipsometry. *Journal of Vacuum Science & Technology A* **22**, 1337–1341 (2004).

150. Adamo, C. & Barone, V. Toward reliable density functional methods without adjustable parameters: The PBE0 model. *The Journal of Chemical Physics* **110**, 6158–6170 (1999).

151. Perdew, J. P., Ernzerhof, M. & Burke, K. Rationale for mixing exact exchange with density functional approximations. *The Journal of Chemical Physics* **105**, 9982–9985 (1996).

152. Choi, J., Puthenkovilakam, R. & Chang, J. P. Effect of nitrogen on the electronic properties of hafnium oxynitrides. *Journal of Applied Physics* **99**, 053705 (2006).

153. Kim, S. K., Kim, Y.-S., Jeon, Y.-A., Choi, J. & No, K.-S. The electronic structures for the optical absorption of Hf-O-N thin films. *J Electroceram* **17**, 197–203 (2006).

154. Yuan, L. *et al.* Suppression of near-edge optical absorption band in sputter deposited hafnium oxynitride via nitrogen incorporation and annealing. *J. Phys. D: Appl. Phys.* **42**, 145302 (2009).

155. Zafar, S., Jagannathan, H., Edge, L. F. & Gupta, D. Measurement of oxygen diffusion in nanometer scale HfO2 gate dielectric films. *Applied Physics Letters* **98**, 152903 (2011).

156. Martínez-Puente, M. A. *et al.* ALD and PEALD deposition of HfO2 and its effects on the nature of oxygen vacancies. *Materials Science and Engineering: B* **285**, 115964 (2022).

157. Wei, J., Jiang, L., Huang, M., Wu, Y. & Chen, S. Intrinsic Defect Limit to the Growth of Orthorhombic HfO2 and (Hf,Zr)O2 with Strong Ferroelectricity: First-Principles Insights. *Advanced Functional Materials* **31**, 2104913 (2021).

158. Islamov, D. R. *et al.* The Evolution of the Conductivity and Cathodoluminescence of the Films of Hafnium Oxide in the Case of a Change in the Concentration of Oxygen Vacancies. *Phys. Solid State* **60**, 2050–2057 (2018).

159. Becker, J. S., Kim, E. & Gordon, R. G. Atomic Layer Deposition of Insulating Hafnium and Zirconium Nitrides. *Chem. Mater.* **16**, 3497–3501 (2004).

160. Bonilla, R. S., Hoex, B., Hamer, P. & Wilshaw, P. R. Dielectric surface passivation for silicon solar cells: A review. *physica status solidi (a)* **214**, 1700293 (2017).

161. Merrifield, R. E., Avakian, P. & Groff, R. P. Fission of singlet excitons into pairs of triplet excitons in tetracene crystals. *Chemical Physics Letters* **3**, 386–388 (1969).

162. Muduli, S. P. & Kale, P. State-of-the-art passivation strategies of c-Si for photovoltaic applications: A review. *Materials Science in Semiconductor Processing* **154**, 107202 (2023).

163. Feldmann, F., Bivour, M., Reichel, C., Hermle, M. & Glunz, S. W. Passivated rear contacts for high-efficiency n-type Si solar cells providing high interface passivation quality and excellent transport characteristics. *Solar Energy Materials and Solar Cells* **120**, 270–274 (2014).

164. Moldovan, A. *et al.* Tunnel oxide passivated carrier-selective contacts based on ultra-thin SiO2 layers. *Solar Energy Materials and Solar Cells* **142**, 123–127 (2015).

165. Heng, J. B. *et al.* >23% High-Efficiency Tunnel Oxide Junction Bifacial Solar Cell With Electroplated Cu Gridlines. *IEEE Journal of Photovoltaics* **5**, 82–86 (2015).

166. McCartin, P. J. Electron-Donor Properties of Zinc Phthalocyanine. *J. Am. Chem. Soc.* **85**, 2021–2022 (1963).

167. Gao, W. & Kahn, A. Electronic structure and current injection in zinc phthalocyanine doped with tetrafluorotetracyanoquinodimethane: Interface versus bulk effects. *Organic Electronics* **3**, 53–63 (2002).

168. C. E. Swenberg, N. E. Geacintov, J. B. Birks. *Organic Molecular Photophysics*. vol. 18 (J. Wiley., 1973).

169. Frackowiak, D. *et al.* Yield of intersystem (singlet–triplet) crossing in phthalocyanines evaluated on the basis of a time in resolved photothermal method. *Journal of Photochemistry and Photobiology A: Chemistry* **141**, 101–108 (2001).

170. Ha, D.-G. *et al.* Exchange controlled triplet fusion in metal–organic frameworks. *Nat. Mater.* **21**, 1275–1281 (2022).

171. Aberle, A. G. Overview on SiN surface passivation of crystalline silicon solar cells. *Solar Energy Materials and Solar Cells* **65**, 239–248 (2001).

172. Lee, S. H., Bhopal, M. F., Lee, D. W. & Lee, S. H. Review of advanced hydrogen passivation for high efficient crystalline silicon solar cells. *Materials Science in Semiconductor Processing* **79**, 66–73 (2018).

173. Burkhard, G. F., Hoke, E. T. & McGehee, M. D. Accounting for Interference, Scattering, and Electrode Absorption to Make Accurate Internal Quantum Efficiency Measurements in Organic and Other Thin Solar Cells. *Advanced Materials* **22**, 3293–3297 (2010).

174. Siegmund, B. *et al.* Exciton Diffusion Length and Charge Extraction Yield in Organic Bilayer Solar Cells. *Advanced Materials* **29**, 1604424 (2017).

175. Schinke, C. *et al.* Uncertainty analysis for the coefficient of band-to-band absorption of crystalline silicon. *AIP Advances* **5**, 067168 (2015).

176. Prashanthan, K. *et al.* Internal electric fields control triplet formation in halide perovskite-sensitized photon upconverters. *iScience* **26**, 106365 (2023).

177. Sinkkonen, J., Novikov, S. & Varpula, A. Characterization of surface states by SPV-transient. *Applied Surface Science* **255**, 662–664 (2008).

178. Verlinden, P. J., Swanson, R. M. & Crane, R. A. 7000 high-eficiency cells for a dream. *Progress in Photovoltaics: Research and Applications* **2**, 143–152 (1994).

179. Smith, D. D. *et al.* Silicon solar cells with total area efficiency above 25 %. in *2016 IEEE 43rd Photovoltaic Specialists Conference (PVSC)* 3351–3355 (2016). doi:10.1109/PVSC.2016.7750287.

180. Prabu, R. T. *et al.* CsPbI3 perovskite solar cell and decoding its skink feature in J-V curve. *Materials Science in Semiconductor Processing* **162**, 107539 (2023).

181. Li, D.-B. *et al.* Eliminating S-Kink To Maximize the Performance of MgZnO/CdTe Solar Cells. *ACS Appl. Energy Mater.* **2**, 2896–2903 (2019).

182. Niederhausen, J. *et al.* Tetracene Ultrathin Film Growth on Hydrogen-Passivated Silicon. *Langmuir* **36**, 9099–9113 (2020).

183. Fujii, T., Takahashi, Y. & Uchida, H. Deposition of tetracene thin films on SiO2/Si substrates by rapid expansion of supercritical solutions using carbon dioxide. *Appl. Phys. Express* **8**, 035504 (2015).

184. Jäckle, S. *et al.* Potential of PEDOT:PSS as a hole selective front contact for silicon heterojunction solar cells. *Sci Rep* **7**, 2170 (2017).

185. Srivastava, A., Sharma, D., Kumari, P., Dutta, M. & Srivastava, S. K. Highly Efficient PEDOT:PSS/Silicon Hybrid Solar Cells via Effective Surface Microengineering of Low-Cost Solar-Grade Silicon Wafers. *ACS Appl. Energy Mater.* **4**, 4181–4198 (2021).

186. Kraut, E. A., Grant, R. W., Waldrop, J. R. & Kowalczyk, S. P. Precise Determination of the Valence-Band Edge in X-Ray Photoemission Spectra: Application to Measurement of Semiconductor Interface Potentials. *Phys. Rev. Lett.* **44**, 1620–1623 (1980).

187. Banerjee, S. & Das, M. K. A review of Al2O3 as surface passivation material with relevant process technologies on c-Si solar cell. *Opt Quant Electron* **53**, 60 (2021).

188. Vincett, P. S., Voigt, E. M. & Rieckhoff, K. E. Phosphorescence and Fluorescence of Phthalocyanines. *The Journal of Chemical Physics* **55**, 4131–4140 (1971).

189. Lee, K. *et al.* 17.6%-Efficient radial junction solar cells using silicon nano/micro hybrid structures. *Nanoscale* **8**, 14473–14479 (2016).

190. Hwang, I., Um, H.-D., Kim, B.-S., Wober, M. & Seo, K. Flexible crystalline silicon radial junction photovoltaics with vertically aligned tapered microwires. *Energy Environ. Sci.* **11**, 641–647 (2018).

191. Lee, K. *et al.* Sunlight-Activatable ROS Generator for Cell Death Using TiO2/c-Si Microwires. *Nano Lett.* **21**, 6998–7004 (2021).

192. Um, H.-D. *et al.* Microgrid Electrode for Si Microwire Solar Cells with a Fill Factor of Over 80%. *Advanced Materials Interfaces* **2**, 1500347 (2015).

193. Adeyeye, A. O. & Shimon, G. Chapter 1 - Growth and Characterization of Magnetic Thin Film and Nanostructures. in *Handbook of Surface Science* (eds. Camley, R. E., Celinski, Z. & Stamps, R. L.) vol. 5 1–41 (North-Holland, 2015).

194. Michael Wal. Time-Correlated Single Photon Counting. (2014).

195. Akselrod, G. M. *et al.* Subdiffusive Exciton Transport in Quantum Dot Solids. *Nano Lett.* **14**, 3556–3562 (2014).

196. Akselrod, G. M. *et al.* Visualization of exciton transport in ordered and disordered molecular solids. *Nat Commun* **5**, 3646 (2014).

197. Wan, Y. *et al.* Cooperative singlet and triplet exciton transport in tetracene crystals visualized by ultrafast microscopy. *Nature Chemistry* **7**, 785–792 (2015).

198. Tisdale, W. A. *et al.* Hot-Electron Transfer from Semiconductor Nanocrystals. *Science* **328**, 1543–1547 (2010).

199. Goodman, A. J., Dahod, N. S. & Tisdale, W. A. Ultrafast Charge Transfer at a Quantum Dot/2D Materials Interface Probed by Second Harmonic Generation. *J. Phys. Chem. Lett.* **9**, 4227–4232 (2018).

200. Ferenc Krausz. From femtochemistry to attophysics. *Physics World* https://physicsworld.com/a/from-femtochemistry-to-attophysics/ (2001).

201. Boyd, R. W. *Nonlinear Optics - 3rd Edition*.

202. Bloembergen, N. & Lee, C. H. Total Reflection in Second-Harmonic Generation. *Phys. Rev. Lett.* **19**, 835–837 (1967).

203. mp-149: Si (Cubic, Fd-3m, 227). *Materials Project* https://next-gen.materialsproject.org/materials/mp-149/#crystal_structure.

204. Holmes, D., Kumaraswamy, S., Matzger, A. J. & Vollhardt, K. P. C. On the Nature of Nonplanarity in the [N]Phenylenes. *Chemistry – A European Journal* **5**, 3399–3412 (1999).

205. Robertson, J. M., Sinclair, V. C. & Trotter, J. The crystal and molecular structure of tetracene. *Acta Cryst* **14**, 697–704 (1961).

206. McGilp, J. F. Optical Second-Harmonic Generation as a Semiconductor Surface and Interface Probe. *physica status solidi (a)* **175**, 153–167 (1999).

207. Tisdale, W. A. *et al.* Hot-Electron Transfer from Semiconductor Nanocrystals. *Science* **328**, 1543–1547 (2010).

208. Radu, I. E. Ultrafast Electron, Lattice and Spin Dynamics on Rare-Earth Metal Surfaces: investigated with linear and nonlinear optical techniques. (2006) doi:10.17169/refubium-12601.

209. Tisdale, W. A. Hot electron dynamics at semiconductor surfaces: implications for quantum dot photovoltaics. (2010).

210. Bloembergen, N. & Pershan, P. S. Light Waves at the Boundary of Nonlinear Media. 17.

211. Shen, Y. R. Surface Second Harmonic Generation: A New Technique for Surface Studies. *Annual Review of Materials Research* **16**, 69–86 (1986).

212. Shen, Y. R. Optical Second Harmonic Generation at Interfaces. *Annual Review of Physical Chemistry* **40**, 327–350 (1989).

213. Heinz, T. F. Chapter 5 - Second-Order Nonlinear Optical Effects at Surfaces and Interfaces. in *Modern Problems in Condensed Matter Sciences* (eds. Ponath, H.-E. & Stegeman, G. I.) vol. 29 353–416 (Elsevier, 1991).

214. Lee, C. H., Chang, R. K. & Bloembergen, N. Nonlinear Electroreflectance in Silicon and Silver. *Phys. Rev. Lett.* **18**, 167–170 (1967).

215. Daum, W., Krause, H.-J., Reichel, U. & Ibach, H. Identification of strained silicon layers at Si-${\mathrm{SiO}}_{2}$ interfaces and clean Si surfaces by nonlinear optical spectroscopy. *Phys. Rev. Lett.* **71**, 1234–1237 (1993).

216. Bloch, J., Mihaychuk, J. G. & van Driel, H. M. Electron Photoinjection from Silicon to Ultrathin Si O 2 Films via Ambient Oxygen. *Phys. Rev. Lett.* **77**, 920–923 (1996).

217. Robertson, J. Band offsets of wide-band-gap oxides and implications for future electronic devices. *J. Vac. Sci. Technol. B* **18**, 1785 (2000).

218. Fomenko, V., Gusev, E. P. & Borguet, E. Optical second harmonic generation studies of ultrathin high-k dielectric stacks. *Journal of Applied Physics* **97**, 083711 (2005).

219. Daum, W. Optical studies of Si/SiO2interfaces by second-harmonic generation spectroscopy of silicon interband transitions. *Appl. Phys. A* **87**, 451–460 (2007).

220. Berera, R., van Grondelle, R. & Kennis, J. T. M. Ultrafast transient absorption spectroscopy: principles and application to photosynthetic systems. *Photosynth Res* **101**, 105–118 (2009).

221. Aspnes, D. E. & Studna, A. A. Dielectric functions and optical parameters of Si, Ge, GaP, GaAs, GaSb, InP, InAs, and InSb from 1.5 to 6.0 eV. *Phys. Rev. B* **27**, 985–1009 (1983).

222. Sabbah, A. J. & Riffe, D. M. Femtosecond pump-probe reflectivity study of silicon carrier dynamics. *Phys. Rev. B* **66**, 165217 (2002).

223. Downer, M. C. & Shank, C. V. Ultrafast heating of silicon on sapphire by femtosecond optical pulses. *Phys. Rev. Lett.* **56**, 761–764 (1986).

224. Menke, S. M., Luhman, W. A. & Holmes, R. J. Tailored exciton diffusion in organic photovoltaic cells for enhanced power conversion efficiency. *Nat Mater* **12**, 152–157 (2013).

225. Kim, I., Kivisaari, P., Oksanen, J. & Suihkonen, S. Diffusion-Driven Charge Transport in Light Emitting Devices. *Materials (Basel)* **10**, 1421 (2017).

226. LaMarr, B. J. *et al.* Measurement and simulation of charge diffusion in a small-pixel charge-coupled device. *JATIS* **8**, 016004 (2022).

227. Stoumpos, C. C., Malliakas, C. D. & Kanatzidis, M. G. Semiconducting Tin and Lead Iodide Perovskites with Organic Cations: Phase Transitions, High Mobilities, and Near-Infrared Photoluminescent Properties. *Inorg. Chem.* **52**, 9019–9038 (2013).

228. Chen, Y. *et al.* Extended carrier lifetimes and diffusion in hybrid perovskites revealed by Hall effect and photoconductivity measurements. *Nat Commun* **7**, 12253 (2016).

229. Greenham, N. C. & Friend, R. H. Semiconductor Device Physics of Conjugated Polymers. in *Solid State Physics* (eds. Ehrenreich, H. & Spaepen, F.) vol. 49 1–149 (Academic Press, 1996).

230. Newman, C. R. *et al.* Introduction to Organic Thin Film Transistors and Design of n-Channel Organic Semiconductors. *Chem. Mater.* **16**, 4436–4451 (2004).

231. Talapin, D. V. & Murray, C. B. PbSe Nanocrystal Solids for n- and p-Channel Thin Film Field-Effect Transistors. *Science* **310**, 86–89 (2005).

232. Grozema, F. C. & Siebbeles, L. D. A. Mechanism of charge transport in self-organizing organic materials. *International Reviews in Physical Chemistry* **27**, 87–138 (2008).

233. Ulbricht, R., Hendry, E., Shan, J., Heinz, T. F. & Bonn, M. Carrier dynamics in semiconductors studied with time-resolved terahertz spectroscopy. *Rev. Mod. Phys.* **83**, 543–586 (2011).

234. Lunt, R. R., Giebink, N. C., Belak, A. A., Benziger, J. B. & Forrest, S. R. Exciton diffusion lengths of organic semiconductor thin films measured by spectrally resolved photoluminescence quenching. *Journal of Applied Physics* **105**, 053711 (2009).

235. Stranks, S. D. *et al.* Electron-Hole Diffusion Lengths Exceeding 1 Micrometer in an Organometal Trihalide Perovskite Absorber. *Science* **342**, 341–344 (2013).

236. Lee, E. M. Y. & Tisdale, W. A. Determination of Exciton Diffusion Length by Transient Photoluminescence Quenching and Its Application to Quantum Dot Films. *J. Phys. Chem. C* **119**, 9005–9015 (2015).

237. de Quilettes, D. W. *et al.* Impact of microstructure on local carrier lifetime in perovskite solar cells. *Science* **348**, 683–686 (2015).

238. Grumstrup, E. M., Gabriel, M. M., Cating, E. E. M., Van Goethem, E. M. & Papanikolas, J. M. Pump–probe microscopy: Visualization and spectroscopy of ultrafast dynamics at the nanoscale. *Chemical Physics* **458**, 30–40 (2015).

239. Zhu, T., Snaider, J. M., Yuan, L. & Huang, L. Ultrafast Dynamic Microscopy of Carrier and Exciton Transport. *Annual Review of Physical Chemistry* **70**, 219–244 (2019).

240. Delor, M., Weaver, H. L., Yu, Q. & Ginsberg, N. S. Imaging material functionality through three-dimensional nanoscale tracking of energy flow. *Nat. Mater.* **19**, 56–62 (2020).

241. Rose, T. S., Righini, R. & Fayer, M. D. Picosecond transient grating measurements of singlet exciton transport in anthracene single crystals. *Chemical Physics Letters* **106**, 13–19 (1984).

242. Wang, J. *et al.* Diffusion dynamics of valley excitons by transient grating spectroscopy in monolayer WSe2. *Appl. Phys. Lett.* **115**, 131902 (2019).

243. Gabriel, M. M. *et al.* Direct Imaging of Free Carrier and Trap Carrier Motion in Silicon Nanowires by Spatially-Separated Femtosecond Pump–Probe Microscopy. *Nano Lett.* **13**, 1336–1340 (2013).

244. Lo, S. S., Shi, H. Y., Huang, L. & Hartland, G. V. Imaging the extent of plasmon excitation in Au nanowires using pump-probe microscopy. *Opt. Lett., OL* **38**, 1265–1267 (2013).

245. Akselrod, G. M. *et al.* Visualization of exciton transport in ordered and disordered molecular solids. *Nature Communications* **5**, 3646 (2014).

246. Kulig, M. *et al.* Exciton Diffusion and Halo Effects in Monolayer Semiconductors. *Phys. Rev. Lett.* **120**, 207401 (2018).

247. Sridharan, A. *et al.* Time-resolved imaging of carrier transport in halide perovskite thin films and evidence for nondiffusive transport. *Phys. Rev. Materials* **3**, 125403 (2019).

248. Li, W. *et al.* Direct Characterization of Carrier Diffusion in Halide-Perovskite Thin Films Using Transient Photoluminescence Imaging. *ACS Photonics* **6**, 2375–2380 (2019).

249. Seitz, M. *et al.* Exciton diffusion in two-dimensional metal-halide perovskites. *Nat Commun* **11**, 2035 (2020).

250. Penzo, E. *et al.* Long-Range Exciton Diffusion in Two-Dimensional Assemblies of Cesium Lead Bromide Perovskite Nanocrystals. *ACS Nano* **14**, 6999–7007 (2020).

251. Saidaminov, M. I. *et al.* Multi-cation perovskites prevent carrier reflection from grain surfaces. *Nat. Mater.* **19**, 412–418 (2020).

252. Li, Z. *et al.* Interlayer Exciton Transport in MoSe2/WSe2 Heterostructures. *ACS Nano* **15**, 1539–1547 (2021).

253. deQuilettes, D. W. *et al.* Impact of Photon Recycling, Grain Boundaries, and Nonlinear Recombination on Energy Transport in Semiconductors. *ACS Photonics* **9**, 110–122 (2022).

254. Landsberg, P. T. *Recombination in Semiconductors*. (Cambridge University Press, Cambridge, 1992). doi:10.1017/CBO9780511470769.

255. Robert F. Pierret. *Semiconductor Device Fundamentals*. (Addison Wesley, 1996).

256. Donald A. Neamen. *Semiconductor Physics And Devices: Basic Principles*. (McGraw-Hill, 2011).

257. Strang, G. On the Construction and Comparison of Difference Schemes. *SIAM J. Numer. Anal.* **5**, 506–517 (1968).

258. Gilbert, J. R., Moler, C. & Schreiber, R. *Sparse Matrices in Matlab: Design and Implementation*. (1991).

259. Saidaminov, M. I. *et al.* High-quality bulk hybrid perovskite single crystals within minutes by inverse temperature crystallization. *Nat Commun* **6**, 7586 (2015).

260. Pazos-Outón, L. M. *et al.* Photon recycling in lead iodide perovskite solar cells. *Science* **351**, 1430–1433 (2016).

261. Courant, R., Friedrichs, K. & Lewy, H. Über die partiellen Differenzengleichungen der mathematischen Physik. *Math. Ann.* **100**, 32–74 (1928).

262. Dong, Y., Zou, Y., Song, J., Song, X. & Zeng, H. Recent progress of metal halide perovskite photodetectors. *J. Mater. Chem. C* **5**, 11369–11394 (2017).

263. Shi, Z. & Jayatissa, A. H. Perovskites-Based Solar Cells: A Review of Recent Progress, Materials and Processing Methods. *Materials* **11**, 729 (2018).

264. Zhang, Q. *et al.* Efficient metal halide perovskite light-emitting diodes with significantly improved light extraction on nanophotonic substrates. *Nat Commun* **10**, 727 (2019).

265. Yang, Y. *et al.* Top and bottom surfaces limit carrier lifetime in lead iodide perovskite films. *Nat Energy* **2**, 16207 (2017).

266. Ninomiya, S. & Adachi, S. Optical properties of wurtzite CdS. *Journal of Applied Physics* **78**, 1183–1190 (1995).

267. Christensen, N., Meyer, R., Knox, L. & Luey, B. Bayesian methods for cosmological parameter estimation from cosmic microwave background measurements. *Class. Quantum Grav.* **18**, 2677–2688 (2001).

268. Dunkley, J., Bucher, M., Ferreira, P. G., Moodley, K. & Skordis, C. Fast and reliable Markov chain Monte Carlo technique for cosmological parameter estimation. *Monthly Notices of the Royal Astronomical Society* **356**, 925–936 (2005).

269. Winslow, S. W., Shcherbakov-Wu, W., Liu, Y., Tisdale, W. A. & Swan, J. W. Characterization of colloidal nanocrystal surface structure using small angle neutron scattering and efficient Bayesian parameter estimation. *J. Chem. Phys.* **150**, 244702 (2019).

270. Eiben, A. E. & Smith, J. E. *Introduction to Evolutionary Computing*. (Springer Verlag, 2003).

271. Ashner, M. N., Winslow, S. W., Swan, J. W. & Tisdale, W. A. Markov Chain Monte Carlo Sampling for Target Analysis of Transient Absorption Spectra. *J. Phys. Chem. A* **123**, 3893–3902 (2019).

272. Ščajev, P., Miasojedovas, S. & Juršėnas, S. A carrier density dependent diffusion coefficient, recombination rate and diffusion length in MAPbI3 and MAPbBr3 crystals measured under one- and two-photon excitations. *J. Mater. Chem. C* **8**, 10290–10301 (2020).

273. Yi, H. T., Wu, X., Zhu, X. & Podzorov, V. Intrinsic Charge Transport across Phase Transitions in Hybrid Organo-Inorganic Perovskites. *Advanced Materials* **28**, 6509–6514 (2016).

274. Yang, Y. *et al.* Comparison of Recombination Dynamics in CH3NH3PbBr3 and CH3NH3PbI3 Perovskite Films: Influence of Exciton Binding Energy. *J. Phys. Chem. Lett.* **6**, 4688–4692 (2015).

275. Kippelen, B., Grun, J. B., Hönerlage, B. & Levy, R. Transient optical nonlinearities in CdS studied by laser-induced grating spectroscopy at room temperature. *J. Opt. Soc. Am. B, JOSAB* **8**, 2363–2369 (1991).

276. Riblet, Ph. *et al.* Determination of the anisotropic ambipolar diffusion coefficient of CdS at room temperature. *Optical Materials* **3**, 139–144 (1994).

277. F. A. Kröger, H. J. Vink, J. Volger. Temperature Dependence of the Hall Effect and the Resistivity of CdS Single Crystals. *Philips Res. Rep.* **10**, 39 (1955).

278. Onuki, M. & Hase, N. Hall Mobility of Holes in CdS Crystals. *J. Phys. Soc. Jpn.* **20**, 171–171 (1965).

279. Li, H. P., Kam, C. H., Lam, Y. L. & Ji, W. Optical nonlinearities and photo-excited carrier lifetime in CdS at 532 nm. *Optics Communications* **190**, 351–356 (2001).

280. Staub, F. *et al.* Beyond Bulk Lifetimes: Insights into Lead Halide Perovskite Films from Time-Resolved Photoluminescence. *Phys. Rev. Applied* **6**, 044017 (2016).

281. Crothers, T. W. *et al.* Photon Reabsorption Masks Intrinsic Bimolecular Charge-Carrier Recombination in CH3NH3PbI3 Perovskite. *Nano Lett.* **17**, 5782–5789 (2017).

282. Kholkin, A. L., Pertsev, N. A. & Goltsev, A. V. Piezoelectricity and Crystal Symmetry. in *Piezoelectric and Acoustic Materials for Transducer Applications* (eds. Safari, A. & Akdoğan, E. K.) 17–38 (Springer US, Boston, MA, 2008). doi:10.1007/978-0-387-76540-2_2.

283. Daum, W., Krause, H.-J., Reichel, U. & Ibach, H. Identification of strained silicon layers at Si-${\mathrm{SiO}}_{2}$ interfaces and clean Si surfaces by nonlinear optical spectroscopy. *Phys. Rev. Lett.* **71**, 1234–1237 (1993).

284. Manaka, T., Lim, E., Tamura, R. & Iwamoto, M. Direct imaging of carrier motion in organic transistors by optical second-harmonic generation. *Nature Photon* **1**, 581–584 (2007).

285. Manaka, T. & Iwamoto, M. Optical second-harmonic generation measurement for probing organic device operation. *Light Sci Appl* **5**, e16040–e16040 (2016).

286. Chen, X., Nadiarynkh, O., Plotnikov, S. & Campagnola, P. J. Second harmonic generation microscopy for quantitative analysis of collagen fibrillar structure. *Nature Protocols* **7**, 654–669 (2012).

287. Huse, N., Schönle, A. & Hell, S. W. Z-polarized confocal microscopy. *JBO* **6**, 480 (2001).

288. Yew, E. Y. S. & Sheppard, C. J. R. Second harmonic generation polarization microscopy with tightly focused linearly and radially polarized beams. *Optics Communications* **275**, 453–457 (2007).

289. Biss, D. P. & Brown, T. G. Polarization-vortex-driven second-harmonic generation. *Opt. Lett., OL* **28**, 923–925 (2003).

290. Stalder, M. & Schadt, M. Linearly polarized light with axial symmetry generated by liquid-crystal polarization converters. *Opt. Lett., OL* **21**, 1948–1950 (1996).

291. Kozawa, Y. & Sato, S. Observation of the longitudinal field of a focused laser beam by second-harmonic generation. *J. Opt. Soc. Am. B, JOSAB* **25**, 175–179 (2008).

292. Fang, C. *et al.* Efficient Second-Harmonic Generation from Silicon Slotted Nanocubes with Bound States in the Continuum. *Laser & Photonics Reviews* **16**, 2100498 (2022).

293. Wang, F. X. *et al.* Surface and bulk contributions to the second-order nonlinear optical response of a gold film. *Phys. Rev. B* **80**, 233402 (2009).

294. Johnson, P. B. & Christy, R. W. Optical Constants of the Noble Metals. *Phys. Rev. B* **6**, 4370–4379 (1972).

295. Wang, T., Halaney, D., Ho, D., Feldman, M. D. & Milner, T. E. Two-photon luminescence properties of gold nanorods. *Biomed. Opt. Express, BOE* **4**, 584–595 (2013).

296. Ngoc, L. L. T., Wiedemair, J., Berg, A. van den & Carlen, E. T. Plasmon-modulated photoluminescence from gold nanostructures and its dependence on plasmon resonance, excitation energy, and band structure. *Opt. Express, OE* **23**, 5547–5564 (2015).

297. Malitson, I. H. Interspecimen Comparison of the Refractive Index of Fused Silica*,†. *J. Opt. Soc. Am., JOSA* **55**, 1205–1209 (1965).

298. Fork, R. L., Martinez, O. E. & Gordon, J. P. Negative dispersion using pairs of prisms. *Opt. Lett., OL* **9**, 150–152 (1984).

299. Technology and Applications Center. Application Note 29: Prism Compressor for Ultrashort Laser Pulses. (2019).

300. Earl Hergert. Detectors: Guideposts on the Road to Selection. https://www.photonics.com/Articles/Detectors_Guideposts_on_the_Road_to_Selection/a25535.

301. Hamamatsu Photonics K.K. Photomultiplier Technical Handbook. (1994).

302. Armstrong, S. R., Pemble, M. E., Stafford, A. & Taylor, A. G. Optical second-harmonic generation from GaAs(100) surfaces: the influence of H2. *J. Phys.: Condens. Matter* **3**, S363 (1991).

303. Zhang, C. Sum Frequency Generation Vibrational Spectroscopy for Characterization of Buried Polymer Interfaces. *Applied Spectroscopy* (2017) doi:10.1177/0003702817708321.

304. Di Cicco, A. *et al.* Broadband optical ultrafast reflectivity of Si, Ge and GaAs. *Sci Rep* **10**, 17363 (2020).

305. Rogers, J. E. *et al.* Observation and Interpretation of Annulated Porphyrins: Studies on the Photophysical Properties of meso-Tetraphenylmetalloporphyrins. *J. Phys. Chem. A* **107**, 11331–11339 (2003).

306. Nishimura, N. *et al.* Photon Upconversion from Near-Infrared to Blue Light with TIPS-Anthracene as an Efficient Triplet–Triplet Annihilator. *ACS Materials Lett.* **1**, 660–664 (2019).

307. Zhang, X., Johnson, J. P., Kampf, J. W. & Matzger, A. J. Ring Fusion Effects on the Solid-State Properties of α-Oligothiophenes. *Chem. Mater.* **18**, 3470–3476 (2006).

308. Namepetra, A., Kitching, E., F. Eftaiha, A., G. Hill, I. & C. Welch, G. Understanding the morphology of solution processed fullerene-free small molecule bulk heterojunction blends. *Physical Chemistry Chemical Physics* **18**, 12476–12485 (2016).

309. Levenson, M. D. & Eesley, G. L. Polarization selective optical heterodyne detection for dramatically improved sensitivity in laser spectroscopy. *Appl. Phys.* **19**, 1–17 (1979).

310. Stiopkin, I. V., Jayathilake, H. D., Bordenyuk, A. N. & Benderskii, A. V. Heterodyne-Detected Vibrational Sum Frequency Generation Spectroscopy. *J. Am. Chem. Soc.* **130**, 2271–2275 (2008).

311. Wilcox, D. E., Sykes, M. E., Niedringhaus, A., Shtein, M. & Ogilvie, J. P. Heterodyne-detected and ultrafast time-resolved second-harmonic generation for sensitive measurements of charge transfer. *Opt. Lett., OL* **39**, 4274–4277 (2014).

312. Burdett, J. J., Gosztola, D. & Bardeen, C. J. The dependence of singlet exciton relaxation on excitation density and temperature in polycrystalline tetracene thin films: Kinetic evidence for a dark intermediate state and implications for singlet fission. *The Journal of Chemical Physics* **135**, 214508 (2011).

313. Frolov, S. V., Kloc, Ch., Schön, J. H. & Batlogg, B. Transient spectroscopy of tetracene single crystals. *Chemical Physics Letters* **334**, 65–68 (2001).

314. Thorsmølle, V. K. *et al.* Morphology Effectively Controls Singlet-Triplet Exciton Relaxation and Charge Transport in Organic Semiconductors. *Phys. Rev. Lett.* **102**, 017401 (2009).

315. Grumstrup, E. M., Johnson, J. C. & Damrauer, N. H. Enhanced Triplet Formation in Polycrystalline Tetracene Films by Femtosecond Optical-Pulse Shaping. *Phys. Rev. Lett.* **105**, 257403 (2010).

316. Burdett, J. J., Müller, A. M., Gosztola, D. & Bardeen, C. J. Excited state dynamics in solid and monomeric tetracene: The roles of superradiance and exciton fission. *The Journal of Chemical Physics* **133**, 144506 (2010).

317. Pabst, M. & Köhn, A. Implementation of transition moments between excited states in the approximate coupled-cluster singles and doubles model. *The Journal of Chemical Physics* **129**, 214101 (2008).

318. G. Vaubel & H. Baessler. Delayed Fluorescence and Triplet Lifetime in Tetracene Crystals. *Basic Solid State Physics* **37**, K31–K34 (1970).

319. Fleming, G. R., Millar, D. P., Morris, G. C., Morris, J. M. & Robinson, G. W. Exciton fission and annihilation in crystalline tetracene. *Aust. J. Chem.* **30**, 2353–2359 (1977).

320. Campillo, A. J., Hyer, R. C., Shapiro, S. L. & Swenberg, C. E. Exciton interactions in crystalline tetracene studied by single picosecond pulse excitation. *Chemical Physics Letters* **48**, 495–500 (1977).

321. van Stokkum, I. H. M., Larsen, D. S. & van Grondelle, R. Global and target analysis of time-resolved spectra. *Biochimica et Biophysica Acta (BBA) - Bioenergetics* **1657**, 82–104 (2004).

322. Fernández-Terán, R. J., Sucre-Rosales, E., Echevarria, L. & Hernández, F. E. A Sweet Introduction to the Mathematical Analysis of Time-Resolved Spectra and Complex Kinetic Mechanisms: The Chameleon Reaction Revisited. *J. Chem. Educ.* **99**, 2327–2337 (2022).

323. Mullen, K. M., Vengris, M. & van Stokkum, I. H. M. Algorithms for separable nonlinear least squares with application to modelling time-resolved spectra. *J Glob Optim* **38**, 201–213 (2007).

324. Sabbah, A. J. & Riffe, D. M. Measurement of silicon surface recombination velocity using ultrafast pump–probe reflectivity in the near infrared. *Journal of Applied Physics* **88**, 6954–6956 (2000).

325. Gunnella, R. *et al.* Ultrafast reflectivity dynamics of highly excited Si surfaces below the melting transition. *Phys. Rev. B* **94**, 155427 (2016).

326. Perkinson, C. F. Interfacial engineering and spectroscopy of spin-triplet excitons for singlet fission sensitization of silicon solar cells. (Massachusetts Institute of Technology, 2023).

327. Kafle, T. R. *et al.* Charge Transfer Exciton and Spin Flipping at Organic–Transition-Metal Dichalcogenide Interfaces. *ACS Nano* **11**, 10184–10192 (2017).

328. Klimov, V. I. Optical Nonlinearities and Ultrafast Carrier Dynamics in Semiconductor Nanocrystals. *J. Phys. Chem. B* **104**, 6112–6123 (2000).

329. Walters, G. *et al.* The quantum-confined Stark effect in layered hybrid perovskites mediated by orientational polarizability of confined dipoles. *Nat Commun* **9**, 4214 (2018).

330. Sadighian, J. C., Wilson, K. S., Crawford, M. L. & Wong, C. Y. Evolving Stark Effect During Growth of Perovskite Nanocrystals Measured Using Transient Absorption. *Front. Chem.* **8**, (2020).

331. Turkay, D., Koroglu, C. & Yerci, S. Analysis of Field-Effect Passivation in Textured and Undiffused Silicon Surfaces. *Phys. Rev. Appl.* **12**, 034026 (2019).

332. Forrest, S. R. Ultrathin Organic Films Grown by Organic Molecular Beam Deposition and Related Techniques. *Chem. Rev.* **97**, 1793–1896 (1997).

333. Proudian, A. P. *et al.* Effect of Diels–Alder Reaction in C60-Tetracene Photovoltaic Devices. *Nano Lett.* **16**, 6086–6091 (2016).

334. Hung, R. R. & Grabowski, J. J. A precise determination of the triplet energy of carbon (C60) by photoacoustic calorimetry. *J. Phys. Chem.* **95**, 6073–6075 (1991).

335. Goldoni, A., Cepek, C. & Modesti, S. The surface triplet exciton of C60(111). *Synthetic Metals* **77**, 189–194 (1996).

336. Yuan, J. *et al.* Single-Junction Organic Solar Cell with over 15% Efficiency Using Fused-Ring Acceptor with Electron-Deficient Core. *Joule* **3**, 1140–1151 (2019).

337. Aulin, Y. V. *et al.* Morphology-Independent Efficient Singlet Exciton Fission in Perylene Diimide Thin Films. *ChemPlusChem* **83**, 230–238 (2018).

338. Anthony, J. E. Functionalized Acenes and Heteroacenes for Organic Electronics. *Chem. Rev.* **106**, 5028–5048 (2006).

339. Purdy, M. *et al.* Aza-Cibalackrot: Turning on Singlet Fission Through Crystal Engineering. *J. Am. Chem. Soc.* **145**, 10712–10720 (2023).

340. Wang, L. *et al.* Interfacial Trap-Assisted Triplet Generation in Lead Halide Perovskite Sensitized Solid-State Upconversion. *Advanced Materials* **33**, 2100854 (2021).

341. Y. Tayebjee, M. J., R. Clady, R. G. C. & W. Schmidt, T. The exciton dynamics in tetracene thin films. *Physical Chemistry Chemical Physics* **15**, 14797–14805 (2013).

342. Nahm, R. K., Bullen, H. J., Suh, T. & Engstrom, J. R. Faster Is Smoother and So Is Lower Temperature: The Curious Case of Thin Film Growth of Tetracene on SiO2. *J. Phys. Chem. C* **121**, 8464–8472 (2017).